# Numerical and Experimental Indoor Channel Analysis for LOS-NLOS Identification at 60 GHz

Pengfei Lyu

Sorbonne Université

Ecole Doctorale Informatique, Télécommunications et Electronique

*Laboratoire Génie électrique et électronique de Paris*

# Numerical and Experimental Indoor Channel Analysis for LOS - NLOS Identification at 60 GHz

Par Pengfei Lyu

Thèse de doctorat d'électronique

Dirigée par Aziz Benlarbi-Delaï

Présentée et soutenue publiquement le 17 juin 2020

Devant un jury composé de :

| | |
|---|---|
| Mme. Martine Liénard, *Professeure* | Rapporteure |
| M. Nel Samama, *Professeur* | Rapporteur |
| M. Sébastien Tixeuil, *Professeur* | Examinateur |
| M. Jean-Christophe Cousin, *Maître de conférences HDR* | Examinateur |
| M. Aziz Benlarbi-Delaï, *Professeur* | Directeur de thèse |
| M. Julien Sarrazin, *Maître de conférences HDR* | Encadrant de thèse |
| M. Zhuoxiang Ren, *Professeur* | Invité |

*Dédicace*

# Acknowledgement

I wish to express my deepest gratitude to my supervisor, Professor Aziz Benlarbi-Delaï. He convincingly guided and encouraged me to be professional and work in the correct direction, even when the road got tough. I also would like to show my deepest gratitude to my co-supervisor, Associate Professor Julien Sarrazin. It is whole-heartedly appreciated that his great advice for my study proved monumental towards the success of this study. Meanwhile, I am indebted to Professor Zhuoxiang Ren. His kind recommendation gives me the precious opportunity to involve my studies and engage in this field. Without persistent help from the above three professors, the aim of this thesis would not have been realized.

I would like to pay my special regards to all the members of my jury: Professor Martine Liénard, Professor Nel Samama, Professor Sébastien Tixeuil, Conference Master HRD Jean-Christophe Cousin. Their suggestions enormously improve the critical details, so that make the thesis mature.

The measurement facilities in the electronic department of Laboratoire Génie électrique et électronique de Paris, in Sorbonne Université, fundamentally supplied the necessary experimental condition. I would like to recognize all of the stuff in the lab for the invaluable assistance that you all provided during this study.

Finally, I wish to acknowledge the great love of my parents. They kept me going on with their support and encouragement.

# Contents

# Introduction

Wireless localization is the process of determining the coordinates of an object in a 2D or 3D physical space. The outdoor wireless localization, represented mainly by the Global Positioning System (GPS), has experienced a great success since its birth in the 1990s. The enormous potential applications make the indoor wireless localization also becoming an attractive field of study in recent years. In healthcare, positioning can be used to track and authenticate moving people or objects to reduce risks to patients. In smart environments, positioning can be applied to monitoring and alarm systems adapted to accidents and theft, automatically switching to save energy and monitor machines, thus improving the automation of industrial installations. In the field of smart entertainment, smart games use localization to adapt the player's condition by detecting its position, motion, and acceleration. The indoor localization is expected replicate the success of the outdoor location.

Among all the current localizing technologies, time-based localization with Ultra-Wideband (UWB) is among the most accurate, especially thanks to its capabilities to discriminate multipath. The 60 GHz frequency band, with up to 8.64 GHz bandwidth, is expected to combine accurate UWB localization and high-speed wireless communication in 5G. One of the bottlenecks in wireless localization is due to the complex phenomenon taking place in the environment (such as reflection, diffraction, etc.) within which electromagnetic waves propagate. Indeed, the bias induced by the multipath is the principal source of error for localization. Especially, when the direct path, i.e., the Line-Of-Sight (LOS), is blocked, the transmission becomes Non-Line-Of-Sight (NLOS), in which the absence of the information about the true distance and direction leads the localizing system to be entirely invalid. Unfortunately, the blockage of 60 GHz direct path is extremely frequent because of the high directivity of such communication, impacting hardly the quality and security of millimeter wave wireless communication.

For communication purpose, LOS blockage is typically mitigated thanks to beam steering capability. Indeed, at 60 GHz, directional antennas are considered in order to mitigate the large free space attenuation and to overcome blockage scenario. Tx and/or Rx antennas scan the angular space in order to find the best suitable link, e.g., leading to the highest received power, which may occur either on a LOS or an NLOS path. This process is known as beam training. Nevertheless, if the communication uses an NLOS link and if this later is used to estimate the range and the direction of the receiver with respect to the transmitter for instance, a large bias is therefore introduced. Consequently; the knowledge of whether the communication takes place on a LOS or on an NLOS component is an important feature. It can provide the system with an indicator that informs if the current position is likely to be well estimated (LOS case) or not (NLOS case). More than simply offering a confidence indicator, it can also be used to mitigate NLOS effect. So, identifying NLOS transmission appears to be an important step towards accurate positioning.

This work considers that the beam training process makes readily available the angular channel knowledge at Tx and/or Rx in the form of a 2D power angular spectrum. Using this spectrum, the different angular clusters are first identified. Then, high-order statistics moments are calculated for each cluster in order to classify them. In particular, it has been found that the kurtosis enables discriminating LOS from

NLOS clusters with promising probabilities. The LOS-NLOS identification in the 60 GHz band is thus the objective of this thesis and the main contributions are twofold:

- Design an efficient clustering method, inspired from image processing, to statistically analyze power angular spectrum while preserving angular cluster shapes;
- Classify and identify LOS and NLOS clusters within the channel using its statistics.

The thesis is organized as follow:

1. In the first chapter, the background of this study is introduced. The potential applications and current technologies of wireless localization are briefly summarized. The trends of 5G wireless communication and the advantages of 60 GHz spectrum are highlighted. After introducing the basic theory of radio channel modeling, current studies on the blockage of direct path for millimeter wave communication are presented, including the blockages caused by outdoor buildings and indoor human activities.

2. In chapter 2, the state of the art regarding NLOS identification is introduced. After briefly exploring the aim of current NLOS identification, the statistical differences between LOS and NLOS transmission are summarized. The current metrics for identification are reviewed in details. The parametric and non-parametric method of identification methods are both reviewed. Clustering is also an important step of NLOS identification and channel modeling. Two classes of clustering algorithms, hierarchical and partitional method, are presented. Then, issues encountered with the widely used K-Power-Means algorithm are highlighted.

3. In chapter 3, the principle of an original spatial clustering method, based on watershed segmentation, is presented in details. Indeed, a clustering method that conserves intact the angular shape of clusters is of utmost importance in the LOS/NLOS identification performed. Furthermore, to obtain meaningful results, a large number of channels is to be analyzed, thereby necessitating to perform clustering many times as well. Consequently, a fast method is required. The watershed segmentation, introduced in this chapter 3 to group power clusters within the power angular spectrum, is a method inspired from image processing. To validate the feasibility of the proposed approach, simulations are performed based on the data generated by the IEEE 802.11ad 60 GHz standard. To evaluate the performance, segmentation by watershed is compared to K-Power-Means and a modified version of K-Power-Means.

4. In chapter 4, the NLOS identification is achieved in both simulation and measurement. According to the 60 GHz channel space-time structure, NLOS clusters are identified after spatial clustering. With the help of antenna directional radiation properties, the symmetry of the cluster in terms of power, time-domain kurtosis, and frequency autocorrelation are introduced as suitable identification metrics. Maximum likelihood Ratio and Artificial Neural Network are used as identification methods. Simulation results are obtained based on the PAS generated by the IEEE 802.11ad channel model, while the measurements are conducted in a laboratory scenario. The performance is evaluated with the error probability of identification.

5. A general conclusion and perspectives end this report.

# Chapter 1

# Context and Background

## Contents



## 1.1 Introduction

The huge potential of new applications provided by the next millimeter wave 5G standard, and particularly the accurate localization function which is built in the system, appeal to new solutions to cope with the main drawbacks generally associated with the indoor positioning system. After a brief presentation of the context dealing with communication and/or localization-based applications, we present the required scientific and technical backgrounds, in terms of relevant metrics, and in terms of channel modeling, to

handle such a study, and we discuss the current wireless localization technologies, operating in 60 GHz band. We conclude this chapter by highlighting the main objectives we target.

# 1.2 Indoor Wireless Localization

## 1.2.1 Potential applications of indoor wireless localization

Wireless localization is the process of determining the coordinates of an object by detecting electromagnetic waves. Depending on the scenarios of application, it can be divided into outdoor and indoor localization. The outdoor wireless localization represented mainly by Global Positioning System (GPS) has taken a great success since its birth in the 1990s: the navigation for aviation, marine, and driving, geographic information for agriculture and environment protection, localization for disaster relief and personal recreation, all relay on GPS [1].

**(a)** **(b)**


Figure 1.1 Current application of indoor localization: (a) transport robot in factory; (b) Amazon Go convenience store without checkout.

The potential applications of indoor wireless positioning are also very abundant. In healthcare, location can be used to track and authenticate moving people or objects to reduce risks to patients. In smart environments, location can be applied to monitoring and alarm systems adapted to accidents and theft, automatically switching to save energy and monitor machines, thus improving the automation of industrial installations. In the field of smart entertainment, smart games use localization to adapt the player's condition by detecting position, motion, and acceleration [2]. Recently, transport robots in factories and Amazon Go convenience store without checkout have been achieved as shown in Figure 1.1. All the above applications need a precise location of users. The indoor localization will replicate the success of the outdoor location. The opportunity for indoor location is attractive: market research shows that the global market for indoor positioning represented approximately US$5.22 billion in 2016, and is expected to reach US$40.99 billion in 2022, compound annual growth rate (composite between 2017-2022) is 42.0% [3].

### 1.2.2 Wireless localization techniques

There are two important metrics to evaluate a localization performance: accuracy and precision. Accuracy is the degree to which the measurement is close to the correct value. Precision is the repeatability of the measurement. The two factors can be used as indicators to evaluate the errors of a positioning system. In addition to the accuracy and precision, the complexity of a localization algorithm, the robustness and scalability of the system, and the cost are also metrics usually considered for localization system design. The performance metrics benchmarking for indoor wireless localization are listed in Table 1.1.

Table 1.1 Performance metrics benchmarking for indoor wireless localization

| | |
|---|---|
| Accuracy | Mean distance error is the average Euclidean distance between the estimated location and the actual location. The accuracy can be considered to be a potential bias or systematic effect/offset of a positioning system. |
| Precision | Evaluate how consistently the system works and reveals the variation in its performance over many trials. The cumulative probability functions (CDF) of the distance error is used for measuring the precision of a system. |
| Complexity | Computing complexity of the positioning algorithm. |
| Robustness | High robustness makes the localization performs normally even when some signals are not available, or when some of the signal features have never be seen before |
| Scalability | The scalability of a system ensures a normal positioning operation when the positioning scope gets large. A location system may need to scale on two axes: geography and density. Geographic scale means that the area or volume is covered. Density means the number of units located per unit geographic area/space per period. |
| Cost | The cost of a positioning system may depend on many important factors, including money, time, space, weight, and energy. |

Localization can utilize almost all of the existing technologies of wireless communication. The mainstream indoor localizing technologies are GPS, cellular localization, Radio-Frequency Identification (RFID), Wireless Local Area Network (WLAN), Bluetooth, Ultra-wide Band (UWB). According to the above six evaluation criteria, these localization technologies have their advantages and disadvantages. GPS is the most robust positioning system, but the blockage of the satellite signal by the buildings can drastically reduce its coverage, accuracy, and robustness. Positioning systems based on existing telecommunications infrastructure are highly robust and cost-effective. However, indoor localization using outdoor equipment exhibits the same problem of coverage and accuracy as GPS. RFID is widely used for the identification of objects thanks to its low cost, low complexity, high flexibility, and high scalability. However, the range of passive RFID is limited. The essence of active RFID is part of WLAN. WLAN and Bluetooth are the most popular for indoor public hotspots because of low cost. The accuracy can be improved by increasing the bandwidth and modifying the positioning method — the wideband of UWB systems exhibits to high accuracy (< 10m).

However, the wideband makes the dispersion caused by the multipath phenomena, and the corresponding positive bias become significant [4]. The performance of these technologies is summarized in Table 1.2. According to the performance summary, UWB is an ideal candidate for excellent positioning

accuracy and accuracy. In practice, the combination of UWB and WLAN is a potential direction for future indoor positioning. However, UWB operating band of 3.1 GHz - 10 GHz is in practice more limited, especially in Europe, due to spectrum regulation mask. Waveform with a 500 MHz bandwidth are therefore typically used in commercial UWB systems such as Ubisense, BeSpoone, Decawave…

Table 1.2 Performance of current technologies of localization from review references [5-9]

| | Accuracy | Precision | Complexity | Scalability | Robustness | Cost |
|---|---|---|---|---|---|---|
| GPS | 5-50m | 99% within 10m | High | Good 2D/3D | Poor | High |
| Cellular | 5-20m | 99.8% within 10m | Medium | Good 2D/3D | Medium | Medium |
| RFID | 10-15cm | 99% within 0.3m | Low | Good 2D | Medium | Low |
| WLAN | 15cm-5m | 90% within 5m | Low | Good 2D/3D | Good | Low |
| Bluetooth | 2-5m | 95% within 2m | Medium | Good 2D | Poor | Low |
| UWB | 10cm | 99% within 0.3m | Medium | Good 2D/3D | Poor | Medium |

## 1.2.3 The basic theory of triangulation-based localization

There are two types of radio-localization. The first type is scene-based localization, such as fingerprinting [10]. This approach performs well but necessitates a priori knowledge regarding the spatial propagation channel which is not easy to obtain in practice and to update as the environments varies. The second type of positioning is triangulation. The process is divided into three steps. In the first step, the distance information between the transmitter and the receiver is extracted from specific characteristic parameters of the received signal, such as received signal strength (RSS), angle of arrival (AOA), or time of arrival (TOA). Since the purpose of this step is to obtain the distance between the terminal and the base station, in other words, the possible range in which the terminal near the base station exists, this step is called "ranging." The second step is to find the coordinates of the terminal through geometric relationships, which is "positioning" the terminal. Because of the error in the measured distance, the coordinates obtained from the measured distance are not accurate. Therefore, the third step is to mitigate the error and statistically estimate the relatively accurate coordinates, which is "error estimation". The procedure of localization is shown in Figure 1.2. UWB localization is mainly used with the triangulation method [11].

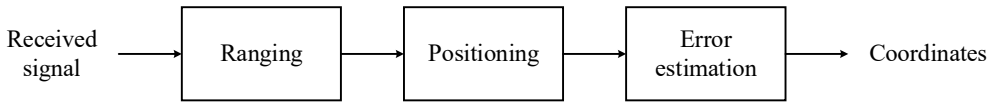


Figure 1.2 Procedure of localization

### 1.2.3.1 Ranging

There are four kinds of ranging methods: RSS, AOA, TOA, and Time Difference of Arrival (TDOA). The principles of the methods are shown in Figure 1.3. If the relationship between distance and power loss is known, the distance between the base station (BS) and the user equipment (UE) can be estimated from

the received signal strength. As shown in Figure 1.3 (a), the possible range between the two nodes in a plane is the curve of the circle in which the UEs locate. The relation about the RSS is the path loss modeling as presented following.

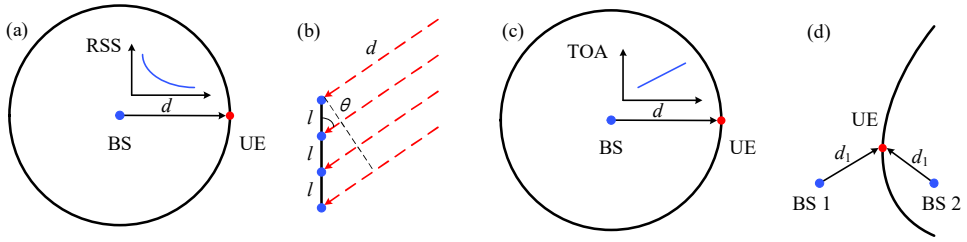


Figure 1.3 Schematic of ranging methods: (a) RSS; (b) AOA; (c) TOA; (d) TDOA

$$P(d)[dB] = P_0[dB] - 10\log_{10}\left(\frac{d}{d_0}\right) + \chi \tag{1.1}$$

Where $P(d)$ is a function of the average received power to distance $d$ in dB; $P_0$ is the received power at the reference distance $d_0$; $\chi$ is an unbiased variance caused by the shadowing effect, which is difficult to know a priori.

The antenna array-based localization commonly uses AOA-based methods. The distance between adjacent antennas array elements is known. If the BS-UE distance $d$ is large enough, the received wave can be assumed to be a plane wave so that the AOA at each element in the array is the same. As shown in Figure 1.3 (b), the delay of each component is:

$$\tau_i = \frac{d}{c} + \frac{l_i \sin\theta}{c} \tag{1.2}$$

Where the indication $i$ is the element index, $l_i$ is the space between the neighboring elements, $\theta$ is the AOA.

The propagation distance is proportional to the propagation time. So the delay of the signal can be used to evaluate the distance, as shown in Figure 1.3 (c).

$$\tau = \frac{d}{c} \tag{1.3}$$

Where $\tau$ is the propagation delay between UE and BS, and $c$ is the speed of light in free space.

The TDOA method is another method based on time estimation. Unlike the estimation of the absolute propagation time of the TOA, the TDOA compares the difference of delay between the signals received from two BSs.

$$\Delta\tau = \tau_1 - \tau_2 = \frac{d_1 - d_2}{c} \tag{1.4}$$

The delay difference forms a curve from which the distance from a point on the curve to two BSs is constant. So this curve in a plane is an hyperbola shown in Figure 1.3 (d). The relative delay between the two signals can be obtained by correlating the received signal with a reference signal for instance. Compared to the TOA, the transmitter and the receiver do not need synchronization with each other. Among these four methods, the attenuation severely influences RSS, and accuracy performance is usually less than angle and time-based methods.

### 1.2.3.2 Positioning

The purpose of the positioning is to find the intersection of the ranging curves obtained by base stations. UE coordinate, $(x, y)$, can be calculated with each coordinate of the $i$-th BS, $(x_i, y_i)$, and the corresponding BS-UE distance $d_i$. For RSS and TOA, $d_i$ is calculate with:

$$d_i = \sqrt{(x - x_i)^2 + (y - y_i)^2} \tag{1.5}$$

For AOA, the AOA directions are:

$$\tan\phi_1 = \frac{y - y_1}{x - x_1}, \quad \tan\phi_2 = \frac{y - y_2}{x - x_2} \tag{1.6}$$

For TDOA, $d_i$ is calculate with:

$$\Delta d_{i0} = d_i - d_0 = \sqrt{(x - x_i)^2 + (y - y_i)^2} - \sqrt{(x - x_0)^2 + (y - y_0)^2} \tag{1.7}$$

With $N$ base stations, equations with the variable of the UE coordinates are established. For positioning the 2D UE coordinates, at least 2 BS are needed to solve equations with two variables $x$ and $y$; while, to determine the 3D UE coordinate $(x, y, z)$, at least 3 BS are necessary.

### 1.2.3.3 Errors in time-based localization

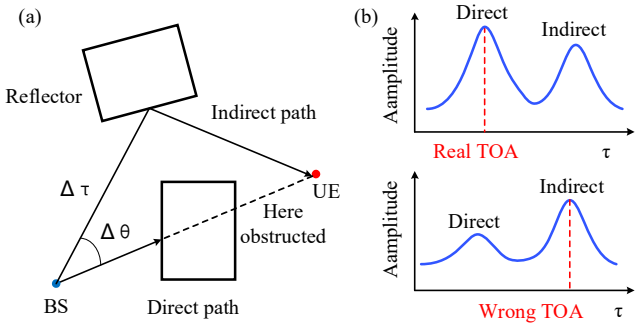


Figure 1.4 Error source of localization

In addition to the errors caused by the thermal noise of the receiver, the main errors in localization are caused by multipaths, which are the reflected paths and the diffracted paths. The reflected path is longer than the direct path, so the signal transmitted along the indirect path reaches the UE later than the direct path, as shown in Figure 1.4 (a). The delay of the indirect path causes the paths to overlap. If the direct path is obstructed, the signal of the direct path will be attenuated such that the direct path signal at the first peak is weaker than the nest peak, as shown in Figure 1.4 (b).

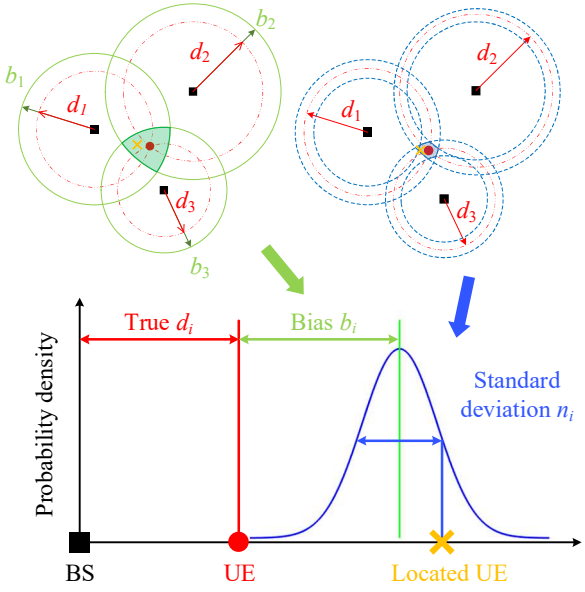


Figure 1.5 Bias and variation induced by the multi-indirect paths

Since both TOA and TDOA are classically based on the measurement of the strongest pulse delay, the misjudgment on the peak cause a possible large deviation on the estimated distance. Furthermore, indirect path with a TOA close to the direct path typically induces inaccuracy in the TOA estimation. The influence of the indirect path on ranging error is shown in Figure 1.5.

The estimated distance $\hat{d}_i$ between the terminal and each of the base station is the sum of the real distance $d_i$, bias $b_i$, and standard deviation $n_i$ as the following formula:

$$\hat{d}_i = d_i + b_i + n_i \tag{1.8}$$

The multipath causing $b_i$, and $n_i$ should be mitigated to enhance the ranging accuracy. Direct path transmission is called Line of Sight (LOS) transmission. If the direct path is blocked and only the indirect path is reserved, all received signal will travel along a larger distance than the actual one between the transmitter and receiver without carrying any information about the exact distance. The transmission of no direct path between the BS and the UE is called Non-Line of Sight (NLOS) transmission. Since there is no information about the exact distance, localization cannot be performed accurately. For AOA and RSS, errors are introduced with a similar principle: the estimated positions follow a biased distribution with a variance.

# 1.3 Millimeter-Wave Localization and Communication

## 1.3.1 Wireless communication in the millimeter band

Millimeter-wave frequency bands have become popular recently as large bandwidth from 500 MHz up to a few Gigahertz are typically available, which enables high data rates. However, operating at mm-wave frequency requires to deal with large free-space attenuation and link blockage. Directional transmission techniques, such as beamforming, can steer the beam away from obstacles, providing extra spatial gain to overcome high attenuation. Beamforming increases the output power by shifting the signal phase of each antenna element to combine low power beams into a beam pointing in a particular direction. With a directional antenna, the typical coverage range of millimeter waves in outdoor situations can be increased to 200 m without interruption [12]. With beamforming, 500 Mbs communication links can be achieved at 28 GHz carrier frequency and 500 MHz bandwidth even in outdoor situations [13]. Based on beamforming, standardization organizations have considered millimeter waves as candidates for the 5G spectrum. Meanwhile, it is potentially used in indoor environments for wireless backhaul and cellular access [14].

## 1.3.2 Advantages of millimeter band for 5G

The fifth generation of wireless networks (5G) is the next-generation wireless communication that satisfies the requirements of ultra-high-speed and robustness of communication. Compared to 4G, 5G system performance and user experience are expected to be significantly improved. The leading indicators of wireless communication are data rate, robustness, latency, power consumption, and cost. The total data rate and peak rate evaluate the transmission rate; the edge rate characterizes robustness. The Next Generation Mobile Network (NGMN) defines the following requirements that the 5G standard should meet [15]: the data rate per thousand users is 10 Mbps; the data rate in large cities is 100 Mbps; in the office environment, the transmission rate is more than 1 Gbps for multiple users; the real-time wireless sensor connection number is more than thousands. Compared with 4G, the spectrum efficiency is much improved, the coverage is improved, the signaling efficiency is enhanced, and the delay is significantly reduced compared with Long Term Evolution (LTE). Based on these requirements, mainstream standardization organizations have released their plans or frameworks. In 2018-2019, 3GPPP released the 15th version standard for 5G radio [16]. In the United States, the Institute of Electrical and Electronics Engineers (IEEE) released the white paper of 5G [17] to stimulate industry dialogue to address all issues of 5G development in 2020 simultaneously. In China, IMT-2020 (5G) published a white paper for the 5G network architecture design [18].

To address the requirements, especially in terms of data rate, 5G considers the use of millimeter wave bands. So far, the spectrum above 24 GHz an up to 52.6 GHz has been given considerations in the 3GPP to support broadband communications. Frequency band ranging such as 24.25-29.5 GHz and 37-40 GHz has been identified for instance. In the release 17 currently under discussions, the spectrum above 52.6 GHz is investigated and the 60 GHz license-free band is given full consideration. Indeed, one interesting feature of

5G is to enable the use of license-free bands along with classical dedicated bands (such as the LTE or the 5G-dedicated 3.5 GHz band for instance).

Interference between users is one of the critical problems in dense networks. Low Signal-to-Interference-plus-Noise Ratio (SINR) and corresponding security risks are the problems in 5G [19]. In 5G, massive Multiple-Input Multiple-Output (MIMO) is induced to facilitate spatial multiplexing and coherent beamforming for multi-users to reduce interference. The base station receives the pilots transmitted by the UE through the uplink to estimate the channel in Time Division Duplex (TDD), or ask for the channel estimate from the UE in Frequency Division Duplexing (FDD), both TDD and FDD modes being considered in 5G. After obtaining the transfer function of the channel, precoding such as zero forced equalization is implemented to generate a beam space orthogonal to the spatial channel: directional beams pointing to a particular target UEs are transmitted to reduce interference between the UEs.

This procedure requires each element in the base station's antenna array to be connected to a full radiofrequency chain including Analog-to-Digital Convertor (ADC) and Digital-to-Analog Convertor (DAC). While this approach is considered in the sub-6 GHz band, a number of issues such as power consumption and cost raise in the millimeter-wave band since the number of array elements becomes extremely large (large gain is required to face the severe free-space attenuation). Consequently, hybrid antenna array mixing analog and digital parts are considered [20], the goal being to reduce the number of ADC/DAC thanks to analog beamformers. By doing so, it is no more possible to generate any precoding (such as zero-forcing for instance) and codebook precoders are instead used. Each code word from a given codebook can be seen as a beamforming vector creating a beam toward a given direction. Spanning all the codeworks of the codebook enables to angularly span a whole cell. This so-called beam-grid concept [21] involves a different way of performing the channel estimation. Indeed, the MIMO channel matrix knowledge is no more possible, so the base station needs to sweep through all possible codebooks to identify the best precoder (if the UE is equipped with multiple antennas too, it has to perform the same process). This process is known as beam-training and was already considered in indoor mm-wave communications in 60 GHz standards or instance (see next section).

### 1.3.3 60 GHz band for indoor communication

Due to the small size of the antenna, 60 GHz is suitable for embedded devices based indoor applications, also being a license-free band across a large number of countries. The attenuation in the 60 GHz band caused by atmospheric and molecular absorption in free space exceeds 10 dB/km [22], which prevents its use for outdoor long-range communication. In indoor scenes with high terminal density, the wall-blockage of 60 GHz waves avoids interference from other users and protects the security of information. On the other hand, thanks to the development of the CMOS process, 60 GHz devices can be integrated into a limited on-chip space [23]. Therefore, portable devices can use a 60 GHz antenna array for beamforming and consume very low energy.

Four standards using the 60 GHz band have been released. ECMA 387 [24], IEEE 802.15.3c [25], IEEE 802.11ad [26-28], and WirelessHD [20]. All allocate the band of 57.24 GHz to 65.88 GHz into 4

channels with central frequencies as 58.32 GHz, 60.48 GHz, 62.64 GHz, 64.80 GHz respectively and bandwidth of 2.16 GHz. The different methods of modulation lead to different data transmission rates. For example, in IEEE 802.15.3c, IEEE 802.11ad, WirelessHD, and ECMA, QPSK offers 2.695 Gbps, 2.079 Gbps, 2.379 Gbps, and 2.016 Gbps, respectively. The standards are summarized in Table 1.3. All the mappings use OFDM modulation. A following-up standard IEEE 802.11ay [29] is hoped to bond 4 of the channels of IEEE 802.11ad together to get a maximum bandwidth of 8.64 GHz and higher transmission rate.

Table 1.3 Typical parameters of 60 GHz standards [20, 24, 25, 28]

| Standard | Central frequency (GHz) | Bandwidth (GHz) | Max data rate with OFDM (Gbps) | | | Range (m) |
|---|---|---|---|---|---|---|
| | | | QPSK | 16QAM | 64QAM | |
| IEEE 802.15.3c | 58.32, 60.48, 62.64, 64.80 | 2.16 | 2.695 | 5.390 | 5.775 | 10 |
| IEEE 802.11ad | | | 2.079 | 4.505 | 6.757 | |
| WirelessHD | | | 2.379 | 4.759 | 7.138 | |
| ECMA 387 | | | 2.016 | 4.032 | -- | |

Similarly to 5G, millimeter-wave beamforming is achieved by codebook-based beam training [30]. IEEE 802.11ad includes a beam training protocol [28]. The protocol is modified with Multiple Sector ID Capture (MIDC) [31]. Beam training must be repeated throughout the movement of the terminal. In order to solve this problem, positioning-based beam tracking [32] is attracting more and more attention as a strategy of beamforming [33]. In beam tracking, the beam of the BS tracks the AOA of UE when the terminal moves to a new location. When the direct link is blocked, beam training will be performed to search for new links. The identification of obstacles is a crucial issue in the conversion of beam tracking and training [7]. Compressive sensing [34] is a potential approach to make the millimeter-wave sparse channel estimation more efficient.

### 1.3.4 Compatible communication and localization in millimeter

In addition to enable high data rates for 5G, mm-wave can achieve high accuracy in positioning systems thanks to small wavelength and/or a large bandwidth. In [35], accuracy of position error less than 0.01m and orientation error less than $1^{o}$ is reported for vehicular networks using 5G mm-wave technology. Several general problems in the domain of mm-wave localization have been studied, such as waveform and ranging feature. Gaussian Raised-Cosine Pulse (RCP), Gaussian pulse, and Sinc-RCP impulse radio waveforms have been identified as suitable waveforms for 5G mm-wave localization [36]. It has been found in [37] that a combination of Time Of Flight (TOF) and AOA signal features can yield decimeter level accuracy for mm-wave localization. In [38], the Cramér-Rao bound (CRB) on position and rotation angle estimation uncertainty is theoretically derived for 5G mm-wave MIMO systems. In [39], a typical communication problem, the comparison between beamforming and MIMO techniques, is studied for localization as well. The study manifests that, thanks to the diversity gain exploitable for retrieving positioning information, MIMO outperforms beamforming in terms of localization and orientation performance. Meanwhile, the adoption of massive antenna arrays makes the positioning insensitive to

multipath for most of geometric configurations regardless the SNR regime.

However, in the 60 GHz band, few works regarding localization have been reported. A 60 GHz transmitter for indoor localization is published in [40] and the measured positioning error is lower than 3 mm within a 5 m distance. A method of localization using a 60 GHz OFDM spectrum was presented in [41, 42] to make the localization compatible with the expected waveform for 5G WLAN. The channel in the residential scenario of IEEE 802.15.3c was used to simulate the millimeter-wave positioning [43], and the mean absolute error of time of arrival (TOA) was lower than 10 ns. The other simulation with a channel of IEEE 802.15.3c [44] in the residential scenario showed the average error of positioning with 60 GHz impulse was lower than 0.1 m. An interferometry UWB system estimates the TDOA for 60-GHz OFDM communication System in [45] with average errors from 0.18 m to 0.61 m in an indoor scenario. Time reversal technology is used to enhance the positioning accuracy of a 60 GHz communication-localization system in [46] which operates at 200 Mbps and achieves 0.0124 m mean positioning error. A triangulate-validate based algorithm [47] is developed for 60 GHz positioning system and achieves sub-meter accuracy. These studies manifested the high accuracy of positioning and the feasibility of the implementation of a 60 GHz band, including in the frame of 5G.

The 8.64 GHz bandwidth of 60 GHz makes delay-based 60 GHz positioning accurate. The large attenuation helps in reducing communication interference, but it also causes the blockage of the direct path, useful for localization. When the direct path is blocked, the beam training strategy will scan the space to look for new links with a sufficiently high SNR above the threshold. The above beam training strategy can guarantee the required Bit Error Rate (BER) wince relatively strong NLOS paths can provide an acceptable SNR. While, blockage of the direct path will result in a larger transmission distance than the actual distance between the transmitter and receiver.

# 1.4 Millimeter-Wave Channel Modeling

Millimeter-wave wireless communication has its inherent characteristics. The propagation loss and precipitation attenuation of millimeter waves in the atmosphere are typically less than a few dB per kilometer. The attenuation of the mm-wave prevents the signal from penetrating well through most of the solid materials. The Root Mean Square (RMS) of the Power Delay Profile (PDP) of the millimeter-wave channel in an urban environment is usually a few nanoseconds; the coherence bandwidth of the channel is less than few hundreds of MHz [48].

## 1.4.1 General channel characteristics

Signal transmission severely affects the performance of 5G wireless communications. The physical transmitting media is the radio channel for communication. The influence of the transmission channel for communication is decisive, so the mathematical modeling of the transmission channel is one of the core tasks for wireless communication research. The channel profile includes small scale and large scale features [49]. Small-scale features typically represent the temporal and spatial dispersion caused by the multipath

propagation of radio waves in space. Small-scale fading results in frequency selectivity in the frequency domain as well as corresponding signal distortion and crosstalk in the time domain. In a linear Single-Input Single-Output (SISO) system between a pair of antennas, small-scale fading in the Spatial Channel Model (SCM) is described by the channel impulse response (CIR): a combination of $L$ impulses with variables of time $t$, Time of Arrival (TOA) $\tau$, Angle of Departure (AOD) $\theta_{AOD}$, and Angle of Arrival (AOA) $\theta_{AOA}$.

$$h\left(t,\tau,\theta_{AoD},\theta_{AoA}\right)=\sum_{l=1}^{L}a_l\delta\left(t-t_l\right)\delta\left(\tau-\tau_l\right)\delta\left(\theta-\theta_{AoD}^{l}\right)\delta\left(\theta-\theta_{AoA}^{l}\right) \tag{1.9}$$

Extending the SISO system to the MIMO system, the CIR between the antenna arrays becomes a matrix as following:

$$H=\begin{bmatrix} h_{11} & h_{12} & \cdots & h_{1n} \\ h_{21} & h_{22} & \cdots & h_{1n} \\ \vdots & \vdots & \ddots & \vdots \\ h_{m1} & h_{m2} & \cdots & h_{mn} \end{bmatrix} \tag{1.10}$$

Every element of the channel matrix $h_{ij}$ is the CIR between the $i$-th component of the receiver antenna array and the $j$-th component of the transmitter antenna array.

The large-scaled shadowing fading is the power loss caused by the attenuation of the radio passing through the obstructers. The shadowing effect reduces the coverage area of transmitters for a given output power. The radar function describes the scattering by a scatterer, and allows to express the received power $P_r$ as :

$$P_r=P_t\frac{G_tG_r\lambda^2\sigma_s}{\left(4\pi\right)^3d_{ts}^2d_{rs}^2} \tag{1.11}$$

Figure 1.6 illustrates the principle of the radar equation. The radio with a wavelength $\lambda$ and power $P_t$ is emitted by the transmitter (Tx) antenna whose gain is $G_t$. After the transmission through a distance $d_{ts}$ from the transmitter to the scatterer, the radio is scattered by the scatterer with a Radar Cross Section (RCS) $\sigma_s$. The scattered wave propagated through distance $d_{rs}$, then received by the receiver (Rx) antenna whose gain is $G_r$. In the absence of scatterer, the radar equation becomes a Friis's equation expressed in free space as:

$$P_r=P_t\frac{G_tG_r\lambda^2}{\left(4\pi\right)^2d_{tr}^2} \tag{1.12}$$

The linear Friis's function is usually converted into logarithm and expressed as a path loss (PL) for the propagating distance $d_{tr}$ from a transmitter to a receiver with the loss factor $a$:

$$PL[dB] = P_r[dB] - P_t[dB] - G_t[dB] - G_r[dB] = 10\log_{10}(ad_{tr}) \tag{1.13}$$

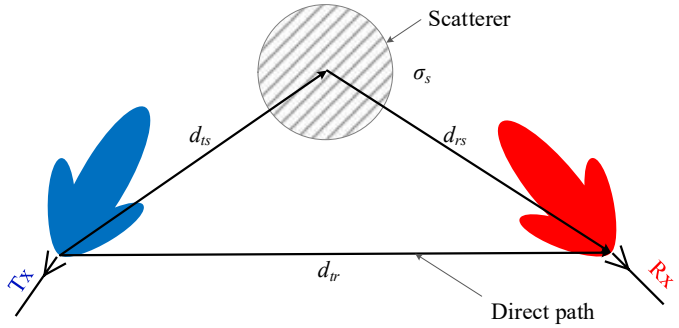


Figure 1.6 Radio diffusing scattered by a scatter with RCS $\sigma_s$

## 1.4.2 Cluster-scattered plane wave-based channel model

The CIR is related to the physical process of radio wave scattering. Most of the current channel models, such as the temporal Saleh-Valenzuela (S-V) model [50] for indoor SISO channels or the 3GPP SCM [51] for outdoor MIMO channels, are based on the same physical CIR model: group-distributed scatterers scatter the transmitted beams between BS and UE antennas in space. Therefore, the CIR is simplified into two parts: the grouping action of clusters and impulses spread behavior inside clusters. In a general expression, each of the $N$ scattering clusters has $M$ components inside:

$$h_{ij}(t,\tau,\theta) = \sum_{n=1}^{N} C_n\left(t^n,\tau^n,\theta^n\right) \tag{1.14}$$

$$C_n\left(t^n,\tau^n,\theta^n\right) = \sum_{m=1}^{M} A_m \delta\left(t - t^{nm}\right)\delta\left(\tau - \tau^{nm}\right)\delta\left(\theta - \theta^{nm}\right) \tag{1.15}$$

Where $t^{nm}$, $\tau^{nm}$ and $\theta^{nm}$ are the time, delay and angle inside clusters respectively, while $A_m$ is the amplitude of each path. The channel model in the 60 GHz narrow band standard, IEEE 802.11ad [28], is based on the cluster-scattered plane wave as well. The IEEE 802.11ad channel model [52] is illustrated in Figure 1.7. Between the $i$-th Rx antenna and $j$-th Tx antenna, the transmitted beam is scattered by $N$ clusters of scatterers, each one having $M$ scattering components distributed in space and time. The distance between Tx and Rx antennas is $d$. The two antennas exhibit in the directions $\theta_{AOD}^{n,m}$ and $\theta_{AOA}^{n,m}$ gains of $G_R(\theta_{AOD}^{n,m})$ and $G_T(\theta_{AOA}^{n,m})$ respectively, where $\theta_{AOA}^{n,m}$ and $\theta_{AOD}^{n,m}$ are AOA and AOD, respectively, of the $m$-th path in the $n$-th cluster. The CIR between the two antennas is modeled as a linear combination of plane waves scattered by a total of $N$ clusters.

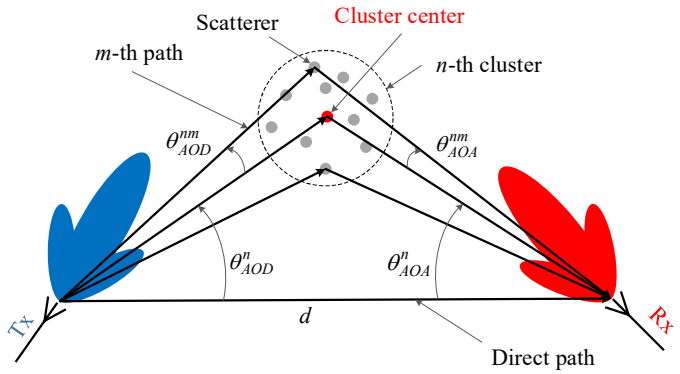


Figure 1.7 A beam scattered by a cluster of the scatterer

The clusters in IEEE 802.11ad channel model are classified as LOS and NLOS. In the situation where Tx and Rx antennas are pointing to each other without any blockage, i.e., at $\theta_0$, the LOS channel is expressed as:

$$h_{LOS} = G_T(\theta_0) G_R(\theta_0) \frac{\lambda}{4\pi d} \exp\left(2\pi j \frac{d}{\lambda}\right) \tag{1.16}$$

Where $\lambda$ is the wavelength of the carrier. When the wall, ceiling, or ground reflects a beam between Tx and Rx, the CIR is a combination of $N$ paths in the NLOS scenario:

$$h_{NLOS} = \sum_{n=1}^{N} \frac{\lambda}{4\pi(d + c\tau_n)} \delta\left(\theta_{AoA} - \theta^n_{AoA}\right) \delta\left(\theta_{AoD} - \theta^n_{AoD}\right) C_n \tag{1.17}$$

Where $\tau_n$ is the TOA of the $n$-th cluster. $C_n$ is the amplitude combining total $M$ paths inside the $n$-th cluster:

$$C_n = \sum_{m=1}^{M} G_T\left(\theta^{nm}_{AoD}\right) G_R\left(\theta^{nm}_{AoA}\right) \exp\left(\pm \frac{|\tau^{nm}|}{\gamma}\right) \exp\left(j\varphi^{nm}\right) \delta\left(\theta_{AoA} - \theta^{nm}_{AoA}\right) \delta\left(\theta_{AoD} - \theta^{nm}_{AoD}\right) \tag{1.18}$$

Where $\tau^{nm}$ is the TOA of the $m$-th path inside the $n$-th cluster. $\varphi^{nm}$ is a random phase. Here, the impulse response is modeled like a Rayleigh according to Poisson process TOA $\tau_m$ with a scale parameter $\gamma$. The AOA and AOD are distributed with piecewise functions in different angle ranges.

## 1.4.3 Parameterizing the statistical model

The geometrical clusters of scatterers are stochastically distributed in the physical space. The corresponding parameters of the above channel model, $\tau_{n,m}$, $\theta^{n,m}_{AOD}$, and $\theta^{n,m}_{AOA}$, are therefore also statistical. So channel modeling is to determine the statistical distribution of the parameters in the cluster-scattering channel model. To simplify the statistical modeling, Wide-Sense Stationary Uncorrelated Scattering

(WSSUS) channel is assumed with two reasonable assumptions: the radio channel is stationary in a broad sense, and the scattering with different path delays are uncorrelated. The assumptions in the WSSUS channel make the channel parameters independently and identically distributed (*i.i.d.*). The statistical PDF of the channel can be parameterized with the expectations and root mean square (RMS) spreads. The expectation of TOA $\bar{\tau}$, RMS spread of TOA $\tau_{\mathrm{RMS}}$, expectation of AOA / AOD $\bar{\theta}$, and $\theta_{\mathrm{RMS}}$ are:

$$\bar{\tau} = \frac{\int_0^T \tau P_h(\tau) d\tau}{\int_0^T P_h(\tau) d\tau} - \tau_a, \ \tau = t - t_0, \ \tau_a = \text{first peak time} \tag{1.19}$$

$$\tau_{RMS} = \sqrt{\frac{\int_0^T (\tau - \bar{\tau} - \tau_a)^2 P_h(\tau) d\tau}{\int_0^T P_h(\tau) d\tau}} \tag{1.20}$$

$$\bar{\theta} = \frac{\int_{-\pi}^{\pi} \theta P_h(\theta) d\theta}{\int_{-\pi}^{\pi} P_h(\theta) d\theta} \tag{1.21}$$

$$\theta_{RMS} = \sqrt{\frac{\int_{-\pi}^{\pi} (\theta - \bar{\theta}) P_h(\theta) d\theta}{\int_{-\pi}^{\pi} P_h(\theta) d\theta}} \tag{1.22}$$

Where $T$ is the length of the time series; Power Delay Profile (PDP) $P_h(\tau)$ and Power Angular Spectrum (PAS) $P_h(\theta)$ are the quantities to measure:

$$P_h(\tau) = \frac{1}{t_e} \int_0^{t_e} |h(t,\tau)|^2 \, dt \tag{1.23}$$

$$P_h(\theta) = \frac{1}{t_e} \int_0^{t_e} |h(t,\theta)|^2 \, dt \tag{1.24}$$

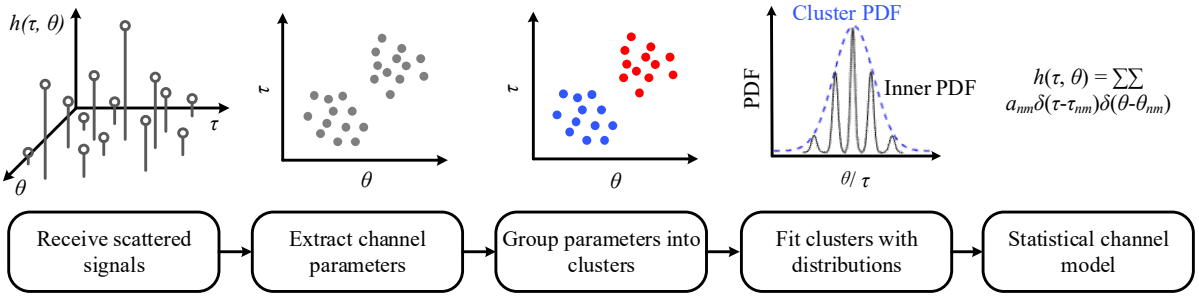


Figure 1.8 The general procedure of a statistical channel modeling

A typical process to model the cluster-based channel involves four steps [53]: collecting the scattered signal, extracting the above channel parameters (e.g., $\bar{\tau}$, $\tau_{\mathrm{RMS}}$, $\bar{\theta}$, $\theta_{\mathrm{RMS}}$), grouping the parameters as clusters, and fitting the clusters with statistical models. The scattered signal can be collected with physical measurement or numerical experiments, such as ray tracing, in different scenarios. The channel parameters ($\tau$, $\theta$) are extracted from the PDP and PAS with an estimation of statistical parameters. The most efficient algorithms fall into two categories: subspace and maximum likelihood. The single variable in the channel is usually estimated with subspace-based methods: MUltiple SIgnal Classification (MUSIC) [54] and Estimation of Signal Parameters via Rotational Invariance Technology (ESPRIT) [55]. The maximum-likelihood based estimation method in the channel model is Space Alternating Generalized Expectation-maximization (SAGE) [56, 57] to estimate multi-variables. Then, the estimated parameters are grouped with a clustering algorithm. The most widely used clustering method for channel modeling is K-Power-Means [55]. Finally, the distribution of the discrete parameter points inside clusters is fitted with an assumed statistical model. The procedure is summarized in Figure 1.8. Following the above procedure, the 60 GHz [58-63] and 28 GHz [64-66] bands were modeled with physical measurements in the indoor scenario. The 3GPP channel modeling of 28 GHz and 73 GHz bands in outdoor [67, 68] were achieved with the same procedure as well.

Depending on the application, the procedure is usually applied in different radio propagation scenarios. For instance, for indoor transmission in the 60 GHz band, the typical measurement campaign considers specific scenarios, such as a conference room [58], office [59], residential [62], and corridor [60, 63]. Summarizing the references, a typical procedure is presented as following. A Rx is placed at a corner or beside a wall of a room as BS. Many Tx locations are selected on tables or in corridors to imitate the UEs. LOS and NLOS transmissions were determined before measurements. In the LOS transmission, the links between Tx and Rx are unobstructed; while, in the NLOS transmission, the links are obstructed with blockers such as computer screens or partitioning panels between office cubicles. Antenna arrays or horn antennas swept in azimuth and elevation directions in the entire space to get the PAS. In terms of measuring instruments, the synchronization and the connecting loss between the transmitter and the receiver are critical considerations. For short-distance indoor measurements, a Vector Network Analyzer (VNA) can be used to guarantee the high synchronization and low connecting loss. After collecting the signal, the parameters are estimated with the SAGE and clustering with K-Power-Means. Finally, inter and intracluster delay and direction spreads are fitted with specific PDFs.

Reflections from walls, ceiling, and ground are the characteristics distinguishing from outdoor scenarios. The regular architectural structure makes the reflections from walls predictable through numerical experiments, such as ray tracing [69]. Ray tracing approximates the full-wave propagation and scattering to ray-like emission and reflection, which is consistent with the high directionality of millimeter-wave while saving simulating time. The effectiveness of ray tracing to model the inter-wall reflection channel was verified to model 60 GHz band propagation [60]. According to the validation, the ray tracing is introduced into IEEE 802.11ad to simplify the channel among walls [52]. The estimating and clustering post-treatment steps were replaced with two discriminated measurement steps. The antennas were artificially pointed at the target cluster direction which was calculated with ray tracing. Then the intracluster configuration was directly measured.

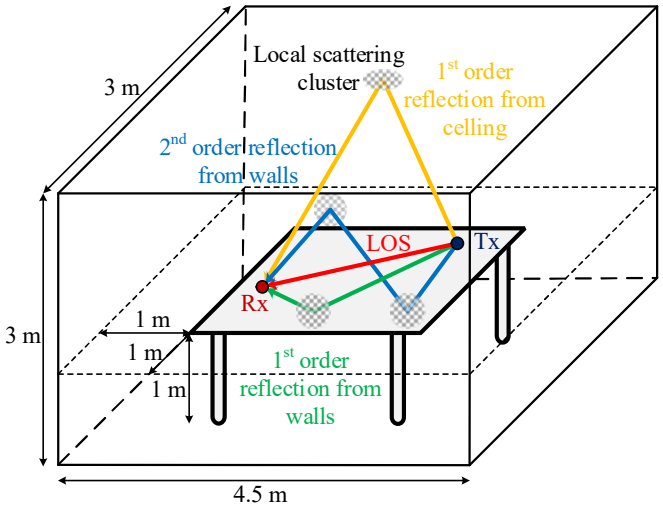


Figure 1.9 3D schematic diagram of the IEEE 802.11ad channel model in a scenario of conference room [52]

Numerical experiments collected the intra-cluster scattering data. The Tx and Rx are both placed on the table with deterministic distance $d$. The TOAs ($\tau_n$), AODs ($\theta^n_{AOD}$), and AOAs ($\theta^n_{AOA}$) inter clusters are gathered with the numerical simulation of ray tracing. The IEEE 802.11ad channel is derived for three kinds of scenarios: conference room, office, living room. For example, the conference scenario channel model is shown in Figure 1.9. The length, width, and height of the conference room are 4.5 m × 3 m × 3 m. A conference table is located at the center of the room. The distance from the table to the walls and the ground are both 1 m. In the simulation, five types of path are considered: LOS, first-order reflections from walls, second-order reflection between two walls, first-order reflection from the ceiling, second-order reflections between wall and ceiling. The statistical characteristics of the cluster parameters were collected using the Monte Carlo method by randomly selecting the locations of Rx and Tx in the simulation. The parameters were fitted with empirical PDFs of the piecewise function.

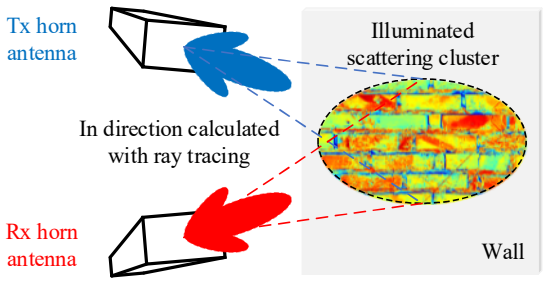


Figure 1.10 Schematic diagram of local scattering cluster illuminated by beams

The intracluster CIRs were grabbed with physical measurements [70] in several similar conference rooms like the scenario plotted in Figure 1.9. Two horn antennas with both 20° half-power beamwidth were used for Rx and Tx. The antennas were mechanically rotated with servo motors. The clustered scattering by walls was measured in the ray directions calculated with ray tracing, as shown in Figure 1.10. The measurement was operated in the frequency domain to obtain the Channel Transfer Function (CTF) of each cluster scattering. Then the frequency domain CTFs were Fourier transformed to PDP $P_h(\tau_m)$ in the time

domain.

$$P_h(\tau_m) = \frac{1}{t_e}\int_0^{t_e} \left|h(t,\tau_m)\right|^2 dt \tag{1.25}$$

The sampled $P_h$ and $\tau_m$ are fitted with a Rayleigh decaying and a Poisson distribution, with respectively, as shown in Figure 1.11.

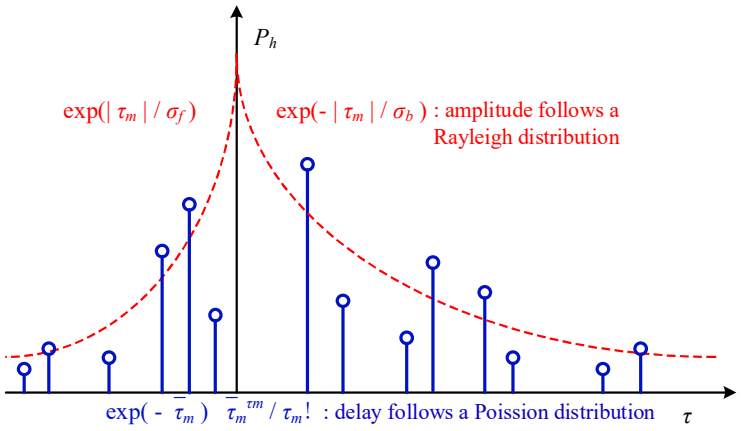


Figure 1.11 The time-domain model intracluster [52]

The variances of the Rayleigh distribution is obtained from the RMS variance of intercluster TOA, $\tau_{RMS}^m$:

$$\sigma^2 = \frac{2}{4-\pi}\left(\tau_{RMS}^m\right)^2 \tag{1.26}$$

The RMS variances for the uphill and downhill of the intracluster are notated as $\sigma_f$ and $\sigma_b$ respectively. The spatial characteristics of the cluster were not extracted because the mechanical angular sweeping with the horn antenna provided a low spatial resolution. Based on an assumption of entirely random scattering, the AODs ($\theta_{AOD}^{nm}$) and AOAs ($\theta_{AOA}^{nm}$) of ray inside clusters were fitted by non-basis Gaussian distribution.

$$\theta_{AOA,AOD}^{nm} = \frac{1}{\left(\theta_{AOA,AOD}^{nm}\right)_{RMS}\sqrt{2\pi}}\exp\left[-\frac{\left(\theta_{AOA,AOD}^{nm} - \bar{\theta}_{AOA,AOD}^{nm}\right)}{2\left(\theta_{AOA,AOD}^{nm}\right)_{RMS}^2}\right] \tag{1.27}$$

Where

$$\bar{\theta}_{AoA,AoD}^{nm} = 0 \tag{1.28}$$

$$\left(\theta_{AoA,AoD}^{nm}\right)_{RMS} = \sqrt{\frac{\int_0^{\Delta\theta}\left(\theta_{AoA,AoD}^{nm}\right)^2 P_h\left(\theta_{AoA,AoD}^{nm}\right)d\theta_{AoA,AoD}^{nm}}{\int_0^{\tau_e} P_h\left(\theta_{AoA,AoD}^{nm}\right)d\theta_{AoA,AoD}^{nm}}} \tag{1.29}$$

The phase $\varphi$ uniformly distributes from –180° to 180°.

## 1.4.4 Modeling blockage for millimeter band channel

The IEEE 802.11ad channel model does not sufficiently consider the attenuation caused by large-scale shadowing. The attenuation of the millimeter-wave is severe. The metal and wood blockage with the wedge, edge, cylinder shapes was studied in 60 GHz band with the Uniform Geometrical Theory of Diffraction (UTD) [71] and validated with measurement. The study manifests that the path loss of 60 GHz radio waves in the NLOS area is higher from 15 dB to 25 dB than the path loss in the LOS area. Meanwhile, the diffraction is so weak that negligible in the indoor transmission [72]. Besides, the blockage of the human body contributes a power loss of no less than 20dB to more than 40dB [73-76]. The weak diffraction causes the millimeter radio waves to propagate in directional beams. Widely spread blockers attenuate the concentrated beams in the indoor scenario. The above two factors aggravate the problem of millimeter-wave blockage: the signal coverage range and spectrum efficiency are shrined [77]. The received power $P_i$ of the $i$-th link can be estimated by with the transmittance ratio $\Gamma_{ij}$ of power by the $j$-th scatterer or blocker, the power fading $g_i$, and the path loss $PL$ of free space as follow:

$$P_i = \frac{g_i}{PL} \prod_{j=1}^{N_i} \Gamma_{ij} \tag{1.30}$$

Where $N_i$ is the number of blockers located across the $i$-th link. So the Signal Interference Ratio (SIR) can be calculated as:

$$SIR = \frac{g_i \Gamma^{N_i} PL_i^{-1}}{\sum_{j \neq i} g_j \Gamma^{N_j} PL_j^{-1}} \tag{1.31}$$

Then the coverage of cellular can be estimated by the coverage probability as $p(SIR > SIR_{thre})$. Meanwhile the spectrum efficiency can be estimated as $\eta_f = E[\log_2(1 + SIR)]$. Because the transmittance ratio has been proven very low, the coverage and spectrum suffered from the increasing of the blocker number. Therefore, the blockage is an indispensable component in the millimeter band channel model.

### 1.4.4.1 The outdoor blockage

The attenuation is assessed with path loss. The probability of LOS transmissions is considered in the outdoor 3GPP channel model [78]. A series of outdoor channels for 28 GHz and 73 GHz were measured to study the LOS probability of millimeter band transmission [67]. The modeling procedure follows a simplified procedure of channel modeling, as shown in Figure 1.12: indiscriminate measurement, clustering, PDF fitting. The purpose of the above measurement activities is to mimic the behavior of BS and EU in actual communication. The receivers were placed on the ground and in the low-rise buildings. The transmitters were located on the rooftops of high buildings. The transmitter antennas were swept obliquely

at a particular solid angle to the position of the receiver. The receiver swept across the entire solid angle. The power threshold was set to be 20 dB below the maximum power level. Due to the high directionality of the radio beam and the high attenuation, the effective scatterer in the outdoor scenario is very spare. So, the received signal was discrete. The step of estimation in the typical modeling procedure was therefore omitted. LOS was defined as a transmission in which the received power was above a certain threshold.

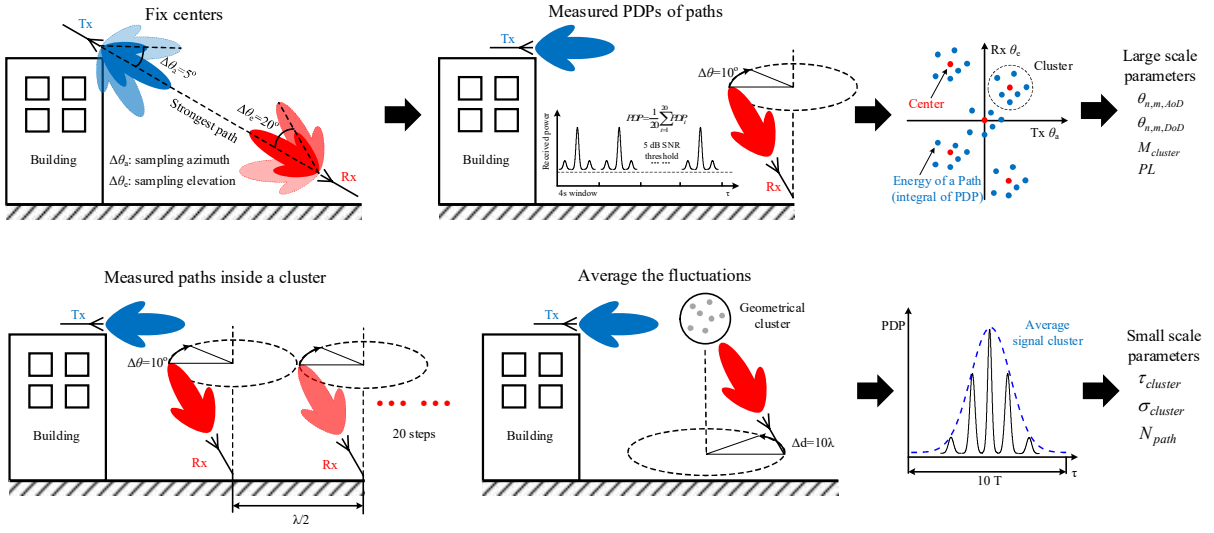


Figure 1.12 Modeling procedure of 3GPP outdoor 28 GHz channel [67]

After clustering the data set, the parameters of the 3GPP channel model were fitted with statistical distributions. In the model, the situations of LOS, NLOS, and outage were modeled with probability functions $p_{LOS}$, $p_{NLOS}$, and $p_{out}$. They are exponential functions for the distance $d$ between the transmitter and receiver, with parameters $a_{out}$, $b_{out}$ and $a_{los}$:

$$p_{out}(d) = \max\left[0, 1 - \exp\left(-a_{out}d + b_{out}\right)\right] \tag{1.32}$$

$$p_{LOS}(d) = \left[1 - p_{out}(d)\right]\exp\left(-a_{los}d\right) \tag{1.33}$$

$$p_{NLOS}(d) = 1 - p_{LOS}(d) - p_{out}(d) \tag{1.34}$$

The experiments manifested $p_{LOS,}$ and $p_{NLOS}$ exponentially decreased with increasing the distance. At locations farther than 200 m from the transmitter, no signal was detected by the receiver, which means $p_{LOS} + p_{NLOS} \approx 0$ at locations with $d > 200$ m.

The actual condition limits the number of samples in physical measurement. A ray-tracing based on the 2D Google map was simulated [79] with the Monte Carlo method to enhance the sampling number. Receivers were uniformly arranged in circles around a transmitter with a 5 m increment of the radius. If a

line connected the TX and RX was not blocked by any part of the buildings, the type of transmission was confirmed as LOS. Then, by counting the number of unblocked links, the result verified the exponential relationship between the LOS probability and Tx-Rx distance. The stochastic geometry theory is induced to generalize the LOS probability model [55] further. The buildings were modeled as rectangles, under the following assumptions:

- The blockers were non-overlapped rectangular buildings;
- Base stations were independent Poisson Point Process (PPP) points;
- The centers, directions, length, and width of the blockers were independent from each other. All of the rectangles around the same pair of Tx-Rx are in the same direction and with the same diagonal length;
- The centers of the blockers were independent PPP points;
- Orientations of rectangular blockers were uniformly distributed in the range of $(0,2\pi]$;

If the Rx falls into the shadowing domain, the link is blocked. Since the blocking rectangles around the Tx-Rx links are assumed the same size, the maximum width of the shadowing domain was the width of blockers as the yellow domain in Figure 1.13. The trajectory of rectangle centroid formed the boundary of the LOS domain.

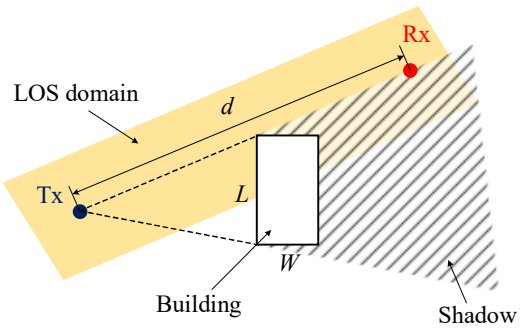


Figure 1.13 The shadowing domain of a Tx-Rx link from an outdoor building

The assumption that the centers of the blocker are PPP implies that the probability of the center falls into a domain is proportional to the area of the domain. After the derivation based on the above assumptions, the expectation of the LOS domain area is:

$$E(S)=\alpha d+\beta \tag{1.35}$$

Where $d$ is the distance between two buildings; $\alpha$ and $\beta$ are the sums and the multiplication of the expectations of building width and length, respectively.

$$\alpha=E(W)+E(L) \tag{1.36}$$

$$\beta = E(W)E(L) \tag{1.37}$$

Because the number of a center falling into the shadowing domain follows PPP, the LOS probability is the probability of no building falling into the LOS domain:

$$p_{LOS}(d) = \exp\left[-(\alpha d + \beta)\right] \tag{1.38}$$

The outdoor experiments validated the exponential LOS probability function. A similar Poisson process is used to model the LOS/NLOS clusters [80].

### 1.4.4.2 The indoor blockage

The blockage of the human body for 60 GHz propagation in the indoor scenario can also be modeled as cluster-based small-scale channel characteristics [81]. The grouped human activity causes clustered fading. Instead of CIR clusters, the fading cluster with an attenuation higher than a certain threshold of CIR was used to describe the blockage. The characteristics of the fading cluster were measured following the typical modeling procedure. A fundamental assumption is that the room is humanly crowded so that the process of human blockage is stationary. This assumption means that the distribution of the process is time-invariant. With such an assumption, the transmission link is spread through the whole office so the human groups can efficiently influence the links. The signal is then recorded in the time slot where humans are always active to capture blocking events. Seven signal parameters were extracted to define the characteristics of a link blocking event: attenuation $A(\tau)$, fading $F(\tau)$, duration $D$, average attenuation $\overline{A}$, maximum attenuation $A_{max}$, the pseudo period $T(n)$ and rising time $t_{rise}$:

$$A(\tau)[dB] = 10\log_{10}\frac{P_h^t(\tau)}{P_h^r(\tau)} \tag{1.39}$$

$$F(\tau)[dB] = A(\tau)[dB] - A_{thre}[dB] \tag{1.40}$$

$$D = \tau_e - \tau_b \tag{1.41}$$

$$\overline{A}[dB] = \frac{3}{D}\int_{\tau_b}^{\tau_e} F(\tau)d\tau \tag{1.42}$$

$$A_{\max}[dB] = \max_{\tau\in[\tau_b,\tau_e]} F(\tau) \tag{1.43}$$

$$T(n) = \tau_b(n+1) - \tau_b(n) \tag{1.44}$$

$$t_{rise} = \arg_{\tau}\left(A_{thre} + 1[dB]\right) - \tau_b \tag{1.45}$$

Where $P^t_h(\tau)$ and $P^r_h(\tau)$ are the PDPs of the transmitted and received signal. With the threshold of thermal noise $A_{thre}$, the fading cluster $F(\tau)$ caused by the blockage is identified. $\tau_b$ and $\tau_e$ are the positive and negative instants of a threshold crossing to record the range of attenuation cluster in order to get the duration $D$ of a fading cluster. $\bar{A}$, $A_{max,}$ and $t_{rise}$ were used for the description of the fading clusters. The results showed that $T$ and $D$ matched lognormal distributions, which means the LOS probabilities inside and outside the fading clusters were exponential functions to the length of the link.

Like the outdoor scenario, the LOS probability was also modeled with stochastic geometry theory as well [82]. The events of human body blockage are assumed to be independent and modeled as a PPP. So the human activity is implicitly assumed ungrouped and passing through the direct link with uniform probability. Human bodies were modeled as cylinders with diameter $W$. A similar blocking event like the outdoor environment is shown as Figure 1.14. It is at the cross-section of the model. The boundary of the LOS domain is the trajectory of the body center.

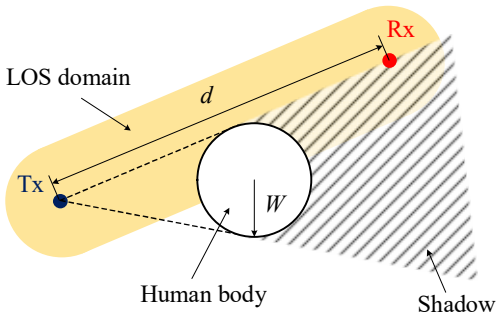


Figure 1.14 The shadowing domain of a Tx-Rx link from an indoor human body

The average area of the shadowing domain is:

$$E(S) = RE(W) + \frac{1}{4}\pi\left[E(W)\right]^2 \tag{1.46}$$

So, after a similar derivation as the outdoor blockage, the LOS probability is obtained:

$$p_{LOS}(d) = \exp\left[-(\alpha d + \beta)\right] \tag{1.47}$$

Where

$$\alpha = E(W) \tag{1.48}$$

$$\beta = \frac{1}{4}\pi\left[E(W)\right]^2 \tag{1.49}$$

## 1.4.5 The solution for blockage

Blockage is one of the critical issues in millimeter band communications. The most practical solution to circumvent this issue is a combination of hybrid beamforming and beam training. Beamforming is a spatial matched filter to shape the radiation pattern using an antenna array typically. In order to cope with the high path loss, the beamforming is used in millimeter band to create a high-gain highly directional beam and to steer it towards desired directions (e.g., towards the strongest path). Assuming narrow-band operation so that antenna the response is not time-dependent across the bandwidth of the signal, the receiver signal $x(t)$ is then obtained from the weighted transmitted signal $s(t)$ by the steering vector $\boldsymbol{a}(\theta)$ of the antenna:

$$x(t,\theta) = \boldsymbol{a}(\theta)s(t,\theta) + \boldsymbol{n}(t) \tag{1.50}$$

$$\boldsymbol{a}(\theta) = \left[1, \exp(-jk_c d\sin\theta), \exp(-2jk_c d\sin\theta), \ldots, \exp\left(-(N-1)jk_c d\sin\theta\right)\right] \tag{1.51}$$

Where $\boldsymbol{n}(t)$ is the Additive White Gaussian Noise (AWGN). The distance determines the steering vector $a(\theta)$ among element $d$ and the center frequency $f_c$. The beamforming is achieved with shifting the individual phase with a weighting vector $\boldsymbol{w}$:

$$P(\theta) = \frac{1}{T}\int_0^T \left|y(t,\theta)\right|^2 dt = \frac{1}{T}\int_0^T \boldsymbol{w}^H(t)x(t,\theta)x^H(t,\theta)\boldsymbol{w}(t)dt = \boldsymbol{w}^H\boldsymbol{R}_x\boldsymbol{w} \tag{1.52}$$

Where $P(\theta)$ is the power angular spectrum (PAS); So to maximize the antenna pattern at direction $\theta$:

$$\max_w P(\theta) = \max_w\left[\boldsymbol{w}^H\boldsymbol{R}_x\boldsymbol{w}\right] \tag{1.53}$$

The $\boldsymbol{R}_x$ is the spatial covariance matrix of the received signal

$$\boldsymbol{R}_x = E\left[x(t,\theta)\right] = \frac{1}{T}\int_0^T x(t,\theta)x^H(t,\theta)dt \tag{1.54}$$

Because the noise is white, the optimization problem is solved as a matched filter [49]:

$$\boldsymbol{w} = \frac{\boldsymbol{a}(\theta)}{\sqrt{\boldsymbol{a}^H(\theta)\boldsymbol{a}(\theta)}} \tag{1.55}$$

The antenna pattern $P(\theta)$ is maximized in the expected direction:

$$P(\theta)=\frac{\boldsymbol{a}^H(\theta)\boldsymbol{R}_x\boldsymbol{a}(\theta)}{\boldsymbol{a}^H(\theta)\boldsymbol{a}(\theta)} \tag{1.56}$$

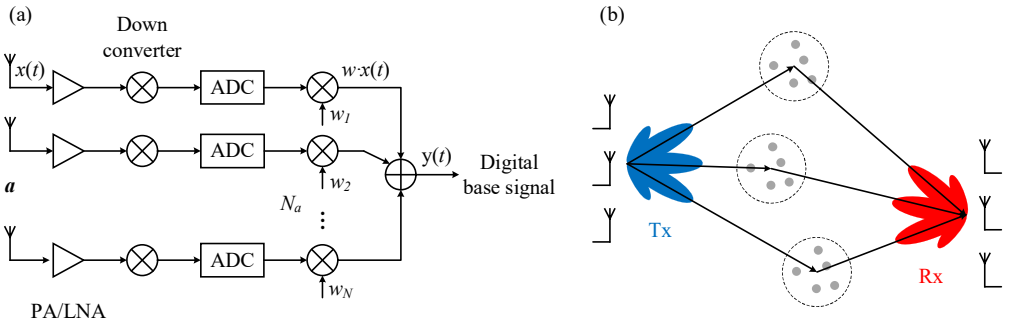


Figure 1.15 Digital beamforming: (a) architecture of receiver and (b) channel estimation

So to apply the precoding/decoding vector $\boldsymbol{w}$, beamforming can use an full-digital architecture for the transmitter and receiver [30]. Taking the receiver as an example, the received signal $x(t)$ of each antenna element is amplified and down-converted before the digital weight $w_n$ is applied, as shown in Figure 1.15 (a). The independent RF front-end of each chain makes receiving more flexible, enabling MIMO channel estimations in configurations shown as in Figure 1.15 (b). Consequently, the AOA and AOD can be estimated with spatial estimators such as MUSIC. However, there are two hardware constraints for full-digital beamforming. First, the RF chain has to be associated with an antenna element. The on-chip space limits the package of the entire chain. Second, the data speed is usually very high (in the Gbps regime) in the millimeter band, so the power consumption is stringent in DAC/ADC components.

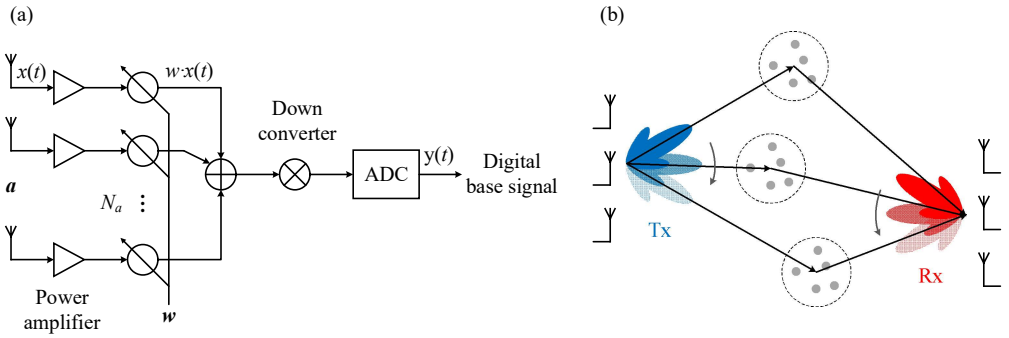


Figure 1.16 Analog beamforming: (a) architecture of receiver and (b) beam training

The second type of beamforming is full-analog. The analog phase-shifter weight the phase of the signal. All of the antennas share a unique RF chain, as presented in Figure 1.16 (a). The power consumption is reduced thanks to only one ADC and fewer components are required. However, only one beam is typically generated due to the lack of information of the MIMO channel. Here, only a SISO channel, already precoded with the vector $\boldsymbol{w}$ is available. Since spatial channel estimation is not feasible, beamforming is combined with beam training: sweeping the beam over the space to find high SNR links as

shown in Figure 1.16 (b).

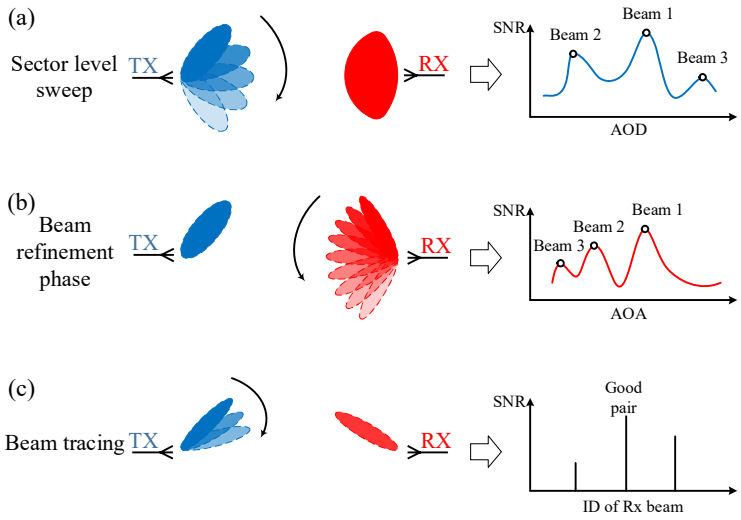


Figure 1.17 Beam training protocol in IEEE 802.11ad: (a) SLS; (b) BRP; (c) BT

In IEEE 802.11ad, a protocol of beam training strategy [28], as shown in Figure 1.17 is proposed. In the Sector Level Sweep (SLS), a beam sweep at Txis performed with quasi-omni antenna pattern used at Rx to search for the best antenna sector. Then, in the Beam Refinement Phase (BRP) step, a finer beam pattern pair is selected. In the Beam Tracking (BT) step, an adjustment is operated for channel changes.

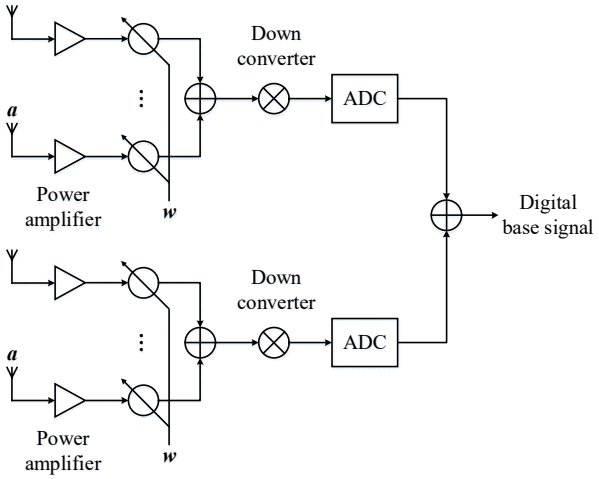


Figure 1.18 Architecture of hybrid beamforming receiver

Since analog beamforming strategy reserves only one beam, it cannot be used for simulating multi-user situation. Therefore, hybrid beamforming is also developed in the millimeter band [83]. The massive antenna array is separated into sub-arrays as shown in Figure 1.18. Each sub-array searches for links with the analog beamforming strategy. The whole antenna array is connected with the digital framework, as shown in Figure 1.18.

## 1.5 Objectives of the Thesis

The effectiveness of the unblocking by codebook based hybrid beamforming has been validated [84]. However, the current beamforming is not compatible with localization. NLOS transmission is the main error source for localization, but the identification of NLOS transmission lacks in the current beamforming strategy. If the direct path is obstructed, the reflected links with high SNR support the communication with a low bit error rate (BER) in the coverage range of transmitters. Nevertheless, the indirect path propagates extra distance and delay. The transmission accurately provides the TOA for positioning only in the LOS scenario, as shown in Figure 1.19. Therefore, the NLOS identification needs to be studied and added to the current beam training framework, to indicate to the system whether the established link can be used for accurate positioning (depending on its nature: LOS or NLOS)

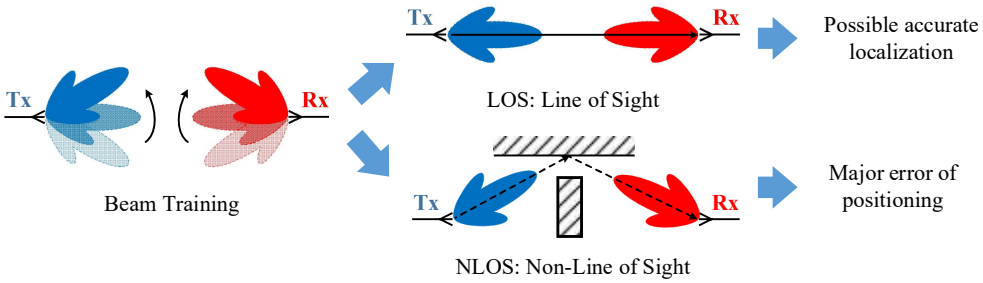


Figure 1.19 The different performance of beam training for communication and localization

In the upcoming work, the NLOS identification will be studied. The chapters are organized as follows. In chapter 2, the state-of-the-art for NLOS identification is investigated. The basic theory of the identified methods is discussed. In chapter 3, the identification will be studied using simulation, which is based on the IEEE 802.11ad channel model. In chapter 4, the simulations are validated with measurements in indoor environment.

## 1.6 Conclusion

In this chapter, the context and the scientific and technical backgrounds of the study are presented and discussed. The indoor localization is attracting attention because of the abundant applications. Compared with other technologies, the triangulation based UWB ranging, especially the TOA and TDOA based ranging, provides higher accuracy for localization. NLOS transmission is one of the significant error sources. The millimeter band is an excellent candidate for indoor localization because of its inherent wideband. The millimeter band takes advantage of the MIMO communication for 5G due to the capacity of interference mitigation in dense networks. Unfortunately, blockage remains a critical issue. This is typically overcome using beamforming and beam training to establish a radio link between Tx and Rx based on an NLOS path. In these situations, the accuracy of positioning is considerably decreased and the goal of this thesis is consequently to propose a methodology to efficiently identify when a communication is being

performed with an NLOS rather than with a LOS path.

# References


[1] R. M. Haralick, S. R. Sternberg, and X. H. Zhuang, "Image-Analysis Using Mathematical Morphology," *IEEE Transactions on Pattern Analysis and Machine Intelligence,* vol. 9, no. 4, pp. 532-550, Jul, 1987.

[2] L. Atzori, A. Iera, and G. Morabito, "The Internet of Things: A survey," *Computer Networks,* vol. 54, no. 15, pp. 2787-2805, Oct 28, 2010.

[3] *Indoor Location Market by Component (Technology, Software Tools, and Services), Deployment Mode (Cloud, and On-premises), Application, Vertical (Transportation, Hospitality, Entertainment, Retail, and Public Buildings), and Region - Global Forecast to 2022,* market report, MarketsandMarkets Research Private Ltd., Oct 2017.

[4] D. Dardari, A. Conti, U. Ferner, A. Giorgetti, and M. Z. Win, "Ranging With Ultrawide Bandwidth Signals in Multipath Environments," *Proceedings of the IEEE,* vol. 97, no. 2, pp. 404-426, Feb, 2009.

[5] H. Liu, H. Darabi, P. Banerjee, and J. Liu, "Survey of wireless indoor positioning techniques and systems," *IEEE Transactions on Systems Man and Cybernetics Part C-Applications and Reviews,* vol. 37, no. 6, pp. 1067-1080, Nov, 2007.

[6] G. Deak, K. Curran, and J. Condell, "A survey of active and passive indoor localisation systems," *Computer Communications,* vol. 35, no. 16, pp. 1939-1954, Sep 15, 2012.

[7] D. Dardari, P. Closas, and P. M. Djuric, "Indoor Tracking: Theory, Methods, and Technologies," *IEEE Transactions on Vehicular Technology,* vol. 64, no. 4, pp. 1263-1278, Apr, 2015.

[8] A. Yassin, Y. Nasser, M. Awad, A. Al-Dubai, R. Liu, C. Yuen, R. Raulefs, and E. Aboutanios, "Recent Advances in Indoor Localization: A Survey on Theoretical Approaches and Applications," *IEEE Communications Surveys and Tutorials,* vol. 19, no. 2, pp. 1327-1346, 2017.

[9] A. Alarifi, A. Al-Salman, M. Alsaleh, A. Alnafessah, S. Al-Hadhrami, M. A. Al-Ammar, and H. S. Al-Khalifa, "Ultra Wideband Indoor Positioning Technologies: Analysis and Recent Advances," *Sensors,* vol. 16, no. 5, May, 2016.

[10] V. Honkavirta, T. Perala, S. Ali-Loytty, and R. Piche, "A Comparative Survey of WLAN Location Fingerprinting Methods," *WPNC: 2009 6th Workshop on Positioning, Navigation and Communication, Proceedings*, pp. 243-251, 2009.

[11] S. Gezici, Z. Sahinoglu, and I. Gvenc, *Ultra-wideband Positioning Systems: Theoretical Limits, Ranging Algorithms, and Protocols*, Reissue edition ed.: Cambridge University Press, 2011.

[12] T. S. Rappaport, S. Sun, R. Mayzus, H. Zhao, Y. Azar, K. Wang, G. N. Wong, J. K. Schulz, M. Samimi, and F. Gutierrez, "Millimeter Wave Mobile Communications for 5G Cellular: It Will Work!," *IEEE Access,* vol. 1, pp. 335-349, 2013.

[13] W. Roh, J. Y. Seol, J. Park, B. Lee, J. Lee, Y. Kim, J. Cho, K. Cheun, and F. Aryanfar, "Millimeter-Wave Beamforming as an Enabling Technology for 5G Cellular Communications: Theoretical Feasibility and Prototype Results," *IEEE Communications Magazine,* vol. 52, no. 2, pp. 106-113, Feb, 2014.

[14] Y. Niu, Y. Li, D. P. Jin, L. Su, and A. V. Vasilakos, "A survey of millimeter wave communications (mmWave) for 5G: opportunities and challenges," *Wireless Networks,* vol. 21, no. 8, pp. 2657-2676, Nov, 2015.

[15] *NGMN Alliance 5G White Paper*, Next Generation Mobile Network (NGMN), Feb 2015.

[16] T. r. G. P. P. (3GPP), *5G NR specifications*, 2017.

[17] *IEEE 5G and Beyond Technology Roadmap White Paper*, Institute of Electrical and Electronics Engineers (IEEE).

[18] *5G Network Architecture Design*, IMT-2020 (5G), Nov 2016.

[19] N. Bhushan, J. Y. Li, D. Malladi, R. Gilmore, D. Brenner, A. Damnjanovic, R. T. Sukhavasi, C. Patel, and S. Geirhofer, "Network Densification: The Dominant Theme for Wireless Evolution into 5G," *IEEE Communications Magazine,* vol. 52, no. 2, pp. 82-89, Feb, 2014.

[20] "WirelessHD Specification Overview," 2010.

[21] J. Flordelis, F. Rusek, F. Tufvesson, E. G. Larsson, and O. Edfors, "Massive MIMO Performance-TDD Versus FDD: What Do Measurements Say?," *IEEE Transactions on Wireless Communications,* vol. 17, no. 4, pp. 2247-2261, Apr, 2018.

[22] *Recommendation P.676-6: Attenuation by Atmospheric Gases*, International Telecommunication Union (ITU), 2005.

[23] T. S. Rappaport, J. N. Murdock, and F. Gutierrez, "State of the Art in 60-GHz Integrated Circuits and Systems for Wireless Communications," *Proceedings of the IEEE,* vol. 99, no. 8, pp. 1390-1436, Aug, 2011.

[24] E. International, "High Rate 60 GHz PHY, MAC and PALs," 2010.

[25] "IEEE Standard for Information technology-- Local and metropolitan area networks-- Specific requirements-- Part 15.3: Amendment 2: Millimeter-wave-based Alternative Physical Layer Extension," 2009.

[26] L. Verma, M. Fakharzadeh, and S. Choi, "Wifi on Steroids: 802.11ac and 802.11ad," *IEEE Wireless Communications,* vol. 20, no. 6, pp. 30-35, Dec, 2013.

[27] T. Nitsche, C. Cordeiro, A. B. Flores, E. W. Knightly, E. Perahia, and J. C. Widmer, "IEEE 802.11ad: Directional 60 GHz Communication for Multi-Gigabit-per-Second Wi-Fi," *IEEE Communications Magazine,* vol. 52, no. 12, pp. 132-141, Dec, 2014.

[28] "ISO/IEC/IEEE International Standard for Information technology--Telecommunications and information exchange between systems--Local and metropolitan area networks--Specific requirements-Part 11: Wireless LAN Medium Access Control (MAC) and Physical Layer (PHY) Specifications Amendment 3: Enhancements for Very High Throughput in the 60 GHz Band (adoption of IEEE Std 802.11ad-2012)," 2014.

[29] Y. Ghasempour, C. R. C. M. da Silva, C. Cordeiro, and E. W. Knightly, "IEEE 802.11ay: Next-Generation 60 GHz Communication for 100 Gb/s Wi-Fi," *IEEE Communications Magazine,* vol. 55, no. 12, pp. 186-192, Dec, 2017.

[30] S. Kutty, and D. Sen, "Beamforming for Millimeter Wave Communications: An Inclusive Survey," *IEEE Communications Surveys and Tutorials,* vol. 18, no. 2, pp. 949-973, 2016.

[31] K. Hosoya, N. Prasad, K. Ramachandran, N. Orihashi, S. Kishimoto, S. Rangarajan, and K. Maruhashi, "Multiple Sector ID Capture (MIDC): A Novel Beamforming Technique for 60-GHz Band Multi-Gbps WLAN/PAN Systems," *IEEE Transactions on Antennas and Propagation,* vol. 63, no. 1, pp. 81-96, Jan, 2015.

[32] A. Tahat, G. Kaddoum, S. Yousefi, S. Valaee, and F. Gagnon, "A Look at the Recent Wireless Positioning Techniques With a Focus on Algorithms for Moving Receivers," *IEEE Access,* vol. 4, pp. 6652-6680, 2016.

[33] S. Jayaprakasam, X. X. Ma, J. W. Choi, and S. Kim, "Robust Beam-Tracking for mmWave Mobile

Communications," *IEEE Communications Letters,* vol. 21, no. 12, pp. 2654-2657, Dec, 2017.

[34] A. Alkhateeb, O. El Ayach, G. Leus, and R. W. Heath, "Channel Estimation and Hybrid Precoding for Millimeter Wave Cellular Systems," *IEEE Journal of Selected Topics in Signal Processing,* vol. 8, no. 5, pp. 831-846, Oct, 2014.

[35] H. Wymeersch, G. Seco-Granados, G. Destino, D. Dardari, and F. Tufvesson, "5g Mm Wave Positioning for Vehicular Networks," *IEEE Wireless Communications,* vol. 24, no. 6, pp. 80-86, Dec, 2017.

[36] X. R. Cui, T. A. Gulliver, J. Li, and H. Zhang, "Vehicle Positioning Using 5G Millimeter-Wave Systems," *IEEE Access,* vol. 4, pp. 6964-6973, 2016.

[37] F. Lemic, J. Martin, C. Yarp, D. Chan, V. Handziski, L. Handziski, G. Fettweis, A. Wolisz, and J. Wawrzynek, "Localization as a Feature of mmWave Communication," *2016 International Wireless Communications and Mobile Computing Conference (Iwcmc)*, pp. 1033-1038, 2016.

[38] A. Shahmansoori, G. E. Garcia, G. Destino, G. Seco-Granados, and H. Wymeersch, "Position and Orientation Estimation Through Millimeter-Wave MIMO in 5G Systems," *IEEE Transactions on Wireless Communications,* vol. 17, no. 3, pp. 1822-1835, Mar, 2018.

[39] A. Guerra, F. Guidi, and D. Dardari, "Single-Anchor Localization and Orientation Performance Limits Using Massive Arrays: MIMO vs. Beamforming," *IEEE Transactions on Wireless Communications,* vol. 17, no. 8, pp. 5241-5255, Aug, 2018.

[40] P. Indirayanti, T. Ayhan, M. Verhelst, W. Dehaene, and P. Reynaert, "A mm-Precise 60 GHz Transmitter in 40 nm CMOS for Discrete-Carrier Indoor Localization," *IEEE Journal of Solid-State Circuits,* vol. 50, no. 7, pp. 1604-1617, Jul, 2015.

[41] A. Jafari, L. Petrillo, J. Sarrazin, D. Lautru, P. De Doncker, and A. Benlarbi-Delai, "TDOA estimation method using 60 GHz OFDM spectrum," *International Journal of Microwave and Wireless Technologies,* vol. 7, no. 1, pp. 31-35, Feb, 2015.

[42] M. Bocquet, C. Loyez, and N. Rolland, "An overview of 60 GHz location systems operating in multipath environments," *International Journal of Microwave and Wireless Technologies,* vol. 3, no. 2, pp. 223-230, Apr, 2011.

[43] X. L. Liang, H. Zhang, T. T. Lu, and T. A. Gulliver, "Extreme learning machine for 60 GHz millimetre wave positioning," *IET Communications,* vol. 11, no. 4, pp. 483-489, Mar 9, 2017.

[44] X. Y. Han, J. J. Wang, W. Shi, Q. N. Niu, and L. W. Xu, "Indoor precise positioning algorithm using 60GHz pulse based on compressive sensing," *Journal of Mathematics and Computer Science-Jmcs,* vol. 16, no. 2, pp. 256-272, 2016.

[45] A. Jafari, T. Mavridis, L. Petrillo, J. Sarrazin, M. Peter, W. Keusgen, P. De Doncker, and A. Benlarbi-Delai, "UWB Interferometry TDOA Estimation for 60-GHz OFDM Communication Systems," *IEEE Antennas and Wireless Propagation Letters,* vol. 15, pp. 1438-1441, 2016.

[46] M. Bocquet, C. Loyez, C. Lethien, N. Deparis, M. Heddebaut, A. Rivenq, and N. Rolland, "A multifunctional 60-GHz system for automotive applications with communication and positioning abilities based on time reversal," *7th European Radar Conference*, pp. 61-64, 2010.

[47] J. Palacios, G. Bielsa, P. Casari, and J. Widmer, "Single- and Multiple-Access Point Indoor Localization for Millimeter-Wave Networks," *IEEE Transactions on Wireless Communications,* vol. 18, no. 3, pp. 1927-1942, Mar, 2019.

[48] Z. Y. Pi, and F. Khan, "An Introduction to Millimeter-Wave Mobile Broadband Systems," *IEEE Communications*

*Magazine,* vol. 49, no. 6, pp. 101-107, Jun, 2011.

[49] S. Salous, *Radio Propagation Measurement and Channel Modelling*: John Wiley & Sons, Ltd, 2013.

[50] A. A. M. Saleh, and R. A. Valenzuela, "A Statistical-Model for Indoor Multipath Propagation," *IEEE Journal on Selected Areas in Communications,* vol. 5, no. 2, pp. 128-137, Feb, 1987.

[51] "Spatial channel model for Multiple Input Multiple Output (MIMO) simulations," 2017.

[52] A. Maltsev, V. Erceg, and E. Perahia, "Channel Models for 60 GHz WLAN Systems," Oct 2010.

[53] R. S. He, B. Ai, A. F. Molisch, G. L. Stuber, Q. Y. Li, Z. D. Zhong, and J. Yu, "Clustering Enabled Wireless Channel Modeling Using Big Data Algorithms," *IEEE Communications Magazine,* vol. 56, no. 5, pp. 177-183, May, 2018.

[54] R. O. Schmidt, "Multiple Emitter Location and Signal Parameter-Estimation," *IEEE Transactions on Antennas and Propagation,* vol. 34, no. 3, pp. 276-280, Mar, 1986.

[55] R. Roy, and T. Kailath, "Esprit - Estimation of Signal Parameters Via Rotational Invariance Techniques," *IEEE Transactions on Acoustics Speech and Signal Processing,* vol. 37, no. 7, pp. 984-995, Jul, 1989.

[56] J. A. Fessler, and A. O. Hero, "Space-Alternating Generalized Expectation-Maximization Algorithm," *IEEE Transactions on Signal Processing,* vol. 42, no. 10, pp. 2664-2677, Oct, 1994.

[57] B. H. Fleury, M. Tschudin, R. Heddergott, D. Dahlhaus, and K. I. Pedersen, "Channel parameter estimation in mobile radio environments using the SAGE algorithm," *IEEE Journal on Selected Areas in Communications,* vol. 17, no. 3, pp. 434-450, Mar, 1999.

[58] C. Gustafson, K. Haneda, S. Wyne, and F. Tufvesson, "On mm-Wave Multipath Clustering and Channel Modeling," *IEEE Transactions on Antennas and Propagation,* vol. 62, no. 3, pp. 1445-1455, Mar, 2014.

[59] X. Y. Wu, C. X. Wang, J. Sun, J. Huang, R. Feng, Y. Yang, and X. H. Ge, "60-GHz Millimeter-Wave Channel Measurements and Modeling for Indoor Office Environments," *IEEE Transactions on Antennas and Propagation,* vol. 65, no. 4, pp. 1912-1924, Apr, 2017.

[60] H. Xu, V. Kukshya, and T. S. Rappaport, "Spatial and temporal characteristics of 60-GHz indoor channels," *IEEE Journal on Selected Areas in Communications,* vol. 20, no. 3, pp. 620-630, Apr, 2002.

[61] P. F. M. Smulders, "Statistical Characterization of 60-GHz Indoor Radio Channels," *IEEE Transactions on Antennas and Propagation,* vol. 57, no. 10, pp. 2820-2829, Oct, 2009.

[62] P. Pagani, N. Malhouroux, I. Siaud, V. Guillet, and W. Li, *Characterization and Modeling of the 60 GHz Indoor Channel in the Office and Residential Environments*, France Telecom Research and Development, Jan 2006.

[63] S. Y. Geng, J. Kivinen, X. W. Zhao, and P. Vainikainen, "Millimeter-Wave Propagation Channel Characterization for Short-Range Wireless Communications," *IEEE Transactions on Vehicular Technology,* vol. 58, no. 1, pp. 3-13, Jan, 2009.

[64] X. F. Yin, C. Ling, and M. D. Kim, "Experimental Multipath-Cluster Characteristics of 28-GHz Propagation Channel," *IEEE Access,* vol. 3, pp. 3138-3150, 2015.

[65] W. Fan, I. Carton, J. O. Nielsen, K. Olesen, and G. F. Pedersen, "Measured wideband characteristics of indoor channels at centimetric and millimetric bands," *Eurasip Journal on Wireless Communications and Networking*, Feb 20, 2016.

[66] G. R. MacCartney, T. S. Rappaport, S. Sun, and S. Deng, "Indoor Office Wideband Millimeter-Wave Propagation Measurements and Channel Models at 28 and 73 GHz for Ultra-Dense 5G Wireless Networks," *IEEE Access,* vol. 3, pp. 2388-2424, 2015.

[67] M. R. Akdeniz, Y. P. Liu, M. K. Samimi, S. Sun, S. Rangan, T. S. Rappaport, and E. Erkip, "Millimeter Wave Channel Modeling and Cellular Capacity Evaluation," *IEEE Journal on Selected Areas in Communications,* vol. 32, no. 6, pp. 1164-1179, Jun, 2014.

[68] M. K. Samimi, and T. S. Rappaport, "3-D Millimeter-Wave Statistical Channel Model for 5G Wireless System Design," *IEEE Transactions on Microwave Theory and Techniques,* vol. 64, no. 7, pp. 2207-2225, Jul, 2016.

[69] M. F. Iskander, and Z. Q. Yun, "Propagation prediction models for wireless communication systems," *IEEE Transactions on Microwave Theory and Techniques,* vol. 50, no. 3, pp. 662-673, Mar, 2002.

[70] A. Maltsev, R. Maslennikov, A. Sevastyanov, A. Khoryaev, and A. Lomayev, "Experimental Investigations of 60 GHz WLAN Systems in Office Environment," *IEEE Journal on Selected Areas in Communications,* vol. 27, no. 8, pp. 1488-1499, Oct, 2009.

[71] R. G. Kouyoumjian, and P. H. Pathak, "Uniform Geometrical Theory of Diffraction for an Edge in a Perfectly Conducting Surface," *Proceedings of the IEEE,* vol. 62, no. 11, pp. 1448-1461, 1974.

[72] M. Jacob, S. Priebe, R. Dickhoff, T. Kleine-Ostmann, T. Schrader, and T. Kurner, "Diffraction in mm and Sub-mm Wave Indoor Propagation Channels," *IEEE Transactions on Microwave Theory and Techniques,* vol. 60, no. 3, pp. 833-844, Mar, 2012.

[73] G. R. MacCartney, S. J. Deng, S. Sun, and T. S. Rappaport, "Millimeter-Wave Human Blockage at 73 GHz with a Simple Double Knife-Edge Diffraction Model and Extension for Directional Antennas," *2016 IEEE 84th Vehicular Technology Conference (Vtc Fall)*, 2016.

[74] T. Mavridis, L. Petrillo, J. Sarrazin, D. Lautru, A. Benlarbi-Delai, and P. De Doncker, "Theoretical and Experimental Investigation of a 60-GHz Off-Body Propagation Model," *IEEE Transactions on Antennas and Propagation,* vol. 62, no. 1, pp. 393-402, Jan, 2014.

[75] T. Mavridis, L. Petrillo, J. Sarrazin, D. Lautru, A. Benlarbi-Delai, and P. De Doncker, "Creeping Wave Model of Diffraction of an Obliquely Incident Plane Wave by a Circular Cylinder at 60 GHz," *IEEE Transactions on Antennas and Propagation,* vol. 62, no. 3, pp. 1372-1377, Mar, 2014.

[76] T. Mavridis, L. Petrillo, J. Sarrazin, A. Benlarbi-Delai, and P. De Doncker, "Near-Body Shadowing Analysis at 60 GHz," *IEEE Transactions on Antennas and Propagation,* vol. 63, no. 10, pp. 4505-4511, Oct, 2015.

[77] T. Y. Bai, and R. W. Heath, "Coverage and Rate Analysis for Millimeter-Wave Cellular Networks," *IEEE Transactions on Wireless Communications,* vol. 14, no. 2, pp. 1100-1114, Feb, 2015.

[78] r. G. P. P. (3GPP), "Further advancements for E-UTRA physical layer aspects," 2010.

[79] M. K. Samimi, T. S. Rappaport, and G. R. MacCartney, "Probabilistic Omnidirectional Path Loss Models for Millimeter-Wave Outdoor Communications," *IEEE Wireless Communications Letters,* vol. 4, no. 4, pp. 357-360, Aug, 2015.

[80] S. Roy, and M. Mehrnoush, "A New Poisson Process-Based Model for LOS/NLOS Discrimination in Clutter Modeling," *IEEE Transactions on Antennas and Propagation,* vol. 67, no. 12, pp. 7538-7549, Dec, 2019.

[81] S. Collonge, G. Zaharia, and G. El Zein, "Influence of the human activity on wide-band characteristics of the 60 GHz indoor radio channel," *IEEE Transactions on Wireless Communications,* vol. 3, no. 6, pp. 2396-2406, Nov, 2004.

[82] K. Venugopal, and R. W. Heath, "Millimeter Wave Networked Wearables in Dense Indoor Environments," *IEEE Access,* vol. 4, pp. 1205-1221, 2016.

[83] R. W. Heath, N. Gonzalez-Prelcic, S. Rangan, W. Roh, and A. M. Sayeed, "An Overview of Signal Processing Techniques for Millimeter Wave MIMO Systems," *IEEE Journal of Selected Topics in Signal Processing,* vol. 10, no. 3, pp. 436-453, Apr, 2016.

[84] S. H. Wu, L. K. Chiu, K. Y. Lin, and T. H. Chang, "Robust Hybrid Beamforming with Phased Antenna Arrays for Downlink SDMA in Indoor 60 GHz Channels," *IEEE Transactions on Wireless Communications,* vol. 12, no. 9, pp. 4542-4557, Sep, 2013.

# Chapter 2

# NLOS Identification: State of The Art

## Contents



## 2.1 Introduction

Performing accurate localization supposes mandatory the existence of LOS signal. Otherwise large location errors may occur making the localization process very sensitive to the environment and to the quality and integrity of the processed signal. It hence seems clear that prior to any signal processing, one must state on the validity of the signal by seeking the presence and the assesment of LOS contribution.

In this chapter, the NLOS identification are investigated. The theoretical frame of NLOS identification and the main works available in the literature are analyzed in detail. Clustering methods are also reviewed as they appear to be a necessary step towards NLOS identification.

## 2.2 NLOS Identification

The distinction between LOS and NLOS components is a problem of supervised pattern recognition [1]. According to the general procedure of pattern recognition, a typical procedure of NLOS identification is shown in Figure 2.1. NLOS identification is a process of understanding the inherent physical characteristics of different transmissions, mathematically modeling the physical features and then statistically deciding the type of transmission from a series of received signals, based on the metrics extracted from the mathematical model.

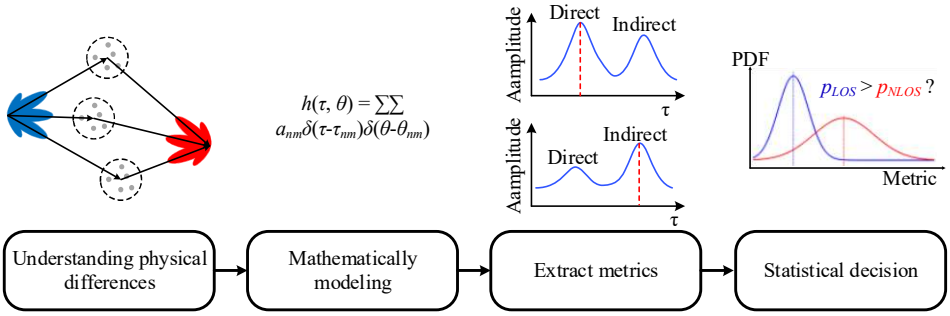


Figure 2.1 Procedure of NLOS identification

The training data supervise testing identification. The performance of the identification involves three factors: the correct recognition for the natural feature of the physical phenomenon, the appropriate selection of the metrics describing the feature, effective statistical method for classifying the different metrics set. The above factors in the current NLOS identification studies will be separately investigated in this section.

### 2.2.1 Survey of current NLOS identification in the litterature

The physical natural difference between NLOS and LOS transmissions is related to the scattering process. It typically influences wireless transmissions, and channel modeling is usually performed in order to assesss communications schemes. It has furthermore a strong influence on localization process and NLOS identification has been therefore been studied for this purpose. However, as mentioned in chapter 1, relatively few works on localization in the millimeter band are reported. Most of the work about indoor localization is in the UWB (3.1-10.6 GHz) and WLAN (2.4 GHz) bands [2]. The WLAN localization is mainly performed using fingerprint [3] instead of triangular geometry. Due to the high positioning accuracy offered by wideband signals, most of the current works of triangular geometry-based localization concentrates on the low-frequency UWB band [4, 5]. Consequently, the studies of NLOS identification mainly focused on UWB as well [6]. The propagation characteristics of UWB are very different from those of the millimeter-wave band. The result of numerical simulations with the Geometrical Theory of Diffraction (GTD) [7] manifested that the attenuation in UWB between the first, second, and third diffraction is 4.04 dB, 9.96 dB, and 11 dB, repectively, for an incident angle of 60°. Because of strong diffraction effects, the multipath phenomenon in the UWB band is significant [8]. Different from the sparse mm-wave channel, the received multipath components are plentiful, even if the antenna used is a

directional antenna pattern [9]. Constrained by the above propagating conditions, a physical model of current NLOS identification in the UWB is defined as identifying which BS in the transmitting environment is unobstructed, as shown in Figure 2.2. In a cellular network, many BSs locate around a UE. The antenna patterns of all the BSs and UE are simplified as omnidirectional. Besides the direct path, the transmitting paths are constructed with abundant indirect paths, as well. If at least one direct path is not obstructed, the scenario is defined as a LOS scenario. The unblocked BS is the LOS station, as shown in Figure 2.2 (a). In contrast, in a NLOS scenario, all the direct path are blocked, that means all the BS are NLOS stations for the UE, as presented in Figure 2.2 (b). The target work of NLOS identification is to distinguish the LOS and NLOS stations by measurement, and then to recognize the NLOS scenario. The above-mentionned works typically use statistical differences in channel features to distinguish LOS from NLOS situations. These methods of identification are discussed in the following.

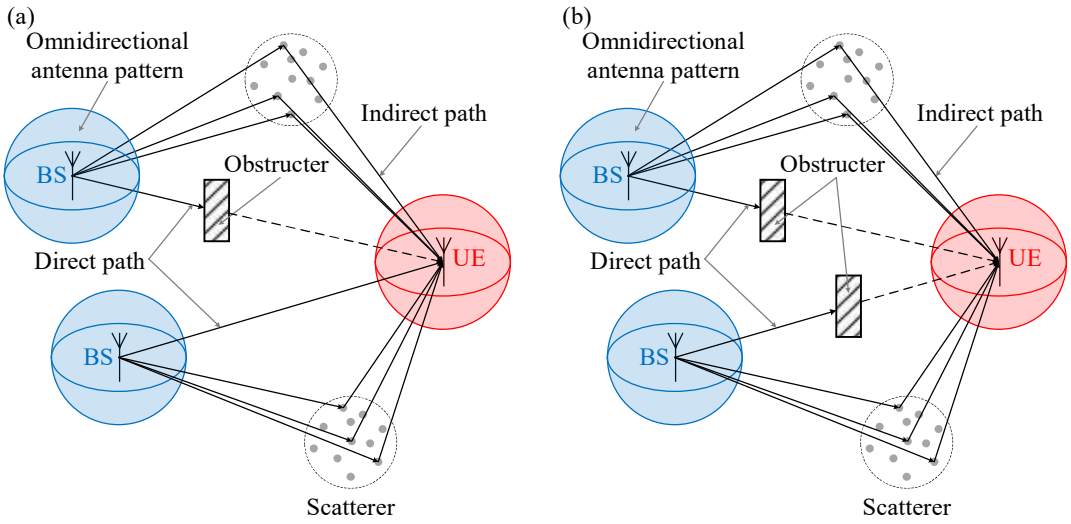


Figure 2.2 Target scenario to identify: (a) LOS scenario; (b) NLOS scenario

## 2.2.2 Statistical differences between LOS and NLOS

In order to determine the metrics for statistical recognition, the scattering process needs to be mathematically modeled. Because of the strong diffraction and rich multipath components, statistical differences between LOS and NLOS transmission in the UWB band primarily occur in the time domain rather than in the space domain (e.g., power angular spectrum…). The channel model in IEEE 802.15.4a [10, 11] for UWB is a cluster-based channel model of Saleh-Valenzuela type. It is a time-domain channel model without spatial descriptions such as AOA and DOA. The channel model consists of eight scenarios: residential, office, outdoor, and industrial, all considering both LOS and NLOS scenarios,. The measurement scenario is labeled as LOS or NLOS before the measurement. The path loss, the means ($\mu_m$ and $\mu_{rms}$) and variances ($\sigma_m$ and $\sigma_{rms}$) of mean excess delay $\bar{\tau}$ and RMS delay spread $\tau_{rms}$ given in the IEEE 802.15.4a channel model [10, 12] are listed in Table 2.1. Due to the scattering attenuation, the path loss of the NLOS transmission is generally much more significant than the LOS transmission in the same scenario. Also, the mean values of mean excess delay and RMS delay spread both appear higher in the NLOS

scenarios than in the LOS scenarios. Large values of NLOS $\mu_m$ are related to long average length of the transmitting path caused by reflections. Large values of NLOS $\mu_{rms}$ indicate that the multipath components are generated by multiple reflections and exhibit a slow decay. On the other hand, the variances $\sigma_m$ and $\sigma_{rms}$, in LOS scenarios are higher than NLOS scenarios. For LOS transmission, the contribution of the direct path is much larger than indirect paths and greatly depends on the individual distances between Tx and Rx. In contrast, the construction among multipath is related to the scattering environment, thus with a small depedency upon the distance between Tx and Rx. Therefore, the variance in the NLOS scenario is relatively stable. The above discussion illustrates how the mathematical channel model of IEEE 802.15.4a can adequately reflect the physical difference between the LOS and NLOS transmissions.

Table 2.1 Path loss, mean excess delay and RMS delay spread in the channel model of IEEE 802.15.4a [12]

| Channel | Scenario | Path loss (PL) [dB] | Mean excess delay ($\bar{\tau}$) | | RMS delay spread ($\tau_{rms}$) | |
|---|---|---|---|---|---|---|
| | | | $\mu_m$[ns] | $\sigma_m$[ns] | $\mu_{rms}$[ns] | $\sigma_{rms}$[ns] |
| CM-1 | Residential (LOS) | 43.9 | 2.6685 | 0.4837 | 2.7676 | 0.3129 |
| CM-2 | Residential (NLOS) | 48.7 | 3.3003 | 0.3843 | 2.9278 | 0.1772 |
| CM-3 | Office (LOS) | 35.4 | 2.0993 | 0.3931 | 2.2491 | 0.3597 |
| CM-4 | Office (NLOS) | 57.9 | 2.7756 | 0.1770 | 2.5665 | 0.1099 |
| CM-5 | Outdoor (LOS) | 45.6 | 3.0864 | 0.4433 | 3.3063 | 0.2838 |
| CM-6 | Outdoor (NLOS) | 73.0 | 4.6695 | 0.4185 | 4.2967 | 0.3742 |
| CM-7 | Industrial (LOS) | 56.7 | 1.3845 | 0.9830 | 1.9409 | 0.7305 |
| CM-8 | Industrial (NLOS) | 56.7 | 4.7356 | 0.0225 | 4.4872 | 0.0164 |

### 2.2.3 Metrics of identification

A metric is an indicator that determines the type of transmission in the statistical decision algorithms. NLOS identification typically uses three kinds of metrics. The first type, as discussed in chapter 1, is the variance $\hat{\sigma}^2$ of range distances $\hat{d}_i$ estimated for a set of $N$ measurements can be directly used as a metric to identify the NLOS transmission.

$$\hat{\sigma}^2 = \frac{1}{N}\sum_{i=1}^{N}\left(\hat{d}_i - \mu\right)^2 \tag{2.1}$$

$$\mu = \frac{1}{N}\sum_{i=1}^{N}\hat{d}_i \tag{2.2}$$

The second type of metric is the channel parameters discussed in the previous section. The channel parameters are valid indicators of the LOS and NLOS. Because the transmission conditions are labeled before the measurement during channel modeling, these parameters can be measured from the received CIR and be related to the type of signal transmission. This offers interesting insights as whether a given metrics

can be useful for LOS/NLOS identification The channel parameters commonly used to identify the type of transmission in reported works are the total energy $E$, mean excess delay $\bar{\tau}$, and the RMS delay spread $\tau_{RMS}$:

$$E = \int_0^T \left|h(\tau)\right|^2 d\tau \tag{2.3}$$

$$\bar{\tau} = \frac{\int_0^T \tau \left|h(\tau)\right|^2 d\tau}{\int_0^T \left|h(\tau)\right|^2 d\tau} \tag{2.4}$$

$$\tau_{RMS}^2 = \frac{\int_0^T (\tau - \bar{\tau})^2 \left|h(\tau)\right|^2 d\tau}{\int_0^T \left|h(\tau)\right|^2 d\tau} \tag{2.5}$$

Some extra parameters of CIR are also used, such as the maximum power $P_{max}$, the amplitude of the first peak in $P_{first}$, and the rise time of the first peak $t_{rise}$:

$$P_{\max} = \max_{\tau} \left|h(\tau)\right|^2 \tag{2.6}$$

$$P_{first} = \left|h(\tau)\right|^2 \Big|_{\min \tau} \tag{2.7}$$

$$t_{rise} = \min\left\{\tau : \left|h(\tau)\right| \geq \sigma_{noise}\right\} - \min\left\{\tau : \left|h(\tau)\right| \geq h_{\max}\right\} \tag{2.8}$$

The third type of metric is the variables to quantify the shape of the PDF of the received CIR. As discussed in chapter 1, the direct path produces a sharp peak, and the dispersion caused by multipath generates small peaks spread over the CIR. The peak generated by the LOS path tends to produce sharp PDFs. A metric to quantify the "sharpness" of the CIR PDF is the kurtosis $\kappa$ which is defined as the standard moment of the fourth-order for the CIR sequence:

$$\kappa = \frac{\mathrm{E}\left[\left(\left|h(\tau)\right| - \mu_{|h(\tau)|}\right)^4\right]}{\mathrm{E}\left[\left(\left|h(\tau)\right| - \mu_{|h(\tau)|}\right)^2\right]^2} = \frac{\mathrm{E}\left[\left(\left|h(\tau)\right| - \mu_{|h(\tau)|}\right)^4\right]}{\sigma_{|h(\tau)|}^4} \tag{2.9}$$

$$\mu_{|h(\tau)|} = \frac{1}{T}\int_0^T \left|h(\tau)\right| d\tau \tag{2.10}$$

## 2.2.4 Statistical decision methods

NLOS identification is statistically seen as a problem of hypothesis testing. The null hypothesis is LOS transmission, and the alternative hypothesis is NLOS transmission. The statistical descriptions of LOS and NLOS transmission features, such as PDF are first obtained using training data (large sample set). The testing is achieved with testing data (small sample set). If the testing data verify the statistical descriptions of the null hypothesis, the null hypothesis cannot be rejected; otherwise, the alternative hypothesis must be accepted. In the reported studies, both parametric and nonparametric methods are used to distinguish transmission types. The performance of the hypothesis testing is evaluated with the probability of type I and type II error. Type I error is the rejection of a true null hypothesis, while type II error is the acceptance of a false alternative hypothesis.

### 2.2.4.1 Parametric testing

The parametric hypothesis testing, such as Maximum Likelihood Ratio (MLR) testing is used both for the ranging-based [13] and channel features-based [12] identifications. In ranging-based identification, the testing feature is the measured distance. As discussed in chapter 1, the ranging error is induced by multipath. Multipath can be described with a cluster-based model. Probabilty of parameters such as Time-Of-Arrival (TOA), Angle-Of-Arrival (AOA), and Angle-Of-Departure (AOD), that described the clusters, are distributed with a certain intracluster statistical model, such as Gaussian, exponential, etc. Therefore, the received signal is a combination of many grouped paths. If the antenna pattern is omnidirectional like in Figure 2.2, the wave propagates through any corner of the space so that the number of reflections is very large. In that case, according to the central limit theorem, no matter the intra-cluster distribution, the parameters to describe the combination of the path clusters follow a Gaussian distribution fluctuation [ref]. Therefore, the distances $\hat{d}$ estimated with the channel parameters are also following a Gaussian distributed fluctuation with a bias $\mu$ and a variance $\sigma^2$, $n \sim \mathcal{N}(\mu, \sigma^2)$. For LOS transmission, the distance can be estimated from the direct path, and the distribution is therefore unbiased ($\mu_{los} = 0$). The distance estimated in the NLOS transmission is biased ($\mu_{nlos} > 0$), and the NLOS variance $\sigma^2_{nlos}$ is much larger than the LOS variance $\sigma^2_{los}$. Thus, the estimated distance $\hat{d}$ can be expressed by the following mathematical expression:

$$\hat{d} = d + n \tag{2.11}$$

where $d$ is the actual distance between a pair of Rx and Tx, and $n$ is a normally distributed fluctuation for the measured distance $\hat{d}$. In NLOS transmissions, $n_{nlos} \sim \mathcal{N}(\mu_{nlos}, \sigma^2_{nlos})$, and in the LOS transmission $n_{los} \sim \mathcal{N}(0, \sigma^2_{los})$, with $\sigma^2_{nlos} > \sigma^2_{los}$. Therefore, under the condition of actual distance $d$, the estimated distance $\hat{d}$ follows the distribution given by (2.11):

$$\hat{d} \sim \begin{cases} f^{los}\left(\hat{d}\middle|d\right) = \mathcal{N}\left(d, \sigma^2_{los}\right), & \text{LOS transmission} \\ f^{nlos}\left(\hat{d}\middle|d\right) = \mathcal{N}\left(d + \mu_{nlos}, \sigma^2_{nlos}\right), & \text{NLOS transmission} \end{cases}, \ \sigma^2_{nlos} > \sigma^2_{los} \tag{2.12}$$

Where $f^{nlos}(\hat{d} \mid d)$ and $f^{los}(\hat{d} \mid d)$ are the posterior PDFs under the condition of actual $d$ with NLOS and LOS transmission respectively. The parameters of the PDFs, $\mu_{los}$, $\sigma_{los}$, and $\sigma_{nlos}$, are obtained with a set of measurements with $N$ samples $\{d_i\}$, $i = 1, 2, \ldots N$, under a reasonable assumption of *i.i.d.* measurements. The joint PDF of $N$ samples is:

$$f^{los}\left(\hat{d}_1,\hat{d}_2,...,\hat{d}_N \middle| \sigma_{los}\right) = \prod_{i=1}^{N} \frac{1}{\left(2\pi\sigma_{los}^2\right)^{1/2}} \exp\left[-\frac{\hat{d}_i^2}{2\sigma_{los}^2}\right] \tag{2.13}$$

$$f^{nlos}\left(\hat{d}_1,\hat{d}_2,...,\hat{d}_N \middle| \mu_{nlos},\sigma_{nlos}\right) = \prod_{i=1}^{N} \frac{1}{\left(2\pi\sigma_{nlos}^2\right)^{1/2}} \exp\left[-\frac{\left(\hat{d}_i-\mu_{nlos}\right)^2}{2\sigma_{nlos}^2}\right] \tag{2.14}$$

Introducing a measurement distances array $\hat{\boldsymbol{d}} = [\hat{d}_1, \hat{d}_2, \ldots \hat{d}_i, \ldots, \hat{d}_N]^T$ , $i = 1, 2, \ldots N$, the above multi-variables PDFs are derived as:

$$f^{los}\left(\hat{\boldsymbol{d}} \middle| \sigma_{los}\right) = \frac{1}{\left(2\pi\sigma_{los}^2\right)^{N/2}} \exp\left[-\frac{\hat{\boldsymbol{d}}^T\hat{\boldsymbol{d}}}{2\sigma_{los}^2}\right] \tag{2.15}$$

$$f^{nlos}\left(\hat{\boldsymbol{d}} \middle| \mu_{nlos},\sigma_{nlos}\right) = \frac{1}{\left(2\pi\sigma_{nlos}^2\right)^{N/2}} \exp\left[-\frac{\left(\hat{\boldsymbol{d}}-\mu_{nlos}\right)^T\left(\hat{\boldsymbol{d}}-\mu_{nlos}\right)}{2\sigma_{nlos}^2}\right] \tag{2.16}$$

With the trained PDFs of ranging distance, the hypothesis testing is described as: if the ranging distance is sampled from the distribution $f^{los}(\hat{\boldsymbol{d}} \mid \sigma_{los})$, the null hypothesis ($H_0$) of LOS transmission cannot be rejected; if it is sampled from $f^{nlos}(\hat{\boldsymbol{d}} \mid \mu_{nlos}, \sigma_{nlos})$, the alternative hypothesis ($H_1$) of NLOS transmission has to be accepted:

$$\begin{aligned} &H_0\text{: } \hat{d} \sim f^{los}\left(\hat{\boldsymbol{d}} \middle| \sigma_{los}\right), \text{ LOS transmission} \\ &H_1\text{: } \hat{d} \sim f^{nlos}\left(\hat{\boldsymbol{d}} \middle| \mu_{nlos},\sigma_{nlos}\right), \text{ NLOS transmission} \end{aligned} \tag{2.17}$$

MLR testing is an effective method to implement the hypothesis testing. If the LOS likelihood $\mathcal{L}(\hat{\sigma}_{los}; \hat{\boldsymbol{d}})$ is larger than the NLOS likelihood $\mathcal{L}(\hat{\mu}_{nlos}, \hat{\sigma}_{nlos}; \hat{\boldsymbol{d}})$ of measurement, the null hypothesis is accepted. In general, the log likelihood function for both LOS and NLOS are in the form of:

$$\ln \mathcal{L}\left(\mu,\sigma;\hat{\boldsymbol{d}}\right) = -\frac{N}{2}\ln\left(2\pi\sigma^2\right) - \frac{\left(\hat{\boldsymbol{d}}-\mu\right)^T\left(\hat{\boldsymbol{d}}-\mu\right)}{2\sigma^2} \tag{2.18}$$

The parameter $\mu$ and $\sigma$ are estimated by maximizing the likelihood function at the zero point of the first-order derivative:

$$\frac{\partial \ln \mathcal{L}\left(\mu,\sigma;\hat{\boldsymbol{d}}\right)}{\partial \mu}=\frac{\left(\hat{\boldsymbol{d}}-\mu\right)^{T}\left(\hat{\boldsymbol{d}}-\mu\right)}{\sigma^{2}}=0 \tag{2.19}$$

$$\frac{\partial \ln \mathcal{L}\left(\mu,\sigma;\hat{\boldsymbol{d}}\right)}{\partial \sigma}=-\frac{N}{\sigma}+\frac{\left(\hat{\boldsymbol{d}}-\mu\right)^{T}\left(\hat{\boldsymbol{d}}-\mu\right)}{\sigma^{3}}=0 \tag{2.20}$$

Solve the above equations with a condition $\hat{\mu}_{los}=0$, the hypothesis testing becomes:

$$\begin{aligned} &H_0\text{: }\ \hat{\sigma}_{los}^2=\frac{1}{N}\hat{\boldsymbol{d}}^T\hat{\boldsymbol{d}},\ \text{LOS transmission}\\ &H_1\text{: }\ \hat{\mu}_{nlos}=\frac{1}{N}\sum_{i=1}^{N}\hat{d}_i,\hat{\sigma}_{nlos}^2=\frac{1}{N}\left(\hat{\boldsymbol{d}}-\hat{\mu}_{nlos}\right)^T\left(\hat{\boldsymbol{d}}-\hat{\mu}_{nlos}\right),\ \text{NLOS transmission}\end{aligned} \tag{2.21}$$

After derivation, the likelihood ratio $L(\hat{\boldsymbol{d}})$ is expressed as:

$$L\left(\hat{\boldsymbol{d}}\right)=\frac{\mathcal{L}\left(\hat{\sigma}_{los};\hat{\boldsymbol{d}}_{los}\right)}{\mathcal{L}\left(\hat{\mu}_{nlos},\hat{\sigma}_{nlos};\hat{\boldsymbol{d}}_{nlos}\right)}=\left(\frac{\hat{\sigma}_{nlos}^2}{\hat{\sigma}_{los}^2}\right)^N=\left[\frac{\left(\hat{\boldsymbol{d}}-\frac{1}{N}\sum_{i=1}^{N}\hat{d}_i\right)^T\left(\hat{\boldsymbol{d}}-\frac{1}{N}\sum_{i=1}^{N}\hat{d}_i\right)}{\hat{\boldsymbol{d}}^T\hat{\boldsymbol{d}}}\right]^N\underset{H_1}{\overset{H_0}{\gtrless}}1 \tag{2.22}$$

For the channel feature-based identification, the hypothesis is regarding the mean excess delay $\bar{\tau}$, the RMS delay spread $\tau_{RMS}$, and the kurtosis $\kappa$:

$$\begin{aligned} &H_0\text{: }\ \hat{\bar{\tau}}\sim f^{los}\left(\bar{\tau}\middle|\mu_{\bar{\tau}}^{los},\sigma_{\bar{\tau}}^{los}\right),\ \ \hat{\tau}_{RMS}\sim f^{los}\left(\tau_{RMS}\middle|\mu_{\tau_{RMS}}^{los},\sigma_{\tau_{RMS}}^{los}\right),\ \ \hat{\kappa}\sim f^{los}\left(\kappa\middle|\mu_{\kappa}^{los},\sigma_{\kappa}^{los}\right),\ \text{LOS}\\ &H_1\text{: }\ \hat{\bar{\tau}}\sim f^{nlos}\left(\bar{\tau}\middle|\mu_{\bar{\tau}}^{nlos}\sigma_{\bar{\tau}}^{nlos}\right),\ \ \hat{\tau}_{RMS}\sim f^{nlos}\left(\tau_{RMS}\middle|\mu_{\tau_{RMS}}^{nlos},\sigma_{\tau_{RMS}}^{nlos}\right),\ \ \hat{\kappa}\sim f^{nlos}\left(\kappa\middle|\mu_{\kappa}^{nlos},\sigma_{\kappa}^{nlos}\right),\ \text{NLOS}\end{aligned} \tag{2.23}$$

The corresponding likelihood of GLRT is a multiplication of the above three likelihood ratios:

$$L\left(\hat{\kappa},\hat{\bar{\tau}},\hat{\tau}_{RMS}\right)=\frac{\mathcal{L}\left(\hat{\mu}_{\bar{\tau}}^{los},\hat{\sigma}_{\bar{\tau}}^{los};\hat{\bar{\tau}}^{los}\right)}{\mathcal{L}\left(\hat{\mu}_{\bar{\tau}}^{nlos},\hat{\sigma}_{\bar{\tau}}^{nlos};\hat{\bar{\tau}}^{los}\right)}\times\frac{\mathcal{L}\left(\hat{\mu}_{\tau_{RMS}}^{los},\hat{\sigma}_{\tau_{RMS}}^{los};\hat{\tau}_{RMS}^{los}\right)}{\mathcal{L}\left(\hat{\mu}_{\tau_{RMS}}^{nlos},\hat{\sigma}_{\tau_{RMS}}^{nlos};\hat{\tau}_{RMS}^{nlos}\right)}\times\frac{\mathcal{L}\left(\hat{\mu}_{\kappa}^{los},\hat{\sigma}_{\kappa}^{los};\hat{\kappa}^{los}\right)}{\mathcal{L}\left(\hat{\mu}_{\kappa}^{nlos},\hat{\sigma}_{\kappa}^{nlos};\hat{\kappa}^{nlos}\right)}\underset{H_1}{\overset{H_0}{\gtrless}}1 \tag{2.24}$$

The mean excess delay $\bar{\tau}$, the RMS delay spread $\tau_{RMS}$, and kurtosis $\kappa$ are fitted with log-normal PDFs in both LOS and NLOS transmission. The difference of the three features between LOS and NLOS transmission was validated with the channel model of IEEE 802.15.4a, as shown in Table 2.1 and Table 2.2.

Table 2.2 Kurtosis calculated with the channel model of IEEE 802.15.4a [12]

| Channel | Scenario | $\mu_\kappa$ | $\sigma_\kappa$ |
|---|---|---|---|
| CM-1 | Residential (LOS) | 4.6631 | 0.5770 |
| CM-2 | Residential (NLOS) | 3.6697 | 0.4886 |
| CM-3 | Office (LOS) | 4.4744 | 0.4579 |
| CM-4 | Office (NLOS) | 2.8154 | 0.3459 |
| CM-5 | Outdoor (LOS) | 4.4509 | 0.5163 |
| CM-6 | Outdoor (NLOS) | 4.8886 | 0.4497 |
| CM-7 | Industrial (LOS) | 4.2637 | 0.7447 |
| CM-8 | Industrial (NLOS) | 2.1141 | 0.1487 |

Table 2.3 Probability of correct testing by MLR with the channel model of IEEE 802.15.4a [12]

| Channel | Scenario | Kurtosis | mean excess delay | RMS delay spread | Joint |
|---|---|---|---|---|---|
| CM-1 | Residential (LOS) | 78.6% | 74.3% | 61.7% | 81.8% |
| CM-2 | Residential (NLOS) | 83.2% | 77.9% | 76.1% | 84.3% |
| CM-3 | Office (LOS) | 99.0% | 88.5% | 73.6% | 97.9% |
| CM-4 | Office (NLOS) | 96.7% | 86.3% | 89.0% | 95.9% |
| CM-5 | Outdoor (LOS) | 66.3% | 98.2% | 93.9% | 98.9% |
| CM-6 | Outdoor (NLOS) | 71.4% | 95.2% | 92.7% | 97.8% |
| CM-7 | Industrial (LOS) | 98.3% | 88.3% | 98.3% | 88.2% |
| CM-8 | Industrial (NLOS) | 98.4% | 100% | 100% | 99.9% |

The performance of the MLR is listed in Table 2.3. The different metric provides different performance, i.e., the probabilities of correct testing between scenarios are different. The testing with RMS delay spread in the LOS Residential scenario gives the lowest correct identification probability 61.7%, while it provides 100% identification in NLOS Industrial scenario. It is interesting to note that the joint use of different features for testing does not necessarily lead to better performance than the use of a single feature.

## 2.2.4.2Non-parametric testing

Currently, non-parametric testing is mainly used for identifying the channel feature in NLOS transmission. In the channel model, the transmission characteristics are parametrized as statistical features. These statistical features are the metrics to define the class of transmission. The nonparametric classifiers for the NLOS identification map an $n$-metric $\mathbb{R}$ set into a set of binary LOS/NLOS labels: $\mathbb{R}^n \rightarrow$ {LOS, NLOS}. The structure of the classifier is usually a weighing network of feature-contribution to the output

label. The constructing process of a classifier is to train the weights of the classifiers with the input metric data by minimizing the total residual from the output labels to the a priori known labels. Two nonparametric methods of testing are typically used for the identification of transmission: the artificial neural network (ANN) and support vector machine (SVM).

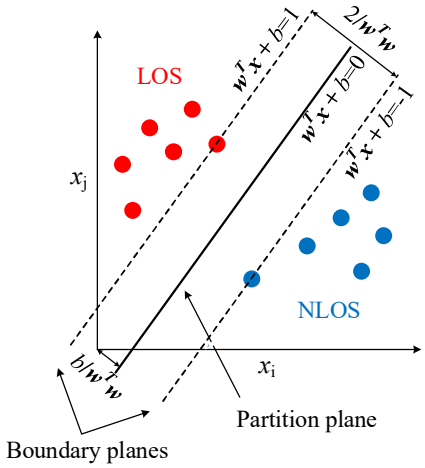


Figure 2.3 Schematic diagram of SVM to distinguish the LOS and NLOS transmission with a hyperplane $\boldsymbol{w}^T\hat{\boldsymbol{x}} + b = 0$

SVM [14] is a linear classifier to partition a $p$-dimensional parameter space into domains by many ($p$ - 1)-dimensional hyperplanes, in order to make each domain containing one and only one cluster of data. The principle of partitioning is to maximize the distance between the separation hyperplane and the nearest data point of any cluster. In that case, the training generalization error is minimized. The above problem is equivalent to look for pairs of paralleled boundary planes of clusters with the largest distances between them. An optimized partitioning plane is one equidistant to the two boundaries, as shown in Figure 2.3. For the LOS/NLOS binary classification, the dimensions $x_i$ of the parameter space are the metrics of channel features, such as total energy $E$, mean excess delay $\bar{\tau}$, RMS delay spread $\tau_{RMS}$, maximum power $P_{max}$, amplitude of the first peak in $P_{first}$, rise time of the first peak $t_{rise}$, and kurtosis $\kappa$. The input data is the input metric vector $\hat{\boldsymbol{x}} = [\hat{x}_1, \hat{x}_2, \ldots, \hat{x}_N]^T$. The data belongs to two clusters: LOS and NLOS. The boundary planes of the clusters passed at least one data of the associated cluster and expressed as $\boldsymbol{w}^T\hat{\boldsymbol{x}} + b = \pm 1$. The LOS data are in the domain of $\boldsymbol{w}^T\hat{\boldsymbol{x}} + b > +1$, and the NLOS data are in the domain of $\boldsymbol{w}^T\hat{\boldsymbol{x}} + b < -1$. By defining the label of classification $y$ as a binary set $y = \{-1, +1\}$, the LOS/NLOS hypotheses can be expressed with the above domain relation:

$$\begin{aligned} H_0 &: y = 1, \text{ if } \boldsymbol{w}^T\hat{\boldsymbol{x}} + b \geq +1, \text{ LOS transmission} \\ H_1 &: y = -1, \text{ if } \boldsymbol{w}^T\hat{\boldsymbol{x}} + b \leq -1, \text{ NLOS transmission} \end{aligned} \tag{2.25}$$

SVM aims to look for boundaries which have maximum distance between them. In mathematics, the searching process is to optimize the weight matrix $\boldsymbol{w}$ and bias $b$ of the boundaries $\boldsymbol{w}^T\hat{\boldsymbol{x}} + b = \pm 1$ to maximize the distance $2 / \boldsymbol{w}^T\boldsymbol{w}$ while ensuring the hypothesis testing (2.25) correct. The correct testing condition of (2.25) is $y(\boldsymbol{w}^T\hat{\boldsymbol{x}} + b) \geq 1$. Consequently, the LOS and NLOS metric clusters are distinguished

by a hyperplane $\boldsymbol{w}^T\hat{\boldsymbol{x}} + b = 0$ at the equidistant position, as shown in Figure 2.3. The above optimization problem can be expressed as:

$$\begin{aligned} &\arg\min_{\boldsymbol{w},b} \frac{1}{2}\boldsymbol{w}^T\boldsymbol{w} \\ &\text{s.t.}\ y_i\left(w_i\hat{x}_i + b\right) \geq 1 \end{aligned} \tag{2.26}$$

Introducing a tolerance vector $\boldsymbol{e}$, the constraint of inequality is transformed into equality:

$$\begin{aligned} &\arg\min_{\boldsymbol{w},b}\left(\frac{1}{2}\boldsymbol{w}^T\boldsymbol{w} + \gamma\frac{1}{2}\boldsymbol{e}^T\boldsymbol{e}\right) \\ &\text{s.t.}\ y_i\left(w_i\hat{x}_i + b\right) = 1 - e_i \end{aligned} \tag{2.27}$$

where $\gamma = \{0, 1$The optimizing problem can be solved by the Lagrange multipliers method. Constraining optimization becomes:

$$\arg\max_{\boldsymbol{w},b,\boldsymbol{e}} \mathcal{L}\left(\boldsymbol{w},b,\boldsymbol{e};\boldsymbol{\lambda}\right) \tag{2.28}$$

Where the Lagrange duality with a Lagrange multiplier vector $\boldsymbol{\lambda} = [\lambda_1, \lambda_2, \ldots, \lambda_N]$ is:

$$\mathcal{L}\left(\boldsymbol{w},b,\boldsymbol{e};\boldsymbol{\lambda}\right) = \frac{1}{2}\left(\boldsymbol{w}^T\boldsymbol{w} + \gamma\boldsymbol{e}^T\boldsymbol{e}\right) - \sum_{i=1}^{N}\lambda_i\left[y_i\left(w_i\hat{x}_i + b\right) - 1 + e_i\right] \tag{2.29}$$

The analyzed maxima are at the zero points of the first-order derivative of the Lagrange duality. However, the problem is usually complex. In that case, the problem is solved by iteration of steepest descent.

Table 2.4 Errors of testing by SVM using measurement data [14]

| Metrics | Type I | Type II | Average |
|---|---|---|---|
| $r_{max}$ | 0.137 | 0.123 | 0.130 |
| $r_{max}$, $t_{rise}$ | 0.092 | 0.109 | 0.100 |
| $P_{max}$, $t_{rise}$, $\kappa$ | 0.082 | 0.090 | 0.086 |
| $P_{max}$, $r_{max}$, $t_{rise}$, $\kappa$ | 0.082 | 0.090 | 0.086 |
| $P_{max}$, $r_{max}$, $t_{rise}$, $\bar{\tau}$, $\kappa$ | 0.086 | 0.090 | 0.088 |
| $P_{max}$, $r_{max}$, $t_{rise}$, $\bar{\tau}$, $\tau_{RMS}$, $\kappa$ | 0.092 | 0.090 | 0.091 |

The performance of the SVM is a list in Table 2.4. Generally, more metric provides a lower probability of error. However, considering all features does no mean the lowest error. Redundant information leads to wrong identification. The performance of identification or classification is evaluated by the probability of

type I and II. For null hypothesis testing, the error type I is the case that rejecting the null hypothesis when it is true. The type II error is the case of accepting the alternative hypothesis. In NLOS identification, the null hypothesis is the LOS transmission, and the alternative hypothesis is the NLOS transmission.

The same metrics of channel features are used in the identification with ANN in [15] as well. The hypothesis of ANN is:

$$\begin{aligned} H_0 &: \hat{E} = E^{los},\ \hat{\tau}_{RMS} = \tau_{RMS}^{los},\ \hat{P}_{first}\hat{\tau}_{first} = P_{first}^{los}\tau_{first}^{los},\ \text{LOS transmission} \\ H_1 &: \hat{E} < E^{los},\ \hat{\tau}_{RMS} > \tau_{RMS}^{los},\ \hat{P}_{first}\hat{\tau}_{first} \neq P_{first}^{los}\tau_{first}^{los},\ \text{NLOS transmission} \end{aligned} \tag{2.30}$$

The schematic diagram of ANN with one output is shown in Figure 2.4. The whole procedure of ANN is a mixture of linear transformation and binary texting: the 3 continuous input variables are weighted by $w^1_{ij}$ and summed up, then they are tested by *gi* and converted to binary variables in the hidden layer. A similar procedure is repeated in the output layer.

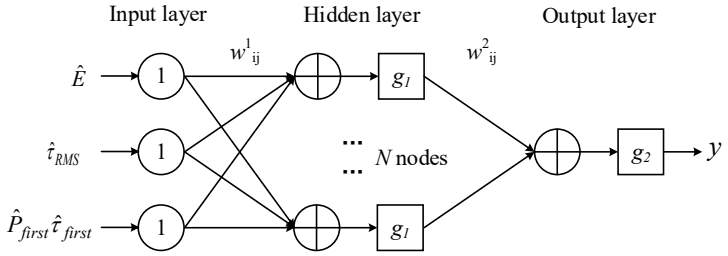


Figure 2.4 Schematic diagram of ANN with a hidden layer of *N* nodes to identify the LOS transmission

In a matrix form, the above schematic diagram of ANN is expressed as the two times of linear transform and binary testing with weight matrices $\underline{\mathrm{W}}_1$ and $\underline{\mathrm{W}}_2$, and binary testing functions $g_1$ and $g_2$, respectively:

$$y(\hat{\boldsymbol{x}}) = g_2\left[\underline{\mathrm{W}}_2 g_1\left(\underline{\mathrm{W}}_1\hat{\boldsymbol{x}}\right)\right] \tag{2.31}$$

Where the input vector of ANN is a set of sampled vector $\hat{\boldsymbol{x}} = [\hat{E},\ \hat{\tau}_{RMS},\ \hat{P}_{first}\hat{\tau}_{first}]^T$. The weight matrices of the hidden and output layers are $\underline{\mathrm{W}}_1$ and $\underline{\mathrm{W}}_2$, with the corresponding entries $w^1_{ij}$ and $w^2_{ij}$. The output vector is $\mathrm{y} \in \{0,1\}$. The testing function $g_1$ is a sigmoid smoothing function to avoid the sharply jumping by the binary sign function:

$$g_1(x) = \frac{2}{1+e^{-2x}} - 1 \tag{2.32}$$

And the testing in the output layer:

$$g_2(x) = x \tag{2.33}$$

The optimizing process is minimizing the error of the output. The priorly labeled vector $y$ identifies the direct path as output "1" and the indirect paths as "0". The total error is expressed as a loss function. The total error is expressed as a loss function:

$$L(y, y_0) = (y - y_0)^2 \tag{2.34}$$

Based on (2.31), the loss function is with a form of multiplication of $w_{ij}$. ANN finds a set of $w_{ij}$ to minimize $L$.

$$\arg\min_{w_{ij}} L(w_{ij}) \tag{2.35}$$

The optimization is implemented with gradient descent to update the components of the weight matrix

$$w'_{ij} = w_{ij} - \gamma \frac{\partial L(w_{ij})}{\partial w_{ij}} \tag{2.36}$$

Considering the $g_1$ form of (2.32):

$$\frac{\partial L(w_{ij})}{\partial w_{ij}} = \frac{\partial L(y, y_0)}{\partial \delta} \frac{\partial y}{\partial w_{ij}} = -2(y - y_0) g\left(\sum_{i=1}^{3} w_{ij} \hat{x}_i\right)\left[1 - g\left(\sum_{i=1}^{3} w_{ij} \hat{x}_i\right)\right] \tag{2.37}$$

The loss function L converges to a local minima when the residual $\Delta w = w'_{ij} - w_{ij}$ is smaller than a threshold.

Table 2.5 Probability of correct testing by ANN [15]

| Metrics | Correct probability |
|---|---|
| $R_{RMS}$ | 72.40% |
| $P_{tot}$ | 78.30% |
| *Joint* | 85.48% |

The performance of the ANN is a list in Table 2.5. Similar to MLR and SVM, the joint metric testing performs better.

The above state-of-the-art regarding NLOS identification with parametric and non-parametric hypothesis testing is summarized in

Table 2.6.

Table 2.6 Current studies on NLOS identification

| Reference | Metric | Method | Work |
|---|---|---|---|
| [13] | Distance variance | GLRT | Providing a framework for LOS/NLOS distinction |
| [16] | Distance variance | Fixed threshold | In a two stages Kalman filter, the NLOS transmission is online identified and mitigated with first-stage linear filter of distance estimation. |
| [17] | Distance residual | Fixed threshold | Introducing kurtosis into distance identification. |
| [18] | Distance residual | HPFF | Hybrid Particle/finite impulse response (FIR) Filter (HPFF) is induced. |
| [19] | Position variance | BST | A Bayesian Sequential Testing (BST) is induced to identify the NLOS transmission for the Kalman filter. |
| [20] | Channel feature | CDF comparison | Validating the kurtosis to identifying the NLOS transmission. The IEEE 802.15 3a is used as the data source. |
| [12] | Channel features | GLRT | NLOS is identified with the UWB channel model of IEEE 802.15 4a. Mean excess delay, RMS delay spread, and kurtosis of CIR are used. |
| [21] | Channel feature | Fixed threshold | Joint conditional testing with RSS, TOA, and RMS delay spread. |
| [22] | Channel feature | Metric comparison | A validation of kurtosis to identify the NLOS transmission of the MIMO channel. The kurtosis is extracted from the average CIR of MIMO channels. |
| [23] | Channel feature | ML testing | A joint TOA/AOA NLOS identification. The AOA is calculated from the assumed Gaussian distributed position. The AOA spread is the metric. |
| [14] | Channel feature | SVM | The NLOS transmission is identified based on the measured UWB CIR. The measuring environment is the whole floor scenario. |
| [24] | Chanel feature | RVM | The identification is achieved with simulation by the channel model of IEEE 802.15.4-2011. The Relative Vector Machine (RVM) performed better than SVM. |
| [15] | Channel feature | ANN and GLRT | A hypothesis testing is implemented with on hybrid Weibull distributed RSS and normally distributed RMS delay spread. The ANN was performed better than hypothesis testing. |
| [25] | Channel feature | LS-SVM | Inducing RSS and Least-square SVM (LS-SVM). |
| [26] | Channel feature | Fixed threshold | Inducing AOA, AOD, and TOA to identify NLOS transmission. |
| [27] | Channel feature | CDF comparison | Channel Frequency Response (CFR) is induced. |
| [28] | Channel | Deep Learning | Induce deep learning to NLOS identfication |

| | | | |
|---|---|---|---|
| | feature | | |
| [29] | CSI | SVM | Induced the CSI as the feature |

### 2.2.5 The problem in the current studies

The current works are mostly focusing on the time domain CIR or corresponding frequency domain CFR. The CIR signal sampling is valid if the antenna is omnidirectional. This assumption is reasonable for the low-frequency UWB band since the multipath scattering environment is very strong and most of the UWB antennas are omnidirectional. Even when the antennas have a certain directivity, the channel impulse response remains heavily affected by numerous multipath. However, as previously discussed, the multipath effect in millimeter channel is sparse. Furthermore, antennas in the millimeter-wave band are typically highly directional to compensate for the free-space. The above two factors make the spatial distribution of the NLOS transmission unique: in one direction, the transmission is LOS, while in the other directions, the transmissions are NLOS. Classical indentification methods based on time features are more likely to fail as the CIRs in millimeter-wave band with directional antennas contain less multipath diversity.

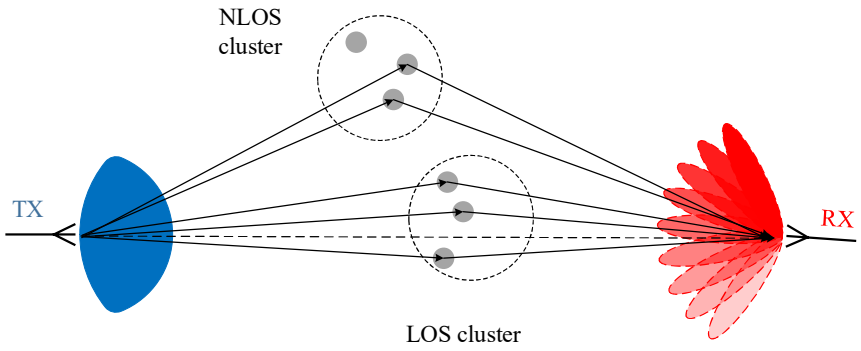


Figure 2.5 Identification of LOS and NLOS cluster in the frame of beam training

In the direction-based identification, the strategy of angular-sweeping in the measurement influences the way one should try to distinguish LOS from NLOS components. Since in most of the current 60 GHz standard, such as IEEE 802.11ad, analog beamforming induces a discrete beam training codebook, the direct path and multipath are not to be received together, but more likely separated (with different codebooks, i.e., different beam configurations), as shown in Figure 2.5. Furthremore, the Rx sweeping over the space according to a discrete codebook, the beam near the direct path might jump over the LOS path, thereby making the direct path lost. In that case, the NLOS identification means to identify the NLOS cluster. Thereby, the LOS/NLOS cluster discrimination is the target in the millimeter band.

## 2.3 Clustering Methods

The clustered-based extracted metrics are fundamental in the procedure of channel modeling. The discrete beam training strategy makes the NLOS/LOS discrimination transforming into a cluster-based identification as well. Therefore, the clustering method is one of the critical issues and are given full consideration in this section.

## 2.3.1 Clustering algorithms

The purpose of clustering is to discover the natural groupings of unlabeled objects with similarities. According to the pattern recognition [1], the clustering problem is unsupervised, which is different from the previous supervised identification (supervised with a pre-marked data set by the training process). A typical clustering process is an optimizing problem: modifying the association relationship between the elements and clusters, then updating the value of dissimilarity among clusters, until the dissimilarity between clusters reaches a global maxima meanwhile the similarity inside clusters reaches a global minima. According to the implementation, the clustering method is divided into two types: down-top hierarchical clustering and top-down partitional clustering [30]. If the input data set is a matrix $\mathbf{X} = \{\boldsymbol{x}_1, \boldsymbol{x}_2, \ldots, \boldsymbol{x}_N\}$ with individual components $\boldsymbol{x}_j = [x_{j1}, x_{j2}, \ldots, x_{jN}]^T$, the clustering algrithm search for $K$ clusters $C = \{C_1, C_2 \ldots C_K\}$. A hierarchical clustering process constructs a tree-like set structure $H$ of $\mathbf{X}$:

$$H = \{H_1, H_2 \ldots H_M\}, M \le N \tag{2.38}$$

in order to make two subsets $H_m$ and $H_l$ ($m > l$) agglomerate the data points in the form of:

$$\left(C_i \in H_m\right) \text{ and } \left(C_j \in H_l\right) \rightarrow \left(C_i \in C_j\right) \text{ or } \left(C_i \bigcap C_j = \varnothing\right) \tag{2.39}$$

In contrast, a partitional clustering process starts with partitioned initializing clusters and then modifies the components of each cluster to seek the subset $C_i$ (partition) with:

$$C = \left\{ C_i, i = 1 \ldots K, K < N \mid C_i \neq \varnothing, C_i \bigcap C_i = \varnothing, \bigcup_{i=1}^{K} C_i = \underline{\mathrm{X}} \right\} \tag{2.40}$$

The signal- and complete-linkages are the most known hierarchical methods. K-means is a widely used partitional clustering method.

### 2.3.1.1 The measure of similarity

Since the clustering algorithm is looking for similar components, the measure of similarity or dissimilarity is the critical consideration. The similarity is defined as a mapping $d$ from the data set $\underline{\mathrm{X}}$ to the positive real set, $d$: $\underline{\mathrm{X}} \times \underline{\mathrm{X}} \rightarrow [0, +\infty)$. A widely used linear measure is Minkowski distance [30] between the component $x_i$ and $x_j$ in the $l$-th cluster:

$$d_{ij} = \left( \sum_{l=1}^{N} \left| x_{il} - x_{jl} \right|^{m} \right)^{\frac{1}{m}} \tag{2.41}$$

According to the selection of index m, the Minkowski distance is specified as Euclidean ($m$ = 2), city-block ($m$ = 1), and sup ($m$ = ∞) distance. Inducing the correlation between $\boldsymbol{x}_i$ and $\boldsymbol{x}_j$, the Minkowski distance transforms into a Mahalanobis distance with the covariance matrix $\underline{S}$ within the cluster:

$$d(i,j) = \left[ \left( \boldsymbol{x}_i - \boldsymbol{x}_j \right)^T \underline{S}^{-1} \left( \boldsymbol{x}_i - \boldsymbol{x}_j \right) \right]^{1/2} \tag{2.42}$$

where the covariance matrix $\underline{S}$ is:

$$\underline{S} = \mathrm{cov}\left( \underline{X}, \underline{X} \right) = E\left[ \left( X - E(X) \right) \left( X - E(X) \right)^T \right] \tag{2.43}$$

A deformation of Mahalanobis is Pearson correlation:

$$d(i,j) = \frac{1}{2}\left(1 - r_{ij}\right), \quad r_{ij} = \frac{\sum_{l=1}^{m} \left( x_{il} - \bar{x}_i \right) \left( x_{jl} - \bar{x}_j \right)}{\sqrt{\sum_{l=1}^{m} \left( x_{il} - \bar{x}_i \right)^2 \sum_{l=1}^{m} \left( x_{jl} - \bar{x}_j \right)^2}} \tag{2.44}$$

### 2.3.1.2 Hierarchical clustering

The hierarchical clustering algorithm updates the Lance-Williams dissimilarity [31, 32] between two data points: if two data points with index $i$ and $j$ are agglomerated into a cluster $i \cup j$, the Minkowski distance between the new cluster and other points $k$ is:

Table 2.7 Specification of different types of hierarchical clustering [31]

| Clustering method | $\alpha$ | $\beta$ | $\gamma$ |
|---|---|---|---|
| Single linkage | 0.5 | 0 | -0.5 |
| Complete linkage | 0.5 | 0 | 0.5 |
| UPGMA | $\frac{\lvert i \rvert}{\lvert i \rvert + \lvert j \rvert}$ | 0 | 0 |
| WPGMA | 0.5 | 0 | 0 |
| WPGMC | 0.5 | -0.25 | 0.5 |

| | | | |
|---|---|---|---|
| UPGMC | $\frac{\lvert i\rvert}{\lvert i\rvert+\lvert j\rvert}$ | $-\frac{\lvert i\rvert\lvert j\rvert}{\left(\lvert i\rvert+\lvert j\rvert\right)^2}$ | 0 |
| Minimum variance | $\frac{\lvert i\rvert+\lvert k\rvert}{\lvert i\rvert+\lvert j\rvert+\lvert k\rvert}$ | $-\frac{\lvert k\rvert}{\lvert i\rvert+\lvert j\rvert+\lvert k\rvert}$ | 0 |

$$d\left(i\cup j,k\right)=\alpha_i d\left(i,k\right)+\alpha_j d\left(j,k\right)+\beta d\left(i,j\right)+\gamma\left|d\left(i,k\right)-d\left(j,k\right)\right| \tag{2.45}$$

According to the coefficients α, β, γ, the hierarchical clustering can be specified as different types: single linkage, complete linkage, average linkage (UPGMA), weighted linkage (WPGMA), median linkage (WPGMC), centroid linkage (UPGMC), and minimum variance, as shown in Table 2.7.

For the usually used Euclidean distance criterion, the Lance-Williams dissimilarity is:

$$d^2\left(i\cup j,k\right)=\frac{1}{2}\left\|\boldsymbol{x}_i-\boldsymbol{x}_k\right\|^2+\frac{1}{2}\left\|\boldsymbol{x}_j-\boldsymbol{x}_k\right\|^2-\frac{1}{4}\left\|\boldsymbol{x}_i-\boldsymbol{x}_j\right\|^2 \tag{2.46}$$

The principle of the single linkage method is selecting the data points with minimum distance into a cluster.

$$\min\left\{d^2\left(i,j\right):i\in A,j\in B\right\} \tag{2.47}$$

Take the single linkage as an example, the algorithm of a typical hierarchical clustering algorithm is shown in Algorithm 2.1.

Algorithm 2.1 Flow of single linkage hierarchical clustering algorithm [33]

1. Calculate the distance $d(i, j)$ for all pairs $(\boldsymbol{x}_i, \boldsymbol{x}_j)$ of the elements in the data set $\underline{\mathrm{X}}$.
2. Find $\boldsymbol{x}_i, \boldsymbol{x}_j \in \underline{\mathrm{X}}$ make for all $\boldsymbol{x}_{i'}, \boldsymbol{x}_{j'} \in \underline{\mathrm{X}}$: $d(i, j) \le d(i', j')$
3. For the pair $(\boldsymbol{x}_i, \boldsymbol{x}_j)$
   Generate a new cluster $c = \boldsymbol{x}_i \cup \boldsymbol{x}_j$
   Update $\underline{\mathrm{X}} = \underline{\mathrm{X}} - \underline{\mathrm{C}}$, $\underline{\mathrm{C}} = \{c\}$
4. If $\underline{\mathrm{X}} = \varnothing$, stop
5. Calculate the distances between all the existing classes $\boldsymbol{x}_i \in \underline{\mathrm{X}}$ and the new cluster $\underline{\mathrm{C}}$. with a recursion of Lance-Williams distance： $d(i, c)$
6. Update $\underline{\mathrm{X}} = \underline{\mathrm{X}} \cup \underline{\mathrm{C}}$, go to 2

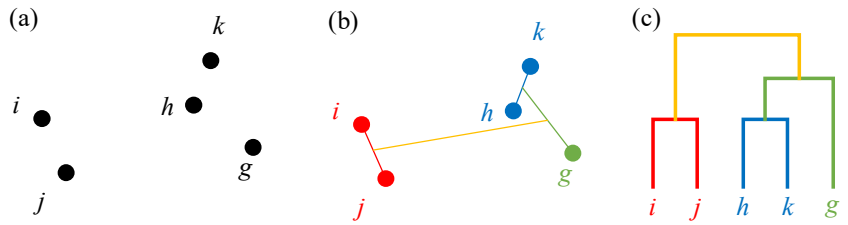


Figure 2.6 Generation of hierarchical clustering: (a) initial data points; (b) hierarchical clusters; (c) binary tree of clusters

The above process is a process of constructing a binary tree. A specific example is shown in Figure 2.6. The nearest neighbor pairs $\{i, j\}$, $\{k, h\}$, $\{g\}$ are generated directly from the initial data set. The nearest cluster neighbors are grouped in further until all of the elements are grouped. The data points finally aggregate into a binary tree of two clusters $\{i, j\}$ and $\{k, h, g\}$.

## 2.3.1.3 Partitional clustering

K-means is a typical and simple partitional clustering algorithm. K-means aims to minimize the sum of the error between the centroid and the components in all of the clusters [34]. K-means minimizes the average Euclidean distance between data points within a cluster and the mean of the cluster. The algorithm of K-means is shown as Algorithm 2.2.

Algorithm 2.2 Flow of K-means clustering algorithm

1. Randomly choose $K$ initial centroid positions $\boldsymbol{c}_1^{(0)},\ldots,\boldsymbol{c}_K^{(0)}$
2. For $i$ = 1 to *MaxIterations*
   a. Assign MPCs to cluster centroids and store indices $\mathcal{I}_l^{(i)}$:

$$\mathcal{I}_l^{(i)} = \arg\min_k \left\{ d\left(\boldsymbol{x}_l, \boldsymbol{c}_k^{(i-1)}\right) \right\} \tag{2.48}$$

$$\mathcal{I}^{(i)} = \left[ \mathcal{I}_1^{(i)} \ldots \mathcal{I}_L^{(i)} \right],\ \mathcal{C}_k^{(i)} = \operatorname{indices}_l\left( \mathcal{I}_l^{(i)} = k \right) \tag{2.49}$$

   b. Recalculate cluster centroids $\boldsymbol{c}_k^{(i)}$ from the allocated distance to coincide with the clusters' centers of gravity:

$$\boldsymbol{c}_k^{(i)} = \frac{\sum_{j \in \mathcal{C}_k^{(i)}} \boldsymbol{x}_j}{M} \tag{2.50}$$

   c. If $\boldsymbol{c}_k^{(i)} = \boldsymbol{c}_k^{(i-1)}$ for all $k = 1,\ldots,K$, then GoTo 3.
   Else Next $i$
3. Return $\mathcal{R}_K = \left[ \mathcal{I}^{(i)}, \boldsymbol{c}_k^{(i)} \right]$

The specific process is shown in Figure 2.7. The input data set of x is shown in Figure 2.7 (a). The positions of initially partitioned clusters are randomly selected in (b). Then, the centroids and distances are updated, until a global minima of intracluster distance is reached.

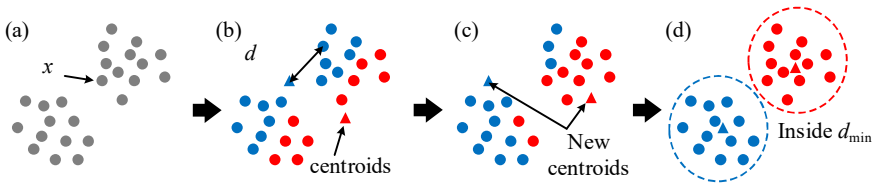


Figure 2.7 Process of K-means algorithm: (a) initial data set; (b) initial clusters; (c) update centroids; (d) calculate distance.

The aim of K-means is looking for global minima, but it is straightforward to fall into local minima due to two factors: initial seed and number of repetitions. To avoid the result that K-means fall into local minima, the k-means++ [35] was used to initialize the centroid of the cluster randomly. The algorithm generates the next initial centroid with a probability that is proportional to the Euclidean distance of the previous centroid. The optimized number of clusters is estimated with specific algorithms, such as silhouettes [36], for which the distances among data points in one cluster are minimized, and the distances among clusters are maximized.

## 2.3.2 Clustering method for the channel model

Most of the current propagation channel model studies use K-means algorithm as the clustering method. The channel parameter set, {AOA, AOD, TOA}, is typically extracted using an antenna array by MUSIC estimation (for unique spatial variable AOA/AOD) or SAGE estimation (for multi-variable, e.g., AOA + TOA), and is then used as input data for K-means. The power of CIR is used as a weight for the clustering. An improved version of K-mean, K-Power-Means [37], is also used in standard channel modeling procedures. During the iterative process, the standard K-Power-Means minimizes the sum of power-weighted distances of parameter points to the centroid associated with the parameter point. The flow chart of K-Power-Means is shown in Algorithm 2.3.

Algorithm 2.3 Flow of K-Power-Means clustering algorithm

1. Randomly choose $K$ initial centroid positions $\boldsymbol{c}_1^{(0)},\ldots,\boldsymbol{c}_K^{(0)}$
2. For $i = 1$ to *MaxIterations*
   a. Assign MPCs to cluster centroids and store indices $\mathcal{I}_l^{(i)}$:

$$\mathcal{I}_l^{(i)} = \arg\min_k \left\{ P_l \cdot \mathrm{MCD}\left( \boldsymbol{x}_l, \boldsymbol{c}_k^{(i-1)} \right) \right\} \tag{2.51}$$

$$\mathcal{I}^{(i)} = \left[ \mathcal{I}_1^{(i)} \ldots \mathcal{I}_L^{(i)} \right],\ \mathcal{C}_k^{(i)} = \operatorname*{indices}_l \left( \mathcal{I}_l^{(i)} = k \right) \tag{2.52}$$

   b. Recalculate cluster centroids $\boldsymbol{c}_k^{(i)}$ from the allocated MPCs to coincide with the clusters' centers of gravity:

$$\boldsymbol{c}_k^{(i)} = \frac{\sum_{j \in \mathcal{C}_k^{(i)}} \left( P_j \cdot \boldsymbol{x}_j \right)}{\sum_{j \in \mathcal{C}_k^{(i)}} P_j} \tag{2.53}$$

   c. If $\boldsymbol{c}_k^{(i)} = \boldsymbol{c}_k^{(i-1)}$ for all $k = 1,\ldots,K$, then GoTo 3.

Else Next $i$

3. Return $\mathcal{R}_K = \left[ \mathcal{I}^{(i)}, \boldsymbol{c}_k^{(i)} \right]$

The Multipath Component Distance (MCD) in the flow chart is the Euclidean distance used to evaluate the difference between individual multipath components in the parameter space [38, 39]. So the MCD between the $i$-th and $j$-th angular points in the Cartesian coordinate system is expressed as:

$$MCD_{AOA/AOD,ij} = \frac{1}{2}\left| \begin{pmatrix} \sin(\theta_i)\cos(\phi_i) \\ \sin(\theta_i)\sin(\phi_i) \\ \cos(\theta_i) \end{pmatrix} - \begin{pmatrix} \sin(\theta_j)\cos(\phi_j) \\ \sin(\theta_j)\sin(\phi_j) \\ \cos(\theta_j) \end{pmatrix} \right| \tag{2.54}$$

The MCD for the TOA between the $i$-th and $j$-th temporal points is:

$$MCD_{TOA,ij} = \frac{\left|\tau_i - \tau_j\right|}{\Delta\tau_{\max}} \cdot \frac{\tau_{std}}{\Delta\tau_{\max}} \tag{2.55}$$

Where

$$\Delta\tau_{\max} = \max_{i,j}\left\{\left|\tau_i - \tau_j\right|\right\} \tag{2.56}$$

The total distance is

$$MCD_{ij} = \sqrt{\left\|MCD_{AOA,ij}\right\|^2 + \left\|MCD_{AOD,ij}\right\|^2 + \left\|MCD_{TOA,ij}\right\|^2} \tag{2.57}$$

## 2.3.3 The problem of K-means frame

The K-means clustering has intrinsic weaknesses: first, the number of clusters has to be assumed before the operation. In order to get the correct number of cluster, k-means has to be repeated several times. Second, an inappropriate initial cluster will lead to a local minima. To solve the initializing problem, the K-means++ algorithm [35] was introduced. Third, K-means treats all the features equally, regardless of the actual correlation among the features. Therefore, the physical shape of the cluster cannot be preserved. The third problem leads to the fact that the channel cluster in the time domain cannot reflect accurately the exponential fading shape for instance [36]. To solve the problem, the CIR has to be fitted with *a priory* known exponential function [40]. However, the *a priory* function destroys the unsupervised nature of K-means. Furthermore, the shape of the channel clusters is not always obtainable. The local scattering characteristics determine spatial distribution. The directional antenna pattern of beamforming in the millimeter band enormously intensifies the local charactersitics of scattering. The narrow beam makes the CIR only influenced by a few path of a local scattering in a narrow domain; by omnidirectional antenna,

lots of path in a large range are illuminated, so local characteristics are not obvious. In that case, the shape of the spatial cluster is entirely unknown and cannot be predefined. The feature weighting method attempts to solve the problem fundamentally [41]. However, the weighting coefficients are estimated empirically. Despite this, the weighting method still performs much unsatisfactory for spatial identification in V-band or higher frequency band [42]. It still cannot preserve the shape of the scattering cluster.

## 2.4 Conclusion

Most of the current studies on NLOS identification are in the sub-6 GHz band. The low attenuation, strong diffraction, and omnidirectional antenna pattern typically encountered in this band make the resulting channel between a transmitter and a receiver experiencing strong multipath effects. Therefore, features in the CIR are typically used to differenciate between LOS and NLOS transmissions. For instance, the large scattering range leads to TOA spreads much broader in NLOS than in LOS transmission. The ranged distance and other channel features are also used to distinguish LOS and NLOS situations as summarized in

Table 2.6. Parametric and non-parametric hypothesis testing are both used to statistically determine the transmission scenario. NLOS identification in the millimeter-wave band has not being paid much interest in the literature so far. Furthermore, millimeter-wave channel, being higly sparse, exhibits different behaviors than in the sub-6 GHz region. Consequently, this PhD work intends to tackle this issue and will specifically use angular spatial features of the channel rather than of the CIR in order to perform NLOS identification. This work is detailed in the chapter 4 of this manuscript. To do so, clustering is an essential step. Among current clustering methods, the current channel modeling widely uses the partitional clustering method, K-Power-Means. The problem of shape-preservation of K-Power-Means remains unsolved so far, and is of utmost importance for NLOS identification in the millimeter-wave band as we intend to use the angular cluster shapes as a feature for classification. Consequently, the next chapter 3 introduces our new clustering method, which appears well suited for millimeter-wave band NLOS identification and also well-suited to handle a big volume of data.

# References

[1] C. M. Bishop, *Pattern Recognition and Machine Learning*: Springer Science+Business Media, LLC, 2006.

[2] H. Liu, H. Darabi, P. Banerjee, and J. Liu, “Survey of wireless indoor positioning techniques and systems,” *IEEE Transactions on Systems Man and Cybernetics Part C-Applications and Reviews,* vol. 37, no. 6, pp. 1067-1080, Nov, 2007.

[3] G. de Blasio, A. Quesada-Arencibia, C. R. Garcia, J. M. Molina-Gil, and C. Caballero-Gil, “Study on an Indoor Positioning System for Harsh Environments Based on Wi-Fi and Bluetooth Low Energy,” *Sensors,* vol. 17, no. 6, Jun, 2017.

[4] H. Wymeersch, J. Lien, and M. Z. Win, “Cooperative Localization in Wireless Networks,” *Proceedings of the IEEE,* vol. 97, no. 2, pp. 427-450, Feb, 2009.

[5] A. Alarifi, A. Al-Salman, M. Alsaleh, A. Alnafessah, S. Al-Hadhrami, M. A. Al-Ammar, and H. S. Al-Khalifa, "Ultra Wideband Indoor Positioning Technologies: Analysis and Recent Advances," *Sensors,* vol. 16, no. 5, May, 2016.

[6] D. Dardari, A. Conti, U. Ferner, A. Giorgetti, and M. Z. Win, "Ranging With Ultrawide Bandwidth Signals in Multipath Environments," *Proceedings of the IEEE,* vol. 97, no. 2, pp. 404-426, Feb, 2009.

[7] R. C. Qiu, "A study of the ultra-wideband wireless propagation channel and optimum UWB receiver design," *IEEE Journal on Selected Areas in Communications,* vol. 20, no. 9, pp. 1628-1637, Dec, 2002.

[8] A. F. Molisch, "Ultra-Wide-Band Propagation Channels," *Proceedings of the IEEE,* vol. 97, no. 2, pp. 353-371, Feb, 2009.

[9] T. Kaiser, F. Zheng, and E. Dimitrov, "An Oveiwiew of Ultra-Wide-Band Systems With MIMO," *Proceedings of the IEEE,* vol. 97, no. 2, pp. 285-312, Feb, 2009.

[10] A. F. Molisch, D. Cassioli, C. C. Chong, S. Emami, A. Fort, B. Kannan, J. Karedal, J. Kunisch, H. G. Schantz, K. Siwiak, and M. Z. Win, "A comprehensive standardized model for ultrawideband propagation channels," *IEEE Transactions on Antennas and Propagation,* vol. 54, no. 11, pp. 3151-3166, Nov, 2006.

[11] A. F. Molisch, K. Balakrishnan, D. Cassioli, C.-C. Chong, S. Emami, A. Fort, J. Karedal, J. Kunisch, H. Schantz, U. Schuster, and K. Siwiak, *IEEE 802.15.4a channel model - final report*, 2004.

[12] I. Guvenc, C. C. Chong, and F. Watanabe, "NLOS identification and mitigation for UWB localization systems," *2007 IEEE Wireless Communications & Networking Conference, Vols 1-9*, pp. 1573-1578, 2007.

[13] J. Borras, P. Hatrack, and N. B. Mandayam, "Decision theoretic framework for NLOS identification," *48th IEEE Vehicular Technology Conference, Vols 1-3*, pp. 1583-1587, 1998.

[14] S. Marano, W. M. Gifford, H. Wymeersch, and M. Z. Win, "NLOS Identification and Mitigation for Localization Based on UWB Experimental Data," *IEEE Journal on Selected Areas in Communications,* vol. 28, no. 7, pp. 1026-1035, Sep, 2010.

[15] M. Heidari, N. A. Alsindi, and K. Pahlavan, "UDP Identification and Error Mitigation in ToA-Based Indoor Localization Systems using Neural Network Architecture," *IEEE Transactions on Wireless Communications,* vol. 8, no. 7, pp. 3597-3607, Jul, 2009.

[16] K. G. Yu, and E. Dutkiewicz, "NLOS Identification and Mitigation for Mobile Tracking," *IEEE Transactions on Aerospace and Electronic Systems,* vol. 49, no. 3, pp. 1438-1452, Jul, 2013.

[17] Y. T. Chan, W. Y. Tsui, H. C. So, and P. C. Ching, "Time-of-arrival based localization under NLOS conditions," *IEEE Transactions on Vehicular Technology,* vol. 55, no. 1, pp. 17-24, Jan, 2006.

[18] J. M. Pak, C. K. Ahn, P. Shi, Y. S. Shmaliy, and M. T. Lim, "Distributed Hybrid Particle/FIR Filtering for Mitigating NLOS Effects in TOA-Based Localization Using Wireless Sensor Networks," *IEEE Transactions on Industrial Electronics,* vol. 64, no. 6, pp. 5182-5191, Jun, 2017.

[19] L. B. Yan, Y. Lu, and Y. R. Zhang, "An Improved NLOS Identification and Mitigation Approach for Target Tracking in Wireless Sensor Networks," *IEEE Access,* vol. 5, pp. 2798-2807, 2017.

[20] L. Mucchi, and P. Marcocci, "A New Parameter for UWB Indoor Channel Profile Identification," *IEEE Transactions on Wireless Communications,* vol. 8, no. 4, pp. 1597-1602, Apr, 2009.

[21] S. Venkatesh, and R. M. Buehrer, "Non-line-of-sight identification on ultra-wideband systems based on received signal statistics," *IET Microwaves Antennas & Propagation,* vol. 1, no. 6, pp. 1120-1130, Dec, 2007.

[22] J. Zhang, J. Salmi, and E. S. Lohan, "Analysis of Kurtosis-Based LOS/NLOS Identification Using Indoor MIMO Channel Measurement," *IEEE Transactions on Vehicular Technology,* vol. 62, no. 6, pp. 2871-2874, Jul, 2013.

[23] C. D. Wann, and H. Y. Lin, "Hybrid TOA/AOA estimation error test and non-line of sight identification in wireless location," *Wireless Communications & Mobile Computing,* vol. 9, no. 6, pp. 859-873, Jun, 2009.

[24] T. V. Nguyen, Y. M. Jeong, H. D. Shin, and M. Z. Win, "Machine Learning for Wideband Localization," *IEEE Journal on Selected Areas in Communications,* vol. 33, no. 7, pp. 1357-1380, Jul, 2015.

[25] Z. L. Xiao, H. K. Wen, A. Markham, N. Trigoni, P. Blunsom, and J. Frolik, "Non-Line-of-Sight Identification and Mitigation Using Received Signal Strength," *IEEE Transactions on Wireless Communications,* vol. 14, no. 3, pp. 1689-1702, Mar, 2015.

[26] J. Y. Shen, and A. F. Molisch, "Indirect Path Detection Based on Wireless Propagation Measurements," *IEEE Transactions on Wireless Communications,* vol. 11, no. 12, pp. 4482-4493, Dec, 2012.

[27] Z. M. Zhou, Z. Yang, C. S. Wu, L. F. Shangguan, H. B. Cai, Y. H. Liu, and L. M. Ni, "WiFi-Based Indoor Line-of-Sight Identification," *IEEE Transactions on Wireless Communications,* vol. 14, no. 11, pp. 6125-6136, Nov, 2015.

[28] J. S. Choi, W. H. Lee, J. H. Lee, J. H. Lee, and S. C. Kim, "Deep Learning Based NLOS Identification With Commodity WLAN Devices," *IEEE Transactions on Vehicular Technology,* vol. 67, no. 4, pp. 3295-3303, Apr, 2018.

[29] X. H. Li, X. Cai, Y. Q. Hei, and R. Y. Yuan, "NLOS identification and mitigation based on channel state information for indoor WiFi localisation," *IET Communications,* vol. 11, no. 4, pp. 531-537, Mar 9, 2017.

[30] R. Xu, and D. Wunsch, "Survey of clustering algorithms," *IEEE Transactions on Neural Networks,* vol. 16, no. 3, pp. 645-678, May, 2005.

[31] F. Murtagh, and P. Contreras, "Algorithms for hierarchical clustering: an overview," *Wiley Interdisciplinary Reviews-Data Mining and Knowledge Discovery,* vol. 2, no. 1, pp. 86-97, Jan-Feb, 2012.

[32] G. N. Lance, and W. T. Williams, "A General Theory of Classificatory Sorting Strategies .1. Hierarchical Systems," *Computer Journal,* vol. 9, no. 4, pp. 373-&, 1967.

[33] C. d. Rham, "La Classification Hiérarchique Ascendante Selon La Méthode des Voisins Réciproques," *Les cahiers de l'analyse des données,* vol. 5, no. 2, pp. 135-144, 1980.

[34] A. K. Jain, "Data clustering: 50 years beyond K-means," *Pattern Recognition Letters,* vol. 31, no. 8, pp. 651-666, Jun 1, 2010.

[35] D. Arthur, and S. Vassilvitskii, "k-means plus plus : The Advantages of Careful Seeding," *Proceedings of the Eighteenth Annual Acm-Siam Symposium on Discrete Algorithms*, pp. 1027-1035, 2007.

[36] P. J. Rousseeuw, "Silhouettes - a Graphical Aid To the Interpretation and Validation of Cluster-Analysis," *Journal of Computational and Applied Mathematics,* vol. 20, pp. 53-65, Nov, 1987.

[37] N. Czink, P. Cera, J. Salo, E. Bonek, J. P. Nuutinen, and J. Ylitalo, "A Framework for Automatic Clustering of Parametric MIMO Channel Data Including Path Powers," *2006 Ieee 64th Vehicular Technology Conference, Vols 1-6*, pp. 114-+, 2006.

[38] M. Steinbauer, H. Ozcelik, H. Hofstetter, C. F. Mecklenbrauker, and E. Bonek, "How to quantify multipath separation," *IEICE Transactions on Electronics,* vol. E85c, no. 3, pp. 552-557, Mar, 2002.

[39] N. Czink, P. Cera, J. Salo, E. Bonek, J. P. Nuutinen, and J. Ylitalo, “Improving clustering performance using multipath component distance,” *Electronics Letters,* vol. 42, no. 1, pp. 33-35, Jan 5, 2006.

[40] R. S. He, W. Chen, B. Ai, A. F. Molisch, W. Wang, Z. D. Zhong, J. Yu, and S. Sangodoyin, “On the Clustering of Radio Channel Impulse Responses Using Sparsity-Based Methods,” *IEEE Transactions on Antennas and Propagation,* vol. 64, no. 6, pp. 2465-2474, Jun, 2016.

[41] R. C. de Amorim, “A Survey on Feature Weighting Based K-Means Algorithms,” *Journal of Classification,* vol. 33, no. 2, pp. 210-242, Jul, 2016.

[42] M. W. Ayech, and D. Ziou, “Terahertz image segmentation using k-means clustering based on weighted feature learning and random pixel sampling,” *Neurocomputing,* vol. 175, pp. 243-264, Jan 29, 2016.

# Chapter 3

# Spatial Clustering

## Contents



## 3.1 Introduction

As discussed in chapter 1, beam training is a strategy to search for available links in space. The protocol in the channel model of IEEE 802.11ad divides the beam training into three steps, Sector Level Sweep (SLS), Beam Refinement Phase (BRP), and Beam Tracking (BT). In the SLS step, the receiver beam sweeps over the whole space in both azimuth and elevation directions, while the transmitter pattern is kept as quasi-omnidirectional. The sweeping is performed according to a fixed codebook, in which the angular sweeping is done using approximately equal intervals throughout the entire space. In that case, the measured power distribution forms a grid along the azimuth and elevation angles. Every square is a sampling cell. The generated grid is a Power Angular Spectrum (PAS) of Angle of Arrival (AOA), as shown in Figure 3.1. The clusters in PAS in Figure 3.1 (b) can be generated in simulation by the convolution between the spatial clustered scattering impulses and the antenna beam patterns used in Figure 3.1 (a). The

PAS clusters inherit the stochastic scattering characteristics of the corresponding geometrical clusters. Therefore, the shape of the PAS cluster is an effective feature to distinguish the LOS and NLOS clusters. Furthermore, this information is available as soon as a beam training process is performed. This offers consequently a potential to identify NLOS clusters at a moderate additional complexity cost.

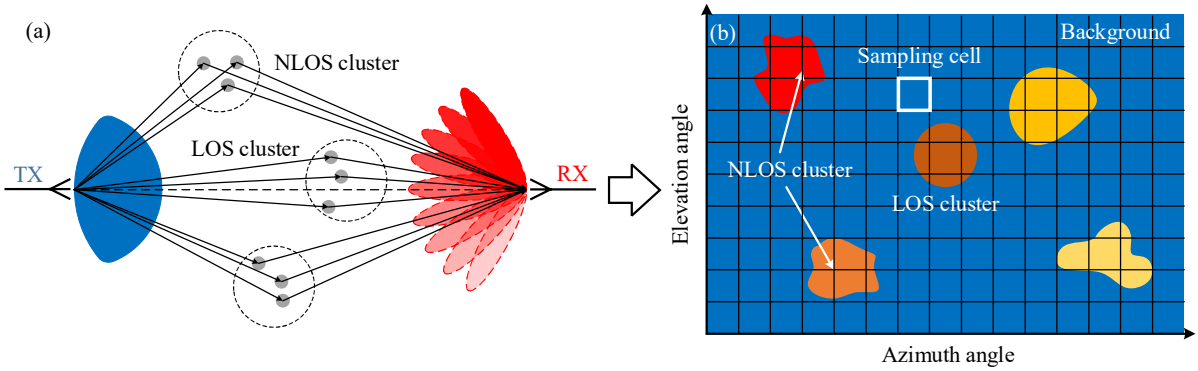


Figure 3.1 The generation of PAS with beam training: (a) SLS step of beam training; (b) PAS generated by beam training.

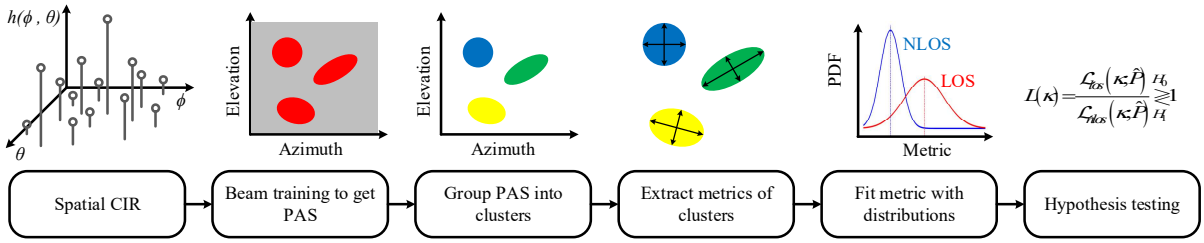


Figure 3.2 Procedure of purposed NLOS identification with the features of PAS cluster

The NLOS identification we propose (see Figure 3.2), using the features of PAS clusters, is somewhat similar to the supervised classification used in the temporal NLOS discrimination in UWB in chapter 2. The transmission characteristics of the 60 GHz channel are acquired with angular sweeping during the beam training process and mapped onto a spatial spectrum in the form of PAS. PAS is distributed in sparse clusters (the sparsity being inherent to millimeter-wave communications [1]), and the background is removed. The background typically corresponds to the noise of the receiver. The shape features of PAS clusters are extracted as metrics to evaluate the transmission situation. Then, the likelihood of LOS and NLOS are compared to identify the transmission type in particular beam directions. In these steps, in order to evaluate the shape associated with the transmission situation, the shape of each PAS cluster needs to be extracted well-preserved. As discussed in chapter 2, the currently widely used K-Power-Means method is ineffective for shape preservation. To solve this problem, a clustering method which can preserve the shapes is needed.

In this chapter, the shape-preserving method we propose for channel clustering is detailed. Unlike common discrete channel parameters that are usually spread onto a non-uniform grid such in time or angular domain, the equal-angular-interval PAS is more similar to a grayscale image. In a digital grayscale image, the pixels are arranged sequentially with each other. The discrete value (integers from 0 to 255) of

each pixel represents the brightness. In another word, a grayscale image is a grid carried discrete intensity information. The power intensity can be regarded as a continuous gray value. The relatively high power constitutes a cluster-like bright foreground, while the lower power range serves as a dark background. The sampling cells are pixels. By analogy, the clustering of PAS can actually take inspiration from the clustering methods in the image processing field. In image processing, the clustering operation is called segmentation, which means a set of operation partitioning a digital image into several segments. In contrast to the global segmentation methods such as Kmeans, the local image processing method, mathematical morphology, can avoid the weakness of neglecting the correlation among neighbor pixels, thereby preserving the shape characteristics of each cluster. If regarding the entire dark background as a cluster, it can achieve the two main targets of clustering for continuous field: extracting illuminated clusters from the dark background and separating the adjacent clusters. This chapter will study the application of mathematical morphology for the PAS clustering.

# 3.2 Watershed Segmentation

## 3.2.1 Imaging processing with mathematical morphology

Mathematical morphology (MM) is an imaging processing method to extract information from the response of various nonlinear transformations, based on set theory and lattice theory. A grayscale image is regarded as a function $f(\boldsymbol{x})$ that maps a set of 2D coordinate $\boldsymbol{x}$ (pixel position) to a surface extended to the third dimension (pixel value). In the situation in Figure 3.1 (b), the variable $\boldsymbol{x}$ is the angle vector ($\phi$, $\theta$) sampled during beam training, where $\phi$ is the azimuth angle, and $\theta$ is the elevation angle. The function $f(\boldsymbol{x})$ maps the whole angular plane to the received power, $f(\boldsymbol{x})$: $X^2 \rightarrow Y$. Where, $\boldsymbol{x} \in X^2$, $X^2$ is a 2D coordinate set of the whole angular plane:

$$X^2 = \left\{ \boldsymbol{x} = (\phi, \theta) \,|\, \phi \in [-\pi, \pi], \theta \in \left[ -\frac{\pi}{2}, \frac{\pi}{2} \right] \right\} \tag{3.1}$$

The generated 3D space is defined with a set $X^2 \times Y$.

$$X^2 \times Y = \left\{ (\phi, \theta, P) \,|\, \phi \in [-\pi, \pi], \theta \in \left[ -\frac{\pi}{2}, \frac{\pi}{2} \right], P \in \mathbb{R}^+ \right\} \tag{3.2}$$

Where $\boldsymbol{y} \in Y$. The idea of MM is remodeling 3D space of an image with other local functions, which are called structuring elements. A structuring element is also a mapping to angular plane, $g(\boldsymbol{x})$: $X_g^2 \rightarrow Y$, where $X_g^2 \subseteq X^2$. The reconstruction is achieved with some basic operations that are defined below.

*Operation* 1: **dilation** [2] $f \oplus g$: $X^2 \oplus X_g^2 \rightarrow Y$ is used to extend the local spaces. It extracts the maximum value of the sum of $f$ and $g$ at each sliding position of $f$:

$$(f \oplus g)(\boldsymbol{x}) = \sup\{f(\boldsymbol{x}-\boldsymbol{x}') + g(\boldsymbol{x}')\} \tag{3.3}$$

*Operation* 2: **erosion** [2] $f \ominus g$: $X^2 \ominus X_g^2 \rightarrow Y$ is used to shrink the local image spaces. It extracts the minimum value of the difference of $f$ and $g$ at each negatively sliding position of $f$:

$$(f \ominus g)(\boldsymbol{x}) = \inf\{f(\boldsymbol{x}+\boldsymbol{x}') - g(\boldsymbol{x}')\} \tag{3.4}$$

A simple illustration of operations 1 and 2 is shown in Figure 3.3. A polyline $f(\boldsymbol{x})$ represents the image. According to (3.3) and (3.4), a simple horizontal line structuring element $g(\boldsymbol{x})$ slides along $f$ (above $f$ for dilation and below $f$ for erosion). The supremum of the sliding trajectory is the result of dilation as shown in Figure 3.3 (a); The erosion extracts the infimum of the trajectory as shown in Figure 3.3 (b)

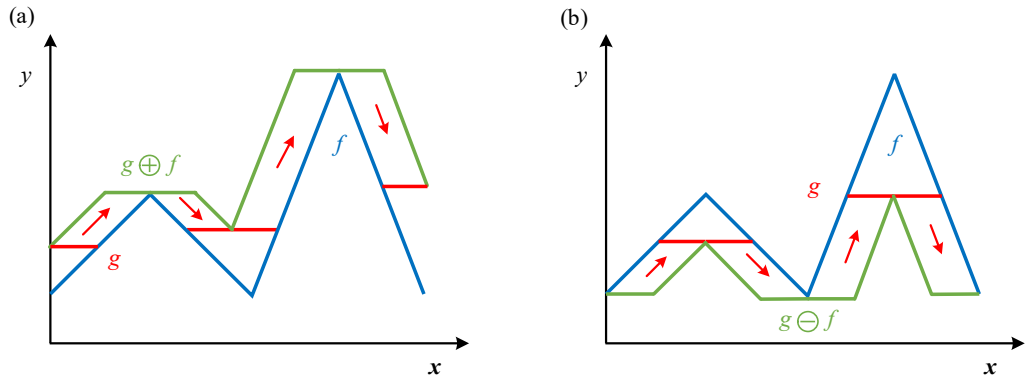


Figure 3.3 schematic diagrams of the operation of (a) dilation and (b) erosion for the image $f(\boldsymbol{x})$ with $g(\boldsymbol{x})$

*Operation* 3: **opening** removes bright peaks that are small in size and break narrow connections between two bright peaks with dilation and erosion:

$$f \circ g = (f \ominus g) \oplus g \tag{3.5}$$

*Operation* 4: **closing** preserves small peaks which are brighter than the background and fills the small gaps between bright peaks with dilation and erosion:

$$f \bullet g = (f \oplus g) \ominus g \tag{3.6}$$

The combination of dilation and erosion seen in Figure 3.3 generates opening and closing as shown in Figure 3.4. Small and insolated particles are removed by the opening operation, while the closing operation fills small and isolated holes. Therefore, those two operations are denoising operations.

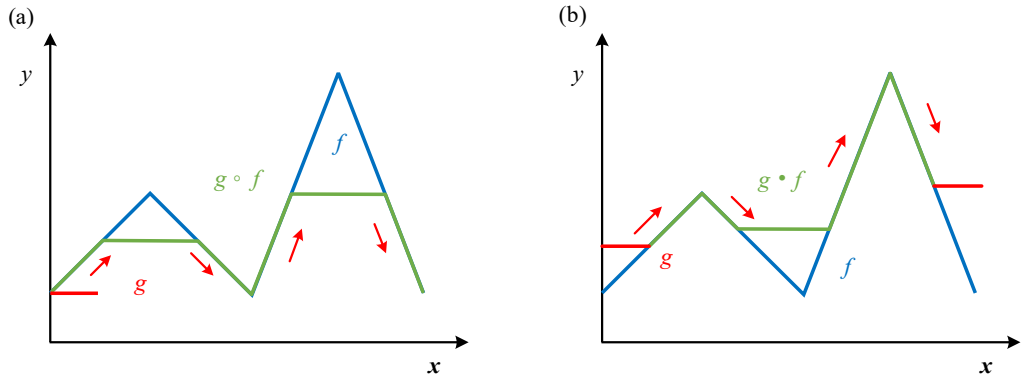


Figure 3.4 schematic diagrams of the operation of (a) open and (b) close for the image $f(\boldsymbol{x})$ with $g(\boldsymbol{x})$

*Operation* 5: **Euclidean distance transformation** [3] $d(\boldsymbol{x}, \boldsymbol{x}')$ is an operation for a binary image. It assigns the value of each pixel $\boldsymbol{x}$ in a subset $A$ of the whole image with the Euclidean distance between $\boldsymbol{x}$ and the nearest nonzero pixel $\boldsymbol{x}'$ :

$$d(\boldsymbol{x}, \boldsymbol{x}') = \inf\left\{\sqrt{\left\|\boldsymbol{x}_i - \boldsymbol{x}'_j\right\|^2} \mid A \subset X^2, \boldsymbol{x}, \boldsymbol{x}' \in A, P_A \neq 0\right\} \tag{3.7}$$

*Operation* 6: **geodesic distance** [4] $d_A(\boldsymbol{x}, \boldsymbol{x}')$ is also on the plane $X^2$. It is the length of the shortest path linked two pixels $\boldsymbol{x}$ and $\boldsymbol{x}'$ in a connected space $A$, as shown in Figure 3.5 (a).

$$d_A(\boldsymbol{x}, \boldsymbol{x}') = \inf\left\{\sqrt{\left\|\boldsymbol{x}_i - \boldsymbol{x}'_j\right\|^2} \mid A \subset X^2, \boldsymbol{x} \in A, \boldsymbol{x}' \in A, A \text{ is connected}\right\} \tag{3.8}$$

A geodesic ball [5] $\Omega$ with a center $\boldsymbol{x}$ and radius $\lambda$ is defined as a domain set $\{\boldsymbol{x}'\}$ whose geodesic distance to $\boldsymbol{x}$ is not larger than $\lambda$

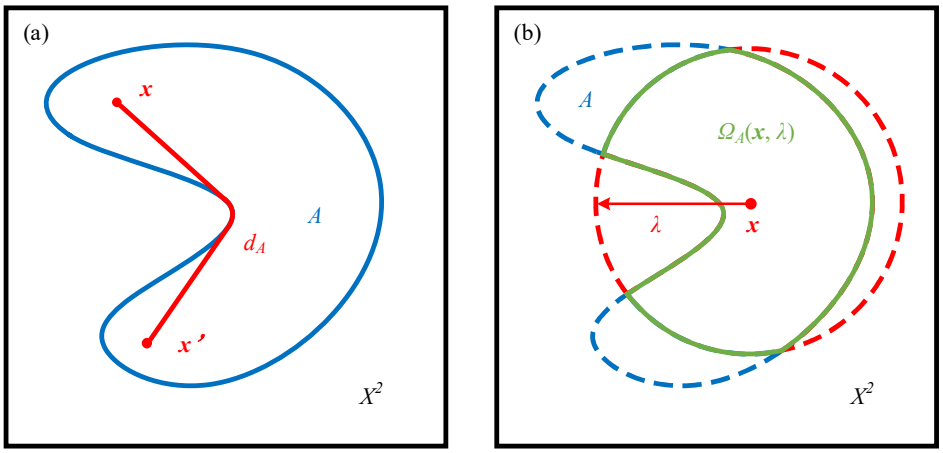


Figure 3.5 (a) geodesic distance: the shortest distance between two points; (b) geodesic ball created with two sets, $A$ and $\boldsymbol{x} \leq \lambda$

$$\Omega_A(\boldsymbol{x}, \lambda) = \left\{\boldsymbol{x}' \in A \mid A \subset X^2, \boldsymbol{x} \in A, d_A(\boldsymbol{x}, \boldsymbol{x}') \leq \lambda\right\} \tag{3.9}$$

According to (3.9), it is the intersection domain between the connected set $A$ and a circle set with radius $\lambda$, which is presented in Figure 3.5 (b).

*Operation* 7: **Geodesic dilation** [5] is the intersection between the geodesic ball Ω and a mark domain $B$:

$$\delta_A^{\lambda}(B)=\left\{\boldsymbol{x}'\in A \mid A\subset X^2, B\subset X^2, \boldsymbol{x}\in A, \Omega_A(\boldsymbol{x},\lambda)\cap B\neq\varnothing\right\} \tag{3.10}$$

Consider (3.9), it can be transformed as [6]:

$$\delta_A^{\lambda}(B)=\left\{\boldsymbol{x}'\in A \mid d_A(B,\boldsymbol{x}')\leq\lambda\right\} \tag{3.11}$$

It can be extended into the geodesic dilation for the grayscale images $f$ under the image $g$, $f < g$, in the direction of $y \in Y$:

$$\delta_g^{\lambda}(f)=\left\{y\in P \mid d_g(f,y)\leq\lambda\right\} \tag{3.12}$$

For digital grayscale images, $\lambda \in \mathbb{N}$ and $\lambda = [0, 255]$. For continuous PAS, $\lambda \in \mathbb{R}^+$.

*Operation* 8: **Reconstruction** [6] is a process of reshaping. If $f$ and $g$ are two grayscale images defined on the same domain and $f <$ g, reconstruction iterates repeating geodesic dilation until convergence:

$$\rho_g(f)=\bigvee_{\lambda>0}\delta_g^{\lambda}(f) \tag{3.13}$$

Reconstruction removes the peaks of the marked image, as shown in Figure 3.6.

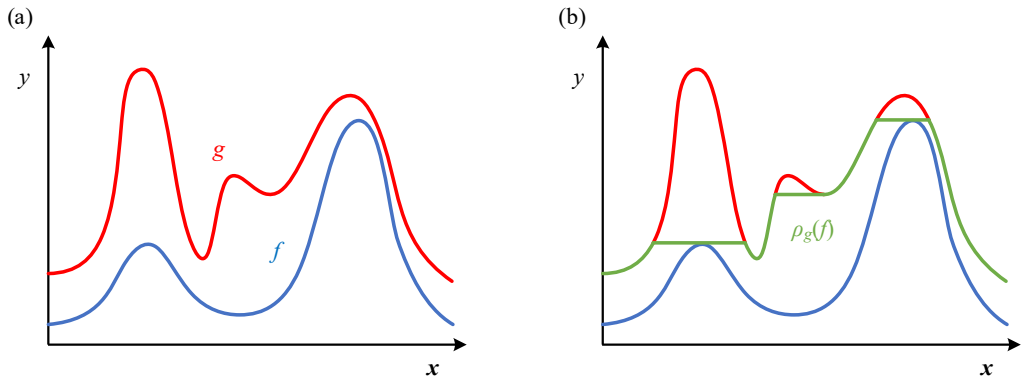


Figure 3.6 schematic diagram of reconstruction: (a) initial functions $f$ and $g$; (b) result of reconstruction.

*Operation* 9: Based on (3.13), **regional maxima** [7] extracts a domain $D_{max}(f)$ with a power tolerance $\varepsilon$, as shown in Figure 3.7.

$$D_{\max}(f)=f-\rho_f(f-\varepsilon) \tag{3.14}$$

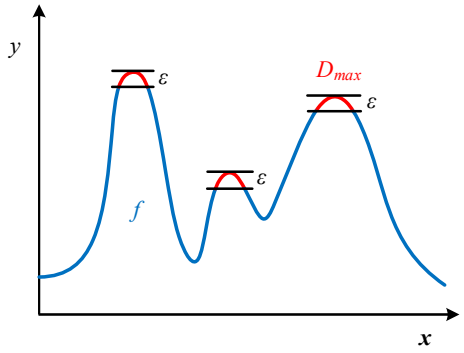


Figure 3.7 schematic diagram of regional maxima

*Operation* 10: **Gradient filters** (1st order derivative), **external gradient**, and **internal gradients** are calculated with dilation and erosion [6]:

$$\nabla f = f \oplus g - f \ominus g \tag{3.15}$$

$$\nabla^{+} f = f \oplus g - f \tag{3.16}$$

$$\nabla^{-} f = f - f \ominus g \tag{3.17}$$

*Operation* 11: with (3.15) to (3.17), **Laplacian filter** (2nd order derivative) [8] is:

$$\nabla^2 f = \nabla^{+} f - \nabla^{-} f \tag{3.18}$$

## 3.2.2 Watershed segmentation

Similar to the case of discrete clustering, image segmentation aims to find the regions with similar properties as well. As described in chapter 2, the similarity measure of discrete clustering is the Minkowski distance. In a continuous and differentiable field, if the elements in a domain have local similarity, the gradient of some features in the domain is low, or the divergence in the domain will have the same tendency. Here, the features that is considered is the Laplacian of the 2D angular map intensity, $\nabla^2 f$, defined as (3.18)

A segment is defined as the valley of a second-order derivative of a field for a convex hull of the origin field. Valleys can be segmented with the central minima and around local maxima. This is the idea of watershed segmentation: watershed segmentation is to find the local minima centers and local maxima boundaries of clusters. It can be linked to a problem of damming watersheds at the maxima to avoid flooding the low basin. The domains enclosed by the watersheds are the target segments, which form the cluster for the channel model. It is the origin of the name “watershed segmentation”.

### 3.2.2.1 The flow of watershed segmentation

The aim of watershed segmentation is presented with an example shown in Figure 3.8. The original image function $f$ is a 3D surface defined in a $X^2Y$ space, which in our case it the PAS. The projection of $f$ onto the $x$-$y$ plane is shown in Figure 3.8 (a) and the projection onto the angular plane to form a contour pattern of power in Figure 3.8 (c). Here, for sake of illustration, $y$ represents the field intensity. However later on, for the actual clustering, $y$ will represent the Laplacian of that field intensity. Segmentation aims to separate the different valleys $s_1$ to $s_4$ by creating watersheds segments (*WS*) at every local maximum, as shown in Figure 3.8 (b). The valleys can be then identified as segments (i.e., clusters in PAS).

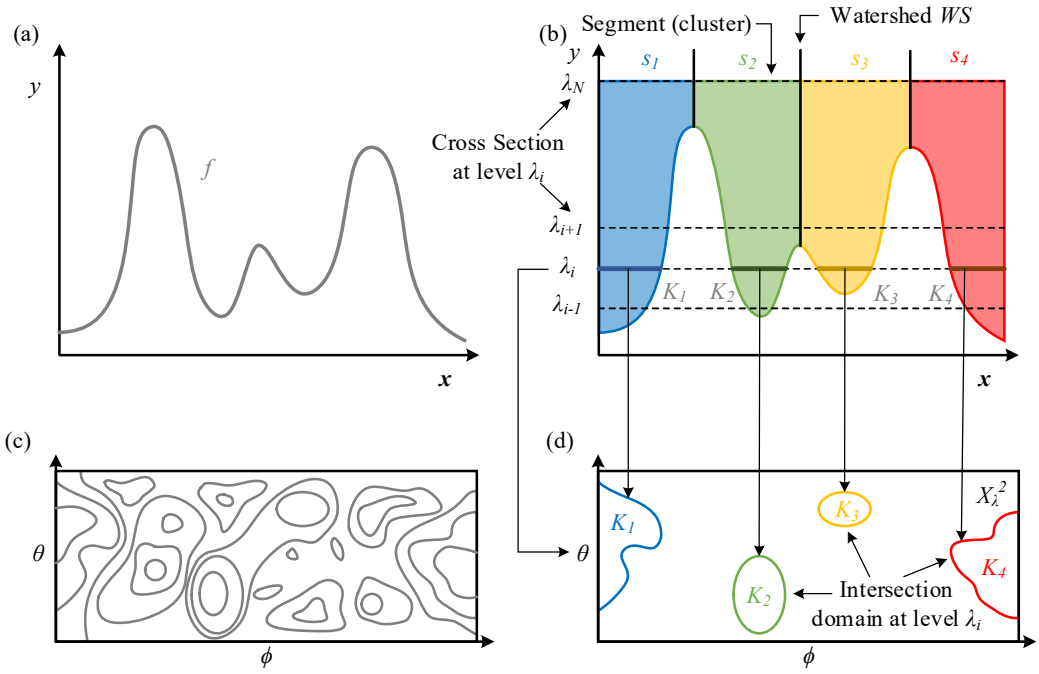


Figure 3.8 schematic diagram of watersheds segmentation: (a) projection of the original image function $f$, a 3D surface, on x-y plane; (b) vertical cross-section of segmentation $s_1$ to $s_4$ which are separated with watersheds *WS*; (c) projecting 3D surface $f$ on to a contour line on angular plane; (d) horizontal cross-section at $y = \lambda_i$.

The idea is to pour water progressively onto the $y$ function. The level of water λ continuously rises from 0 to $\lambda_{max}$. The surface of the water so poured is represented by the intersection of the cross-section plane $X_\lambda^2$ at level $\lambda$ with the function surface $f$ as shown in Figure 3.8 (d). This intersection plane $X_\lambda^2$ is then separated into isolated domains $K_1$ to $K_4$. Here, $K_i$ and $K_j$ are unconnected (isolated): $K_i \cap K_j = \varnothing$. To achieve the clustering, i.e., to find out the watersheds, the plane $X_\lambda^2$ horizontally intersects the curve $f$ at level $\lambda = 0$, continuously rising to level $\lambda = \lambda_{max}$. Since the valley is narrow at the bottom and broad at the top, during the level rising, the domains $K_i$ in the cross-section plane $X_\lambda^2$ extend and are reshaped with the reconstruction operation (3.13) until adjacent to each other (or reach the top level to stop). When this so occurs, the boundaries are stored as watersheds. The critical point of watershed is therefore to find out the boundaries between neighbor basins when the basins extend from low level to high level.

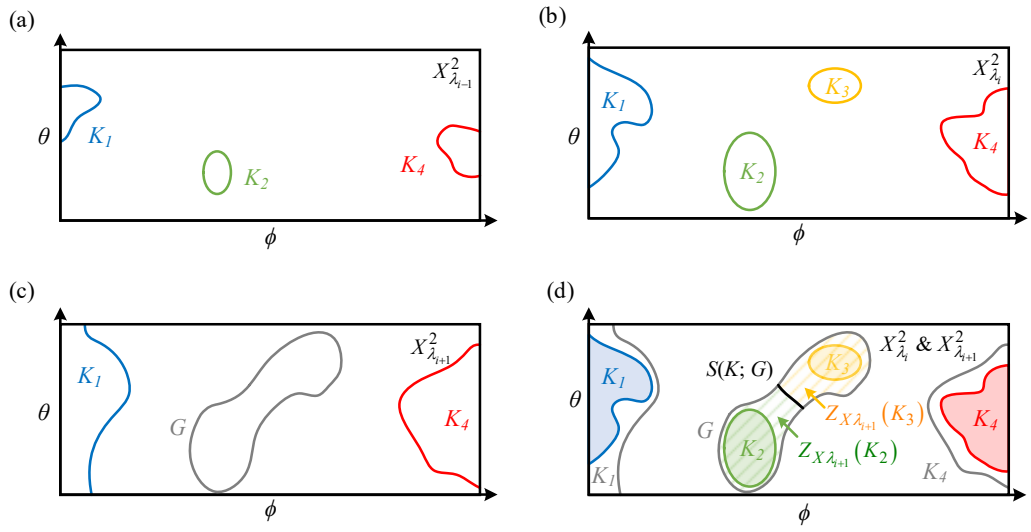


Figure 3.9 update Zone of Influence (IZ): connected domains on (a) $X^2_{\lambda_{i-1}}$, (b) $X^2_{\lambda_i}$ and (c) $X^2_{\lambda_{i+1}}$; (d) $X^2_{\lambda_i}$ and $X^2_{\lambda_{i+1}}$ to create IZ.

The flow of watershed corresponding to Figure 3.8 is shown in Figure 3.9. The figures (a) to (c) corresponds to the cross-sections at level $y = \lambda_{i-1}$ , $y = \lambda_i$, and $y = \lambda_{i+1}$ in Figure 3.8 (b). When the water reaches $y = \lambda_{i-1}$, the basins $S_1$, $S_2$, and $S_4$ are flooded. The flooded domains are the three domains $K_1$, $K_2$, and $K_4$ in Figure 3.9 (a). The flooded domain is denoted as $W_i = \cup K_j$. When the sampling plane moves to $y = \lambda_i$, a new domain $K_3$ is flooded in Figure 3.9 (b). It is the minima of the basin $S_3$. When the plane moves from level $y = \lambda_i$ to $y = \lambda_{i+1}$, $S_2$ and $S_3$ combine so that a new domain $G$ appears in Figure 3.9 (c). The new domain $G$ in Figure 3.9 corresponds to a combination of segments $S_2$ and $S_3$ so $G$ needs to be separated according to $K_2$ and $K_3$ ($S_2$ and $S_3$ represent two different clusters that need to be uniquely distinguished). To achieve this, two concepts are defined. The geodesic balls of $K_i$, $Z_{X_\lambda}(K_i)$, are called the Zone of Influence (IZ), as defined in (3.19). The boundary enclosing those IZ is called Skeleton by Zone of Influence (SKIZ) $S(K, X^2_\lambda)$, as defined in (3.20). The generation of $S(K, X^2_{\lambda_{i+1}})$ is here created with $K_2$ and $K_3$.

*Operation* 12: **Zone of Influence (IZ)** [9, 10] $Z_{X\lambda}(K_i)$ is the subset of points in $X_\lambda{}^2$ at a finite geodesic distance from $K_i$ and closer to $K_i$ than any other $K_j$.

$$Z_{X_\lambda}(K_i) = \left\{ \boldsymbol{x} \in X^2_\lambda \middle| \begin{array}{c} d_{X_\lambda}(\boldsymbol{x}, K_i) < +\infty, \\ \forall j \neq i, d_{X_\lambda}(\boldsymbol{x}, K_i) < d_{X_\lambda}(\boldsymbol{x}, K_j) \end{array} \right\} \tag{3.19}$$

*Operation* 13: **Skeleton by Zone of Influence (SKIZ)** [9, 10] $S(K, G)$ is the complement set of all the IZ with:

$$S(K;G) = G - \bigcup_i Z_{X_\lambda}(K_i) \tag{3.20}$$

In Figure 3.9 (d), $Z_{X_\lambda}(K_2)$ is the domain closest to $K_2$ rather than $K_3$:

$$Z_{X_\lambda}(K_2)=\left\{\boldsymbol{x}\in G\middle| d_{X_\lambda}(\boldsymbol{x},K_2)<d_{X_\lambda}(\boldsymbol{x},K_3)\right\} \tag{3.21}$$

While, $Z_{X_\lambda}(K_3)$ is the domain closest to $K_3$ rather than $K_2$:

$$Z_{X_\lambda}(K_3)=\left\{\boldsymbol{x}\in G\middle| d_{X_\lambda}(\boldsymbol{x},K_3)<d_{X_\lambda}(\boldsymbol{x},K_2)\right\} \tag{3.22}$$

Therefore, SKIZ is the bound equidistance to $K_2$ and $K_3$ :

$$S(K;G)=G-\left[Z_{X_\lambda}(K_2)+Z_{X_\lambda}(K_3)\right]=\left\{\boldsymbol{x}\in G\middle| d_{X_\lambda}(\boldsymbol{x},K_3)=d_{X_\lambda}(\boldsymbol{x},K_2)\right\} \tag{3.23}$$

It is the difference of the connected domain $G$ and the sum of all IZ inside $G$. The other extended domains $K_1$ and $K_4$ are the new local minima of $\nabla^2 f$ at current level, which are isolated with other $K_j$. They are reconstructed from the $\lambda_i$ by (1.13) to create the set of the minima $m_i$ at the level $y = \lambda_{i+1}$. The flooded domain at this level is $W_{i+1} = \cup\, Z_{X_{i+1}}(K_j) \cup K_j$. The above process repeats until the maximum level is reach. At the end of the process, the different isolated domains $K$ and the zones of influences $Z$ represent the clusters as (3.26). The watershed $WS$ is the complement of the flooded domain at level $\lambda_N$: $WS = W_N^C = X^2_{\lambda_N} - W_N$ as (3.27). The full flow of watershed is shown in Algorithm 3.1.

Algorithm 3.1 The general flow watershed segmentation

4. Initialize the flooded domain $W_1 = \varnothing$.
5. For $i$ = 1 to $Max\ \lambda_N$
   a. Creates new minima $m_{i+1}(f)$ at level $\lambda_i$ with reconstruction $\rho_g(f)$ (3.13):

$$m_{i+1}(f)=\rho_{K^{i+1}}\left(K^i\right) \tag{3.24}$$

   Where

$$K^i=\left[\bigcup_j K_j\right]_{X^2_{\lambda_i}} \tag{3.25}$$

   b. Create IZ with (3.19).
   c. Update the flooded domain $W_i$:

$$W_{i+1}=\left[\bigcup_j IZ_{X_{\lambda_i}}(K_j)\right]\bigcup m_{i+1} \tag{3.26}$$

   Next $i$
6. Extract the final SKIZ with (3.20) at the top level:

$$WS=W_N^c=X^2_{\lambda_N}-W_N \tag{3.27}$$

7. Return $SKIZ$ and $W_N$

The K-Power-Means introduced in chapter 2 looks for a global minimum. The procedure of watershed

transformation illustrates that it is a local method. The extension of IZ boundaries is operated by reconstructing adjacent IZ in $x$ direction at the level $\lambda_i$ and $\lambda_{i+1}$. The reconstruction smoothing operation here is to avoid the singularities at the boundaries. It is the essential difference between K-Power-Means and watershed segmentation.

### 3.2.2.2 The solution of the over-segmentation problem

One of the critical problems of watershed segmentation is the sensitivity regarding the fluctuations around the cluster. The micro-concave domains will be incorrectly divided into clusters and small pieces nearby clusters. Furthermore, isolated weak pulses need to be removed from the whole PAS. In simulation, the isolated pulse are rays generated away from the main cluster because of the tail of the AoA/AoD PDF. Interestingly, as seen in the next chapter, isolated pulses do also exist in experimental results as spread distributed speckles. Two operations are used to mitigate this issue: a speckle removal operation and cluster-vicinity over-segmentation removal.

#### 3.2.2.2.1 Speckle removal

A denoising filter is used to remove the isolated noise pixels in the background. To do so, image processing operations are applied: a combination of opening (3.5) and closing (3.6) operations and then a process of smoothing using restructuration (3.13). The results can be seen in Figure 3.10. Compared with the original PAS in Figure 3.10 (a), the CIR generates spread distributed speckles in Figure 3.10 (b). Those isolated noise pixels are removed in Figure 3.10 (c).

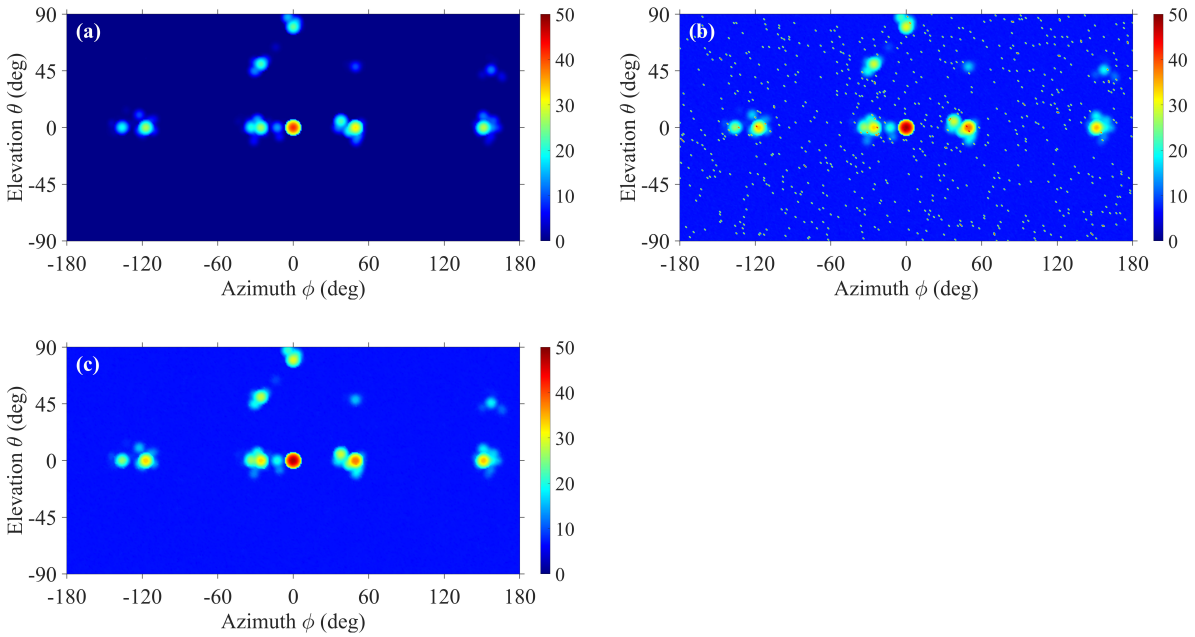


Figure 3.10 PAS with (a) no noise; (b) AWGN noise on CIR and isolated pulse noise on PAS; (c) denoised of (b)

#### 3.2.2.2.2 Cluster-vicinity over-segmentation removal

Even with the isolated pulse removed, over-segmentation still occurs in the vicinity of clusters, due to their large fluctuation. One example of such an over-segmentation is shown onto the PAS in Figure 3.11. The over-segmentation can be observed with both beam widths of 5° and 20°. It is therefore a general issue for PAS segmentation. In Figure 3.11 (a), obvious fine divided clusters generated with beam with 5° concentrated in the top-left corner. For larger beam with of 20°, the fine clusters over-segmented revolve the actual clusters in Figure 3.11 (b).

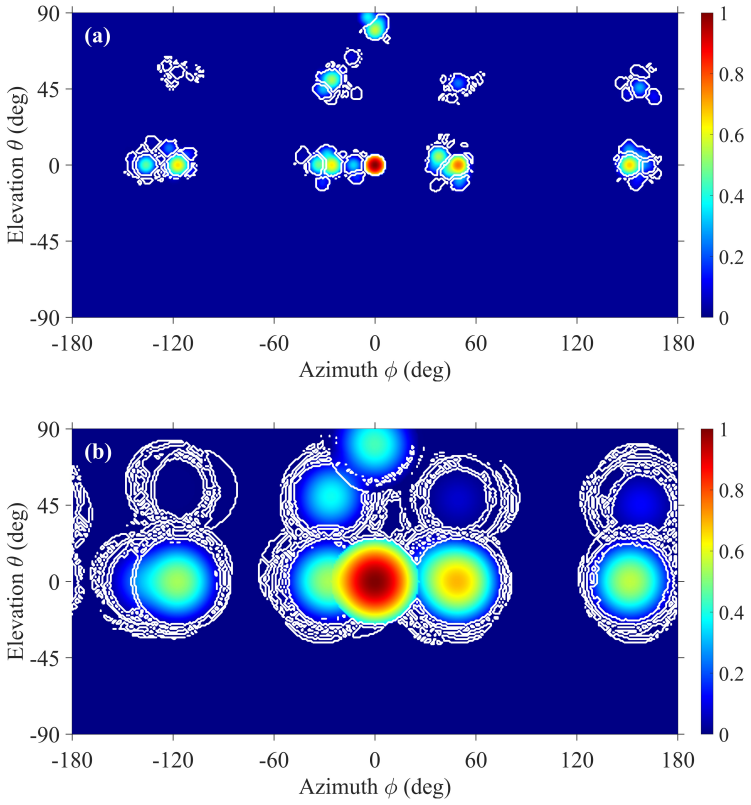


Figure 3.11 Over-segmentation of the PAS with beam width of (a) 5° and (b) 20°.

The watershed algorithm in Figure 3.8 contains two stages: extension of IZ and extracting IZ. One constraint of IZ extraction is that it is limited within a "connected domain $G$" as in Figure 3.9 (d). Therefore, the boundaries of clusters and background can be used to mitigate the over-segmentation, as Figure 3.12. Generalizing the SKIZ extraction operation, the general extension of isolated domain can be view as an extraction of SKIZ with an absence of dual domain and outbound of $G$, as the disappearing of $K_2$ in Figure 3.12 (a). Therefore, the extension in Figure 3.12 (a) is a SKIZ extraction within the whole cross-section plane $X_{\lambda_i}^2$. In Figure 3.12 (b) the free space is an overlapped domain of ZI domains $Z_{X_{\lambda_i}}(K_1)$ and $Z_{X_{\lambda_i}}(K_2)$. In this case, no SKIZ can be extracted from the absence $G$, until $K_1$ and $K_2$ extend enough to touch each other and extracting SKIZ between them. All of the clusters will be identified without any constraint, even the fluctuated small clusters in over-segmentation.

To avoid that, the minima regions of the gradient field are first extracted through the maximum regions of the PAS field with eq.(3.14) and are selected as markers. The IZ containing one and only one marker is regarded as a segment while the over-segments of the background ought to be merged into a whole. To do so, the background is marked with the watershed of the Euclidean distance, using (3.7), as $G_1$ (see Figure 3.12 (c)) The Euclidean distance as specified in (3.7) is the distance between each pixel and the nearest zero pixel in the foreground markers. $G_2$ as well, the watershed extraction is constrained again with boundaries $G_1$ and $G_2$. In that case, only the watersheds of marked domain $K_2$ in Figure 3.12 (c) can be preserved by extracting the equidistance boundaries as the definition of watershed (3.19). Unmarked clusters like the $K_1$ will be ignored since the equidistance cannot be evaluated due to the lack of markers (boundary $G_2$ for $K_2$).

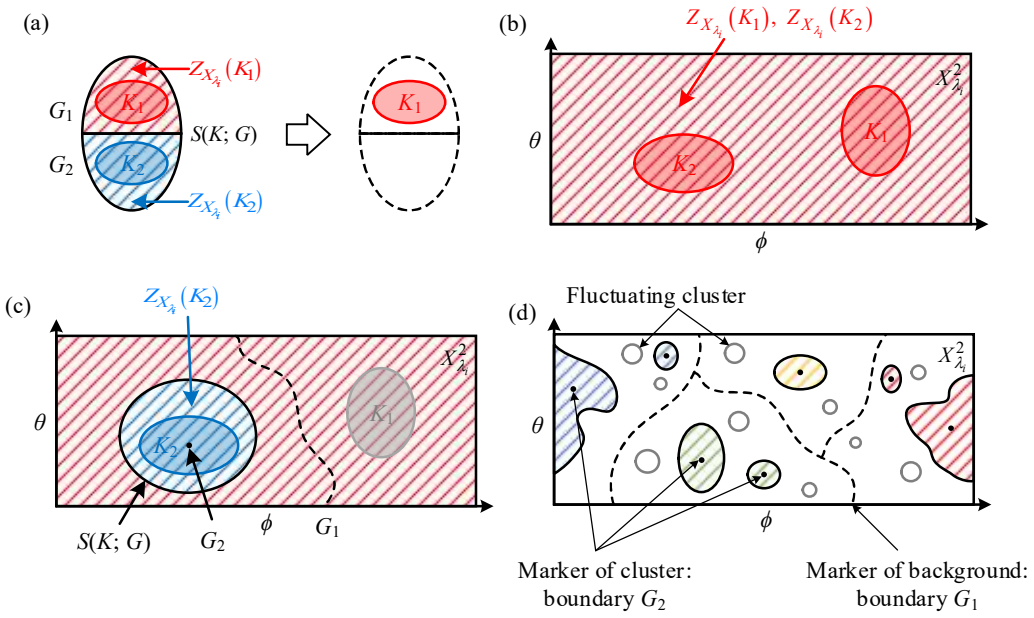


Figure 3.12 Mechanism to mitigate over-segmentation by markers: (a) open-bound SKIZ extraction; (b) segmentation without markers; (c) keeping clusters by adding makers of clusters and background as the boundaries; (d) role of makers to cover over-segmentation.

Algorithm 3.2 Flow of watershed segmentation solving the over-segmentation problem

1. **Extract gradient field**: calculate the curvature with the Laplacian filter $\nabla^2 f$ (3.18).
2. **Extract the mark of foreground**: Removing the isolated points with a combination of opening (3.5) and closing (3.6). Then smooth it with restructuration (3.13). Get locations of $N$ regional power maxima of the foreground as centroid positions with (3.14).
3. **Extract the mark of background**: the marks are the curves equidistant to the clusters in the foreground. The distances of every point in the foreground marker are calculated (3.7). Then the markers of the background are the watershed line built with watershed transformation Algorithm 3.1.
4. **Group clusters**: combining the foreground, local maxima, and marker of background, the indices are assigned with watershed transformation Algorithm 3.1.

A modified watershed segmentation flow which can achieved what is illustrated in in Figure 3.12 (d)

is presented in Algorithm 3.2.

# 3.3 PAS Simulated with 60 GHz Channel Model

To validate the feasibility of segmentation for 60 GHz PAS with the watershed method, simulations are performed based on the angular power data obtained from the channel model of IEEE 802.11ad in the conference scenario.

## 3.3.1 Model of AOA in IEEE 802.11ad

The channel model in IEEE 802.11ad has been obtained by Monte Carlo sampling of ray tracing data. A schematic diagram of AOA and AOD is shown in Figure 3.13. A pair of Rx and Tx is placed on a table in the center of a conference room. The LOS beam is transmitted directly from Tx to Rx, while walls and the ceiling reflect the NLOS transmission paths. The table obstructs the beam focusing toward the ground. In order to get the angular coordinate in the PAS in Figure 3.1 (b), the positive and negative axes of azimuth and elevation are defined. The AOA and AOD of LOS beams are defined as $\phi = \theta = 0°$. The direction of the antenna beam at $\phi = \theta = 0°$ is defined as the positive direction. As shown in Figure 3.13 (a), the counterclockwise rotating direction of the radio beam is defined as the negative axis of azimuth for both AOA and AOD; the elevation is positive at the upper hemisphere and negative at the lower hemisphere. is considered as the positive axis of elevation in Figure 3.13 (b).

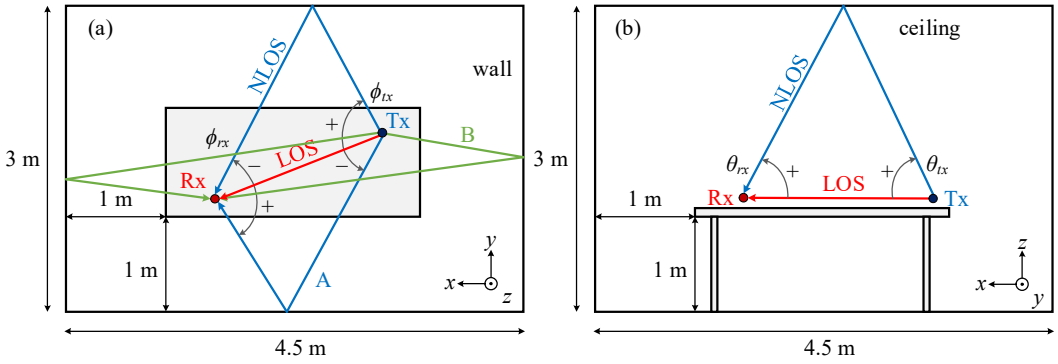


Figure 3.13 AOA and AOD in (a) top view and (b) front view of IEEE 802.11ad channel model in the conference scenario.

AOA and AOD in IEEE 802.11ad are cluster-based. Eighteen intra-cluster angles are considered, Gaussian distributed. The statistical distributions of the seventeen clusters are empirical piecewise functions. Only the first and second reflections are considered in the model. For the four first-reflection clusters reflected by walls, the AOA and AOD azimuths (path A and B) reflected by orthogonal walls are correlated with each other. Their relation in the positive and negative azimuth angle are:

$$\begin{cases} \phi_B \geq \left(\frac{140}{90}\right)\cdot\phi_A + 62^0 \\ \phi_B \leq \left(\frac{140}{90}\right)\cdot\phi_A + 82^0 \\ \phi_B \leq 180^0 \\ \phi_A \geq 0^0 \end{cases} \quad \begin{cases} \phi_B \leq \left(\frac{140}{90}\right)\cdot\phi_A - 62^0 \\ \phi_B \geq \left(\frac{140}{90}\right)\cdot\phi_A - 82^0 \\ \phi_B \geq -180^0 \\ \phi_A \leq 0^0 \end{cases} \tag{3.28}$$

The distribution of one elevation angle cluster contributed by the first-order reflections from the ceiling is:

$$p_\theta(\theta) = \begin{cases} 0 & \theta < 56.6^0 \\ 0.0023\cdot\theta\text{-}0.1302 & 56.6^0 \leq \theta < 83^0 \\ \text{-}0.0087\cdot\theta + 0.7810 & 83^0 \leq \theta < 90^0 \\ 0 & \theta = 90^0 \end{cases} \tag{3.29}$$

The distribution of four elevation angle clusters contributed by the second-order reflections from walls and ceiling is:

$$p_\theta(\theta) = \begin{cases} 0 & \theta < 30^0 \\ 0.0028\cdot\theta\text{-}0.0833 & 30^0 \leq \theta < 52^0 \\ \text{-}0.0056\cdot\theta + 0.3500 & 52^0 \leq \theta < 63^0 \\ 0 & \theta \geq 63^0 \end{cases} \tag{3.30}$$

The AOA and AOD elevation clusters of the second-order reflections from walls are correlated. The distributions are divided into eight segments:

$$\begin{cases} \phi_{tx1} = 180^\circ\cdot u_1 \\ \phi_{rx1} = \phi_{tx1} \end{cases} \quad \begin{cases} \phi_{tx2} = 180^\circ\cdot u_2 \\ \phi_{rx2} = \phi_{tx2} \end{cases}$$
$$\begin{cases} \phi_{tx3} = 180^\circ\cdot(u_3 - 1) \\ \phi_{rx3} = \phi_{tx3} \end{cases} \quad \begin{cases} \phi_{tx4} = 180^\circ\cdot(u_4 - 1) \\ \phi_{rx4} = \phi_{tx4} \end{cases}$$
$$\begin{cases} \phi_{tx5} = 180^\circ\cdot(u_5 - 1) \\ \phi_{rx5} = \phi_{tx5} + 180^\circ \end{cases} \quad \begin{cases} \phi_{tx6} = 180^\circ\cdot(u_6 - 1) \\ \phi_{rx6} = \phi_{tx6} + 180^\circ \end{cases} \tag{3.31}$$
$$\begin{cases} \phi_{tx7} = 180^\circ\cdot u_7 \\ \phi_{rx7} = \phi_{tx7} - 180^\circ \end{cases} \quad \begin{cases} \phi_{tx8} = 180^\circ\cdot u_8 \\ \phi_{rx8} = \phi_{tx8} - 180^\circ \end{cases}$$

Where $u_1$ to $u_8$ are *i.i.d.* variables uniformly distributed in the range of [0, 1]. The PDF generated with (3.28) to (3.31) are shown in Figure 3.14.

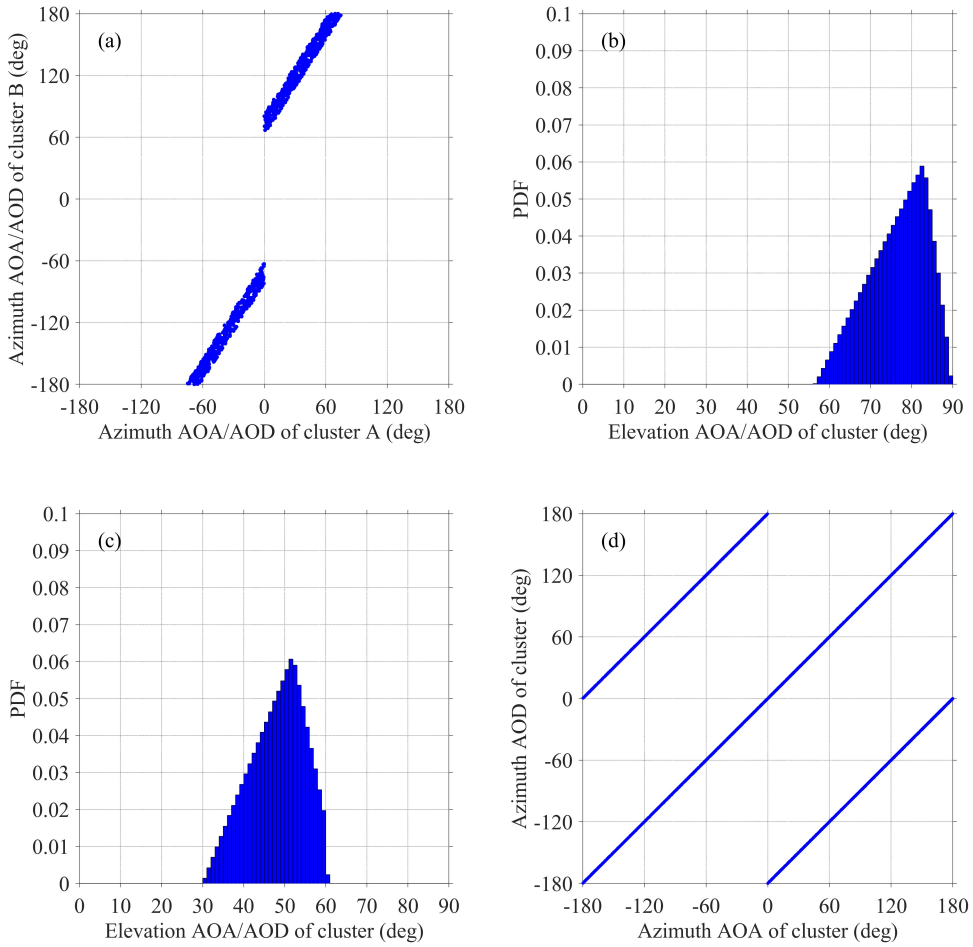


Figure 3.14 Statistical characteristic of AOA and AOD: (a) relation between azimuth clusters created by the first-order reflection by walls; (b) PDF of elevation with the first-order reflection by ceiling; (c) PDF of elevation with the first-order reflection between ceiling and walls; (d) relation between azimuth AOA and AOD of clusters.

The antenna beam is modeled with a combination of Gaussian-shaped main lobe and constant-leveled side lobe. The circularly symmetric Gaussian function of the main lobe is:

$$G(\theta,\phi) = G_0 \exp\left[-\alpha\left(\theta^2+\phi^2\right)\right] \tag{3.32}$$

Where

$$\alpha = \frac{4\ln 2}{\theta_{hpbw}^2} \tag{3.33}$$

$$G_0 = \left[\frac{1.6162}{\sin\left(\theta_{hpbw}/2\right)}\right]^2 \tag{3.34}$$

$\theta_{hpbw}$ is the 3dB Half Power Beam Width (HPBW). The side lobe is the pattern larger than $2.6\theta_{hpbw}$. Integration of the antenna gain over the whole solid angle results in unity, the side lobe is set as

$$G[dB] = -0.4111 \cdot \log_{10}\left(\theta_{hpbw}\right) - 10.597 \tag{3.35}$$

As an example, the antenna pattern model creates a normalized antenna pattern of HPBW = 10° as shown in Figure 3.15.

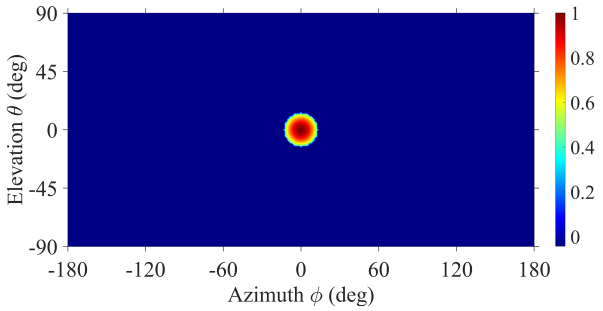


Figure 3.15 Normalized antenna pattern of 10° created with the channel model of IEEE 802.11ad.

## 3.3.2 Simulation parameters

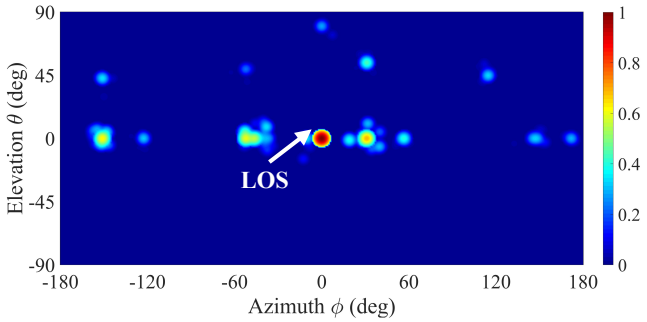


Figure 3.16 Normalized PAS created with 5 ° beam width

One thousand realizations are generated to verify watershed segmentation. While using an omnidirectional Tx antenna, the Rx directional beam scans across the angular space. The scanning interval is 1° in order to obtain a high spatial resolution. In order to study the influence of beam width on the watershed segmentation method, the beamwidth of the Rx antenna varies in a range of 5° to 29° with a 2° sampling step. An oversampling factor of 8 is selected to increase the time resolution. A PAS example generated with a 5 ° beam width is shown in Figure 3.16.

# 3.4 Clustering for 60 GHz Channel by Watershed

## 3.4.1 Intermediate results of watershed algorithm

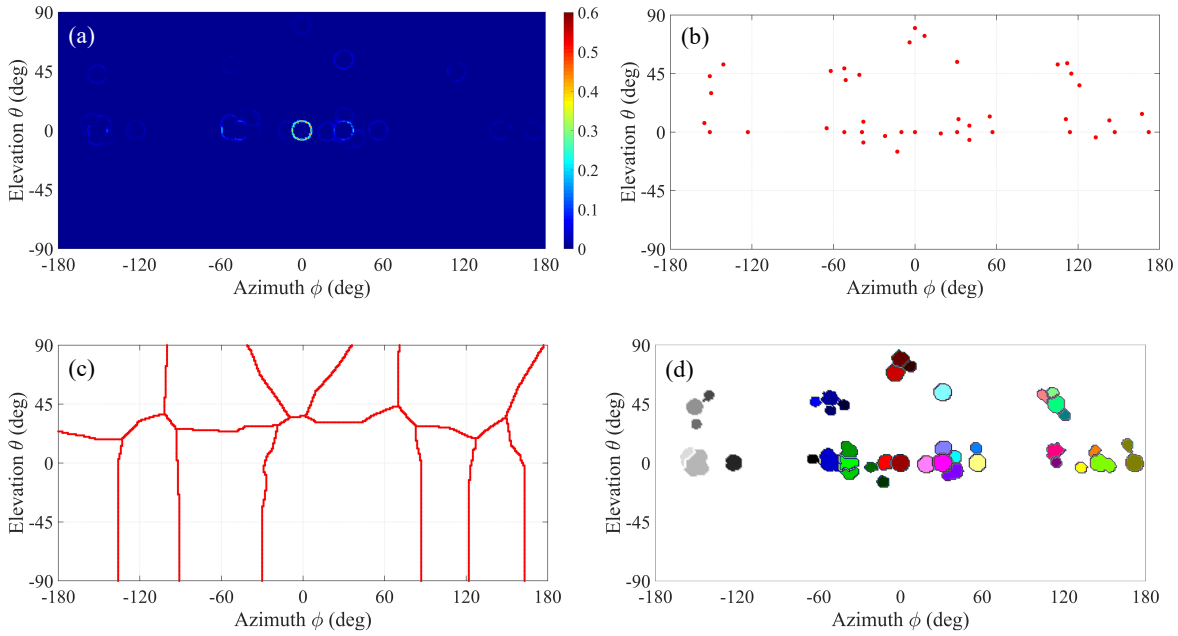


Figure 3.17 Result of the watershed algorithm at different steps: (a) gradient field; (b) local maxima as front markers; (c) maximum distance curves as backmarkers; (d) clusters marked with different colors.

Figure 3.17 presents the intermediate results of the watershed segmentation of the noiseless PAS shown in Figure 3.16. According to Algorithm 3.2, this example illustrates the results of four steps for watershed segmentation. Without loss of generality, the PAS is normalized to its peak value. A Laplacian filter extracts the gradient field of the original PAS as shown in Figure 3.17 (a). The marker of the illuminated foreground is the local maxima in Figure 3.17 (b) whereas the background is marked with the watershed curves of the Euclidean distance field determined with (3.7) in Figure 3.17 (c). Finally, the PAS clusters in Figure 3.17 (d) are obtained with the watershed segmentation. The watershed transformation acts on the combination of gradient field, foreground, and background. Comparing the original PAS in Figure 3.16 with the clusters in Figure 3.17 (d), Algorithm 3.1 meets the original expectation in the schematic diagram of watershed segmentation in Figure 3.8. One important parameter in the process is the shape of the marker $g$ in (3.3) and (3.4), that influences the denoising and smoothing operation. A $g$ is a $n \times n$ matrix with values to make the matrix like disk, square, diamond. In this study, a $3 \times 3$ matrix has been found to perform well, although depending on the angular step of the PAS 2D map, this operator may be adjusted to obtained optimal clustering performance.

### 3.4.2 Comparing methods

Because watershed segmentation aims to solve the problem in K-Power-Means, K-Power-Means is one of the methods we should benchmark our approach with. Besides, in order to investigate the influence of the pretreatments in modified watershed transformation, such as the markers of foreground and background in Algorithm 3.2, the same pretreatments are introduced in the standard K-Power-Means as another benchmarking method. First, fixed local maxima replace the iterative searching for centroids. Opening and closing operations are used to remove the isolated point noise the field similarly to watershed segmentation. Second, since the background marker is hard to accomplish, a threshold is used to remove the background directly. The threshold is selected using Otsu's method [11]. Otsu's method distinguishes the foreground and background of a high-contrast image by finding the maximum separation of the intensity histogram. The flowchart of the modified K-Power-Means algorithm is shown in Algorithm 3.3.

Algorithm 3.3 Flowchart of modified K-Power-Means algorithm

1. Extract locations of $N$ local maxima power as centroid positions $c_1^{(0)}, \dots, c_N^{(0)}$. Remove the isolated point noise with a combination of opening (3.5) and closing (3.6), then smooth it with restructuration (3.13).
2. Remove the background with a threshold $P_{thre}$ which is the first bin of total $M$ bins $p_i(P_l)$ in the power intensity histogram with the $N$ components in the field:

$$P_{thre} = \arg\max_i p_i\left(P_l\right) \tag{3.36}$$

3. Assign MPCs to cluster centroids and store indices $\mathcal{I}_l^{(i)}$

$$\mathcal{I}_l^{(i)} = \arg\min_n \left\{ P_l \cdot \mathrm{MCD}\left(\boldsymbol{x}_l, \boldsymbol{c}_n^{(i-1)}\right) \right\} \tag{3.37}$$

$$\mathcal{I}^{(i)} = \left[ \mathcal{I}_1^{(i)} \dots \mathcal{I}_L^{(i)} \right], \ \mathcal{C}_k^{(i)} = \operatorname*{indices}_l \left( \mathcal{I}_l^{(i)} = k \right) \tag{3.38}$$

4. Return $\mathcal{R}_n = [\mathcal{I}^{(i)}, c_n^{(i)}]$

### 3.4.3 Simulation results

#### 3.4.3.1 Results of watershed segmentation

Figure 3.18 shows the result of watershed segmentation for the PAS with beam widths of 5°, 13°, 21°, and 29°. White closed curves are the labels for illuminated foreground clusters. The dark blue domain is the background domain. Cluster labels clearly distinguish adjacent foreground domains. Most of the power in the foreground is gathered into clusters, and the background with week power intensity is clearly excluded from clusters. Intuitively, the watershed segmentation achieves the two main purposes of clustering: extracting the illuminated foreground from the dark background, and distinguishing different illuminated domains. Furthermore, clustering can clearly be achieved with different beam widths. Another important observation is that the cluster shapes are well preserved.

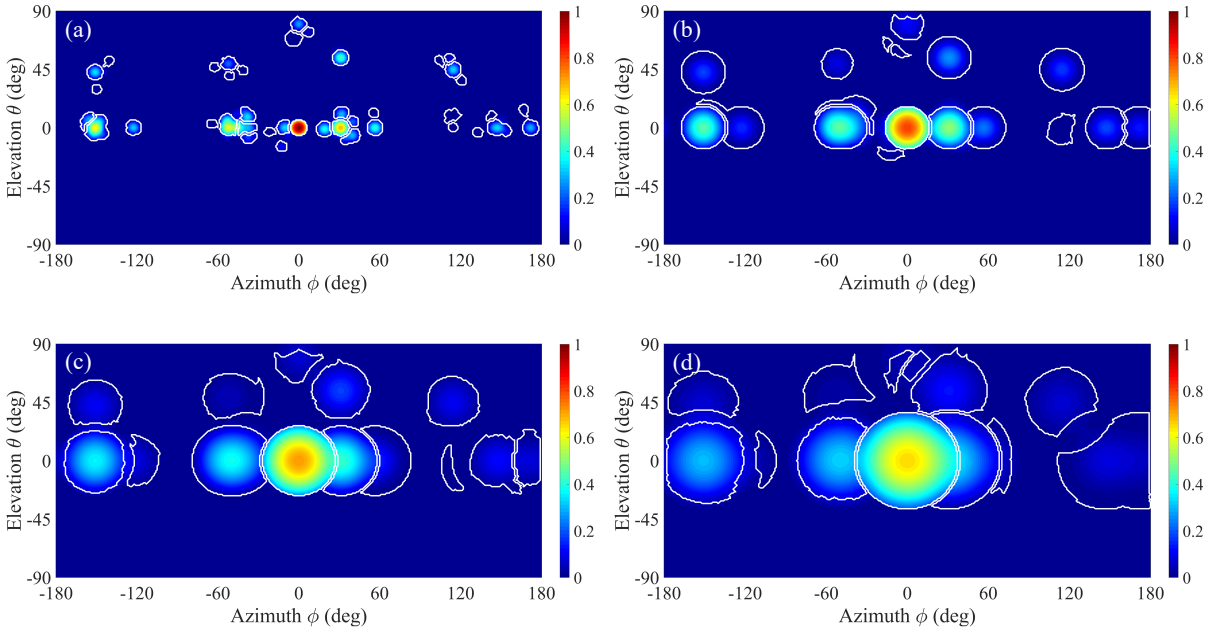


Figure 3.18 Result of segmentation with watershed transformation with beam width of (a) 5°; (b) 13°; (c) 21°; (d) 29°

### 3.4.3.2 Results of standard K-Power-Means

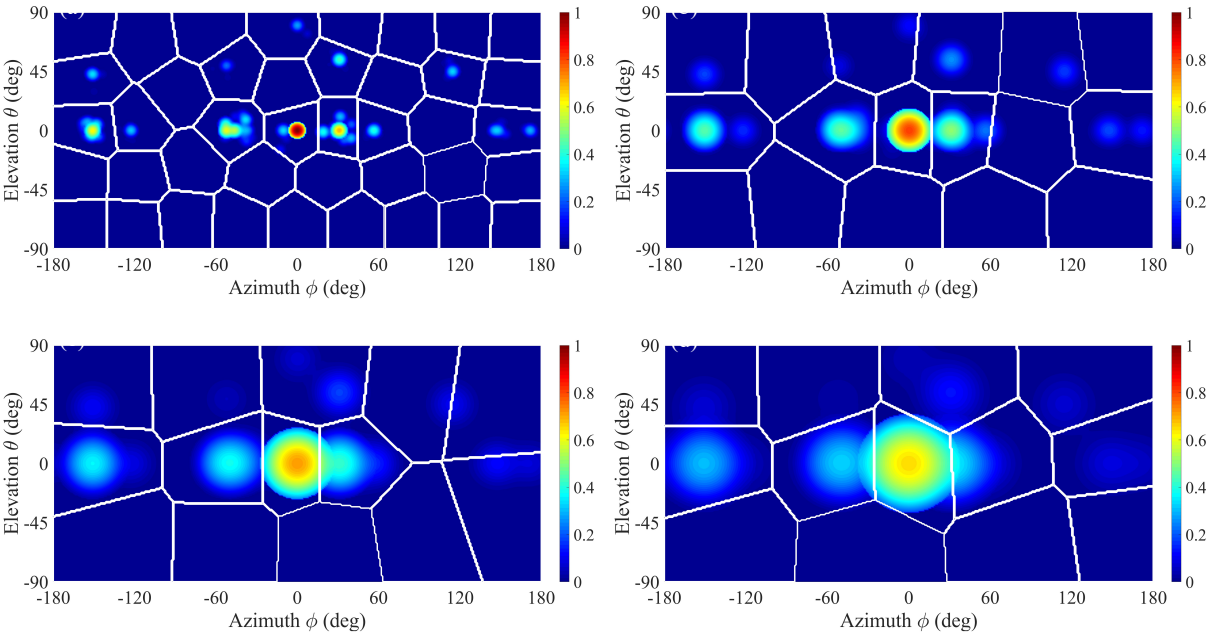


Figure 3.19 Result of segmentation with standard K-Power-Means with beam width of (a) 5°; (b) 13°; (c) 21°; (d) 29°

Using the standard K-Power-Means method, the entire angular space is divided into several polygons bounded by white straight lines, as shown in Figure 3.19. In the example in Figure 3.19 (a), the illuminated foreground is roughly divided into large ranges, without distinguishing adjacent clusters in detail. Even

worse, parts of the dark background are also enclosed into clusters. As the beam width increases in Figure 3.19 (b), (c), and (d), complete high-power-intensity regions are split and arranged into different clusters. The above phenomena manifest that the standard K-Power-Means method is not sensitive to the correlation between adjacent regions. The shape of the cluster is not a polygon. So the polygon division results in either the power leaking from the cluster into the adjacent domain, or the dark background is circled into the cluster. It is consistent with the conclusions of the state-of-the-art in chapter 2. So from these results, we can intuitively anticipate that K-power-means will not performed well in clustering PAS, especially for studying the statistics of the clusters' shapes as we intend to do for NLOS identification.

### 3.4.3.3 Results of modified K-Power-Means

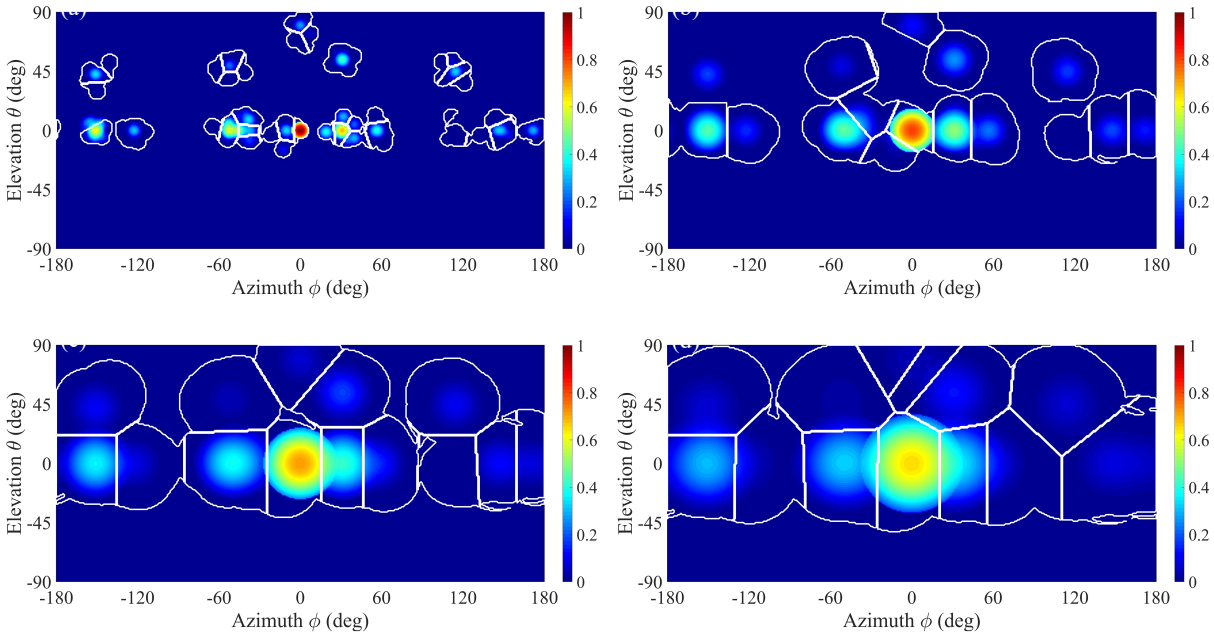


Figure 3.20 Result of segmentation with modified K-Power-Means with beam width of (a) 5°; (b) 13°; (c) 21°; (d) 29°

The result of modified K-Power-Means clustering is shown in Figure 3.20. With a narrow beamwidth of 5° in Figure 3.20 (a), most clusters of the illuminated foreground can be identified, and the dark background is eliminated. However, as the beam width increase to 13°, 21°, and 29° in Figure 3.20 (b), (c), and (d), respectively, the foreground markers do not improve the straight boundaries of the polygons in the original K-Power-Means. Introduced foreground markers can find the location of certain clusters and thresholds can remove part of the background. However, part of the background is still enclosed into clusters, even in narrow beam transmission. In that case, the shapes of the clusters are only the shape of a uniform threshold instead of the individual cluster shapes. In the case of wide beam, the effect of threshold disappears. Without the individual description of the cluster shape by the watershed transform, the adjacent clusters cannot be distinguished robustly and clearly for a wide beam. Therefore, while the preprocessing step introduced in this modified version improves the classical, it fails in accurate PAS clustering for wide beams. So, although this modified version outperforms the classical K-power-means algorithm, the

watershed approach appears much more robust in keeping intact the shapes of the cluster and removing the background.

## 3.5 Performance of Clustering

In addition to the above intuitive comparison among K-Power-Means, modified K-Power-Means, and watershed transformation clustering methods, the performance of four aspects need also to be evaluated: the number of obtained clusters, the separation between foreground and background, the distinction among adjacent clusters, and the running time of the algorithm.

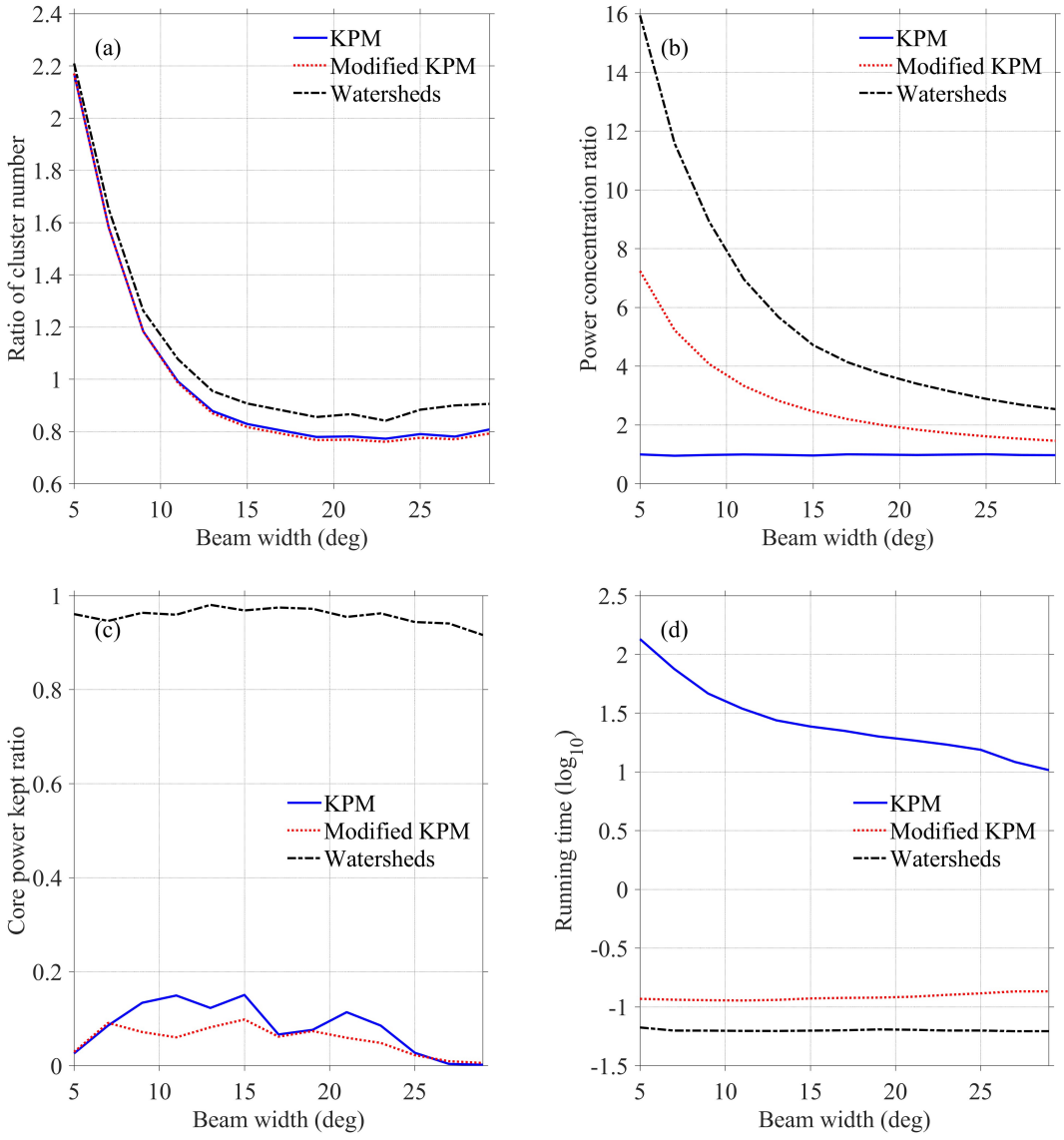


Figure 3.21 Performance of clustering methods

Clusters in the continuous field are generated with Gaussian distributed channel clusters. Therefore, we evaluate the number of clusters with the following ratio: the number of clusters estimated with

clustering algorithm over the number of clusters generated with by channel model：

$$\frac{Number\ of\ estimated\ clusters}{Number\ of\ cluster\ generated\ by\ channel} \tag{3.39}$$

The performance is shown in Figure 3.21 (a). The three algorithms have the same trend. The narrow beam provides higher spatial resolution, so a larger number of clusters can be distinguished. As the beam width increases, the clusters become larger, and the corresponding number of clusters decreases. In wide beam transmission, the number of clusters provided by the watershed algorithm is closer to the number of channel clusters than the other two methods. It is also interesting to observe that all three algorithms overestimate the number of clusters when the beamwidth is narrow. Indeed, each cluster contains a few rays only, and for a given channel realization, a cluster can easily be interpreted as several clusters if the rays are sparsely angularly separated.

The separation between the foreground and background can be evaluated with a ratio: the power density of all clusters over the power density of the whole angular plane:

$$\frac{\sum power\ density\ of\ grouped\ cluster}{power\ density\ of\ whole\ angular\ plane} \tag{3.40}$$

The performance is presented in Figure 3.21 (b). K-Power-Means cannot remove the background. The power of the entire PAS is brought into the foreground, which is the sum of all clusters. Therefore, the ratio of the power sum of all clusters to the power sum of the entire PAS is one and is always one regardless of the beamwidth. After adding the threshold, the background can be partially removed, and the curve rises. However, because background components cannot be entirely removed and some background power is also included in the cluster, the ratio is not the highest. Watershed segmentation provides the most significant separation between the three algorithms. However, for wide beams, the power density ratio decreases as the clustered power density is diluted into the background.

K-Power-Means and modified K-Power-Means often split clusters, which is an undesirable effect and the integrity of clusters should be therefore assessed. To assess this effect, the metric we use is the ratio of the power in the preserved illuminated cluster over the power in the damaged illuminated cluster. So, the first step is to determine a practical definition of a preserved cluster.

For continuous PAS 2D map, the elements of a cluster are pixels, whose values depend on the field intensity within that cluster. A cluster is therefore a set of pixels with similar intensity compared with the neighbor domain. Because the field is continuous and derivative, the 2nd order derivative field exists. So, a cluster is enclosed by the edge of a slope. Therefore, the edge are the elements pixels at the boundary with highest 2nd order derivative. Because the intensity cluster is a continuous domain, the 2nd order derivative forms a continuous closed edge. So, the pixels inside this closed edge belong to a preserved cluster. Pixels belonging to cluster with discontinuous 2nd order derivative edge belong to damaged clusters. We subsequently define the following metric:

$$\frac{\sum power\ inside\ preserved\ cluster}{\sum power\ \ inside\ damage\ cluster} \tag{3.41}$$

As shown in Figure 3.21 (c), the ratio of watershed segmentation is almost one, which means that almost all of the clusters are completely preserved. In contrast, the ratios of K-Power-Means and modified K-Power-Means are very close to zero: the two clustering algorithms destroy most of the clusters.

Finally, the algorithm running time is assessed. With ray tracing tools being more and more advanced, they can be used for channel modeling. This means that a large number of channel realizations need to be generated and analyzed, generating a hugh volume of data. Consequently, a fast clustering method is highly desirable. The theoretical time complexity of K-Means is $O(ndkt)$, where n is the number of the data points, $d$ is the number of dimensions, $k$ is the number of clusters and t is the number of iterations. The simulations have been run with a laptop (CPU 2.60 GHz, RAM 8.00 GB) and the obtained logarithmic running time is shown in Figure 3.21 (d). When the beam is wide, the number of clusters decreases, so the required calculation time reduces acordingly. Standard K-Power-Means takes multiple iterations to avoid local minima, so it needs two to three orders of magnitude of simulation time than the modified K-Power-Means or watershed segmentation. While iteration is not necessary for the modified K-Power-Means, it still needs to compute the random initial centroids, which is time consuming. The watershed segmentation appears as the fastest method among the three.

# 3.6 Conclusion

In this chapter, an original clustering method proposed that is based on an image processing approach. In particular, the clustering of PAS is studied with the watershed segmentation method. In millimeter-wave communications, the beam training strategy that scans the whole angular space to identify a strong enough link makes the PAS readily available at Tx and Rx ends. The obtained 2D angular map represents a continuous field-amplitude, which needs to be clustered for channel modeling, or for NLOS identification as it is the case in this thesis. In this chapter, we have shown that watershed transformation, which locally reconstructs the gradient field, is more suitable than classical techniques such as the well-known K-mean algorithm to extract illuminated clusters from the dark background and separate the adjacent clusters in the PAS. Furthermore, simulations with the IEEE 802.11ad channel model manifested that watershed segmentation preserves the shapes of clusters. However, the standard K-Power-Means ignores the correlation between adjacent elements and therefore fails to preserve the shape of clusters. To benchmark our watershed-based clustering method, we also proposed a modified K-power-mean algorithm. Here also, it has been found that our proposed method outperforms the K-power-mean algorithm, especially to preserve the shape of the cluster, which is an essential criterion for the NLOS identification that is proposed and investigated in chapter 4.

# References


[1] G. H. Song, J. Brady, and A. Sayeed, “Beamspace Mimo Transceivers for Low-Complexity and near-Optimal Communication at Mm-Wave Frequencies,” *2013 IEEE International Conference on Acoustics, Speech and Signal Processing (Icassp)*, pp. 4394-4398, 2013.

[2] R. M. Haralick, S. R. Sternberg, and X. H. Zhuang, “Image-Analysis Using Mathematical Morphology,” *IEEE Transactions on Pattern Analysis and Machine Intelligence,* vol. 9, no. 4, pp. 532-550, Jul, 1987.

[3] L. Vincent, “Exact Euclidean Distance Function by Chain Propagations,” *1991 IEEE Computer Society Conference on Computer Vision and Pattern Recognition*, pp. 520-525, 1991.

[4] C. Lantuejoul, and S. Beucher, “On the Use of the Geodesic Metric in Image-Analysis,” *Journal of Microscopy-Oxford,* vol. 121, no. Jan, pp. 39-49, 1981.

[5] C. Lantuejoul, and F. Maisonneuve, “Geodesic Methods in Quantitative Image-Analysis,” *Pattern Recognition,* vol. 17, no. 2, pp. 177-187, 1984.

[6] L. Vincent, “Morphological grayscale reconstruction in image analysis: Applications and efficient algorithms,” *IEEE Transactions on Image Processing,* vol. 2, no. 2, pp. 176-201, Apr, 1993.

[7] L. Najman, and H. Talbot, *Mathematical Morphology from Theory to Applications*: iSTE Ltd., 2010.

[8] L. J. Vanvliet, and I. T. Young, “A Nonlinear Laplace Operator as Edge Detector in Noisy Images,” *Computer Vision Graphics and Image Processing,* vol. 45, no. 2, pp. 167-195, Feb, 1989.

[9] S. Beucher, and F. Meyer, *Mathematical Morphology in Image Processing, Chapter 12*: Taylor & Francis Inc., 1993.

[10] S. Beucher, and C. Lantuéjoul, “Use of Watersheds in Contour Detection,” in The International Workshop on Image Processing, Rennes, France, 1979.

[11] N. Otsu, “Threshold Selection Method from Gray-Level Histograms,” *IEEE Transactions on Systems Man and Cybernetics,* vol. 9, no. 1, pp. 62-66, 1979.

# Chapter 4

# Spatial NLOS Identification

## Contents

# 4.1 Introduction

In this chapter, the space-time structure of the channel is used to identify NLOS transmissions. It consists in a 4D space composed of Angle-Of-Arrival (AOA) in elevation ($\theta$) and in azimuth ($\phi$), of excess delay, and power. An example of a channel parameter space created by a realization of the IEEE 802.11ad channel model is shown in Figure 4.1 where power dimension is always represented in a color scale. The azimuth AOA-excess delay-power 3D space in Figure 4.1 (a), the elevation AOA- excess delay -power 3D space in Figure 4.1 (b), and the azimuth AOA-elevation AOA- excess delay -power 4D space in Figure 4.1 (d) illustrate a noticeable spread of parameter points along excess delay direction. However, in spatial evaluation, they are mostly grouped as clusters in the azimuth AOA-elevation AOA 2D space as seen in Figure 4.1 (c). Intuitively, relationship between time and space cannot be observed: the temporal and spatial characteristics look independent from each other. Therefore, it is reasonable to group the clusters spatially, and then to classify different statistical intra-cluster features in time domain, in frequency domain, and in angular domain. Because the beam training strategy searches the highest power links, the space-time structure of the channel is clustered by power as well.

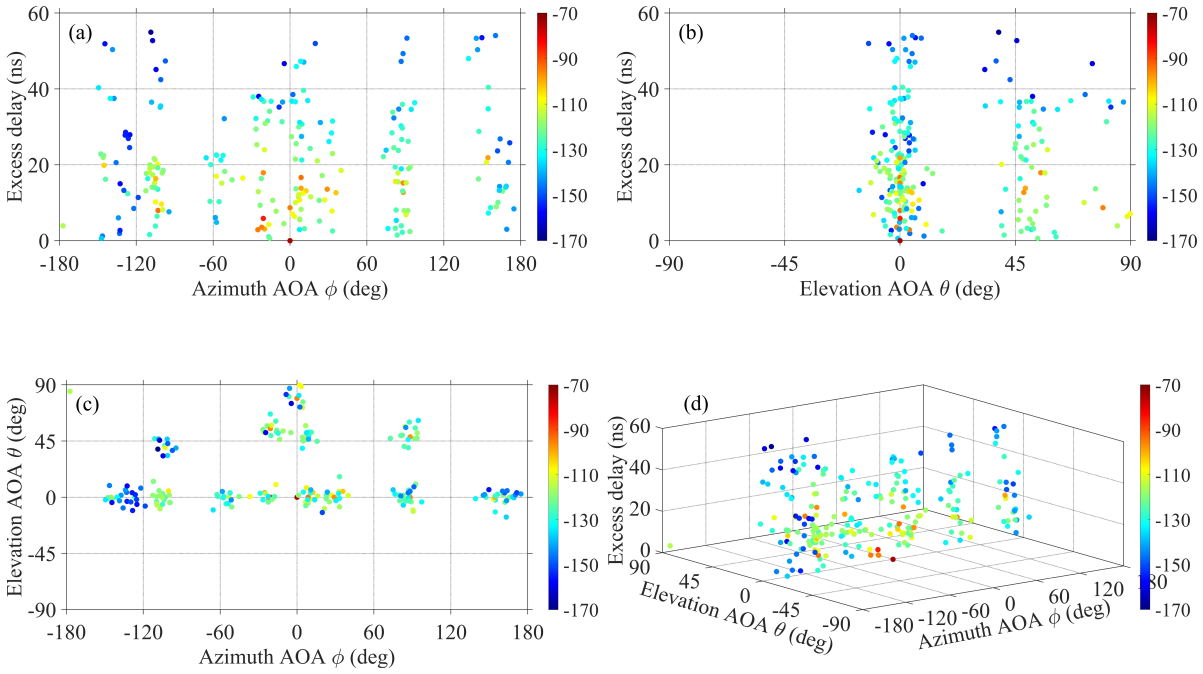


Figure 4.1 Temporo-spatial channel parameter points in (a) azimuth AOA-excess delay, (b) elevation AOA- excess delay, (c) azimuth AOA- elevation AOA and (d) azimuth AOA- elevation AOA - excess delay relations.

The flow of spatial NLOS identification that is investigated in this chapter is shown in Figure 4.2. The PAS is generated with Monte Carlo simulations or actual measurements. If the channel parameter space is discrete (such as obtained with the IEEE 802.11ad channel model), it is clustered with the K-Power-Means algorithm. If the channel parameter space is continuous (such as obtained either with the IEEE 802.11ad channel model convolved with antenna radiation pattern or with measurements), it is clustered with the watershed algorithm. The intra-cluster power/time/frequency kurtosis in spatial domain is introduced as a

useful metric for identifying the type of transmission in this chapter. The statistical features such Probability Density Function (PDF) and Cumulative Distribution Function (CDF) are then fitted with appropriate functions and maximum Likelihood Ratio (MLR) testing and Artificial Neural Network (ANN) are used to classify the types of transmission. The feasibility of the above flow is tested with the IEEE 802.11ad channel model and is then validated with experiments in an actual laboratory scenario.

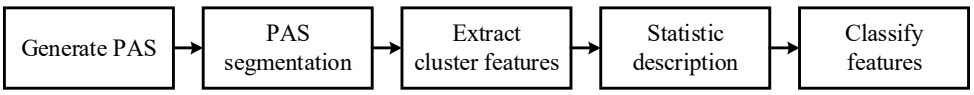


Figure 4.2 Flow of spatial NLOS identification

# 4.2 Methods of Identification

## 4.2.1 Metric of identification

### 4.2.1.1 Features in time and frequency domain

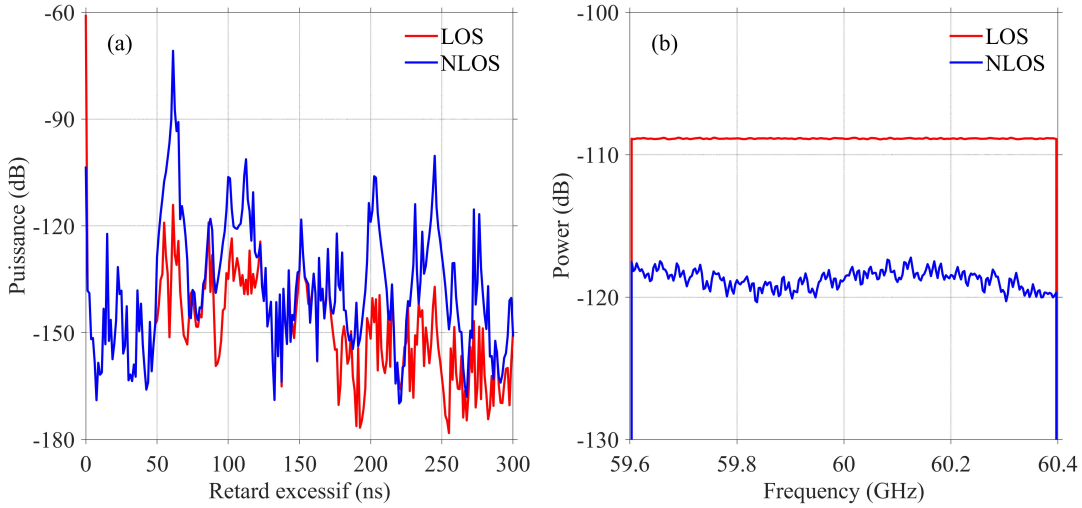


Figure 4.3 (a) CIR and (b) CFR of the LOS and NLOS clusters of PAS generated by the IEEE 802.11ad channel model.

As seen earlier, the LOS transmission cluster can be jointly identified in time and space domains. An example of the Channel Impulse Response (CIR) in power and the Channel Frequency response (CFR) is shown in Figure 4.3. In the time domain, the first peak in the LOS CIR is much stronger than the other peaks. However, the second peak in the NLOS CIR cluster is stronger. In general, the LOS CIR fluctuates less than NLOS CIRs, which implies that the shape of the Probability Density Functions (PDFs) of LOS cluster would be typically narrower than the PDF of NLOS clusters for instance. In the frequency domain,

the selective behavior of the channel can be observed in the CFR. The LOS CFR is flat, while the NLOS CFR exhibits fluctuations. Since the transmission in the IEEE 802.11ad channel modeling was measured in a narrow band of 800 MHz, the frequency selectivity is not very serious. Even so, the coherence of the CFR can still provide useful information regarding NLOS clusters.

So, based on this reflection, the feature we intend to analyze as a possible signature of the channel nature is the power, and more specifically its variation in time, frequency, and later on in angular domain. To do so, the CIR peaks in Figure 4.3 (a) can be characterized with kurtosis, while the frequency fluctuation in the CFR can be identified with the coherence bandwidth. The metrics to identify the above features are a critical issue. The metrics used to identify the types of transmission should intrinsically be able to model the scattering dispersion resulting effects in the CIR/CFR while being independent with respect to the distance between Rx and Tx. The strong CIR peak is a characteristic of LOS transmission in Figure 4.3. However, a strong power peak appears not only in the LOS transmission but also in NLOS transmission at short Rx-Tx distance for instance. Different from the distance-related metrics such as total received energy and excess delay, the standard moment is an intrinsic characteristic independent from the Rx-Tx location. Standard moments are the center moment (higher than 2nd order) normalized by the $k$ power of standard deviation:

$$\frac{E\left[\left(X-\mu_X\right)^k\right]}{\left(\sqrt[2]{E\left[\left(X-\mu_X\right)^2\right]}\right)^k} \tag{4.1}$$

Where $\mu_X$ is the mean of variable $X$. The Kurtosis is the 4-th order standard moment to evaluate the PDF. High order moments are sensitive to the fluctuation of data, while lower order standard moment is more robust. The Kurtosis is the lowest order standard moment. The kurtosis of CIR $h(\tau)$ is:

$$\kappa=\frac{E\left[\left(\left|h(\tau)\right|-\mu_{|h(\tau)|}\right)^4\right]}{E\left[\left(\left|h(\tau)\right|-\mu_{|h(\tau)|}\right)^2\right]^2} \tag{4.2}$$

The kurtosis given in equation (1.40) is therefore the feature that will be used later on to characterize the behavior power in the time domain.

In frequency domain, the selectivity of the CFR $H(f)$ is characterized by the coherence bandwidth. This feature is calculated by the autocorrelation between the frequency transfer function $H(f)$ and itself with a lag of frequency difference $\Delta f$ in frequency domain, within the transmitted bandwidth $B$:

$$R(\Delta f)=\frac{1}{B}\int_0^B\left|H(f)H(f-\Delta f)\right|df \tag{4.3}$$

The coherence bandwidth is then defined as the bandwidth for the first cross-zero point of the above

frequency autocorrelation (4.3) to evaluate the bandwidth over which the channel can be considered flat. However, the direct autocorrelation is weighted by the power level of the received signal. Therefore, the difference between LOS and NLOS is typically not strong as illustrated in Figure 4.4 (a).

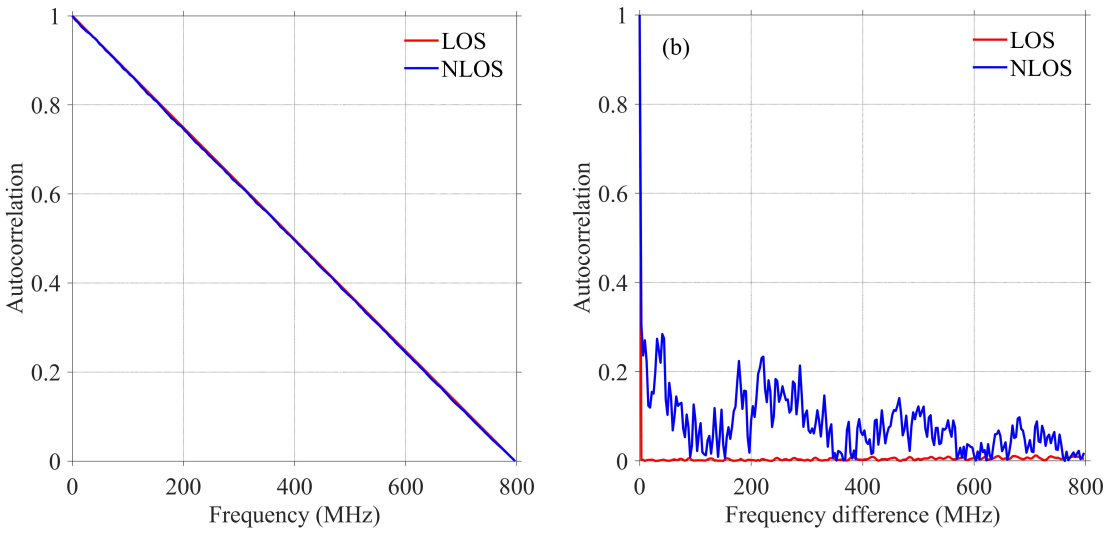


Figure 4.4 Autocorrelation of $H(f)$ (a) with and (b) without mean value

To mitigate the influence of power, the mean value $\mu_H$ of $H(f)$ is first subtracted as:

$$R(\Delta f)=\frac{1}{B}\int_0^B\left|\left(H(f)-\mu_H\right)\left(H(f-\Delta f)-\mu_H\right)\right|df \tag{4.4}$$

With the highly directional antenna pattern, the ideal LOS signal only randomly fast fluctuates because of the thermal noise at the receiver. Therefore, after removing the mean value, the LOS autocorrelation is equal to 1 only when $\Delta f = 0$ and almost vanishes for any other $\Delta f \neq 0$, as shown in Figure 4.4 (b). However, the NLOS signal is resulting from some reflection and scattering process. So its frequency selective behavior is also manifested in the frequency domain as shown in Figure 4.4 (b) with the autocorrelation slow fluctuation. The above difference can be quantified by the average autocorrelation given by (4.5) and will be used as a feature for NLOS identification later on.

$$R_f=\frac{1}{B}\int_0^B R(\Delta f)d\Delta f \tag{4.5}$$

## 4.2.1.2 Feature variations in angular domain

In the angular spatial domain, limited by the capacity of the beam training strategy, the coarse spatial sampling and the limited selectivity of antenna beams make difficult the accurate evaluation of spatial PDF. As an alternative, the shape of the angular clusters in the PAS 2D map is an effective way to investigate the characteristics of the scattering behaviors in LOS or NLOS transmission. A canonical example is shown in

Figure 4.5 where the phenomenon occurring within the channel can be observed on the received PAS within a given cluster (results are obtained with a developed code base on Method-of-Moment as detailed in Annex I). The Tx pattern in the beam training is here omnidirectional while the Rx pattern formed by the antenna array is almost rotational symmetric. In Figure 4.5 (a), the transmitted power pattern is preserved due to the absence of scattering objects in the LOS transmission. Thus, the PAS within this LOS cluster exhibits an almost rotational symmetric, identical to the Rx radiation pattern. However, in Figure 4.5 (b), the PAS is randomly deformed by the stochastically distributed scatterers. Even when reflected by smooth reflectors, NLOS clusters are affected. Indeed, the PAS of a cluster reflected by the curvature of a reflector surface is also deformed as seen in Figure 4.5 (c). This illustrates the motivation of our work. Although the capacity of spatially classifying the clusters is limited by the resolution of beam training, the identification could still be achieved. Consequently, in this chapter, we intend to analyze deeper the clustered PAS features in order to assess their suitability for NLOS identification.

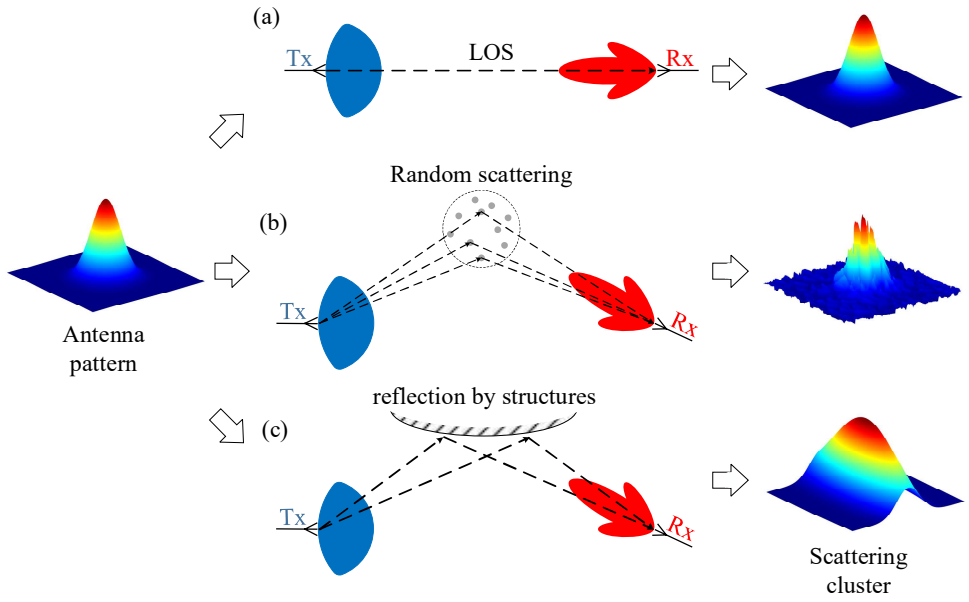


Figure 4.5 Deformation of scattering cluster due to: (a) LOS transmission; (b) random scattering; (c) mirror-like reflection (details regarding the numerical simulations are to be found in Annex I)

After clustering the PAS at the Rx using the method described in chapter 3, cluster shapes in the PAS need to be analyzed using some metrics, similarly to what has been done in the previous section in time and frequency domain. Specifically, we have found that the kurtosis matrix used to evaluate PDF shape in the previous section is also efficient in describing the cluster in the spatial domain such as in Figure 4.5. The stochastic variable $X$ is now the angular coordinate ($\phi$, $\theta$), where $\phi$ is the azimuth angle and $\theta$ is the elevation angle. The probability is substituted by $P(\phi_i, \theta_i)$ which is either the power calculate with (4.6):

$$P(\theta,\phi)=\frac{1}{T}\int_0^T h(\tau,\theta,\phi)\,d\tau \tag{4.6}$$

where $T$ is the channel duration, the time-domain kurtosis (i.e., kurtosis of the CIR, eq. (4.2)), or the frequency autocorrelation (eq. (4.4)) *within* clusters. ($P(\phi_i, \theta_i)$ is obtained from the channel when the

antenna beam is directed towards the angle ($\phi_i$, $\theta_i$), but ray contributions within the whole beam are naturally taken into account to determine the features). Because of 2D angular space, the shape of a cluster is evaluated with a $P$ (power, time kurtosis or frequency autocorrelation)-weighted co-kurtosis matrix:

$$\Sigma_k = \begin{bmatrix} k_{11}(\phi,\phi) & k_{12}(\phi,\theta) \\ k_{21}(\theta,\phi) & k_{22}(\theta,\theta) \end{bmatrix} \tag{4.7}$$

Where the elements $k_{ij}$ are the weighted co-kurtosis with respect to azimuth and elevation angles:

$$k_{11} = \frac{\sum \left(\phi_i - \bar{\phi}_i\right)^2 \left(\phi_i - \bar{\phi}_i\right)^2 P(\phi_i,\phi_i)}{\sum P(\phi_i,\phi_i)} / \sigma_{11}^2 \tag{4.8}$$

$$k_{12} = k_{21} = \frac{\sum \left(\phi_i - \bar{\phi}_i\right)^2 \left(\theta_i - \bar{\theta}_i\right)^2 P(\phi_i,\theta_i)}{\sum P(\phi_i,\theta_i)} / \sigma_{12}^2 \tag{4.9}$$

$$k_{22} = \frac{\sum \left(\theta_i - \bar{\theta}_i\right)^2 \left(\theta_i - \bar{\theta}_i\right)^2 P(\theta_i,\theta_i)}{\sum P(\theta_i,\theta_i)} / \sigma_{22}^2 \tag{4.10}$$

with $\sigma$ is the azimuth or elevation standard deviation weighted with $P$ being either power, time-domain kurtosis, or frequency autocorrelation:

$$\sigma_{11} = \frac{\sum \left(\phi_i - \bar{\phi}_i\right)\left(\phi_i - \bar{\phi}_i\right) P(\phi_i,\phi_i)}{\sum P(\phi_i,\phi_i)} \tag{4.11}$$

$$\sigma_{12} = \sigma_{21} = \frac{\sum \left(\phi_i - \bar{\phi}_i\right)\left(\theta_i - \bar{\theta}_i\right) P(\phi_i,\theta_i)}{\sum P(\phi_i,\theta_i)} \tag{4.12}$$

$$\sigma_{22} = \frac{\sum \left(\theta_i - \bar{\theta}_i\right)\left(\theta_i - \bar{\theta}_i\right) P(\theta_i,\theta_i)}{\sum P(\theta_i,\theta_i)} \tag{4.13}$$

The weighted symmetry is an interesting feature to represent the shape of clusters. The ratio of minimum and maximum eigenvalues (principal component analysis) of the co-kurtosis matrix can be used to characterize the spatial symmetry of the kurtosis of the different clusters' features $P$. The principal component analysis is performed by calculating the ratio $\hat{R}$ of the minimum over the maximum eigenvalues through the decomposition of the co-kurtosis matrix (4.7) as:

$$\Sigma_k = \left[\boldsymbol{P}_1 \boldsymbol{P}_2\right] \begin{bmatrix} \lambda_1 & 0 \\ 0 & \lambda_2 \end{bmatrix} \left[\boldsymbol{P}_1 \boldsymbol{P}_2\right]^{-1} \tag{4.14}$$

where $\lambda_1$ and $\lambda_2$ are the two eigenvalues with the corresponding eigenvectors $\boldsymbol{P}_1$ and $\boldsymbol{P}_2$.

## 4.2.2 Methods of Feature classification

In our work, three features can describe a PAS, namely, the power matrix eigen ratio $\hat{R}_P$, the time-domain kurtosis matrix eigen ratio $\hat{R}_t$, and the frequency autocorrelation matrix eigen ratio $\hat{R}_f$. Therefore, the features construct a data point ($\hat{R}_P$, $\hat{R}_t$, $\hat{R}_f$) or each cluster in the parameter space. Since LOS transmission are beneficial for localization, it is therefore defined as the null hypothesis, $H_0$, of the hypothesis testing, while the alternative hypothesis, $H_1$, is the NLOS transmission:

$$\begin{aligned} H_0&: \text{ LOS transmission with features } \hat{R}_P^{los}, \hat{R}_t^{los} \text{ and } \hat{R}_f^{los} \\ H_1&: \text{ NLOS transmission with features } \hat{R}_P^{nlos}, \hat{R}_t^{nlos} \text{ and } \hat{R}_f^{nlos} \end{aligned} \tag{4.15}$$

### 4.2.2.1 Maximum Likelihood Ratio testing

Two classifiers are investigated for hypothesis testing: Maximum Likelihood Ratio (MLR) testing and Artificial Neural Network (ANN). The aim of MLR is testing the probability distribution from which the likelihood of the observations is sampled. Therefore, the features are generally evaluated by the probability density function $f(R \mid \boldsymbol{\theta}^{los})$ and $f(R \mid \boldsymbol{\theta}^{nlos})$ with parameter vectors $\boldsymbol{\theta}^{los}$ and $\boldsymbol{\theta}^{nlos}$, and the hypotheses in (4.15) are adjusted to:

$$\begin{aligned} H_0&: \hat{R}_P \sim f^{los}\left(R_P \mid \boldsymbol{\theta}_P^{los}\right), \quad \hat{R}_t \sim f^{los}\left(R_t \mid \boldsymbol{\theta}_t^{los}\right), \quad \hat{R}_f \sim f^{los}\left(R_f \mid \boldsymbol{\theta}_f^{los}\right), \text{ LOS} \\ H_1&: \hat{R}_P \sim f^{nlos}\left(R_P \mid \boldsymbol{\theta}_P^{nlos}\right), \quad \hat{R}_t \sim f^{nlos}\left(R_t \mid \boldsymbol{\theta}_t^{nlos}\right), \quad \hat{R}_f \sim f^{nlos}\left(R_f \mid \boldsymbol{\theta}_f^{nlos}\right), \text{ NLOS} \end{aligned} \tag{4.16}$$

With the estimated parameters, the likelihood ratio of certain distribution of the eigen value ratio ($\hat{R}_P$, $\hat{R}_t$, $\hat{R}_f$) with the condition of distribution parameter $\boldsymbol{\theta}$ for the testing cluster feature $\hat{x}$ is

$$L\left(\hat{x}\right) = \frac{\mathcal{L}\left(\hat{\boldsymbol{\theta}}^{los}; \hat{x}\right)}{\mathcal{L}\left(\hat{\boldsymbol{\theta}}^{nlos}; \hat{x}\right)} \underset{H_1}{\overset{H_0}{\gtrless}} 1 \tag{4.17}$$

Where, $\mathcal{L}(\hat{\theta}; \hat{x})$ is a likelihood function. The parameter vector of the likelihood functions, $\hat{\theta}$, is the one optimized by maximum likelihood estimation. Therefore, the joint likelihood ratio of power matrix eigen ratio $\hat{R}_P$, temporal kurtosis matrix eigen ratio $\hat{R}_t$, and frequency autocorrelation matrix eigen ratio $\hat{R}_f$ is given by:

$$L\left(\hat{R}_P,\hat{R}_t,\hat{R}_f\right)=\frac{\mathcal{L}\left(\hat{\boldsymbol{\theta}}_P^{los};\hat{R}_P\right)}{\mathcal{L}\left(\hat{\boldsymbol{\theta}}_P^{nlos};\hat{R}_P\right)}\times\frac{\mathcal{L}\left(\hat{\boldsymbol{\theta}}_t^{los};\hat{R}_t\right)}{\mathcal{L}\left(\hat{\boldsymbol{\theta}}_t^{nlos};\hat{R}_t\right)}\times\frac{\mathcal{L}\left(\hat{\boldsymbol{\theta}}_f^{los};\hat{R}_f\right)}{\mathcal{L}\left(\hat{\boldsymbol{\theta}}_f^{nlos};\hat{R}_f\right)}\underset{H_1}{\overset{H_0}{\gtrless}}1 \tag{4.18}$$

### 4.2.2.2 Artificial Neural Network

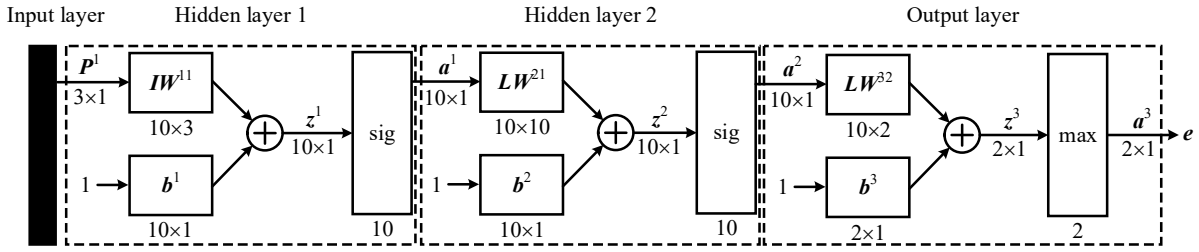


Figure 4.6 Architecture of the Artificial Neural Network used for NLOS identification

The second method to classify the features is ANN. The ANN for NLOS identification is constructed with one input layer, two hidden layers, and one output layer, as shown in Figure 4.6. In general, the output vector of the ($k$+1)-th layer $\boldsymbol{a}^{k+1}$ is a linear transfer of the input vector from the ($k$)-th layer $\boldsymbol{a}^k$, then modulated by an activation function $f$:

$$\boldsymbol{a}^{k+1}=f\left(\boldsymbol{W}^{k+1,k}\boldsymbol{a}^k+\boldsymbol{b}^k\right) \tag{4.19}$$

Specific to the ANN in Figure 4.6, the whole network can be expressed as:

$$\boldsymbol{a}^3=sig\left(\boldsymbol{LW}^{32}\cdot sig\left(\boldsymbol{LW}^{21}\cdot sig\left(\boldsymbol{IW}^{21}\boldsymbol{P}^1+\boldsymbol{b}^1\right)+\boldsymbol{b}^2\right)+\boldsymbol{b}^3\right) \tag{4.20}$$

The input is the parameter vector $\boldsymbol{P}^1 = [\hat{R}_P,\ \hat{R}_t,\ \hat{R}_f]^T$. There are ten neurons in all the hidden layers. The input matrix in the first hidden layer $\boldsymbol{IW}^{11}$ is a 10×3 matrix. The 10×10 matrix $\boldsymbol{LW}^{21}$ in the hidden layer and 10×2 matrix $\boldsymbol{LW}^{32}$ in the output layer are the weight matrices. $\boldsymbol{b}^1$, $\boldsymbol{b}^2$ and $\boldsymbol{b}^3$ are the bias vectors in the layer 1, 2, and 3, respectively. An activation function maps the input set to an output set. For null hypothesis testing, the output set of the whole network ought to be {-1, 1}, while the output of the linear weighted combination part is a real set. Therefore, the activation of output is a map $\mathbb{R} \rightarrow$ {-1, 1}. The simplest activation function is a step function. But the step function induces a singularity at the origin and underivative. To avoid this issue, the activation functions in the hidden layers are both nonlinear tangent sigmoid function $sig(x) = 2 / (1 + e^{-2x}) - 1$ whose curve is plotted in Figure 4.7. The curve linearly increases in the range of [-1, 1], while approximately being constant to +1 at the top bound and to -1 at the bottom bound. The activation function of the output layer is a normalization function $sig(x) = \exp(x) / \sum\exp(x)$. It proportionally maps an input vector into a range of [0, 1]. The normalization function makes the output label of ANN into a hypothesis testing result in the range $a^3 \in [0, 1]$.

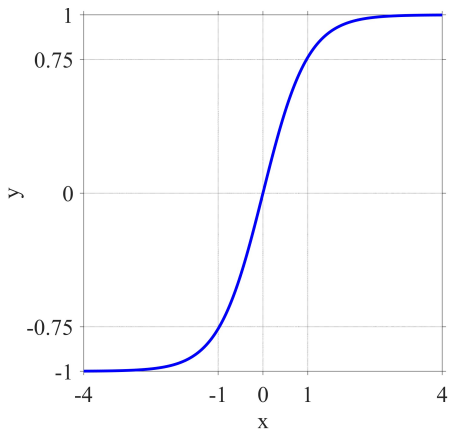


Figure 4.7 Tangent sigmoid function

ANN training aims to optimize the weight matrices in order to minimize the error between the training result $\boldsymbol{a}^3$ and the label $\boldsymbol{y}$:

$$\boldsymbol{e} = \left( \boldsymbol{y} - \boldsymbol{a}^3 \right)^2 \tag{4.21}$$

To achieve the above aim, a training process of ANN is implemented with the back-propagation algorithm [6]: the error propagates from the output back the input to optimize the weight matrices so that reaching an error threshold. The $i$-th output and bias at the $k$-th layer are $a_i^k$ and $b_i^k$, with a weight factor $w_{ij}^k$ to evaluate the input from the $j$-th neuron $a_j$. Then, the element of (4.19) in every layer is:

$$a_i^k = sig\left( w_{ij}^k a_j^{k-1} + b_i^k \right) \tag{4.22}$$

The iteration updates the weight $w_{ij}^k$ towards the direction of error gradient for the weight $w_{ij}^k$

$$w_{ij}^{k+1} = w_{ij}^k + \frac{\partial e_i^k}{\partial w_{ij}^k} \tag{4.23}$$

The gradient is

$$\frac{\partial e_i^k}{\partial w_{ij}^k} = \frac{\partial e_i^k}{\partial a_i^k} \frac{\partial a_i^k}{\partial z_i^k} \frac{\partial z_i^k}{\partial w_{ij}^k} = 2a_i^{k-1} \left[ sig'\left( y_i - a_i^k \right) \right] \left( y_i - a_i^k \right) \tag{4.24}$$

Where $sig'(x)$ is the derivative of the tangent sigmoid function:

$$sig'(x) = \frac{4\exp(-2x)}{\left[ 1 + \exp(-2x) \right]^2} \tag{4.25}$$

The training starts to iterate at an initial condition of uniform distributed $w_{ij}^{k}$, and achieve convergence when it matches the converging condition. There are two converging conditions in training: the cross-entropy constraint that $-\sum a^3 \cdot \log(y) < 0.1$, or reaching the maximum iterative number 1000. ANN repeats 20 pieces of training to avoid the local minima in the optimization process. Those numbers are empirically chosen.

# 4.3 Numerical simulation

With the channel model of IEEE 802.11ad, the feasibility of NLOS identification is tested. As a first validation step, the NLOS identification methodology is firstly implemented directly on the discrete data obtained by the IEEE 802.11ad channel model using the angular variations of the power feature only. Then, as a second step, the Rx PAS is obtained by convolving the discrete channel angular response with the antenna pattern. The NLOS identification is then applied on these PAS by analyzing the angular variations of all three features, namely, the power, the time-domain kurtosis (i.e., kurtosis of the CIR), and the frequency autocorrelation.

## 4.3.1 Identification on clustered discrete channel angular response

The clusters nature is here evaluated using the angular variations of the power feature using the discrete channel response created by the IEEE 802.11ad channel model. First, the channel needs to be grouped angularly into clusters. An implementation example of a clustered two-dimensional discrete angular power distribution map is shown in Figure 4.8. Clustering is achieved by the standard K-Power-Means method. Four scenarios are considered in the model: a conference scenario where the Rx and Tx antennas are placed on a table, a conference scenario where a Rx antenna is arranged on a table and Tx antenna is suspended from the ceiling, a working cubicle scenario in an office, and a living room scenario. In the working cubicle scenario, the Rx is the laptop placed on a working desk, while the Tx is hanging from the ceiling. In the living room scenario, the Rx is placed on a TV set against a wall, while the Tx is randomly placed in the central region of the living room. The LOS component, indicated by an arrow in the figures, is generated by a single ray in the channel model. Different multipath clusters are labeled with distinguishable markers. The clusters grouped by the k-means algorithm are represented by the different colors. One obvious result is that the clusters grouped by K-Power-Means are not precisely the same as the channel model generated clusters. Notably, the points arrowed in (a) to (d) in Figure 4.8 are the direct paths generated by the channel model. The direct paths are grouped into LOS clusters with nearby indirect paths by K-Power-Means. Furthermore, when NLOS clusters are close to each other, the K-Power-Means algorithm cannot distinguish them and will be therefore treated as a single cluster in the following LOS/NLOS kurtosis calculation. The above inconsistency comes from the nature of the cluster-based channel model and cluster grouping method. As discussed in chapter 1 and 3, the channel model generates clusters according to statistical distribution without considering the correlation among the elements inside a cluster. Unfortunately, the connections between adjacent elements are also neglected by searching the local minima of the distance between the centroid and the elements inside each cluster with

K-Power-Means presented in chapter 2. It especially makes the direct path location arbitrary within the LOS cluster, instead of at the center of the cluster. It influences the statistical symmetry of the cluster to be estimated and will ultimately affect the performance of LOS/NLOS identification.

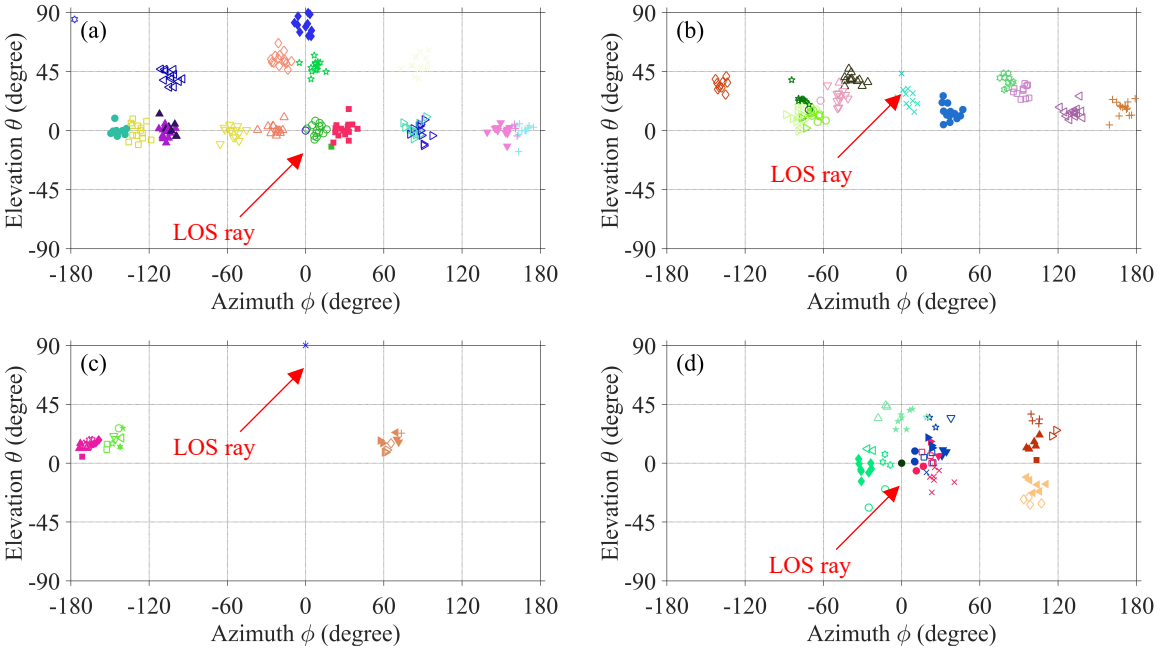


Figure 4.8 AOA clustering (different colors) using k-means algorithm: (a) conference scenario with 2 antennas on a table; (b) conference scenario with Rx antenna on a table and Tx antenna hanging from the ceiling; (c) working cubicle scenario; (d) living room scenario.

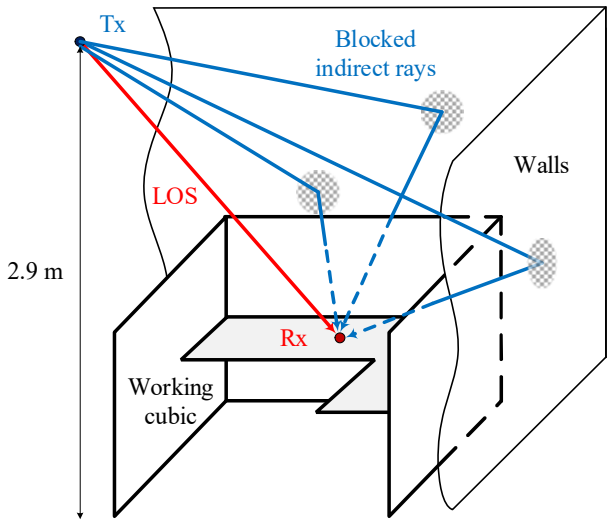


Figure 4.9 Schematic diagram of LOS and NLOS rays blocked by the working cubic

According to 1.4.3 in chapter 1, the clustering results in Figure 4.8 (a) and (b) are based on an hybrid model of intercluster distribution simulated by ray-tracing and measured intracluster distribution in a conference room, which is relatively empty compared to the other two scenarios in the model. The

distributions are illustrated in 3.3.1 chapter 3. The sparse furniture allows the wave propagating over a long distance with few obstructions so that reflections are more likely to occur on the walls and the ceiling. Because the walls and ceiling enclosed the entire indoor space, the reflection is uniformly distributed, instead of being selective towards any particular directions. Therefore, clusters and ray components inside them are both abundant and spread widely in the upper-half space (the table blocks the reflection paths in the lower half-space). However, the spatial arrangements in scenarios in Figure 4.8 (c) and Figure 4.8 (d) are different. In the working cubic scenario, the Tx is hung under the ceiling, so the LOS path is at 90° elevation angle. The working cubic almost surrounds the laptop Rx so it will most likely block the indirect paths, as shown in Figure 4.9. Thereby the number of clusters reduces as in Figure 4.8 (c). In the living room, the furniture and appliances exist almost everywhere. On the one hand, small objects massively diffuse the wave in all directions, meanwhile, on the other hand, large reflectors partition the space and obstructs the path scatted from other directions. Therefore, the clusters in Figure 4.8 (d) concentrate within a particular domain.

Based on the above clustered results, the power kurtosis is calculated to evaluate the shape of these clusters, i.e., using (4.7) to (4.13) with $P(\theta_i, \phi_i)$ being the channel power for a given direction $(\theta_i, \phi_i)$. PDF and Cumulative Distribution Function (CDF) results of the eigenvalue-ratio of the kurtosis matrix as (4.14) determined from angular clusters are shown in Figure 4.11. They statistically describe the symmetry of the cluster shapes. When the ratio close to 1, the kurtosis of the cluster shape is more symmetric between elevation and azimuth planes. From Figure 4.11, it can be observed that LOS clusters are much less symmetric than NLOS clusters as the ratio of minimum over maximum eigenvalues is statistically much larger in the LOS case than in the NLOS case. This result comes from the clustering method itself rather than from the physical phenomenon involved in the channel. Indeed, as discussed in chapter 3, K-Power-Means does not consider the correlation between adjacent elements. So instead of being fixed at the cluster center, the direct ray can be randomly assigned into a cluster with any indirect ray component. In general, the intensity of the direct ray in LOS clusters is much stronger than indirect rays. When the direct ray is being located at the edge of a LOS cluster by K-Power-Means, the power-weighted kurtosis becomes very large. The bias in the kurtosis matrix becomes therefore significant. After randomly initializing the centroids by kmeans++, the K-Power-Means searches for the local minima of each cluster but ignores the correlation between the elements inside clusters. After clustering, the positions of the direct ray inside the LOS cluster are much different: if it is at the center of the cluster in Figure 4.10 (a), the similarity of LOS cluster will be very high; otherwise, when it is at the edge in Figure 4.10 (b), the cluster is asymmetrical.

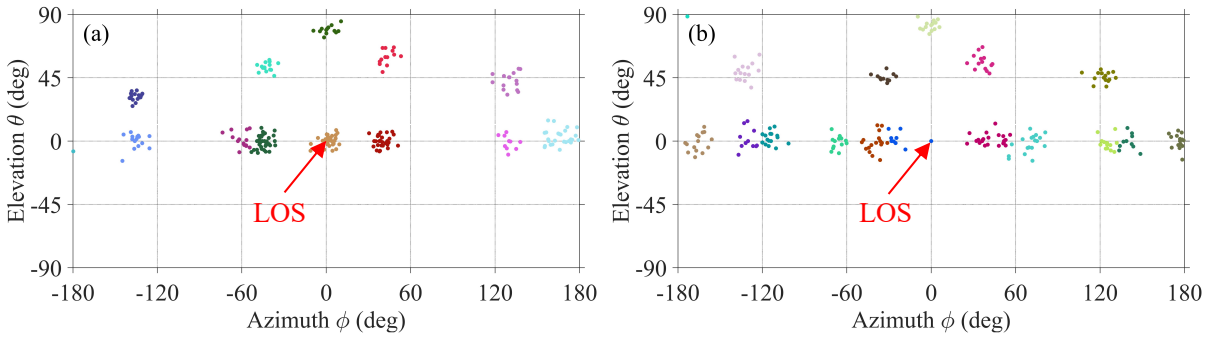


Figure 4.10 Direct ray clustered at (a) center and (b) edge of LOS clusters

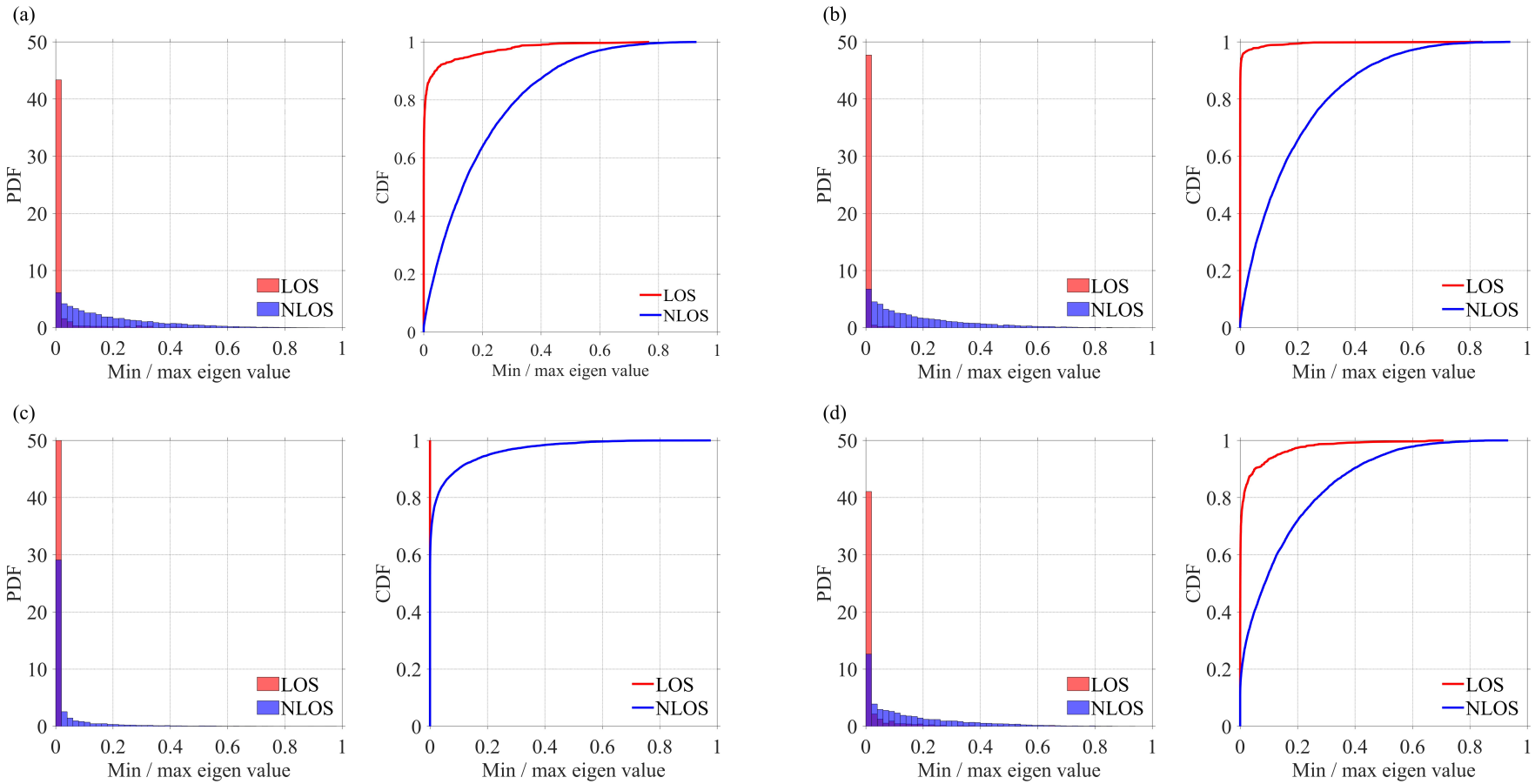


Figure 4.11 PDF and CDF of Ratios of minimum over maximum eigenvalues: (a) conference scenario with 2 antennas on a table; (b) conference scenario with Rx antenna on a table and the Tx antenna is hanging from the ceiling; (c) working cubicle scenario; (d) living room scenario.

So, if the direct path cannot be hold at the center in order to preserve the shape of the cluster, the clusters are statistically biased. From the statistical results of 250 samples, the clustering algorithm, by not preserving the shapes of clusters, causes the biases to be random. Thus, LOS clusters statistically exhibit weak symmetry. For instance, in the first scenario (Figure 4.11 (a)), there is a 90% probability that the min/max ratio is less than 0.02 for LOS clusters, while the probability is only 12.5% for NLOS clusters. According to the above discussion, K-Power-Means has difficulty to maintain the shapes of clusters. In the conference scenario, a higher LOS ratio than NLOS ratios in Figure 4.11 (a) and (b) manifest higher asymmetricity in LOS kurtosis than in NLOS kurtosis. The relative empty conference room makes the scattering in this scenario caused mainly by the reflection on the surfaces of the walls and ceiling. The shape of the cluster is mainly formed by the layered structure and roughness of the wall surfaces. The geometric features of the layered and roughness reflectors are irregular, therefore scattering inside clusters is uniform. In this case, the kurtosis of the corresponding NLOS clusters is stochastic as well. Besides, the sparse furniture makes the clusters spread widely and abundantly distributed, which further disperses the distribution of NLOS clusters. The above factors make the NLOS clusters more symmetrical than the LOS clusters. In contrast, in the office scenario, working cubicles obstructs most reflection paths. The rays diffused by the edges of the working cubicles contribute to the main components inside clusters. The diffracting rays are directionally selective, which aggravates the bias of the NLOS kurtosis matrix. Therefore, the asymmetry of the NLOS clusters is more similar to that of LOS clusters in Figure 4.11 (c). Similar to the office scenario, in the living room, NLOS clusters carry more regular geometric information about objects. The large obstructers partition the space and filter the NLOS clusters in further, which intensify the geometry selective of NLOS clusters. Therefore, the NLOS clusters are more asymmetric, as shown in Figure 4.11 (d). This analysis further justifies to study the NLOS identification based directly on the PAS rather than on the discrete angular channel response.

### 4.3.2 Identification on PAS

The NLOS identification based on the PAS follows the flow-chart given in Figure 4.2. The PAS is firstly obtained by convolving the discrete IEEE 802.11ad channel with antenna radiation pattern. The PAS is then segmented with the watershed algorithm. The cluster features are then extracted and statistically described in order to finally identify whether a cluster is LOS or NLOS.

Monte Carlo simulations are performed to obtain sufficient amount of data for a statistical description of the performance. The scenario is as per as the beam training strategy described in the section 1.4.5 of chapter 1: the Tx antenna is omnidirectional, while the directional Rx antenna rotates across the whole angular space. The scanning step is $1^{o}$. The beam pattern of the antenna model is a single main lobe with a symmetric Gaussian shape, in order to evaluate the deformation of the cluster by the scattering. The half-power beamwidth of the Rx antenna is taken as $5^{o}$ (this value is chosen to allow for comparison with the actual antenna used in the measurement in the next section). An oversampling factor of 8 is used in the IEEE 802.11ad channel model generation to increase the time resolution. 250 simulations are typically realized, unless otherwise stated, which take approximately 7 hours on a computer with a 4 core CPU 3.4 GHz (only to generate the channels).

### 4.3.2.1 Power angular clustering

An example of 5º-HPBW PAS clustered with the watershed algorithm is shown in Figure 4.12. The continuous PAS corresponds to the channels in the different scenarios in Figure 4.8. The results of continuous clusters segmented by watersheds are different from the discrete clustering results by K-Power-Means. One reason is that, due to the channel spatial convolution by the beam pattern, the positions of the PAS clusters are different from the discrete channel. The other reason is the difference between the two clustering algorithms: K-Power-Means is influenced by the random initial condition, while, the watershed is relative deterministic.

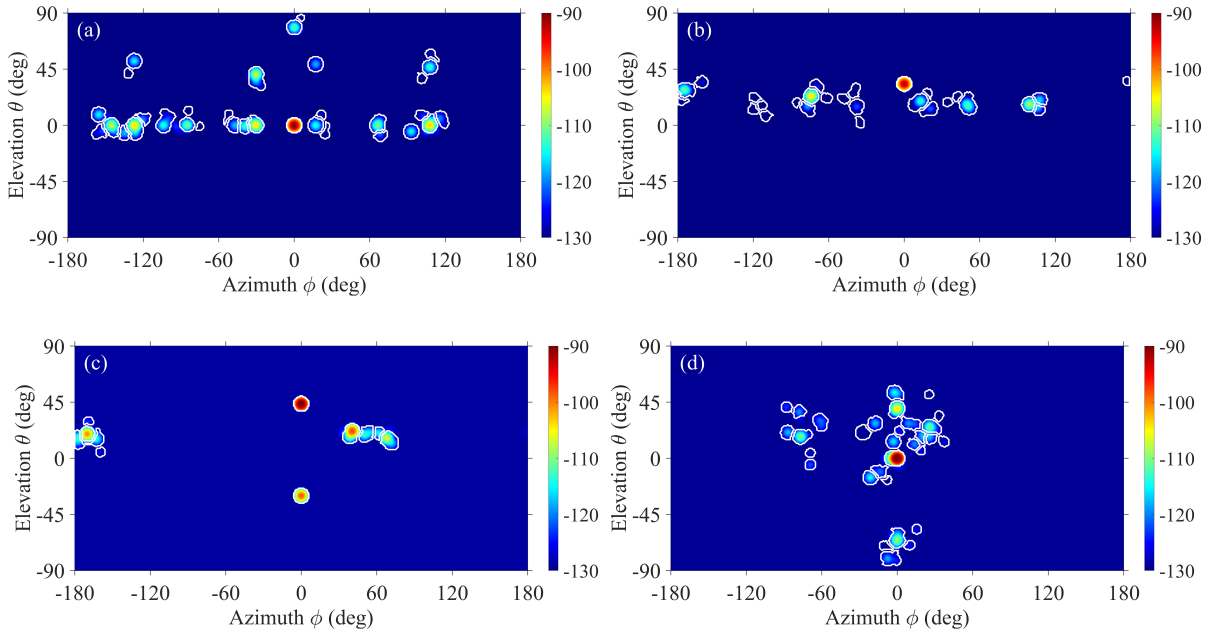


Figure 4.12 5º-HPBW PAS (in dB) clustering using watershed algorithm: (a) conference scenario with 2 antennas on a table; (b) conference scenario with Rx antenna on a table and Tx antenna hanging from the ceiling; (c) working cubicle scenario; (d) living room scenario.

### 4.3.2.2 Statistical characteristics inside a cluster

#### 4.3.2.2.1 Statistical features extraction procedure

Firstly, the statistical features of the minimum eigenvalue over the maximum eigenvalue ratio in PAS clusters are described with PDF and CDF. The sample-set is constructed with 250 simulation implementations sampled by the Monte Carlo method, repeated for four different indoor scenarios in the IEEE 802.11ad channel model, namely, conference scenario with 2 antennas on a table, conference scenario with Rx antenna on a table and Tx antenna is hanging from the ceiling, working cubicle scenario, and living room scenario.

Secondly, the PDF and CDF are then fitted with Beta distributions in order to obtain reference parameters that will be used for classification in the next section. To be consistent with the min/max eigen value ratio range from 0 to 1, the PDF of Beta distribution is defined within an interval [0, 1]. The PDF of Beta distribution [7] is a normalized linear combination of two power functions with two decisive parameters:

$$f_B\left(x \mid a,b\right)=\frac{x^{a-1}\left(1-x\right)^{b-1}}{\int_0^1 x^{a-1}\left(1-x\right)^{b-1}\,dx}=\frac{1}{B\left(a,b\right)}x^{a-1}\left(1-x\right)^{b-1} \tag{4.26}$$

Where $B(a, b)$ is the Beta function expressed as:

$$B\left(a,b\right)=\int_0^1 t^{a-1}\left(1-t\right)^{b-1}\,dt \tag{4.27}$$

The parameters $a$ and $b$ are obtained with maximum likelihood estimation. The log-likelihood function of Beta distribution for $N$ *i.i.d.* samples ($x_1, x_2 \ldots x_N$) is:

$$\begin{aligned}\ln \mathcal{L}_B\left(a,b;x\right)&=\sum_{i=1}^{N}\ln \mathcal{L}_{Bi}\left(a,b;x_i\right)\\&=\left(a-1\right)\sum_{i=1}^{N}\ln x_i+\left(b-1\right)\sum_{i=1}^{N}\ln\left(1-x_i\right)-N\ln B\left(a,b\right)\end{aligned} \tag{4.28}$$

Then, the maxima of likelihood function are estimated as the zero point of the first order deviation with respect to the parameters $a$ and $b$:

$$\frac{\partial \ln \mathcal{L}_B\left(a,b;x\right)}{\partial a}=\sum_{i=1}^{N}\ln x_i+N\left[\varphi\left(a+b\right)-\varphi\left(a\right)\right]=0 \tag{4.29}$$

$$\frac{\partial \ln \mathcal{L}_B\left(a,b;x\right)}{\partial b}=\sum_{i=1}^{N}\ln\left(1-x_i\right)+N\left[\varphi\left(a+b\right)-\varphi\left(b\right)\right]=0 \tag{4.30}$$

Where $\varphi(\alpha)$ is the digamma function, defined as the logarithmic derivative of the gamma function $\Gamma(a)$:

$$\varphi\left(a\right)=\frac{\partial \ln \Gamma\left(a\right)}{\partial a} \tag{4.31}$$

Considering an approximation of $\varphi(\hat{a}) \approx \ln(\hat{a} - 0.5)$ with an assumption that a and b are not too small, the parameters can be estimated [7] by the measured samples $\hat{x}$ to maximize the likelihood function with (4.29) and (4.30) [2]:

$$\hat{a} \approx \frac{\frac{1}{2}\left[1-\prod_{i=1}^{N}(1-\hat{x}_i)^{\frac{1}{N}}\right]}{1-\prod_{i=1}^{N}(\hat{x}_i)^{\frac{1}{N}}-\prod_{i=1}^{N}(1-\hat{x}_i)^{\frac{1}{N}}} \tag{4.32}$$

$$\hat{b} \approx \frac{\frac{1}{2}\left[1-\prod_{i=1}^{N}(\hat{x}_i)^{\frac{1}{N}}\right]}{1-\prod_{i=1}^{N}(\hat{x}_i)^{\frac{1}{N}}-\prod_{i=1}^{N}(1-\hat{x}_i)^{\frac{1}{N}}} \tag{4.33}$$

The general fit goodness is tested with Kolmogorov–Smirnov testing. Kolmogorov–Smirnov testing is a robust hypothesis testing with a null hypothesis that the two sets of data are sampled from the same distribution. The principle of Kolmogorov–Smirnov testing evaluates the maximum distance $D$ between the empirical CDF $F_n(x)$ of sample sets and the target statistical model CDF $F(x)$ [8] :

$$D = \sup_x \left| F_n(x) - F(x) \right| \tag{4.34}$$

According to law of large numbers, no matter specific $F(x)$, if $F(x)$ is continuous and the sampling number $n$ goes to infinite, $G(x) = | F_n(x) - F(x) |$ becomes a Weiner process. Notice the random variable $| F_n(x) - F(x) | \in [0, 1]$, therefore $G(x)$ is notated with a Brownian bridge $B(t)$: $\{W_t \mid W_0 = W_T = 0, t \in [0, T]\}$ (a Weiner process $W_t$ in the range of [0, 1] and with a constraint of zero $W_0 = 0$ and $W_T = 0$ at the ends of the time series $t = 0$ and $t = T$). Then, the maximum distance is:

$$D = \lim_{n\to\infty} \sqrt{n} D_n = \sup_x \left| B\left(F(x)\right) \right| \tag{4.35}$$

The supremum of Brownian bridge is with Kolmogorov–Smirnov distribution. The CDF of Kolmogorov–Smirnov distribution is:

$$CDF(d) = P(D_n \le d) = 1 - 2\sum_{n=1}^{\infty}(-1)^{n-1}\exp\left(-2n^2d^2\right) \tag{4.36}$$

Which can be approximately by [9].

$$P(D_n \le d) = \frac{n!}{n^n} t_{kk},\ t_{kk} \text{ is the element of matrix } T = H^n \tag{4.37}$$

$$H = \begin{bmatrix} \left(1-h^1\right)/1! & 1 & \cdots & 0 \\ \left(1-h^2\right)/2! & \left(1-h^1\right)/1! & \cdots & 0 \\ \vdots & \vdots & \ddots & \vdots \\ \left(1-h^n\right)/n! & \left(1-h^{1-n}\right)/(1-n)! & \cdots & \left(1-h^1\right)/1! \end{bmatrix} \tag{4.38}$$

Where $h \in [0, 1]$. Therefore, the evaluation of fitting goodness becomes a hypothesis testing with the maximum distance following the Kolmogorov–Smirnov distribution.

#### 4.3.2.2.2 Angular behavior of power features

The statistical features of the minimum eigenvalue over the maximum eigenvalue ratio in PAS clusters are shown in the Figure 4.13. Both PDF and CDF from Monte Carlo simulations and Beta distributions from fitting approach can be observed. A fair agreement exists between Monte Carlo results and Beta distributions for all scenarios, especially on PDF curves and on NLOS CDF. A good agreement is more difficult to obtain for LOS curves that are relatively discontinuous. It can be qualitatively observed here that the LOS clusters exhibit a large symmetry in all scenarios as the PDFs tend to rapidly grow when the min/max eigen value ratios reach 1. In particular, it is observed that 90 % of the min/max eigen value ratios in LOS transmission are concentrated in a range from 0.5 to 1. For NLOS clusters, PDFs appear more uniformly distributed and that there is no specific tendency for min/max eigen value ratios to be equal to 1. This shows that NLOS clusters exhibit statistically less symmetry. The LOS cluster behavior is also observed in the LOS CDF curves, where an exponential-like increase occurs as ratios get close to 1. The wide min/max eigen value ratios spread observed in the NLOS PDF is represented by the almost linear behavior of the NLOS CDF curves. These results mean that, as expected, statistically, the LOS clusters preserve the symmetry of the antenna pattern while the shapes of NLOS clusters are stochastically deformed by the random scattering. Also, the LOS and NLOS CDF curves are clearly separated from each other in all of the four scenarios which indicates that it is a promising indicator for LOS/NLOS discrimination. The symmetries (b) and (c) are slightly more preserved than the other two scenarios. The Tx antennas in (b) and (c) hang from the ceiling and are therefore much higher than surrounding scattering objects. Hence the LOS transmission is less influenced by the scattering in the environment. In contrast, in the living room ((d)), the LOS transmission is more likely influenced by many scattering objects. For this reason, the symmetry of LOS clusters in the living room is weaker than others.

#### 4.3.2.2.3 Angular behavior of time-domain kurtosis feature

The statistical ratios of time-domain kurtosis matrix and Beta distribution-fitted curves are shown in Figure 4.14. It is the PDF and CDF sampled by the Monte Carlo method, and fitted curve with the Beta distribution of LOS and NLOS transmission: minimum eigenvalue over maximum eigenvalue ratio of power kurtosis matrix. Different from the power matrix ratio, here 90% of the ratios are generally within a narrow range from 0.9 to 1 in all four scenarios. In the conference room, 100% of the ratio of temporal kurtosis for the LOS cluster concentrates in the range of [0.6, 1], while, in the living room, the 100% range is [0.7, 1]. Consequently, it appears that the difference between LOS and NLOS CDF with time-domain kurtosis is larger than with the angular domain power feature. The reason is that, compared with the power metric in the pure spatial domain, the temporal dispersion provides an additional dimension of information about the difference between the LOS and NLOS transmission. Strong dispersion in the complex scattering environment enlarges the difference between the LOS and NLOS clusters, which is highly noticeable in temporal kurtosis.

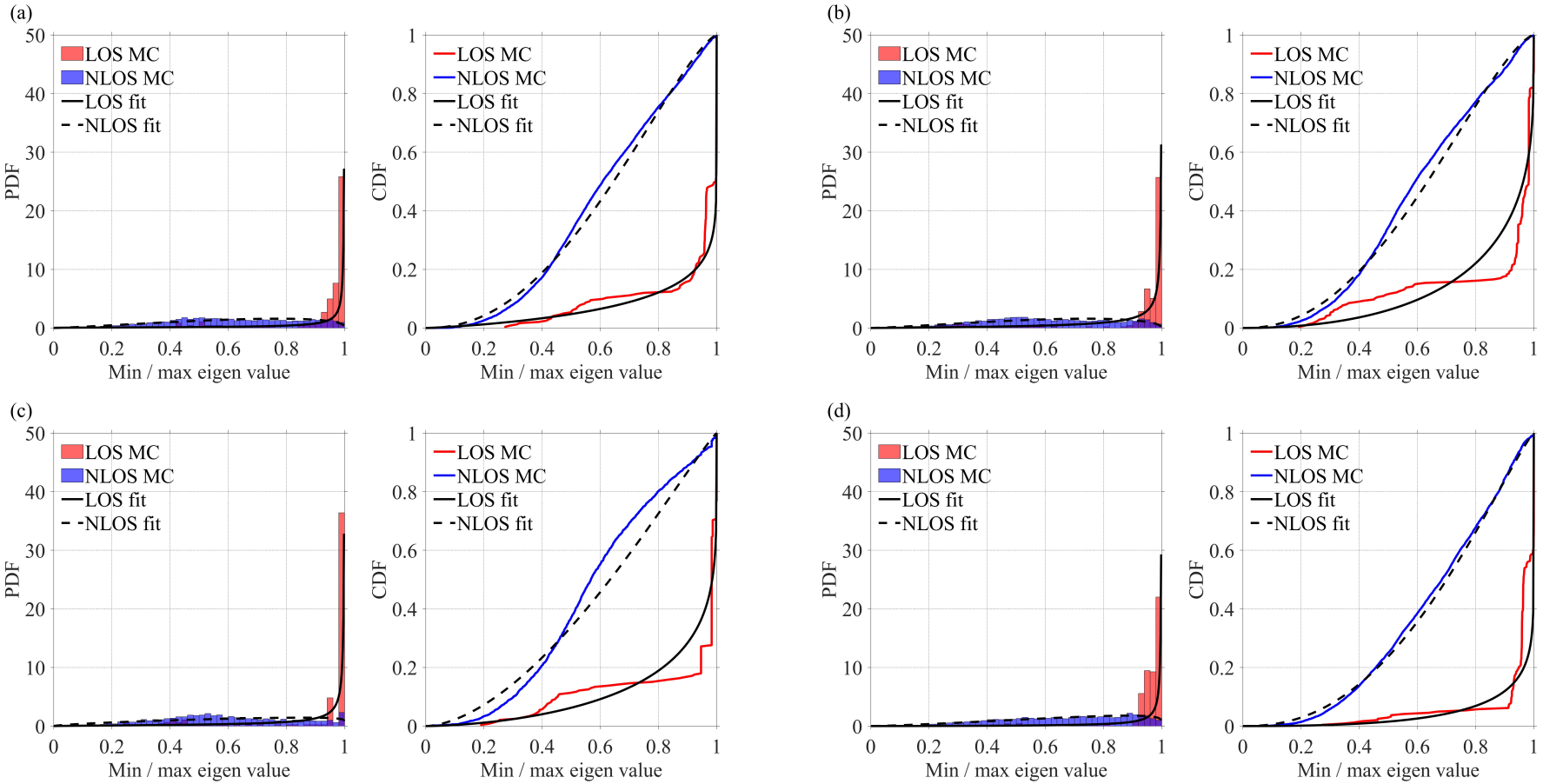


Figure 4.13 The PDF and CDF sampled by Monte Carlo method, and fitted curve with Beta distribution of LOS and NLOS transmission: minimum eigenvalue over maximum eigenvalue ratio of power kurtosis matrix in (a) conference scenario with 2 antennas on a table; (b) conference scenario with Rx antenna on a table and Tx antenna is hanging from the ceiling; (c) working cubicle scenario; (d) living room scenario.

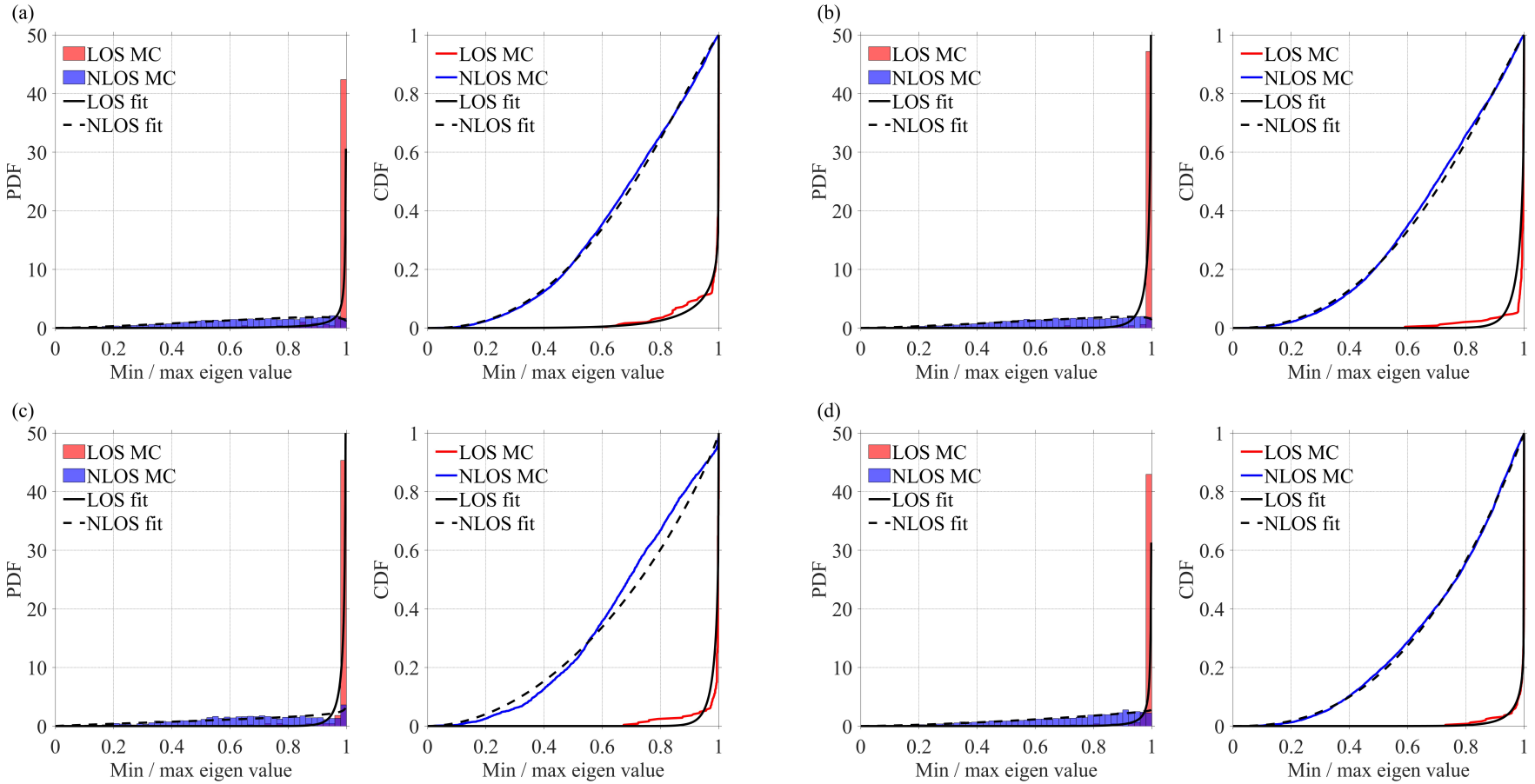


Figure 4.14 The PDF and CDF sampled by Monte Carlo method, and fitted curve with Beta distribution of LOS and NLOS transmission: minimum eigenvalue over maximum eigenvalue ratio of time-domain kurtosis matrix in (a) conference scenario with 2 antennas on a table; (b) conference scenario with Rx antenna on a table and Tx antenna is hanging from the ceiling; (c) working cubicle scenario; (d) living room scenario.

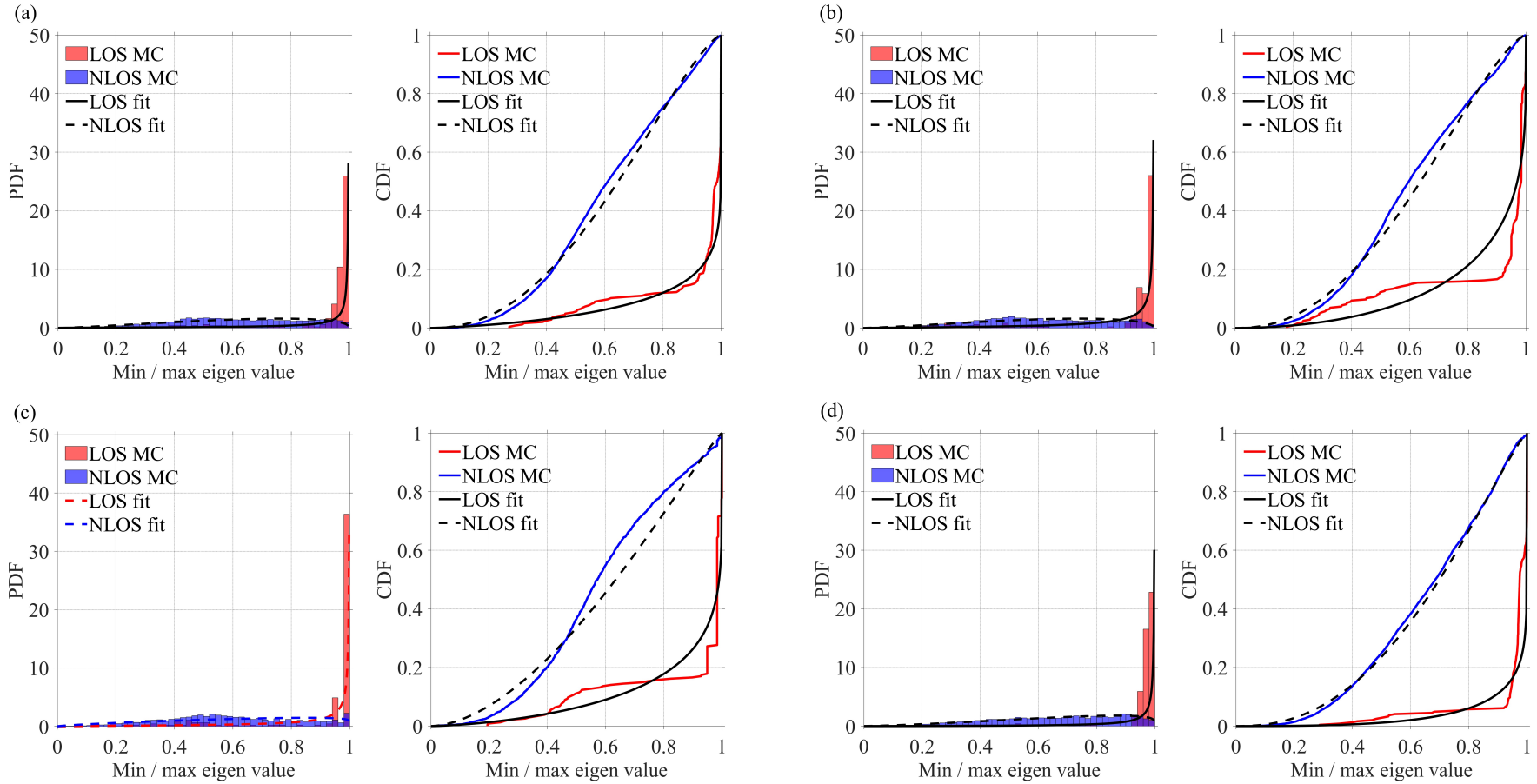


Figure 4.15 The PDF and CDF sampled by Monte Carlo method, and fitted curve with Beta distribution of LOS and NLOS transmission: minimum eigenvalue over maximum eigenvalue ratio of frequency kurtosis matrix in (a) conference scenario with 2 antennas on a table; (b) conference scenario with Rx antenna on a table and Tx antenna is hanging from the ceiling; (c) working cubicle scenario; (d) living room scenario.

Naturally, the sampling frequency plays here an important role in the performance of this feature to identify LOS from NLOS. Indeed, the sampling frequency, hence the sampling time step, influences the capacity to discriminate multipath, and multipath effect is what give the unique signature in LOS and NLOS clusters. In these simulations, the symbol rate is 800 $\times 10^6$symbol/sec and an oversampling factor of 8 is used. So, the sampling frequency is $f_s$ = 6.4 GHz, which is very high.

#### 4.3.2.2.4 Frequency domain features

The statistical ratios of mean frequency autocorrelation kurtosis matrix and the Beta distribution-fitted curves are shown in Figure 4.15. Similar to the power and time domain metrics, a clear distinction between LOS and NLOS PDF and CDF can be observed for all four scenarios. The statistical behavior is also similar: LOS clusters exhibit more symmetry than NLOS clusters. However, the large differences between LOS and NLOS noticed in the time domain are not so reflected in this frequency domain feature.

#### 4.3.2.2.5 Fitting agreement discussion

Table 4.1 Parameters of Beta distribution and RMSE between fitted and empirical CDF

| CM | | Power eigen ratio | | | | Time eigen ratio | | | | Frequency eigen ratio | | | |
|---|---|---|---|---|---|---|---|---|---|---|---|---|---|
| | | *a* | *b* | RMSE | K-S *p* | *a* | *b* | RMSE | K-S *p* | *a* | *b* | RMSE | K-S *p* |
| LOS | 1 | 1.20 | 0.09 | 0.09 | $4.77\times10^{-12}$ | 3.87 | 0.08 | 0.07 | $3.88\times10^{-6}$ | 1.28 | 0.09 | 0.10 | $2.08\times10^{-9}$ |
| | 2 | 1.81 | 0.27 | 0.07 | $3.09\times10^{-9}$ | 24.86 | 0.34 | 0.09 | $1.91\times10^{-9}$ | 1.69 | 0.24 | 0.08 | $9.10\times10^{-10}$ |
| | 3 | 1.71 | 0.20 | 0.08 | 0 | 23.27 | 0.31 | 0.09 | $1.09\times10^{-15}$ | 1.59 | 0.18 | 0.08 | $5.42\times10^{-11}$ |
| | 4 | 1.96 | 0.10 | 0.12 | 0 | 10.12 | 0.09 | 0.07 | $2.08\times10^{-10}$ | 2.08 | 0.10 | 0.14 | 0 |
| NLOS | 5 | 2.26 | 1.36 | 0.03 | 0 | 2.38 | 1.13 | 0.01 | $2.40\times10^{-6}$ | 2.30 | 1.38 | 0.03 | 0 |
| | 6 | 2.36 | 1.49 | 0.03 | 0 | 2.42 | 1.13 | 0.01 | $2.56\times10^{-5}$ | 2.40 | 1.50 | 0.03 | 0 |
| | 7 | 1.73 | 1.10 | 0.06 | 0 | 1.90 | 0.87 | 0.04 | $1.47\times10^{-13}$ | 1.78 | 1.13 | 0.06 | 0 |
| | 8 | 2.34 | 1.16 | 0.02 | $1.42\times10^{-11}$ | 2.48 | 0.98 | 0.01 | 0.03 | 2.40 | 1.19 | 0.02 | $1.04\times10^{-9}$ |

The parameters of the Beta distribution and the Root Mean Squared Error (RMSE) between fitted and empirical CDF for eight channels are listed in Table 4.1. The eight channels CM1 to CM8 are respectively: LOS transmission in a conference scenario with two antennas are on a table (CM1), LOS transmission in a conference scenario with Rx antenna is on a table and the Tx antenna is hanging on the ceiling (CM2), LOS transmission in a working cubicle scenario (CM3), LOS transmission in a living room (CM4), NLOS transmission in a conference scenario with two antennas are on a table (CM5), NLOS transmission in a conference scenario with Rx antenna is on a table and the Tx antenna is hanging on the ceiling (CM6), NLOS transmission in a working cubicle scenario (CM7), NLOS transmission in a living room (CM8). The usual evaluation of goodness-of-fit, *p*-values of almost all the Kolmogorov–Smirnov testing, are nearly zero. In the Figure 4.15, the deviation between the fitted and twisting Monte Carlo sampled LOS CDF is very serious. On the other hand, the very concentrate LOS PDF makes the tail of CDF very sharp. A little bias will lead to a massive distance between the fitted and sampled curve. The piecewise function describing the AOA in the IEEE 802.11ad channel model leads to a large trail in the CDF. Although the smooth Beta function matches the condition of continuous CDF function in the Kolmogorov–Smirnov

goodness of fit testing, the step and large trail empirical CDF still makes the *p*-value of Kolmogorov–Smirnov testing very small. Despite the low fitting goodness, the fitted Beta model can still be used in the maximum likelihood ratio testing, thanks to the enormous difference between the LOS and NLOS CDF. We however calculated the RMSE between the fitted and empirical CDF as listed in Table 4.1. The RMSE of NLOS CDF fitting is generally lower than 0.06, while, the RMSE of LOS CDF fitting is in the range from 0.07 to 0.14. Altough RMSE of LOS fitting is higher than NLOS fitting, most of the LOS RMSE is lower than 0.1. So, the LOS fitting is still efficient for the hypothesis testing.

#### 4.3.2.3 Performance of NLOS identification Features classification

As discussed in the state of the art in chapter 2, the NLOS identification is a classification problem to decide whether the transmission is LOS or NLOS. The aim of classification problem is to find suitable metrics and classifiers so that probability of incorrect decision for any individual identification event can be decreased. The first step is training the statistical model. The statistical model, in the form of MLR and ANN classifiers, is fitted with the training data set to obtain the parameters, such as the parameter of statistical distribution PDF and weighted matrix of ANN. Due to the channel data in the form of time-space separation, the features are extracted in the spatial cluster. The features are power integrated the CIR calculated with (4.6), time-domain kurtosis calculated with (4.2), and average frequency auto-correlation calculated with (4.5). Then spatial metrics about the above features are $\hat{R}_P$, $\hat{R}_t$, and $\hat{R}_f$, which are the ratio of minimum over maximum eigenvalue of the kurtosis matrix calculated with (4.14) in the angular domain. The above three metrics are combined as a sample point, ($\hat{R}_P$, $\hat{R}_t$, and $\hat{R}_f$). 250 samples, i.e., channel realizations, are used to train the parameters of the classifiers. For MLR, the parameters are $a$ and $b$ of Beta distribution (4.26); for ANN, the parameters are the weighted matrices $\boldsymbol{w}$ and linear bias vectors $\boldsymbol{b}$ in (4.20). Then, as the second step, the trained classifiers are used to identify the individual testing sample, in other words, classify the set of transmission which the testing data point belongs to. Another 250 samples are used to test the classifiers. The testing step aims to evaluate the performance and chose a suitable classifier. Each testing sample is used as the input of the trained classifiers. For MLR, a training sample is used to calculate the likelihood function (4.28) of each of the three metrics. Then, the likelihood functions are used to calculate the joint maximum likelihood ratio (4.18). By comparing the likelihood of LOS and NLOS transmission, a decision of the type of transmission can be obtained. For ANN, a training sample is used at the network's input layer, then the decision, +1 (LOS) or -1 (NLOS), is obtained from the output layer of the network. Any individual decision can be correct or incorrect.

Therefore, the performance of the classifiers is evaluated with the probability of incorrect decisions for a set of testing data. According to statistical decision theory, for a null hypothesis testing, the error can be classified as two types: type I error (reject the true null hypothesis $H_0$) and type II error (non-reject the false alternative hypothesis $H_1$). According to (4.15), for NLOS identification, the null hypothesis is the LOS transmission, while the alternative hypothesis is the NLOS transmission. So, type I error is that a LOS transmission is identified as NLOS transmission, and type II error is that a NLOS transmission is classified as LOS transmission. Thereby, the error is evaluated by comparing the decided type of transmission by the classifiers, and the actual type of transmission of the sample data. By counting the number of the above two types of error, the probabilities of errors are obtained. The probabilities of the two types error are shown in

Table 4.2 for the four LOS channels. The errors of different scenarios and the method of classification are distinct. In general, MLR provides a much higher type I error than type II. Most of the type I error probability tested by MLR is higher than 0.1, especially when the Rx and Tx antennas are both on the table in a conference scenario (CM-1), the type I error is higher than 0.2. One reason for the errors is that the goodness of fit limits the testing performance of joint MLR for the above small probability events. The LOS CDF of fitted power matrix ratio in CM-1 is generally lower than the simulated CDF. Therefore, the likelihood value calculated by the fitted LOS PDF is underestimated. While, in other scenarios, the fitted CDF fluctuates around the simulated CDF. So, the tested type II errors are not very high. Both types of errors tested by ANN are much lower than the results of MLR in all scenarios. Especially in the CM-1 and CM-3 scenario, the type I error of ANN is only 1/4 and 1/15 of the results of MLR. ANN estimates the linear structure of three features, thus distinguishes the transmissions better than only with the multiplication PDF by MLR. In summary, the ANN performs much better than MLR for NLOS identification.

Table 4.2 Probabilities of error tested by MLR and ANN for NLOS identification

| Channel | | Maximum Likelihood Ratio | | | | Artificial Neural Network |
|---|---|---|---|---|---|---|
| | | $\hat{R}_P$ | $\hat{R}_t$ | $\hat{R}_f$ | $\hat{R}_P\hat{R}_t\hat{R}_f$ | $(\hat{R}_P,\ \hat{R}_t,\ \hat{R}_f)$ |
| CM-1 | Type I | 0.3052 | 0.1408 | 0.2441 | 0.2113 | 0.0512 |
| | Type II | 0.0634 | 0.0685 | 0.0682 | 0.0668 | 0.0616 |
| CM-2 | Type I | 0.2074 | 0.0691 | 0.2166 | 0.1567 | 0.0865 |
| | Type II | 0.1457 | 0.1172 | 0.1392 | 0.1305 | 0.0398 |
| CM-3 | Type I | 0.1600 | 0.0550 | 0.1600 | 0.1550 | 0.0096 |
| | Type II | 0.0905 | 0.1007 | 0.0861 | 0.0871 | 0.0576 |
| CM-4 | Type I | 0.1972 | 0.0394 | 0.1362 | 0.0640 | 0.0421 |
| | Type II | 0.0570 | 0.0693 | 0.0594 | 0.0583 | 0.0472 |
| Average | Type I | 0.2175 | 0.0761 | 0.1892 | 0.1467 | 0.0473 |
| | Type II | 0.0891 | 0.0889 | 0.0882 | 0.0857 | 0.0515 |

# 4.4 Experimental validation

## 4.4.1 Conditions of experiments

### 4.4.1.1 Measurement environment of laboratory scenario

To verify the effectiveness of the above method for NLOS identification, an experimental validation is conducted in a laboratory environment. Measurements are performed in a quasi-rectangle room in a microwave wireless facilities lab at Sorbonne University. The size of the room is approximately 10.25 m × 7.52 m. The distance between the ground and the ceiling is 2.93 m. The floor plan and the real scene of the measuring environment are illustrated in Figure 4.16. Five glass windows in front of the room occupy more

than half of a wall and directly contact with the ceiling. The wall below the windows is metallic. The other three walls are constructed with aerated concrete and covered with plaster plates. Mineral fiber ceiling boards constitute the ceiling. Metallic lightboxes and ventilations are regularly arranged on the ceiling. An almost cubic anechoic chamber in a Faraday cage is placed along a wall. The chamber is fabricated with dense copper mesh in order to isolate the electromagnetic wave between the inner and outer environments. The 3D near-field scanner located by the windows is constructed with an aluminum alloy frame and a foamed plastic open square cavity. Tables for experiments are placed along the other walls. Most of the objects on the tables are electronic instruments and computers. This furniture arrangement in this environment can be considered as an approximation to the situation in the open office and conference room scenarios investigated in the IEEE802.11ad channel model. Measurements are randomly implemented in the zones which are marked as closed circles in the floor plane (both Tx and Rx being in the same zone for a given set of experiments with distance between Tx and Rx ranging from 0.5 to 2.5 meters).

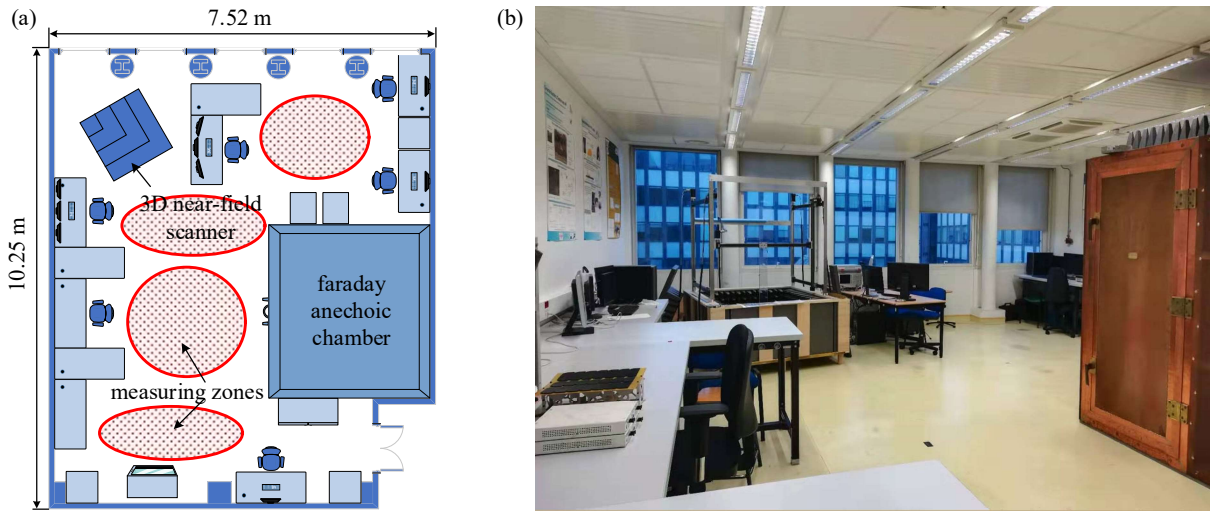


Figure 4.16 (a) The floor plane and (b) the real scene of the measuring scenario.

## 4.4.1.2 Measurement system

The measurement configuration set-up aims at emulating a beam training strategy and is illustrate in Figure 4.17 (c) and (d). In order to obtain the PAS, a Vector Network Analyzer (VNA) fabricated by Rohde & Schwarz Inc. is used to measure the scattering parameter S21, i.e., the propagation channel, between Tx and Rx antennas. The VNA maximum output power is 4 dBm at 60 GHz [10]. The Tx antenna is a dipole antenna produced by Flann Microwave Ltd. It has an omnidirectional pattern of 360° azimuth coverage and 60° elevation coverage [11]. The nominal gain is 2 dB. A pyramid horn antenna fabricated by QuinStar Technology Inc. is used to generate a directional Rx pattern. The Rx pattern is quasi-symmetric with 10.1° 3-dB beamwidth in E-plane and 13.1o 3-dB beamwidth in H-plane [12]. The mid-band gain is 24 dB. The angular scanning of the Rx antenna in the beam training strategy is achieved by the cooperating rotation between horizontally and vertically rotating motors. The azimuth rotating motor is a rotation stage using a stepper Motor produced by Newport Inc. with a resolution of ±20 $\mu$-degrees [13]. The elevation rotating motor is a piezo-driven motor fabricated by SmarAct Inc. and its resolution as a rotation stage is ±15

$\mu$-degrees [14]. The adjustable angular velocity of SmarAct motor is a benefit to resist the gravity of the horn antenna, thereby provides a robust angular resolution during the vertical rotation. All motors and the VNA are controlled by a desktop computer using Matlab.

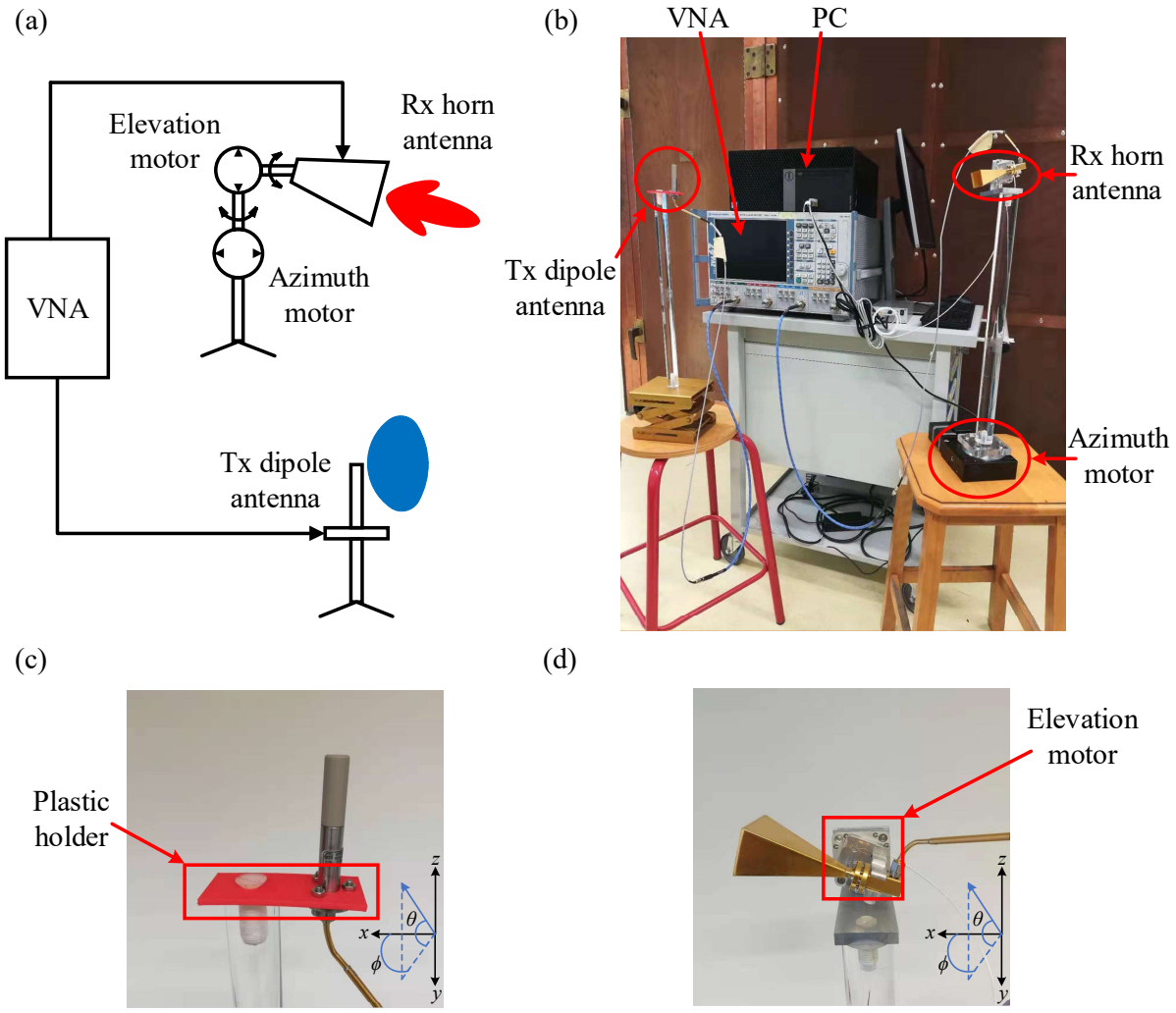


Figure 4.17 (a) The schematic; (b) the real system of the measuring system; (c) plastic fixed holder of Tx dipole antenna; (d) elevation motor of Rx horn antenna .

The above components compose the measuring system as shown in Figure 4.17: the VNA, the elevation motor control unit, and the desktop computer is placed on a mobile workbench. The dipole Tx antenna is fixed at one end of a plastic-based support rod. A lift is connected to the other end of the rod to adjust the height of the antenna. The stand of the dipole antenna is made of plastic to limit strong interaction with the antenna pattern. The horizontal and vertical motor is installed at the two ends of another plastic support rod. The two antennas are connected to VNA with two 1.5 m cables. A set of MATLAB code drives the measuring system. The Tx omnidirectional dipole antenna is fixed on a plastic holder to avoid the reflection by the metal holder, as shown in Figure 4.17 (c). The plastic holder is manufactured by 3D printing. The elevation motor of the Rx horn antenna is shown in Figure 4.17 (d). The motor is fixed with a metal holder. Because the pattern of horn antenna is directional with low side lobes

and the output port is far away from the holder, the radiated field is not much reflected by the metal holder.

#### 4.4.1.3 Measurement strategy

The $S_{21}$ parameter measurements are performed over the full bandwidth of 8.64 GHz considered in the IEEE 802.11ad standard, from 57.24 GHz to 65.88 GHz. Similar to the measurements performed during the IEEE 802.11ad channel modeling, the first-order and second-order reflections are guaranteed to be received in the experiment. This means that twice the diagonal distance of the cubic room, i.e., $d$ = 26.1 m, is the maximum distance range in order to guarantee that all first and second-order reflections are captured in the CIR. So, the corresponding frequency interval is set to $\Delta f$ = 11.5 MHz, thereby 752 frequency points being sampled within the band. The IF bandwidth is fixed to 1 kHz, as a tradeoff between SNR performance and acquisition time. The frequency sweeping is operated three times over the whole band for each angular sample at the same Tx-Rx location, then taking the average over the three measurements to reduce the thermal noise of the receiver. The spatial sampling range is from -180° to 180° in the azimuth direction. Since the holder limits the rotation of the vertical motor in the negative elevation direction, the range is -45° to 90° in the elevation direction. The parameters of the measurements are summarized in Table 4.3 as well as those used for modeling the IEEE 802.11ad channel. The measurement in this study uses a smaller angular step and a larger bandwidth. Besides, by using an omnidirectional antenna at Tx, the measurement in this study is also more similar to the beam training scenario. Therefore, the proposed experimental set-up has the capacity to validate the results previously identified by simulation with the IEEE 802.11ad channel model. Totally 150 Rx-Tx location pairs are randomly sampled in the measuring zones. The Rx-Tx distances are randomly selected in a range from 0.5 m to 2.5 m. To form the training set, 100 samples are randomly selected from the 150 measurements set. Then, another 100 samples are randomly selected to form the testing set. This operation is performed three times and the average error probability is then calculated. This approach somehow compensates for the issue of small set learning.

Table 4.3 Comparation between the parameters of the purposed measurement and IEEE 802.11ad measurement

| Parameters | Proposal measurement | IEEE 802.11ad measurement |
|---|---|---|
| Bandwidth | 8.64 GHz | 800 MHz |
| Time resolution | 0.12 ns | 1.25 ns |
| Frequency sample number | 752 | 52 |
| Frequency resolution | 11.5 MHz | 12.5 MHz |
| Transmit power | 4 dBm | 2 dBm |
| Rx beam width (E/H plane) | 10.1° / 13.1° | 40° / 40° |
| Tx beam width (E/H plane) | 360 ° / 60 ° | 40° / 40° |
| Tx antenna gain | 2 dB | 18 dB |
| Rx antenna gain | 24 dB | 18 dB |
| Sampling range in azimuth | [-180°, 180 °] | [-180°, 180 °] |
| Sampling range in elevation | [-45 °, 90 °] | [-90 °, 90 °] |
| Spatial sampling interval | 5° | 10° |

## 4.4.2 Measurement Results

### 4.4.2.1 Results in time and frequency domain

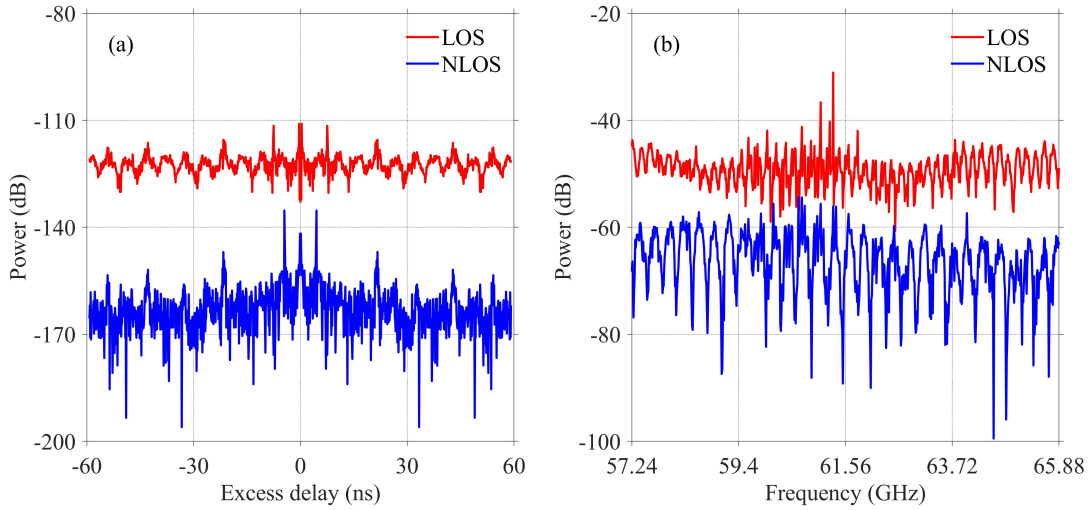


Figure 4.18 (a) CIR and (b) CFR of the LOS and NLOS signal measured in the laboratory scenario.

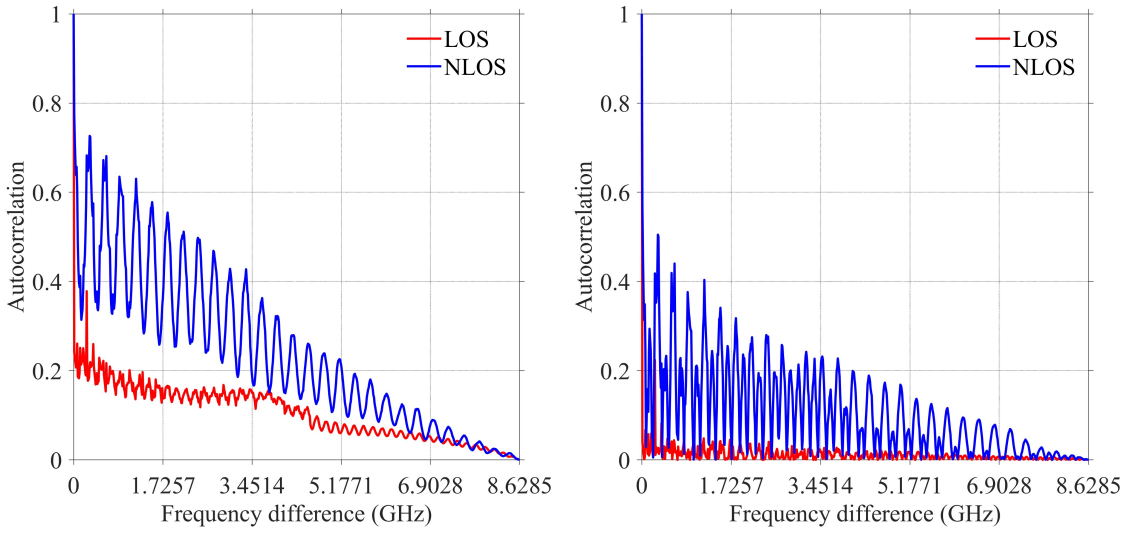


Figure 4.19 Autocorrelation of $H(f)$ (a) with and (b) without mean value

An example of the measured CFR and the CIR inverse Fourier transformed from CFR is shown in Figure 4.18. Similar to simulated CIR in Figure 4.3, there are two sharp side peaks beside the peak of NLOS CIR. While the simulated LOS CFR in Figure 4.3 is very flat, the measured one fluctuates much more. This is due to the fact that even when the Rx beam is aligned with the LOS towards the Tx antenna in

the measurement setup, the Rx radiation pattern having a certain beam width (not being a Dirac-type shape), it can collect multipath as well as the LOS. Furthermore, multiple reflections in between Tx and Rx antennas can occur. Finally, it is to be noted that the measuring band is here 8.64 GHz, which is much broader than the 800 MHz band in the simulation. Therefore, it is anticipated that the difference between measured LOS and NLOS frequency autocorrelation PDF will be weaker than with simulation results. The autocorrelations are shown in Figure 4.19.

#### 4.4.2.2 Results in space domain

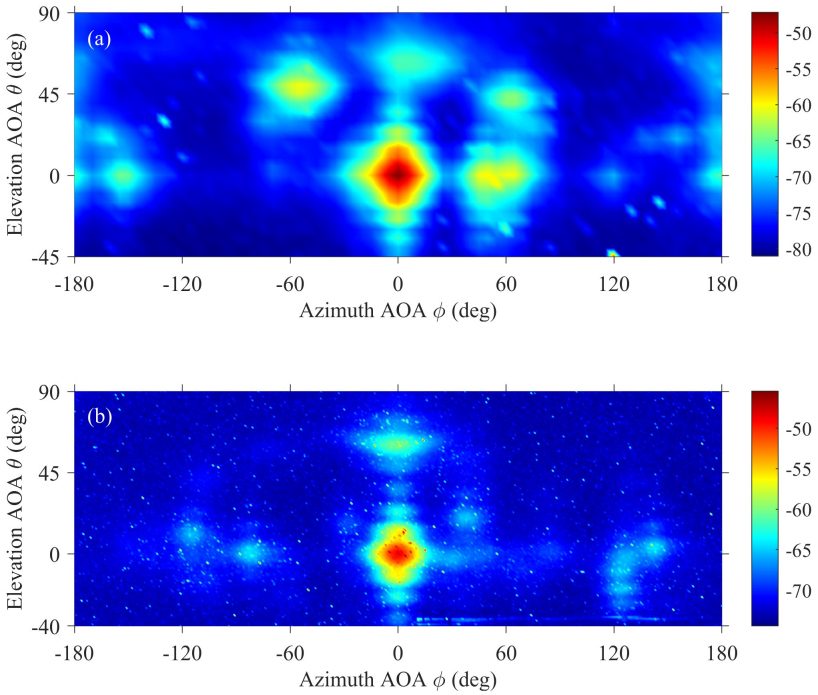


Figure 4.20 PAS measured in different Rx-Tx places with a Rx-antenna rotating interval of (a) 5° and (b) 1°.

The PAS measured with different rotating steps (for 2 different Rx-Tx places) is shown in Figure 4.20. The PAS is obtained by:

$$P(\phi,\theta)=\frac{1}{B}\int_0^B S_{21}(f,\phi,\theta)\,df \tag{4.39}$$

Where, $S_{21}(f, \phi, \theta)$ is the S-Parameter describing the power transformed from port 1 to port 2, $B$ is the sampling band, $f$ is the frequency, $\phi$ and $\theta$ are the azimuth and elevation angles. The shapes of clusters sampled with 5° intervals are in the form of a polygon while the PAS generated with 1° step is much smoother than the PAS of 5° step. However, entirely sampling such a 2D-PAS map with a 1° step needs more than 60 hours with our current setup. In actual wireless communication systems, although the scanning time is much less than in our experiments thanks to electronic beam scanning capabilities, scanning with very small angular step size is also too time-resource-consuming. That means PAS with low

resolution is (or will be) a common situation in most millimeter-wave wireless systems.

In both PAS in Figure 4.20, it can be noticed that there are spread distributed speckles which are granular interference stochastically distributed in PAS. It is an inherent characteristic of images detected by the wave coherence, such as radar and ultrasound detector. The speckles are typically generated by the random coherence of the wave scattered by the objects spread wider than the concentrated reflectors or grouped scatterers. The wider spread scattering is view as a type of backscattering. The received backscattering signal can be viewed as the incoherent sum of $N$ backscattered waves:

$$A\exp(j\varphi)=\sum_{i=1}^{N}A_i\exp(j\varphi_i) \tag{4.40}$$

Where phases $\varphi_i$ of each scattering component is uniformly distributed in (-π, π) and independent from amplitude $A_i$. If the number of scatterers is sufficiently high, the central limit theorem leads to a complex form:

$$A\exp(j\varphi)=z_1+jz_2 \tag{4.41}$$

Where, the real and image part $z_1$ and $z_2$ are independent and identically distributed zero-biased Gaussian variables with variance $\sigma$ / 2. Physical meaning of $\sigma$ is the Radar Cross Section (RCS) of the observed resolution cell. The joint probability density function (PDF) of the two parts is [15] :

$$p(z_1,z_2)=\frac{1}{\pi\sigma}\exp\left(-\frac{z_1^2+z_2^2}{\sigma}\right) \tag{4.42}$$

Then, the PDF of power intensity $I=A^2=z_1^2+z_2^2$ is:

$$p(I)=\frac{1}{\sigma}\exp\left(-\frac{I}{\sigma}\right) \tag{4.43}$$

Here, the mean of the intensity is equal to $\sigma$. The intensity carries information about the average backscattering coefficient related to the resolution cell. Therefore, they are one type of noise for the clustering and therefore need to be removed by a smoothing method. In the following identification, the speckles are removed with the open and close operation described in chapter 3. The size of the opening and closing marker should be determined according to the RCS of the observed resolution cell. In this study, a basic 3×3 matrix is empirically used as the marker. 3-pixel is the minimum size of the maker. Here, 3-pixel is used to minimize the influence of the marker to the actual scattering clusters.

### 4.4.3 Identification on PAS

#### 4.4.3.1 Power angular clustering

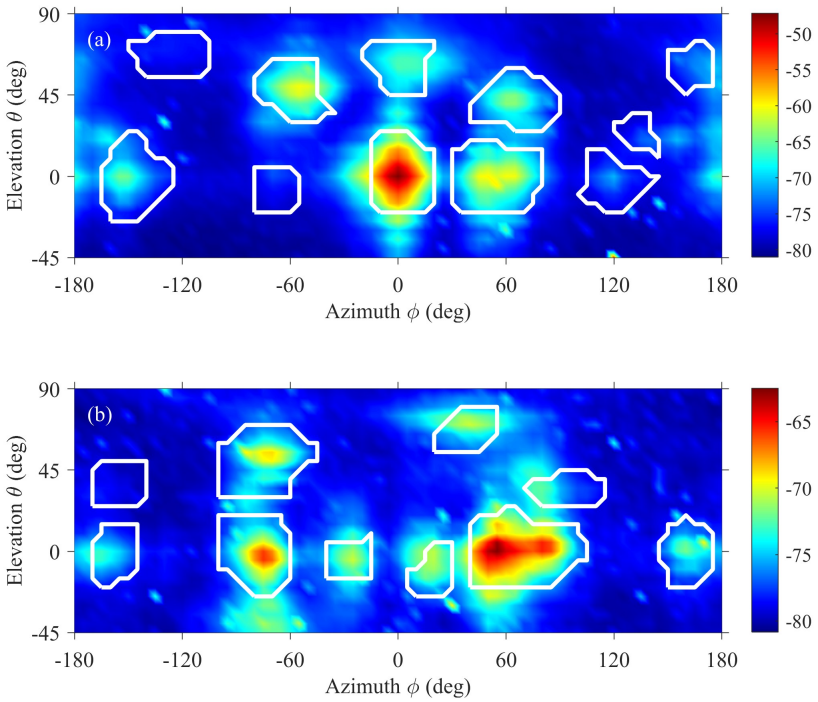


Figure 4.21 Measured PAS clustering using watershed algorithm: (a) LOS; (b) NLOS.

The clusters segmented by the watershed method are shown in Figure 4.21. The performance of watershed segmentation for measured PAS is lower than with simulated PAS: the shape of the clusters appears to be less preserved. In simulation, the PAS is generated by the convolution between the discrete spatial channel and the Gaussian antenna pattern model whose edge is sharp, as shown in Figure 4.22 (a). The sharp edges of the clusters make the 2nd order derivative of the power angular field enclosing the power cluster perfectly along the edges of the clusters. The clear gradient field leads to a watershed segmentation that well preserves the shapes of clusters. In the actual measurement, the PAS is detected by the physical antenna pattern. The physical pattern is smooth, which brings the smooth clusters. The edges of the valleys in the gradient field is deformed from the edges of clusters in Figure 4.22 (b). The 2nd order derivative of PAS is not obvious. Hence, the shapes of clusters cannot be preserved by watershed segmentation as well as in simulation.

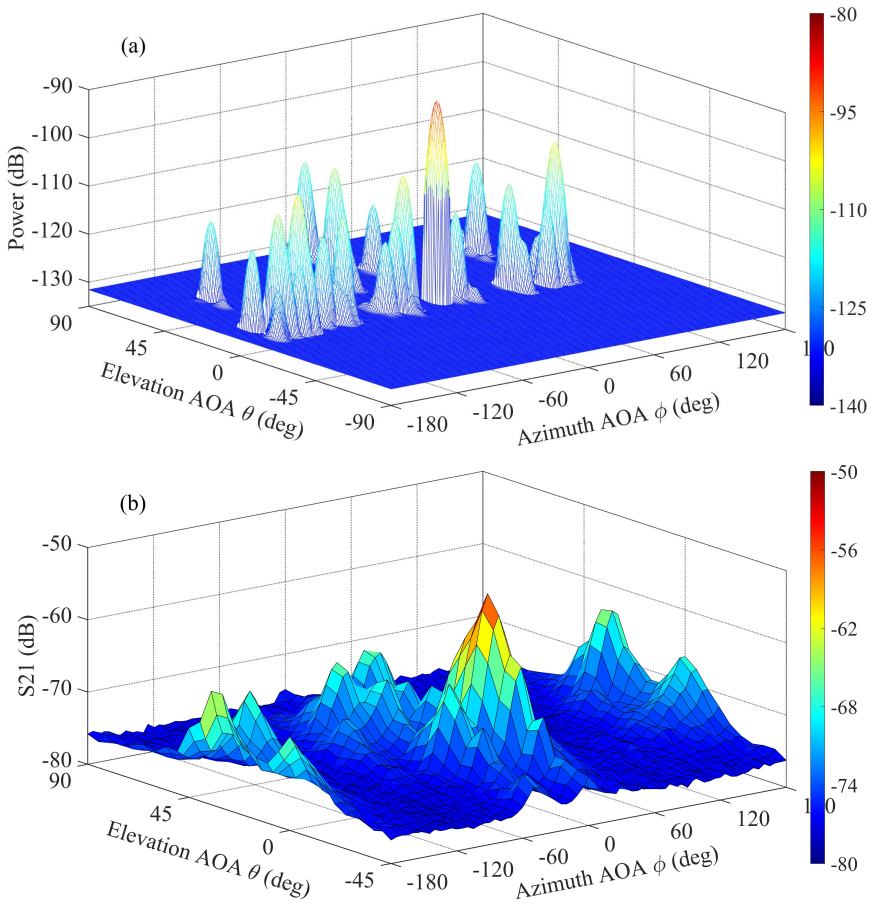


Figure 4.22 Comparation between (a) simulated and (b) measured PAS

### 4.4.3.2 Statistical characteristics inside cluster

The PDF and CDF of power, temporal, and frequency kurtosis min/max eigen value ratio are shown in Figure 4.23. It means that the statistical difference between LOS and NLOS features is less significant than with the simulation situation. The weak distinction between LOS and NLOS features could be somehow qualitatively predicted by observing the signals in Figure 4.18. We empirically found that the PDFs of the three features can be fitted with Generalized Extreme Value (GEV) distribution. The PDF of GEV is given by:

$$f_G\left(x \mid \gamma,\mu,\sigma\right)=\begin{cases}\dfrac{1}{\sigma}\exp\left[-\left(1+\gamma\dfrac{x-\mu}{\sigma}\right)^{-1/\gamma}\right]\left(1+\gamma\dfrac{x-\mu}{\sigma}\right)^{-(1+1/\gamma)}, & \gamma\neq 0\\ \dfrac{1}{\sigma}\exp\left[-\exp\left(-\dfrac{x-\mu}{\sigma}\right)-\dfrac{x-\mu}{\sigma}\right], & \gamma=0\end{cases} \tag{4.44}$$

Where $\gamma$, $\mu$, and $\sigma$ are parameters. The log-likelihood function of GEV distribution for $N$ *i.i.d.* samples ($x_1$, $x_2$ … $x_N$) is:

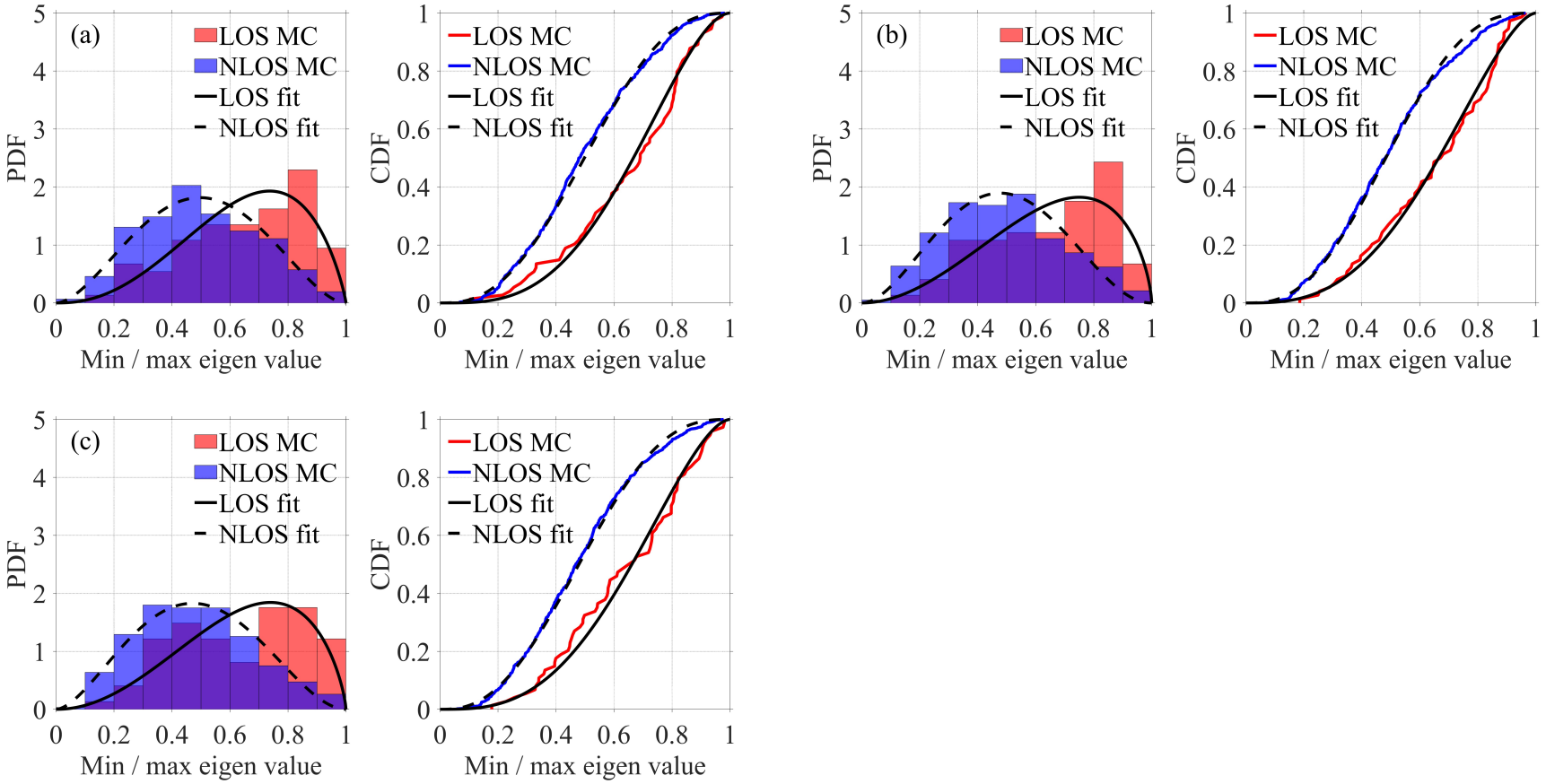


Figure 4.23 Measured PDF and CDF and the curve-fitted with generalized extreme value distribution of LOS and NLOS transmission: minimum eigen value over maximum eigen value ratio of (a) power kurtosis matrix; (b) temporal kurtosis matrix; (c) frequency kurtosis matrix.

$$\ln \mathcal{L}_G(\gamma,\mu,\sigma;x)=\begin{cases}-n\ln\sigma-\left(1+\dfrac{1}{\gamma}\right)\displaystyle\sum_{i=1}^{N}\ln\left(1+\gamma\frac{x_i-\mu}{\sigma}\right)-\sum_{i=1}^{N}\left(1+\gamma\frac{x_i-\mu}{\sigma}\right)^{-1/\gamma}, & \gamma\neq 0\\ -n\ln\sigma-\displaystyle\sum_{i=1}^{N}\exp\left(-\frac{x_i-\mu}{\sigma}\right)-\sum_{i=1}^{N}\frac{x_i-\mu}{\sigma}, & \gamma=0\end{cases} \tag{4.45}$$

Due to the complex expression, an analytical solution of the first-order deviation equations is hard to find. Instead of an analytical solution, the minima of the above likelihood can be solved with the Newton-Raphson method [16]. Defining the parameters as a vector $\boldsymbol{\theta} = [\gamma, \mu, \sigma]^T$, the iterative formula to update the parameter vector in the direction of the log-likelihood gradient $\nabla \ln \mathcal{L}_G(\theta; x)$ is :

$$\theta^{i+1}=\theta^{i}+I(\theta)^{-1}\nabla\ln\mathcal{L}_G(\theta;x) \tag{4.46}$$

Where $I(\theta)$ is a 3x3 Fisher information matrix:

$$I(\theta)=E\left[\frac{\partial^2\ln\mathcal{L}_G(\theta;x)}{\partial\theta\partial\theta'}\right] \tag{4.47}$$

with the following matrix elements:

$$I_{11}(\theta)=E\left(\frac{\partial^2\ln\mathcal{L}_G(\theta;x)}{\partial\sigma^2}\right)=\frac{1}{\sigma^2\gamma^2}\left(1-2\Gamma(2+\gamma)+p\right) \tag{4.48}$$

$$I_{12}(\theta)=I_{21}(\theta)=E\left(\frac{\partial^2\ln\mathcal{L}_G(\theta;x)}{\partial\sigma\partial\gamma}\right)=-\frac{1}{\sigma\gamma^2}\left(1-\gamma+\frac{1-\Gamma(2+\gamma)}{\gamma}-q+\frac{p}{\gamma}\right) \tag{4.49}$$

$$I_{13}(\theta)=I_{31}(\theta)=E\left(\frac{\partial^2\ln\mathcal{L}_G(\theta;x)}{\partial\sigma\partial\mu}\right)=-\frac{1}{\sigma^2\gamma}\left(p-\Gamma(2+\gamma)\right) \tag{4.50}$$

$$I_{22}(\theta)=E\left(\frac{\partial^2\ln\mathcal{L}_G(\theta;x)}{\partial\gamma^2}\right)=-\frac{1}{\gamma^2}\left[\frac{\pi^2}{6}+\left(1-\gamma+\frac{1}{\gamma}\right)^2-\frac{2q}{\gamma}+\frac{p}{\gamma^2}\right] \tag{4.51}$$

$$I_{23}(\theta)=I_{32}(\theta)=E\left(\frac{\partial^2\ln\mathcal{L}_G(\theta;x)}{\partial\mu\partial\gamma}\right)=-\frac{1}{\sigma\gamma}\left(q-\frac{p}{\gamma}\right) \tag{4.52}$$

$$I_{33}(\theta) = E\left(\frac{\partial^2 \ln \mathcal{L}_G(\theta;x)}{\partial \mu^2}\right) = \frac{p}{\sigma^2} \tag{4.53}$$

where, with the gamma function $\Gamma(\alpha)$ and $\varphi(\alpha)$ are in the form of (4.31), and where the parameters $p$ and $q$ are:

$$p = (1+\gamma)^2 \Gamma(1+2\gamma) \tag{4.54}$$

$$q = \Gamma(2+\gamma)\left(\varphi(1+\gamma) + \frac{1+\gamma}{\gamma}\right) \tag{4.55}$$

Table 4.4 Parameters of GEV and $p$-value of Kolmogorov–Smirnov goodness of fit testing

| Features | Power eigen ratio | | Temporal kurtosis eigen ratio | | Frequency correlation eigen ratio | |
|---|---|---|---|---|---|---|
| | LOS | NLOS | LOS | NLOS | LOS | NLOS |
| $\gamma$ | -0.5960 | -0.2464 | -0.6062 | -0.2148 | -0.5451 | -0.1942 |
| $\mu$ | 0.6083 | 0.4252 | 0.60813 | 0.4143 | 0.5936 | 0.4055 |
| $\sigma$ | 0.2309 | 0.1896 | 0.2250 | 0.1874 | 0.2314 | 0.1841 |
| K-S $p$-value | 0.9070 | 0.3961 | 0.7082 | 0.4304 | 0.5541 | 0.5708 |

The parameters of the GEV and the $p$-values of the Kolmogorov–Smirnov testing at a significant level of 0.05 for the three statistical features are shown in Table 4.4. The goodness of fitting for the measured PDF is very high. Compared with the fitting for simulated PDF, all of the measured $p$-values are higher than the significance of 0.05, even near to 1 for the LOS power eigen ratio.

$$p = (1+\gamma)^2 \Gamma(1+2\gamma) \tag{4.56}$$

$$q = \Gamma(2+\gamma)\left(\varphi(1+\gamma) + \frac{1+\gamma}{\gamma}\right) \tag{4.57}$$

## 4.4.3.3 Features classification

To evaluate the performance of classification such as done with the simulation result in section 4.3, the probabilities of type I and type II errors are shown in Table 4.5. Due to the weak difference between the LOS and NLOS CDF of features in Figure 4.23, the performance of MLR is much worse than in the simulation performance. The type I error is near 1/3. Even the type II is also near 0.3. To enhance the classification performance, the number of neurons for each ANN layer and the number of raining reputation have been both increased to 100, while keeping the number of hidden layers as 2. The minimum

probabilities of type I and II are both limited below 0.2, which is somewhat acceptable and much better than the performance of MLR.

Table 4.5 Probabilities of error tested by MLR and ANN with measured features

| Error | Maximum Likelihood Ratio | | | | Artificial Neural Network |
|---|---|---|---|---|---|
| | $\hat{R}_P$ | $\hat{R}_t$ | $\hat{R}_f$ | $\hat{R}_P\hat{R}_t\hat{R}_f$ | $(\hat{R}_P,\ \hat{R}_t,\ \hat{R}_f)$ |
| Type I | 0.3713 | 0.3832 | 0.4371 | 0.3533 | 0.1548 |
| Type II | 0.2892 | 0.2827 | 0.2885 | 0.2878 | 0.1627 |

# 4.5 Conclusion

In this chapter, the space-time structure of transmission channel is used to perform LOS/NLOS identification. Using the 2D power angular spectrum (PAS) obtained over the 57-66 GHz band at Rx after the first stage of a beam training process, a 3D space composed of Angle-Of-Arrival (AOA) in elevation ($\theta$) and in azimuth ($\phi$) and of excess delay is generated. After a clustering process performed in the 2D angular space using the image-processing method described in chapter 3, intra-cluster statistical features are determined. It has been found that power kurtosis in the time/frequency/space domain is a promising metric in order to discriminate LOS from NLOS. In particular, the min/max ratio of eigen values obtained by a decomposition of the co-kurtosis matrix, i.e., principal component analysis, has been found to be a sufficient criterion to discriminate LOS from NLOS clusters. This ratio corresponds to a weighted symmetry, and it appears that LOS clusters exhibit much less symmetry than NLOS clusters. These findings came from extensive simulations using the IEEE802.11ad channel model, to which antenna radiation pattern effect has been introduced. Identification has been then performed using Artificial Neural Network (ANN) and Maximum Likelihood Ratio (MLR) in both simulation and experiments. Under the evaluation of Type I and II errors, the performance of identification with ANN has been found to outperform MLR in all investigated scenarios in identifying NLOS from LOS clusters. Out of the 26230 NLOS clusters investigated in the four simulation scenarios, 94.85% have been correctly identified as NLOS and out of the 1000 testing LOS clusters, 95.27% have been correctly identified as LOS. In measurements, out of the 1212 NLOS clusters investigated in the four simulation scenarios, 84.52% have been correctly identified as NLOS and out of the 150 testing LOS clusters, 83.73% have been correctly identified as LOS.

# References

[1] C. Bourlier, N. Pinel, and G. Kubické, *Method of Moments for 2D Scattering Problems: Basic Concepts and Applications*: ISTE, Ltd. and John Wiley & Sons, Inc., 2013.

[2] P. F. Lyu, X. Y. Xu, S. Yan, and Z. X. Ren, "60 GHz Indoor Propagation With Time-Domain Geometric-Optics," *IEEE Transactions on Magnetics,* vol. 52, no. 3, Mar, 2016.

[3] N. Pinel, and C. Bourlier, *Electromagnetic Wave Scattering from Random Rough Surfaces: Asymptotic Models*: John Wiley & Sons, Inc., 2013.

[4] R. Piesiewicz, C. Jansen, D. Mittleman, T. Kleine-Ostmann, M. Koch, and T. Kurner, “Scattering analysis for the modeling of THz communication systems,” *IEEE Transactions on Antennas and Propagation,* vol. 55, no. 11, pp. 3002-3009, Nov, 2007.

[5] *Effects of building materials and structures on radiowave propagation above about 100 MHz-P Series Radiowave propagation,* Recommendation ITU-R P.2040-1, P Series Radiowave propagation.

[6] M. Riedmiller, and H. Braun, “A Direct Adaptive Method for Faster Backpropagation Learning - the Rprop Algorithm,” *1993 Ieee International Conference on Neural Networks, Vols 1-3*, pp. 586-591, 1993.

[7] "Beta Distributions," *Continuous Univariate Distributions*, N. L. Johnson, S. Kotz and N. Balakrishnan, eds., pp. 210-275: John Wiley & Sons, Inc, 1995.

[8] M. A. Stephens, "Kolmogorov, A.N. (1933) On the Empirical Determination of a Distribution," *Breakthroughs in Statistics Volume II: Methodology and Distribution*, S. Kotz and N. L. Johnson, eds., pp. 106-114: Springer-Verlag New York, Inc., 1992.

[9] G. Marsaglia, W. W. Tsang, and J. Wang, “Evaluating Kolmogorov's Distribution,” *Journal of Statistical Software,* vol. 8, no. 18, 2003.

[10] *R&S®ZVA Vector Network Analyzer Specifications*, Rohde & Schwarz GmbH & Co.

[11] *Data sheet of Omni Directional Antenna Series MD249*, Flann Microwave Ltd.

[12] *Product Documents of Standard Gain Horns QWH at V Band*, QuinStar Technology, Inc.

[13] *FCR100 Data Sheet*, Newport Corporation.

[14] *Spec Sheet of SR-4011 Rotation Stage*, SmarAct Inc.

[15] F. Argenti, A. Lapini, L. Alparone, and T. Bianchi, “A Tutorial on Speckle Reduction in Synthetic Aperture Radar Images,” *IEEE Geoscience and Remote Sensing Magazine,* vol. 1, no. 3, pp. 6-35, Sep, 2013.

[16] P. Prescott, and A. T. Walden, “Maximum Likelihood Estimation of the Parameters of the Generalized Extreme-Value Distribution,” *Biometrika,* vol. 67, no. 3, pp. 723-724, 1980.

# Conclusion and Perspective

To help reducing the positioning error introduced in rich indoor multipath transmissions, this thesis solves the identification of Line-of-Sight (LOS) and Non-Line-of-Sight (NLOS) problem and hence contributes to provide accurate 60 GHz localization systems.

Compared with other radio-based technologies, the triangulation based UWB ranging, especially the TOA and TDOA based ranging, provides theoretically very high accuracy for localization. Due to its wide band, the millimeter band is hence an excellent candidate for indoor localization, and particularly the unlicensed 60 GHz with an available bandwidth close to 8.64 GHz. The millimeter band takes advantage of the MIMO communication for 5G due to its capacity of interference mitigation in dense networks. Unfortunately, blockage remains a critical issue. This is typically overcome using beamforming and beam training to establish a radio link between Tx and Rx based on an NLOS path. However, NLOS transmission is one of the significant error sources in indoor localization, due to the longer propagating distance compared with the actual distance between the transmitter and receiver. Unfortunately, the serious attenuation or even blockage in millimeter wave band makes NLOS transmission quite common situations. In these situations, the accuracy of positioning is considerably decreased and the goal of this thesis is consequently to propose a methodology to efficiently identify when a communication is being performed with a NLOS path rather than a LOS path.

Most of the current studies on NLOS identification are in the sub-6 GHz band. The low attenuation, strong diffraction, and omnidirectional antenna pattern typically encountered in this band make the resulting channel between a transmitter and a receiver experiencing strong multipath effects. Therefore, features in the Channel Impulse Response (CIR) are typically used to differentiate between LOS and NLOS transmissions. The ranged distance and other channel features are also used to distinguish LOS and NLOS situations. Parametric and non-parametric hypothesis testing are both used to statistically determine the transmission scenario. NLOS identification in the millimeter-wave band has not being paid much interest in the literature so far. Furthermore, millimeter-wave channel, being highly sparse, exhibits different behaviors than in the sub-6 GHz region. Angular spatial features of the channel rather than of the CIR are used in order to perform NLOS identification. To do so, clustering is an essential step. Among current clustering methods, the current channel modeling widely uses the partitional clustering method, K-Power-Means. The problem of shape-preservation of K-Power-Means remains unsolved so far, and is of utmost importance for NLOS identification in the millimeter-wave band as we intend to use the angular cluster shapes as a feature for classification.

To extract the clustered feature in mm-wave band, the clustering of PAS is studied with the watershed segmentation method. In millimeter-wave communications, the beam training strategy that scans the whole angular space to identify a strong enough link makes the PAS readily available at Tx and Rx ends. The obtained 2D angular map represents a continuous field-amplitude, which needs to be clustered for channel modeling, or for NLOS identification as it is the case in this thesis. Watershed transformation, which locally reconstructs the gradient field, is more suitable than classical techniques such as the well-known

K-mean algorithm to extract illuminated clusters from the dark background and separate the adjacent clusters in the PAS. Indeed, simulations with IEEE 802.11ad channel model manifested that watershed segmentation preserves the shapes of clusters. However, the standard K-Power-Means ignores the correlation between adjacent elements and therefore fails to preserve the shape of clusters. Through the pretreatment by operations of mathematical morphology benefits to promote the performance, global optimization to look for the global minima limits the K-Power-means. It is the essential difference between watershed and K-Power-Means. To benchmark our watershed-based clustering method, we also proposed a modified K-power-mean algorithm. Here also, it has been found that our proposed method outperforms the K-power-mean algorithm, especially to preserve the shape of the cluster. The power density in the clusters segmented by watershed method is much higher than the ordinary modified K-Power-Means methods. The running time of the watershed method is lower than the K-Power-Means methods.

The space-time structure of transmission channel is used to perform LOS/NLOS identification. Using the 2D power angular spectrum (PAS) obtained over the 57.24 GHz to 65.88 GHz band at Rx after the first stage of a beam training process, a 3D space composed of Angle-Of-Arrival (AOA) in elevation ($\theta$) and in azimuth ($\phi$) and of excess delay is generated. After a clustering process performed in the 2D angular space using the watershed segmentation method, intra-cluster statistical features are determined. It has been found that kurtosis matrix in the time/frequency/space domain is a promising metric in order to discriminate LOS from NLOS. In particular, the minimum over maximum ratio of eigen values obtained by a decomposition of the co-kurtosis matrix, i.e., principal component analysis, has been found to be a sufficient criterion to discriminate LOS from NLOS clusters. This ratio corresponds to a weighted symmetry, and it appears that LOS clusters exhibit much less symmetry than NLOS clusters. The deformed symmetry is generated by the stochastically scattering by the randomly distributed particular structure in the space. The physical process is illustrated by the electromagnetic simulation with Method of Moment (MOM). These findings came from extensive simulations using the IEEE 802.11ad channel model including the effect of antenna radiation pattern. Identification has been then performed using Artificial Neural Network (ANN) and Maximum Likelihood Ratio (MLR) in both simulations and experiments. For MLR, the Probability Density Function (PDF) of the metrics is fitted with Beta distribution with different parameters while the ANN structure is composed of two hidden layers. Under the evaluation of Type I and II errors, the performance of identification with ANN has been found to outperform MLR in all investigated scenarios in identifying NLOS from LOS clusters. The simulation is validated in a laboratory scenario. Driven by a Vector Network Analyzer (VNA), the signal is transmitted by an omnidirectional dipole Tx antenna and received by a directional horn Rx antenna. According to the beam training strategy, the Rx antenna is rotated with motors in both azimuth and elevation. The obtained samples are also hypothesis tested with MLR and ANN. Generalized Extreme Value (GEV) is used to fit the PDF of measured metrics. Out of the 26230 NLOS clusters investigated in the four simulation scenarios, 94.85% have been correctly identified as NLOS and out of the 1000 testing LOS clusters, 95.27% have been correctly identified as LOS. In measurements, out of the 1212 NLOS clusters investigated in the four simulation scenarios, 84.52% have been correctly identified as NLOS and out of the 150 testing LOS clusters, 83.73% have been correctly identified as LOS. The performance of ANN still outperforms MLR. The measurement validates therefore the simulation.

This work can be furtherly studied in several aspects. First, except the power, time-domain kurtosis, and frequency autocorrelation, more physical features can be introduced to assess the nature of NLOS

transmissions, specially by investigation the random dispersion. Indeed, the typical deterministic scattering by walls, ceiling, ground, etc. is well studied in the literature while the dispersion caused by random scattering from furniture and human motion have not been given much interest so far. Based on those specific physical signatures, more mathematical metrics, such as non-stationary dynamic of statistical parameters, could also be used for identification. Also, with the advance of machine learning field, more classification methods could be tested. For instance, Convolutional Neural Network (CNN) and Generative Adversarial Network (GAN), used for image and speech signal processing, are recently attracting a lot of attention because of its high capacity of classification, particularly valuable to study NLOS identification. Finally, the NLOS identification is to be embedded in current wireless communication systems. To achieve this aim, more effective beam training strategy and spatial signal estimation method with high resolution are also necessary research targets.

# Appendix A

# Physical Mechanism of Identification

## Contents



As the discussion in chapter 2, NLOS identification is a recognition of the physical characteristics of radio scattering. As discussed in chapter 1, for the 60 GHz indoor NLOS identification, three characteristics different from the low-frequency outdoor identification: high material attenuation and high directional antenna pattern to take over the high attenuation. After clustering with watershed segmentation, the intracluster scattering characteristics are the identifying features. In the IEEE 802.11ad model, the simplest clusters are generated by two typical structures for the indoor scenarios, layered wall, and rough surface. To further clarify the intracluster physical mechanism, the scattering is simulated with a full-wave electromagnetic simulation method, Method of Moment (MOM), to solve the scattering of the two particular geometrical structures.

## A.1 Brief Introduction of MOM

MOM is an integral equation (IE) method. The advantage of IE is the simulation in the large and open domain. In this study, it is used to simulate the scattering for a particular structure in the indoor scenario.

### A.1.1 Continuous integral equations

The wave equations from the Maxwell equation in the frequency domain are:

$$\nabla \times \boldsymbol{E} = -j\omega\mu_0 \boldsymbol{H} \tag{A.1}$$

$$\nabla \times \boldsymbol{H} = \boldsymbol{J} + j\omega\varepsilon \boldsymbol{E} \tag{A.2}$$

Where $\boldsymbol{H}$ is the magnetic field vector and $\boldsymbol{E}$ is the electric field vector. $\omega$ is the angular frequency. $\varepsilon$ is the complex permittivity and $\mu$ is the permeability. The boundary conditions between two media $\Omega_0$ and $\Omega_1$ are:

$$\hat{\boldsymbol{n}} \times \left( \boldsymbol{E}_0 - \boldsymbol{E}_1 \right) = 0 \tag{A.3}$$

$$\hat{\boldsymbol{n}} \cdot \left( \boldsymbol{H}_0 - \boldsymbol{H}_1 \right) = 0 \tag{A.4}$$

Where $\hat{\boldsymbol{n}}$ is the normal vector of the boundary surface. Without loss of generality, the simulation is constrained in the 2D ($x$, $z$) plane. The reflection of TE and TM incident wave at a surface $S$ between two media $\Omega_0$ and $\Omega_1$ are shown in Figure A.1. The incident wave vector $\boldsymbol{k}_i$ with incident angle $\theta_i$ is reflected by the surface as reflected wave vector $\boldsymbol{k}_r$ with reflecting angle $\theta_r$, and transmitted wave vector $\boldsymbol{k}_t$ with the transmitted angle $\theta_t$.

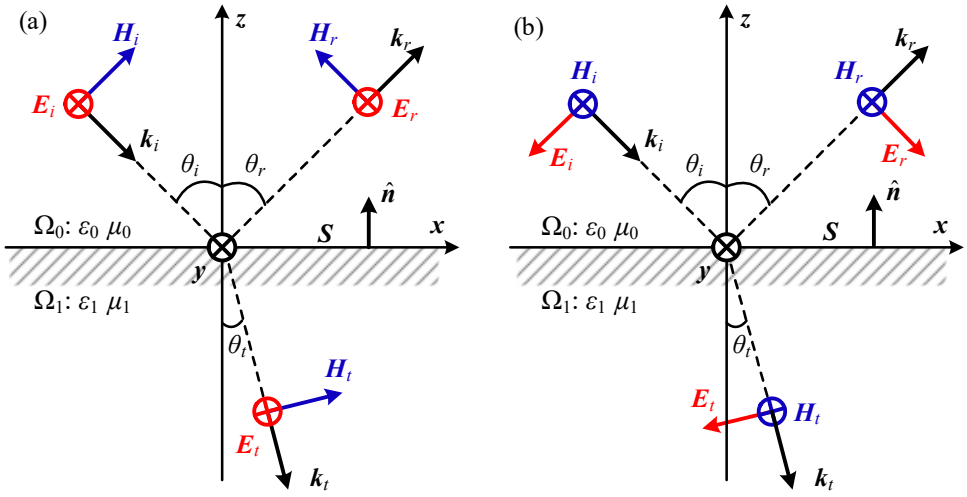


Figure A.1 Reflection of (a) TE and (b) TM waves at a surface S

In Figure A.1 (a), $\boldsymbol{E} = \phi(\boldsymbol{r})\hat{\boldsymbol{y}}$. In Figure A.1 (b) , $\boldsymbol{H} = \phi(\boldsymbol{r})\hat{\boldsymbol{y}}$. Therefore, with $k = \omega\sqrt{\varepsilon_i \mu_0}$ , the vector Maxwell equations (A.1) and (A.2) are simplified as scalar Helmholtz equations in 2D:

$$\nabla^2 \phi_i(\boldsymbol{r}) + k_i^2 \phi_i(\boldsymbol{r}) = 0, r \in \Omega_i \tag{A.5}$$

The vector boundary conditions (A.3) and (A.4) are simplified as a scalar boundary condition of TE and TM in Figure A.1:

$$\begin{cases} \phi_0(\boldsymbol{r}) = \phi_1(\boldsymbol{r}) \\ \hat{\boldsymbol{n}} \cdot \nabla \phi_0(\boldsymbol{r}) = \hat{\boldsymbol{n}} \cdot \rho_{01} \nabla \phi_1(\boldsymbol{r}) \end{cases}, \boldsymbol{r} \in S \tag{A.6}$$

For TE polarization, $\rho_{01} = 1$; for TM polarization, $\rho_{01} = \varepsilon_0/\varepsilon_1$.

For a linear system, the response of a source is a linear combination of the responses of an impulse point source. The response at position $\boldsymbol{r}$' of an impulse point source $\delta(\boldsymbol{r} - \boldsymbol{r}')$ at position $\boldsymbol{r}$ can be described with the Green function $g(\boldsymbol{r}, \boldsymbol{r}')$ for Helmholtz equations:

$$\nabla^2 g_i(\boldsymbol{r},\boldsymbol{r}') + k_i^2 g_i(\boldsymbol{r},\boldsymbol{r}') = \delta(\boldsymbol{r}-\boldsymbol{r}'), \boldsymbol{r},\boldsymbol{r}' \in \Omega_i \tag{A.7}$$

For 2D problem, the Green function in the $i$-th media is

$$g_i(\boldsymbol{r},\boldsymbol{r}') = \frac{j}{4} H_0^{(1)}\left(k_i|\boldsymbol{r}-\boldsymbol{r}'|\right) \tag{A.8}$$

where $H_0^{(1)}$ is the zeroth-order Hankel function of the first kind. By the Huygens principle, the boundary $C$ of domain $\Omega$ is considered as a concentration of the point sources. The field in domain $\Omega$ can be transformed into radiation of the boundary $C$ under an incident field, which is achieved with considering the Green theorem:

$$\iint_\Omega \left(f_1\nabla^2 f_2 - f_2\nabla^2 f_1\right) dr = \oint_C \left(f_1\nabla f_2 - f_2\nabla f_1\right)\cdot d\boldsymbol{S} \tag{A.9}$$

The scalar integral equations are obtained by (A.5), (A.6), (A.7) and (A.9) [1]:

$$\phi_{inc}(\boldsymbol{r}') = \frac{1}{2}\phi_0(\boldsymbol{r}') - P\int_C \phi_0(\boldsymbol{r})\frac{\partial g_0(\boldsymbol{r},\boldsymbol{r}')}{\partial n} dS + \int_C g_0(\boldsymbol{r},\boldsymbol{r}')\frac{\partial \phi_0(\boldsymbol{r})}{\partial n} dS \tag{A.10}$$

$$0 = -\frac{1}{2}\phi_0(\boldsymbol{r}') - P\int_C \phi_0(\boldsymbol{r})\frac{\partial g_1(\boldsymbol{r},\boldsymbol{r}')}{\partial n} dS + \int_C \frac{1}{\rho_{01}} g_1(\boldsymbol{r},\boldsymbol{r}')\frac{\partial \phi_0(\boldsymbol{r})}{\partial n} dS \tag{A.11}$$

Where $P$ means Cauchy principal value. Therefore, the field $\phi(\boldsymbol{r}')$ can be expressed as the combination of impulse radiation of surface point currents $\phi(\boldsymbol{r})$ and $\partial\phi(\boldsymbol{r}) / \partial n$, under the incident field $\phi_{inc}(\boldsymbol{r}')$. It matches the requirement of the linear system. The first and second terms of (A.10) and (A.11) are the Neumann boundary condition, while the third terms are the Dirichlet boundary conditions. The unknown variables are the surface currents $\phi(\boldsymbol{r})$ and $\partial\phi(\boldsymbol{r}) / \partial n$.

# A.1.2 Discrete linear equations

The linear IE of (A.10) and (A.11) in form $\mathcal{L}(f) = g$ can be solved with discrete equations. Where $\mathcal{L}$ is the integral equation operator, $f$ is the unknown function and $u$ is the known function. An approximate solution of $f$ is expending the unknown variables with $N$ bias functions $f_1, f_2, \ldots, f_n$:

$$\hat{f} = \sum_{n=1}^{N} a_n f_n \tag{A.12}$$

Therefore, IE is discretized with a residual $\varepsilon$ as:

$$\mathcal{L}(f) \approx \mathcal{L}\left(\hat{f}\right) = \sum_{n=1}^{N} a_n \mathcal{L}(f_n) + \varepsilon = u \tag{A.13}$$

To minimize the residual $\varepsilon$, inducing $M$ weighting functions $w_1$, $w_2$, …, $w_M$, to make each $w_m$ orthogonal to the residual $\langle w_m, \varepsilon \rangle = 0$:

$$\left\langle w_m, \mathcal{L}\left(\hat{f}\right)\right\rangle = \sum_{n=1}^{N} a_n \left\langle w_m, \mathcal{L}(f_n)\right\rangle = \left\langle w_m, u\right\rangle \tag{A.14}$$

Therefore, the EI $\mathcal{L}(f) = u$ is discrete as linear equations:

$$\underline{Z}\boldsymbol{x} = \boldsymbol{b} \tag{A.15}$$

The element of the impedance matrix $\underline{Z}$ and excitation vector $\boldsymbol{b}$ are $Z_{mn} = \langle w_m, \mathcal{L}(f_n)\rangle$ and $b_m = \langle w_m, u\rangle$. MOM select the weight function by a point-matching method with $w_m = \delta(x - x_m)$. Therefore, the elements become:

$$Z_{mn} = \mathcal{L}\left[f_n(x_m)\right] \tag{A.16}$$

$$b_m = u(x_m) \tag{A.17}$$

The discretization of IEs (A.10) and (A.11) is the discretization of the boundary surface into elements. Then the field of each point in the domain can be solved by a linear combination of the radiations by the surface currents on all of the surface elements, according to discrete equations (A.15). The essence of IEs (A.10) and (A.11) are the combinations of Neumann and Dirichlet boundary conditions. So, specifying the equation (A.15) for parts of Neumann boundary conditions in (A.10) and (A.11) :

$$\mathcal{L} = \int_{-L/2}^{L/2} \sqrt{1 + \left(\frac{dz}{dx}\right)^2}\, g(\boldsymbol{r}, \boldsymbol{r}')\, dx \tag{A.18}$$

$$f = \frac{\partial \phi(\boldsymbol{r})}{\partial n} \tag{A.19}$$

Or for parts of Dirichlet boundary conditions:

$$\mathcal{L} = \int_{-L/2}^{L/2} \frac{\partial g(\boldsymbol{r}, \boldsymbol{r}')}{\partial n} dx \tag{A.20}$$

$$f = \phi(\boldsymbol{r}) \tag{A.21}$$

And the unknown function is the incident wave $u = \phi_{inc}(\boldsymbol{r})$. After derivation, a general impedance matrix $\underline{Z}$ with mixed boundary conditions is obtained [1]:

$$\underline{Z} = \begin{bmatrix} \underline{Z}_{Neu} & \underline{Z}_{Dir} \\ \underline{Z}_{Neu,k_0 \to k_1} & \dfrac{1}{\rho_{01}} \underline{Z}_{Dir,k_0 \to k_1} \end{bmatrix} \tag{A.22}$$

Where the elements for the blocks $\underline{Z}_{Neu}$ with Neumann boundary condition are:

$$Z_{mn} = \begin{cases} \dfrac{1}{2} - \dfrac{j\Delta_n}{4\pi} \dfrac{\gamma_n'}{1+\gamma_n^2}, & m = n \\ -\dfrac{j\Delta_n}{4} \dfrac{H_1^{(1)}\left(k_0 \left|\boldsymbol{r}_n - \boldsymbol{r}_m\right|\right)}{\left|\boldsymbol{r}_n - \boldsymbol{r}_m\right|} \left[\gamma_n \left(x_n - x_m\right) - \left(z_n - z_m\right)\right], & m \neq n \end{cases} \tag{A.23}$$

The elements for the blocks $\underline{Z}_{Dir}$ with Dirichlet boundary condition are:

$$Z_{mn} = \begin{cases} \dfrac{j\Delta_n \sqrt{1+\gamma_n^2}}{4} \left[1 + \dfrac{2j}{\pi} \ln\left(0.164 k_0 \Delta_n \sqrt{1+\gamma_n^2}\right)\right], & m = n \\ \dfrac{j\Delta_n \sqrt{1+\gamma_n^2}}{4} H_0^{(1)}\left(k_0 \left|\boldsymbol{r}_n - \boldsymbol{r}_m\right|\right), & m \neq n \end{cases} \tag{A.24}$$

Where, $\gamma_n = dz_n / dx_n$ and $\Delta_n = \beta_n - \alpha_n \leq \lambda_0 / 10$. For $\underline{Z}_{Neu,k0 \to k1}$, the Cauchy principal value is 0.5, while, it is -0.5 for $\underline{Z}_{Neu}$ The excitation vector $\boldsymbol{b}$ on the $N$ discrete surface elements is:

$$\boldsymbol{b} = \left[\phi_{inc}(\boldsymbol{r}_1), \phi_{inc}(\boldsymbol{r}_2), \cdots, \phi_{inc}(\boldsymbol{r}_N), 0, 0, \cdots, 0\right]^T \tag{A.25}$$

The unknown variable vector $\boldsymbol{x}$ of the $N$ discrete surface elements is:

$$\boldsymbol{x} = \left[\phi_0(\boldsymbol{r}_1), \phi_0(\boldsymbol{r}_2), \cdots, \phi_0(\boldsymbol{r}_N), \frac{\partial \phi_0(\boldsymbol{r}_1)}{\partial n}, \frac{\partial \phi_0(\boldsymbol{r}_2)}{\partial n}, \cdots, \frac{\partial \phi_0(\boldsymbol{r}_N)}{\partial n}\right]^T \tag{A.26}$$

Then, the specific form of equations (A.15) can be solved with general methods, such as LU

decomposition.

# A.2 Typical Geometrical Structures for Indoor Scenarios

As discussed in chapters 1 and 2, the simplest clustered channel of IEEE 802.11ad is formed by the reflections of the walls in the conference room. There are two particular structures of the walls: layered structures and rough surfaces. The two structures mainly generate the intra-cluster radio propagating feature. A typical interior wall of an office scenario is with a layered structure [2], as shown in Figure A.2. An aerated concrete wall body is covered with two plaster planes. The standard thickness of the plaster plane is 12 mm. The air gap is assumed to be 10 mm. The thickness of the aerated concrete wall body is 55 mm. The total 100 mm thickness is measured in a microwave wireless facilities lab at Sorbonne University.

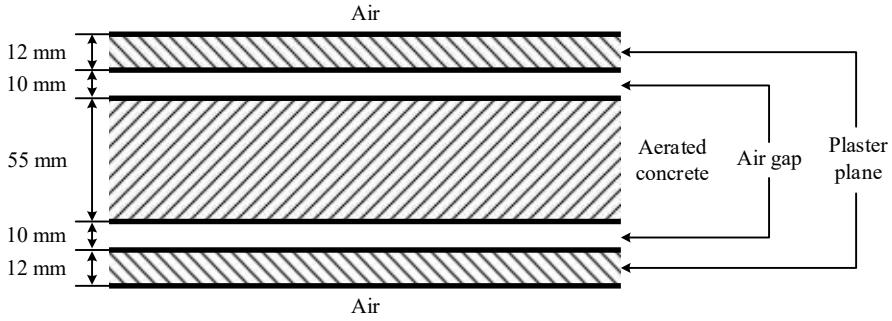


Figure A.2 Layered structure of walls

The second type of structure is the rough surface. The rough surface for 2D MOM is a 1D autocorrelated random line. The height profile $c_z(x)$ is the autocorrelation between two heights on the surface of position $x_1$ and $x_2$:

$$c_z(x) = \langle z(x_1) z(x_1 + x) \rangle = \frac{1}{L} \int_0^L z(x_1) z(x_1 + x) dx_1 \tag{A.27}$$

The random heights $z$ is a convolution between $c_z(x)$ and random numbers $s$, which can be obtained by inverse Fourier transformation [3]:

$$z = \sqrt{c_z(x)} * s = \mathcal{F}^{-1}\left[\sqrt{C_z(k)} S(k)\right] \tag{A.28}$$

Where $C_z(k)$ is the Power Spectral Density (PSD) of $z(x)$. $S(k) = \mathcal{F}[s]$. To make z is real, there is a constraint $S^*(-k) = S(k)$. A Gaussian white process $s$ matches this constraint, and provide a power spectrum of unitary variance $C_s(k) = 1$. The Fourier transform of the Gaussian process is also a Gaussian process. The Probability Density Function (PDF) of the Gaussian spatial distribution is:

$$p_z = \frac{1}{\sigma_z \sqrt{2\pi}} \exp\left[ -\frac{(z - z_0)^2}{2\sigma_z^2} \right] \tag{A.29}$$

Where $\sigma_z$ is the standard deviation. The autocorrelation $c_z(x)$ can be Gaussian:

$$c_z(x) = \sigma_z^2 \exp\left( -\frac{x^2}{L_c^2} \right) \tag{A.30}$$

Where $L_c$ is the correlation length. The corresponding PSD are

$$C_z(x) = \sigma_z^2 L_c \sqrt{\pi} \exp\left( -\frac{k^2 L_c^2}{4} \right) \tag{A.31}$$

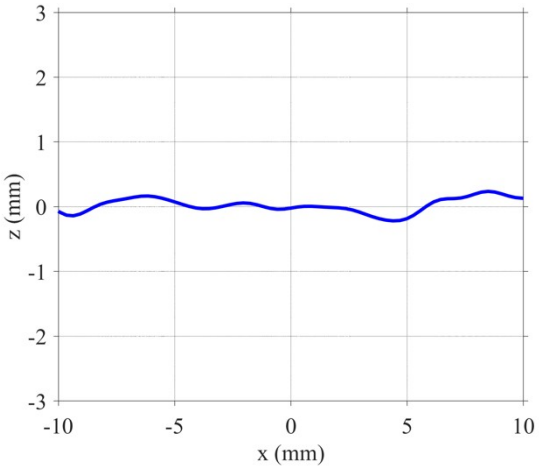


Figure A.3 Local graph of rough surface

With typical parameters for plaster surface $L_c$ = 1.7 mm and $\sigma_z$ = 0.15 mm [4], the random surface is generated for simulation as shown in Figure A.3.

# A.3 Dielectric Properties of Materials

A material model suggested by the International Telecommunication Union (ITU) is used in this simulation. The complex relative permittivity is

$$\varepsilon'_r = \varepsilon_r + j \frac{\sigma}{\omega \varepsilon_0} \tag{A.32}$$

Where the relative permittivity $\varepsilon_r$ and electric conductivity $\sigma$ are [5]

$$\varepsilon_r = af^b \tag{A.33}$$

$$\sigma = cf^d \tag{A.34}$$

Table A.1 Parameters in ITU material model [5]

| | *a* | *b* | *c* | *d* |
|---|---|---|---|---|
| Air | 1 | 0 | 0 | 0 |
| Plaster | 2.94 | 0 | 0.0116 | 0.7076 |
| Concrete | 5.31 | 0 | 0.0326 | 0.8095 |
| Brick | 3.75 | 0 | 0.038 | 0 |

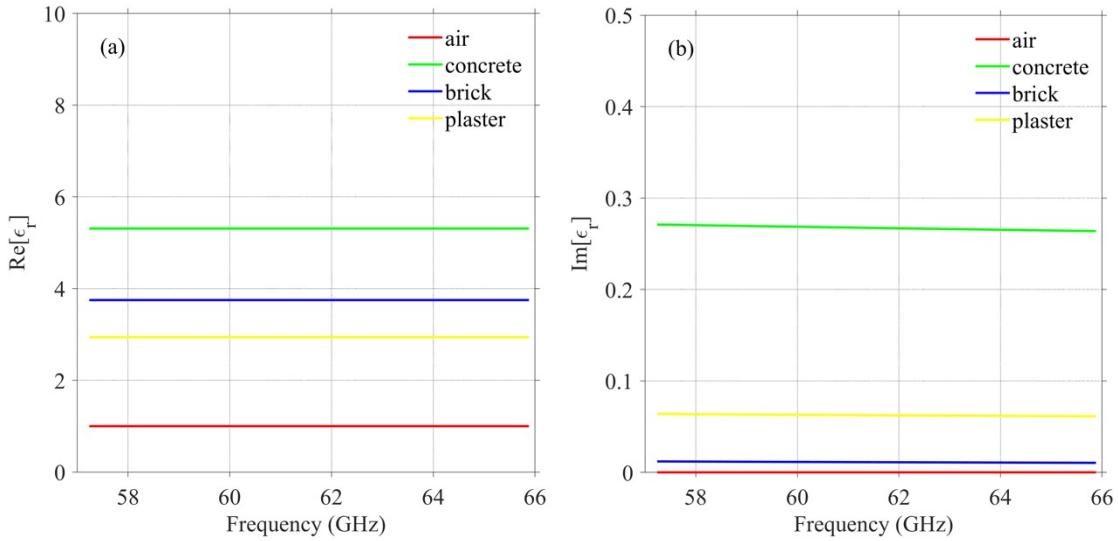


Figure A.4 (a) Real and (b) imaginary part of the complex relative permittivity

The parameters a and b are listed in Table A.1. The real and complex relative permittivity for air, plaster, and concrete with the ITU material model are listed in Figure A.4. In the simulation, the parameters of brick are used to replace concrete for aerated concrete.

# A.4 Simulation result

With the above material characteristics, the scattering by the above structure is simulated. The antenna pattern of IEEE 802.11ad is the Gaussian model. The antenna pattern and the near-field of 45° incident beam for both TE and TM wave are shown in Figure A.5.

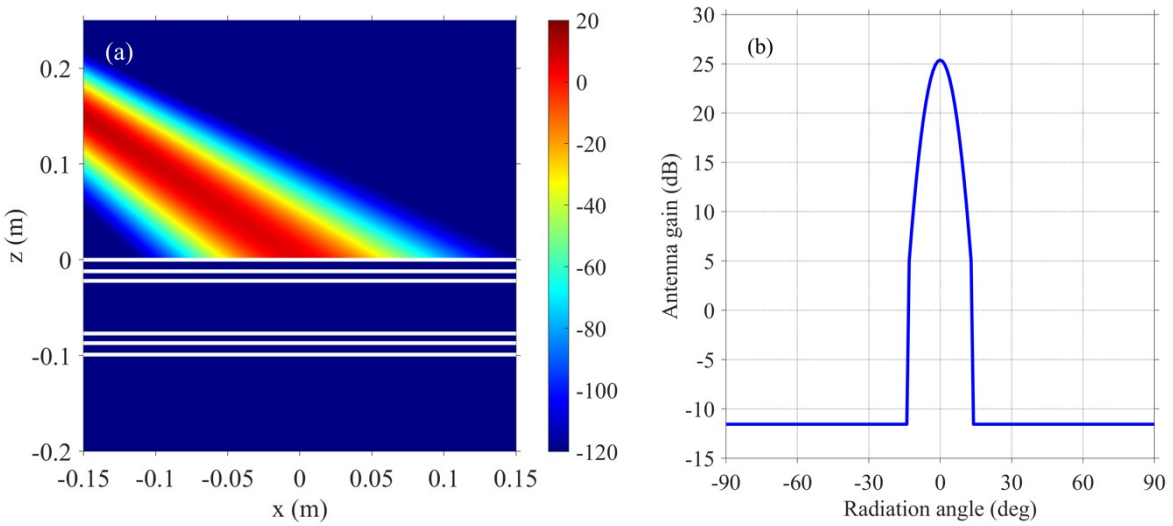


Figure A.5 (a) Near-field of 45° incident beam with (b) ideal Gaussian antenna pattern of 5° HPBW.

Apart from the near-field scattering, the far-field scattering is more valuable to evaluate to the scattering characteristics. The far-field scattering is indicated with the Radar Cross Section (RCS):

$$RCS = \lim_{r'\to\infty} 2\pi r' \left| \frac{\phi_{sca}}{\phi_{inc}} \right| \tag{A.35}$$

Where $\phi_{sca}$ and $\phi_{inc}$ are near-field scattering and incident field. Inducing a far-field approximation when $r' \to \infty$, $|\boldsymbol{r} - \boldsymbol{r}'| \approx r' - \boldsymbol{k}_{sca} \cdot \boldsymbol{r}$, the Green function is simplified as:

$$g(\boldsymbol{r}, \boldsymbol{r}') = \frac{j}{4} H_0^{(1)}\left(k_0 |\boldsymbol{r} - \boldsymbol{r}'|\right) \approx \frac{j}{4}\sqrt{\frac{2}{\pi k_0 r'}} \exp\left[ j\left( k_0 r' - \boldsymbol{k}_{sca} \cdot \boldsymbol{r} - \frac{\pi}{4} \right)\right] \tag{A.36}$$

Considering the IE (A.10) as well, the RCS is derived as:

$$RCS = \frac{\left|\phi_{sca}^{\infty}\right|^2}{4|k_0|} \tag{A.37}$$

Where

$$\phi_{sca}^{\infty} = -\frac{1}{\phi_{inc}} \int_S \left[ j\boldsymbol{k}_{sca} \cdot \hat{\boldsymbol{n}} \phi_0(\boldsymbol{r}) + \frac{\partial \phi_0(\boldsymbol{r})}{\partial n} \right] \exp\left(-j\boldsymbol{k}_{sca} \cdot \boldsymbol{r}\right) dS \tag{A.38}$$

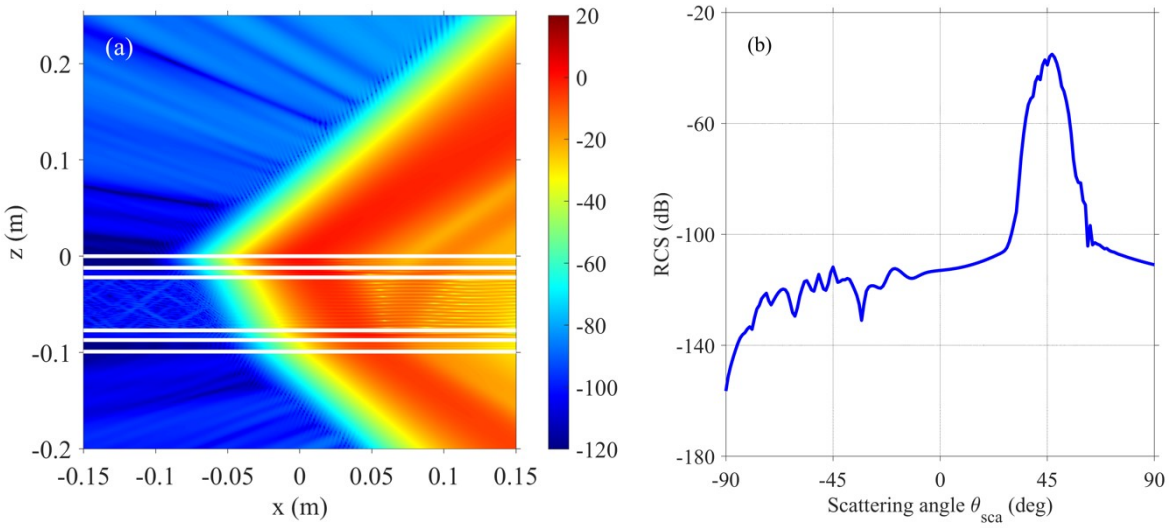


Figure A.6 (a) Near-field scattering and (b) far-field RCS of TE wave incident on a layered wall.

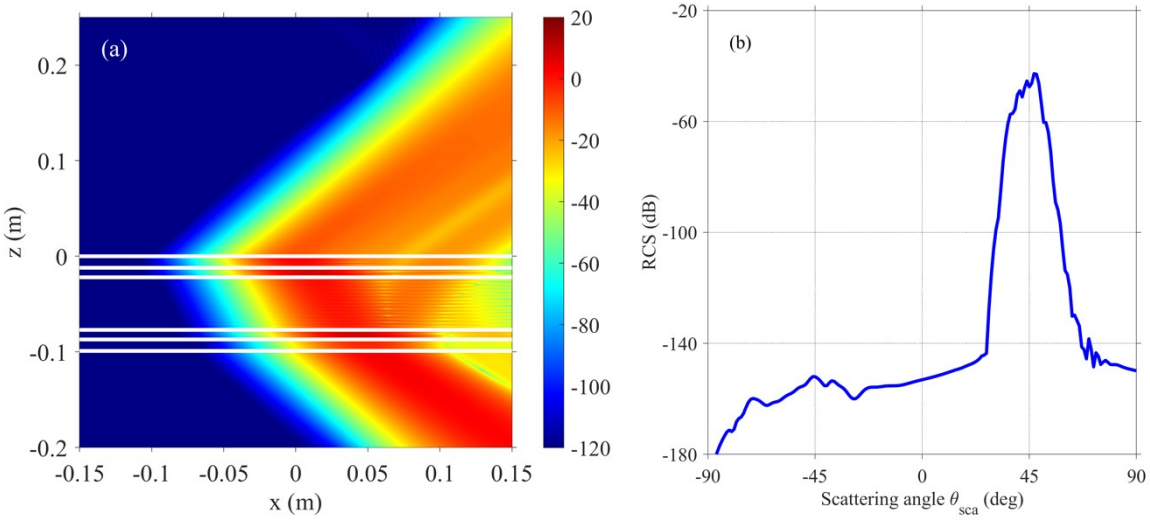


Figure A.7 (a) Near-field scattering and (b) far-field RCS of TM wave incident on a layered wall.

The near-field and far-field scattering of TE and TM incident wave for the layered wall are shown in Figure A.6 and Figure A.7. Both the near-fields mainly scattering in the direction of 45°. Weak scattering side-lobs are below -100 dB. Instead of breaking into pieces, the scattering beams preserved as whole clusters in the far-field RCS. Comparing with the ideal Gaussian antenna pattern in Figure A.5 (b), the shapes of the RCS clusters are deformed by the coherence inside the geometrical structure.

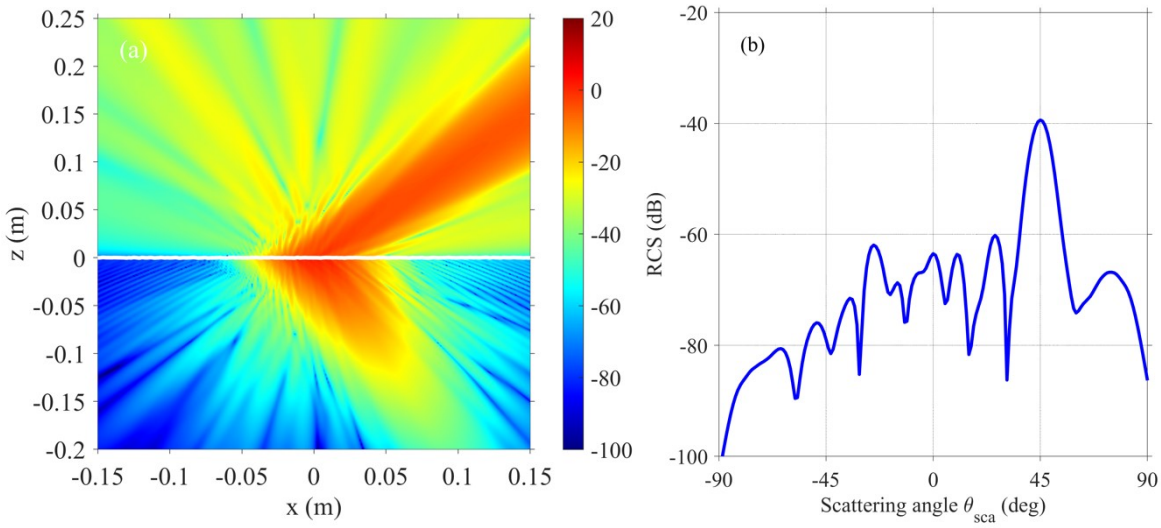


Figure A.8 (a) Near-field scattering and (b) far-field RCS of TE wave incident on a rough plaster surface.

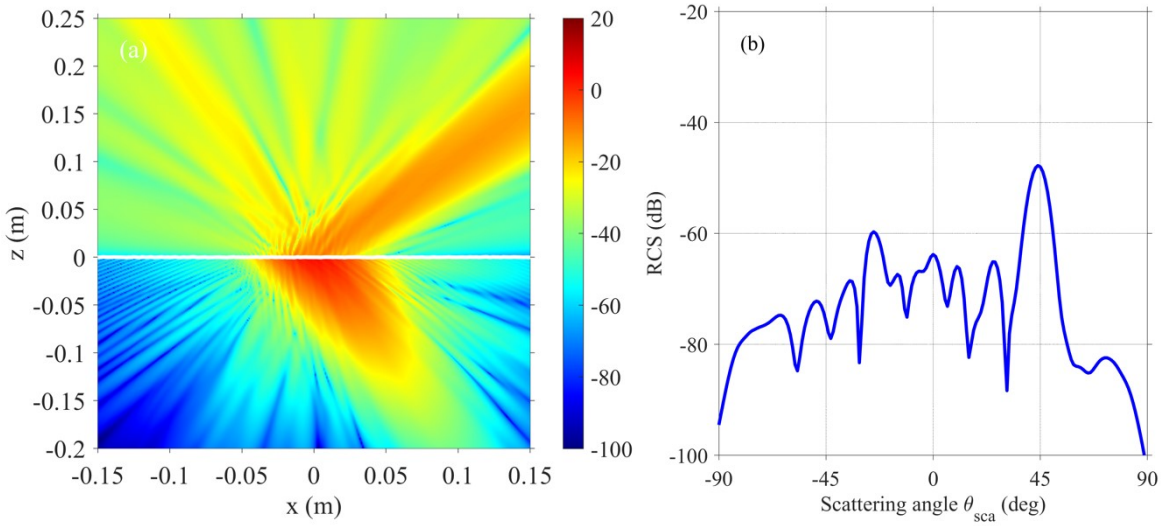


Figure A.9 (a) Near-field scattering and (b) far-field RCS of TM wave incident on a rough plaster surface.

The near-field and far-field scattering of TE and TM incident wave for rough plaster surface are shown in Figure A.8 and Figure A.9. Different from the shape-preservation of the scattering by the layered wall, the incident beam shape breaks into pieces in far-field RCS. The side-lobes are higher than -80 dB and almost comparable with the main lobs. With the scattering by the rougher severe surface or randomly distributed independent objects, the scattering in far-field will be more spread. Therefore, the widespread spatial clusters are an apparent physical feature for NLOS identification.

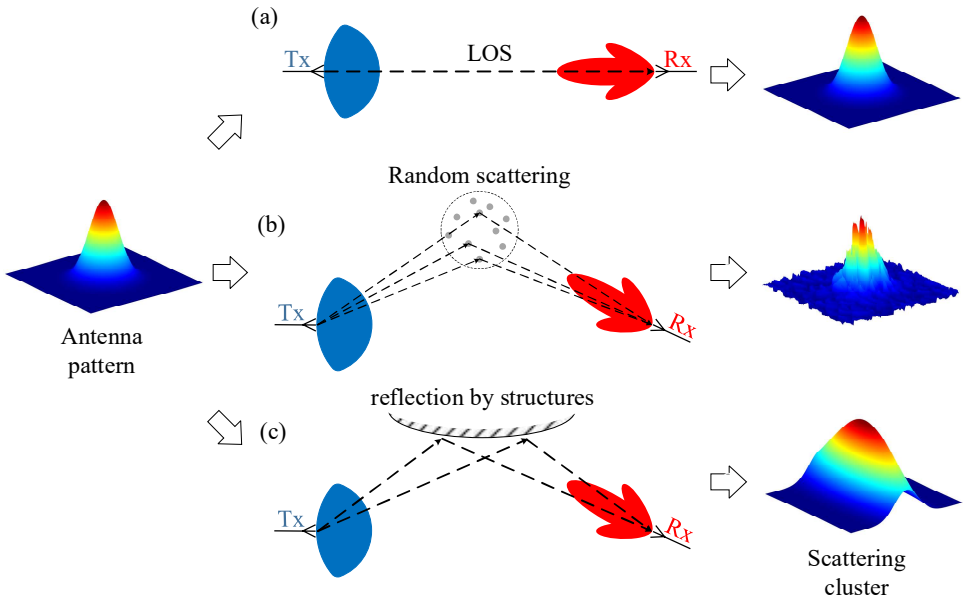


Figure A.10 Deformation of scattering cluster due to: (a) LOS transmission; (b) random scattering; (c) particular structures.

Based on the result of simulation with MOM, a physical feature for the NLOS identification with narrow beams is obvious. The shape of the angular clusters in the PAS 2D map is an effective way to investigate the characteristics of the scattering behaviors in LOS or NLOS transmission. A canonical example is shown in Figure A.10 where the phenomenon occurring within the channel can be observed on the received PAS within a given cluster. The Tx pattern in the beam training is here omnidirectional while the Rx pattern formed by the antenna array is almost rotational symmetric. In Figure A.10 (a), the transmitted power pattern is preserved due to the absence of scattering objects in the LOS transmission. Thus, the PAS within this LOS cluster exhibits an almost rotational symmetric, identical to the Rx radiation pattern. However, in Figure A.10 (b), the PAS is randomly deformed by the stochastically distributed scatterers. Even when reflected by smooth reflectors, NLOS clusters are affected. Indeed, the PAS of a cluster reflected by particular complex structure a reflector surface, such as multi-layer, is also deformed as seen in Figure A.10 (c). This illustrates the motivation of our work. Although the capacity of spatially classifying the clusters is limited by the resolution of beam training, the identification could still be achieved. Consequently, in this thesis, we intend to analyze deeper the clustered PAS features in order to assess their suitability for NLOS identification.

# References

[1] C. Bourlier, N. Pinel, and G. Kubické, *Method of Moments for 2D Scattering Problems: Basic Concepts and Applications*: ISTE, Ltd. and John Wiley & Sons, Inc., 2013.

[2] P. F. Lyu, X. Y. Xu, S. Yan, and Z. X. Ren, "60 GHz Indoor Propagation With Time-Domain Geometric-Optics," *IEEE Transactions on Magnetics,* vol. 52, no. 3, Mar, 2016.

[3] N. Pinel, and C. Bourlier, *Electromagnetic Wave Scattering from Random Rough Surfaces: Asymptotic Models*: John Wiley & Sons, Inc., 2013.

[4] R. Piesiewicz, C. Jansen, D. Mittleman, T. Kleine-Ostmann, M. Koch, and T. Kurner, “Scattering analysis for the modeling of THz communication systems,” *IEEE Transactions on Antennas and Propagation,* vol. 55, no. 11, pp. 3002-3009, Nov, 2007.

[5] *Effects of building materials and structures on radiowave propagation above about 100 MHz-P Series Radiowave propagation,* Recommendation ITU-R P.2040-1, P Series Radiowave propagation.

# List of Figures

# List of Tables

# List of Algorithms

# List of Publication

[1] Pengfei Lyu, Julien Sarrazin, Xiaoyu Xu, Shuai Yan, Aziz Benlarbi-Delaï and Zhuoxiang Ren, “Study of Statistical Characteristics of Channel Model with Ray Tracing Based Geometrical Optics method”, 22st International Conference on the Computation of Electromagnetic Fields (Compumag), Paris, France, July 15-19, 2019;

[2] Pengfei Lyu, Julien Sarrazin, Zhuoxiang Ren and Aziz Benlarbi-Delaï, “Identification de situations LOS ou NLOS en ondes millimétriques basée sur les statistiques angulaires du canal de propagation”, 21ème Journées Nationales Microondes, Caen, France, May14-17, 2019 ;

[3] Pengfei Lyu, Julien Sarrazin, Zhuoxiang Ren and Aziz Benlarbi-Delaï, “Identification of LOS and NLOS Clusters Based on Angular (AOA) Features at 60 GHz”, 2ème Workshop International Technologies de l'Information et communication sous le thème IoT au service d'une Ville intelligente, Lille, France, July 1-12, 2019.

[4] Pengfei Lyu, Aziz Benlarbi-Delaï, Zhuoxiang Ren, Julien Sarrazin, "Spatially Clustering with Watershed Transformation for Millimeter Wave Indoor Channel Modelling", to be submitted

# Résumé de la Thèse

## Contents



# 1. Contexte et Historique

## 1.1. Introduction

Avec l'émergence des objets connectés, de l'IoT et de la nouvelle norme de communication 5G, les applications potentielles requérant la localisation indoor ou la continuité de localisation réapparaissent et suscitent, depuis quelques années déjà, de nombreuses études et recherches.

Avec une fréquence centrale de 60 GHz et une bande passante de 8,64 GHz la norme IEEE 802.11ad est un candidat potentiel pour résoudre le problème de localisation tout en assurant simultanément une communication très haut débit. Cette capacité de localiser avec précision un objet communicant est liée d'une part à la fréquence porteuse qui permet, par traitement de la phase du signal, une résolution millimétrique, mais aussi à la bande passante qui permet, par traitement des temps d'arrivées, outre une résolution centimétrique, de s'affranchir des trajets multiples notamment liés au contexte indoor.

Cette norme prometteuse pose toutefois un problème lié au caractère directionnel de la propagation dans le domaine millimétrique, et qui est donc particulièrement sujette au blocage des ondes directes. En effet aucun calcul de coordonnées spatio-temporelles ne peut être entrepris si les signaux d'intérêt traités ne proviennent pas d'une propagation en ligne directe (LOS pour Line Of Sight) entre l'objet à localiser et le (ou les) site(s) de référence. Cette limitation induit par conséquent une nouvelle problématique dans le domaine de la localisation qui consiste à s'assurer, dans les signaux en jeu, de la présence de la composante liée à l'existence d'un trajet direct. Cela revient aussi à identifier, dans ces signaux, les composantes NLOS issues principalement des réflexions multiples. L'objectif de ce mémoire est d'identifier, dans la bande centrée autour de 60GHz, les composantes LOS et NLOS et d'atténuer les effets de ces dernières pour ne laisser subsister, dans le calcul de la localisation, que la composante directe.

# 1.2. Localisation à l'Intérieur

La localisation sans fil est le processus qui consiste à déterminer, principalement par les techniques de triangulation ou de « fingerprinting », les coordonnées spatiales d'un objet en détectant les ondes électromagnétiques. En extérieur, elle est représentée principalement par le très populaire système de positionnement global (GPS). En « indoor », ses applications potentielles, très nombreuses et variées, peuvent l'amener au même niveau de popularité que le GPS.

Le processus de localisation fondée sur la triangulation est divisé en trois étapes. Dans la première étape, les informations de distance entre l'émetteur et le récepteur sont extraites des paramètres caractéristiques du signal reçu, tels que l'intensité du signal reçu (RSS : *Received Signal Strenght*), l'angle d'arrivée (AOA : *Angle Of Arrival*) et le temps d'arrivée (TOA : *Time Of Arrival*). La deuxième étape consiste à trouver les coordonnées du terminal par le biais de relations géométriques. En raison des erreurs systématiques ou aléatoires dans la distance mesurée, les coordonnées obtenues à partir de la distance mesurée ne sont, par nature, pas très précises. Par conséquent, la troisième étape consiste à réduire ces erreurs et à estimer, en se fondant sur une approche statistique les coordonnées de l'objet connecté.

Dans la majorité des situations rencontrées, la CIR (*Channel Impulse Response*) exhibe des pics dont l'intensité est en lien direct avec les temps d'arrivée du signal direct et des différentes répliques. Le premier pic correspond donc au chemin direct et les pics suivants aux contributions de trajets multiples. Toutefois si le chemin direct est obstrué, il en résulte une confusion quant à la classification des pics de la CIR qui se révèle être préjudiciable pour la localisation basée sur la TOA. Pour les autres métriques comme l'AOA et le RSS, les erreurs introduites obéissent aux mêmes règles. Il en résulte dans tous les cas, des positions estimées qui suivent une distribution statistique biaisée admettant une variance plus au moins grande en fonction de la proportion des trajets multiples relativement à celle du trajet direct.

# 1.3. Localisation et Communication par Ondes Millimétriques

La cinquième génération de réseaux sans fil (5G) est la prochaine génération de communication sans fil qui répond entr'autres aux exigences de l'ultra-haut débit et de la robustesse. Grâce à la formation de

faisceaux, apportée par les techniques massive MIMO (*Multiple Input Multiple Output*), et aux solutions qu'elle induit en termes de portée et de connexité, les organismes de normalisation considèrent les ondes millimétriques comme un excellent candidat pour répondre aux exigences de la norme 5G. Par ailleurs, en raison de la faible taille de l'antenne, la bande considérée convient aux applications intérieures basées sur des dispositifs intégrés, d'autant qu'elle ne nécessite pas de licence particulière dans un grand nombre de pays. Parmi les normes utilisant la fréquence de 60 GHz, citons la norme IEEE 802.11ad, qui attribue la bande comprise entre 57,24 GHz et 65,88 GHz. Toutes ces potentialités aident à réduire les interférences entre les utilisateurs (ISI), et à améliorer le gain spatial de la liaison radioélectrique.

Par conséquent, du point de la communication, un chemin direct bloqué n'est pas rédhibitoire. En effet grâce à la stratégie de formation de voies, d'autres chemins sont explorés pour rétablir la liaison et maintenir une bonne qualité de service en termes de SNR ou de BER. Cette solution n'est naturellement d'aucun secours pour la localisation. Il convient donc de proposer des modélisations ou caractérisations de canal qui mettent l'accent sur la probabilité de présence d'un trajet direct.

# 1.4. Modélisation du Canal à Ondes Millimétriques

Le profil typique d'un canal comprend des caractéristiques à petite échelle et des caractéristiques à grande échelle. Les caractéristiques à petite échelle représentent généralement les dispersions temporelle et spatiale causées par la propagation par trajets multiples des ondes radio dans l'espace. Elles entraînent une sélectivité en fréquence, ainsi qu'une distorsion du signal et une diaphonie. L'évanouissement à grande échelle est la fluctuation de la puissance moyenne du signal mesuré sur de grandes distances (plusieurs dizaines de longueurs d'onde). Les effets d'ombrage et d'affaiblissement résultant réduisent la zone de couverture.

La plupart des modèles de canaux actuels, les canaux SISO (*Single Input-Single Output*) en intérieur ou les canaux MIMO en extérieur, sont basés sur le même modèle physique de CIR : les diffuseurs répartis par groupes rétrodiffusent les faisceaux émis entre les stations de base (BS) et les antennes UE (*User Equipment*) dans l'espace. Par conséquent, le CIR est simplifié en deux parties : le comportement des groupes et le comportement à l'intérieur des groupes. La CIR est modélisée comme une combinaison linéaire d'ondes planes diffusées par un groupe. Les clusters dans le modèle de canal IEEE 802.11ad sont classés comme LOS et NLOS. Les amas géométriques de diffuseurs sont distribués de façon stochastique dans l'espace physique. Les paramètres correspondants du modèle de canal ci-dessus, TOA, AOA et AOD (*Angle of Departure*), sont donc également statistiques. Ainsi, la modélisation des canaux consiste à déterminer la distribution statistique des paramètres dans le modèle des canaux de diffusion en grappes.

Un processus typique de modélisation du canal à base de grappes comprend quatre étapes : la collecte du signal diffusé, l'extraction des paramètres du canal, le regroupement des paramètres en grappes et l'ajustement des grappes avec les modèles statistiques. Le signal diffusé peut être collecté par des mesures physiques ou des expériences numériques, telles que le tracé de rayons. Les paramètres du canal sont extraits du profil de retard de puissance (PDP) et du spectre angulaire de puissance (PAS) avec une estimation des paramètres statistiques. Les paramètres estimés sont regroupés à l'aide d'un algorithme de

regroupement, comme K-Power-Means. Enfin, la distribution des points de paramètres discrets à l'intérieur des grappes est ajustée à l'aide d'un modèle statistique. En raison de la faible probabilité de présence du trajet direct dans le canal 60 GHz, le tracé de rayon est introduit dans la norme IEEE 802.11ad pour collecter, numériquement, les données du signal. Les étapes de post-traitement d'estimation et de mise en grappes ont été remplacées par deux étapes de mesure discriminante. Les antennes sont pointées artificiellement vers la direction du faisceau cible, qui a été calculée à l'aide du tracé de rayon. Ensuite, la configuration intra-classe est directement mesurée avec l'antenne cornet.

Le modèle de canal IEEE 802.11ad ne prend pas suffisamment en compte l'atténuation causée par l'ombrage à grande échelle, en particulier la transmission distincte LOS et NLOS. Dans le scénario extérieur, les expériences ont montré que les probabilités de transmission LOS et NLOS diminuent de façon exponentielle avec l'augmentation de la distance. Par conséquent, le modèle de canal extérieur à ondes millimétriques, les transmissions LOS et NLOS ont été modélisées par des fonctions de probabilité exponentielles empiriques par rapport à la distance entre l'émetteur et le récepteur. Les fonctions de probabilité exponentielle des transmissions NLOS causées par le blocage des bâtiments à l'extérieur et le blocage du corps humain à l'intérieur sont expliquées mathématiquement avec la théorie de la géométrie stochastique.

Le blocage étant l'un des problèmes critiques en bande millimétrique. La solution la plus pratique pour contourner ce problème est une combinaison de formation de faisceaux couplée à une technique d’apprentissage de faisceaux qui consiste à effectuer un balayage et rechercher le meilleur SNR.

La formation de faisceaux est un filtre spatial adapté qui peut utiliser soit une architecture numérique soit une architecture analogique. Le choix de l’une ou l’autre se fera sur des critères d’énergie, de complexité ou de coût.

## 1.5. Objectifs de la Thèse

La formation de faisceau actuelle, complétement opérationnelle et efficace pour les communications très haut débit, n'est absolument pas adaptée à la localisation. En effet, la transmission NLOS, principale source d'erreur dans la détermination des coordonnées spatiales d’un objet, n’est pas identifiée dans la stratégie actuelle de formation de faisceau. Il est par conséquent impérieux de procéder, dans le cadre d’une nouvelle approche dans la formation des voies, à l'identification des composantes NLOS. C’est ce que nous proposons de faire dans ce mémoire.

# 2. État des lieux

## 2.1. NLOS Identification

La distinction entre les composantes LOS et NLOS peut s’apparenter à un problème de reconnaissance de formes supervisée. L'identification NLOS est donc un processus qui consiste à comprendre les

caractéristiques physiques inhérentes aux différents modes de propagation, à modéliser mathématiquement ces caractéristiques, puis à décider, après analyse statistique, du type de mode de transmission.

La différence physique naturelle entre les transmissions de type NLOS et de type LOS est liée au processus de diffusion. Les études actuelles sur l'identification des modes NLOS se sont principalement concentrées sur la technologie UWB principalement entre 3,1 GHz à 10,6 GHz. Contrairement au canal à ondes millimétriques, peu dense en termes de trajets multiples, les composantes multitrajets reçues sont ici nombreuses. Dans ce cas, si au moins une voie directe n'est pas obstruée, le scénario est défini comme un scénario LOS. Par conséquent, le travail cible de l'identification NLOS pour la transmission UWB actuelle consiste à distinguer, par la mesure, les stations LOS et NLOS, puis à identifier le scénario NLOS. Les travaux mentionnés ci-dessus utilisent généralement des différences statistiques dans les caractéristiques des canaux pour distinguer les situations LOS des situations NLOS.

Le processus physique doit être modélisé mathématiquement. En raison de la forte diffraction et de la richesse des composantes multitrajets, les différences statistiques entre la transmission LOS et la transmission NLOS dans la bande UWB, se produisent principalement dans le domaine temporel plutôt que dans le domaine spatial. En raison de la diffusion, l'affaiblissement du signal issu du trajet NLOS est généralement beaucoup plus important que celui issu du trajet LOS. Des valeurs moyennes plus élevées, et donc biaisées, et une plus grande variance du retard moyen sont obtenus dans le cadre d’un scénario NLOS.

Les mesures, extraites du modèle mathématique, permettent de définir, grâce à des algorithmes de décision statistique, une métrique qui détermine le type de transmission. L'identification NLOS utilise généralement trois types de métriques. Le premier type est la variance des portées estimées pour un ensemble de mesures qui peuvent être directement utilisées comme mesure pour identifier la transmission NLOS. Le deuxième type de métrique concerne les paramètres du modèle de canal ci-dessus, tels que TOA et AOA. Le troisième type de métrique est constitué des variables permettant de quantifier la forme de la PDF du CIR reçu.

La décision statistique est considérée comme un problème de test d'hypothèse (type test de Kolmogorov-Smirnov). Pour l'identification NLOS, l'hypothèse nulle est la transmission LOS, et l'hypothèse alternative est la transmission NLOS. Dans les études rapportées, des méthodes paramétriques et non paramétriques sont utilisées pour distinguer les types de transmission. La méthode paramétrique typique, utilisée pour l'identification NLOS, est le rapport de maximum de vraisemblance (MLR, *Maximum Likelihood Ratio*), tandis que les méthodes non paramétriques utilisées sont la machine à vecteur supporté (SVM) et le réseau neuronal artificiel (ANN). La performance du test d'hypothèse est évaluée avec la probabilité d'erreur de type I et de type II. L'erreur de type I est le rejet d'une véritable hypothèse nulle (identifier LOS comme NLOS), tandis que l'erreur de type II est l'acceptation d'une fausse hypothèse alternative (reconnaître NLOS comme LOS). Les études actuelles montrent que les méthodes non paramétriques offrent de meilleures performances que les méthodes paramétriques.

Les travaux actuels se concentrent principalement sur le CIR, dans le domaine temporel ou le CFR (*Channel Frequency Response*), dans le domaine fréquentiel. Cependant, l'effet des trajets multiples dans le canal millimétrique reste, en vertu de la grande directivité des antennes utilisées, assez faible, mais une

grande variabilité dans les distributions spatiales des transmissions est à souligner. En effet on peut, pour certaines directions, se trouver dans un scénario LOS et pour d'autres pas très éloignées des précédentes, dans un scénario NLOS. Les méthodes classiques d'identification basées sur des caractéristiques temporelles sont plus susceptibles d'échouer car les CIR en bande millimétrique avec des antennes directives contiennent moins de diversité de trajets multiples. Dans l'identification basée sur les directions d'arrivée ou de départ, la stratégie de balayage angulaire influence la façon dont on doit essayer de distinguer les composantes LOS des composantes NLOS. Comme dans la plupart des normes actuelles de 60 GHz, telles que la norme IEEE 802.11ad, la formation analogique de faisceaux induit un codebook d'entraînement de faisceaux discrets, le trajet direct et le multitrajet ne doivent pas être reçus ensemble, mais plus probablement séparés (avec des codebooks différents, c'est-à-dire des configurations de faisceaux différentes). De plus, la Rx balayant l'espace selon un codebook discret, le faisceau proche du chemin direct pourrait sauter par-dessus le chemin LOS, rendant ainsi le chemin direct « invisible ». Dans ce cas, l'identification NLOS signifie identifier le cluster NLOS. Ainsi, la discrimination de l'amas LOS/NLOS est l'objectif visée dans la bande millimétrique.

## 2.2. Méthodes de Regroupement

L'objectif du regroupement est de découvrir les groupements naturels d'objets non étiquetés présentant des similitudes. K-means est une méthode de regroupement partiel largement utilisée qui vise à minimiser la somme des erreurs entre le centroïde et les éléments de toutes les grappes. Elle minimise la distance euclidienne moyenne entre les points de données d'un groupe et la moyenne du groupe, ce qui signifie que le but de K-means est de rechercher des minima globaux. Une version améliorée de K-means, K-Power-Means, est également utilisée dans les procédures standard de modélisation des canaux. Au cours du processus itératif, le K-Power-Means standard minimise la somme des distances pondérées en fonction de la puissance des points de paramètres par rapport au centroïde associé au point de paramètre.

Le clustering de la K-means présente des faiblesses intrinsèques : tout d'abord, le nombre de clusters doit être supposé avant l'opération. Afin d'obtenir le nombre correct de grappes, la moyenne K doit être répétée plusieurs fois. Deuxièmement, une grappe initiale inappropriée conduira à un minimum local. Pour résoudre le problème d'initialisation, l'algorithme K-means++ a été introduit. Troisièmement, K-means traite toutes les caractéristiques de manière égale, quelle que soit la corrélation réelle entre les caractéristiques. Par conséquent, la forme physique de la grappe ne peut pas être préservée. Pour résoudre ce problème, le CIR doit être équipé d'une fonction exponentielle connue de l'homme. Cependant, une fonction prioriale détruit la nature non supervisée de la moyenne K.

# 3. Regroupement Spatial

## 3.1. Segmentation des Bassins Versants

Contrairement aux paramètres des canaux discrets communs qui sont généralement répartis sur une

grille non uniforme, comme dans le domaine temporel ou angulaire, le PAS à intervalle angulaire égal est plus proche d'une image en niveaux de gris. Dans une image numérique en niveaux de gris, une image est une grille portant des informations d'intensité discrètes. L'intensité de puissance peut être considérée comme une valeur de gris continue. La puissance relativement élevée constitue un avant-plan lumineux en forme de grappe, tandis que la gamme de puissance inférieure sert d'arrière-plan sombre. Les cellules d'échantillonnage sont des pixels. Par analogie, le clustering du PAS peut en fait s'inspirer des méthodes de clustering dans le domaine du traitement de l'image. Dans le traitement de l'image, l'opération de regroupement est appelée segmentation, ce qui signifie un ensemble d'opérations divisant une image numérique en plusieurs segments. Contrairement aux méthodes de segmentation globale telles que Kmeans, la méthode de traitement d'image locale, la morphologie mathématique, peut éviter la faiblesse de négliger la corrélation entre les pixels voisins, préservant ainsi les caractéristiques de forme de chaque cluster. Les vallées peuvent être segmentées avec les minima centraux et autour des maxima locaux. C'est l'idée de la segmentation des bassins versants : la segmentation des bassins versants consiste à trouver les centres des minima locaux et les limites des maxima locaux des groupes. Elle peut être liée à un problème de barrage des bassins versants au niveau des maxima pour éviter d'inonder le bassin inférieur. Les domaines délimités par les bassins versants sont les segments cibles qui constituent le groupe pour le modèle de canal.

## 3.2. PAS Simulé avec le Modèle de Canal de 60 GHz

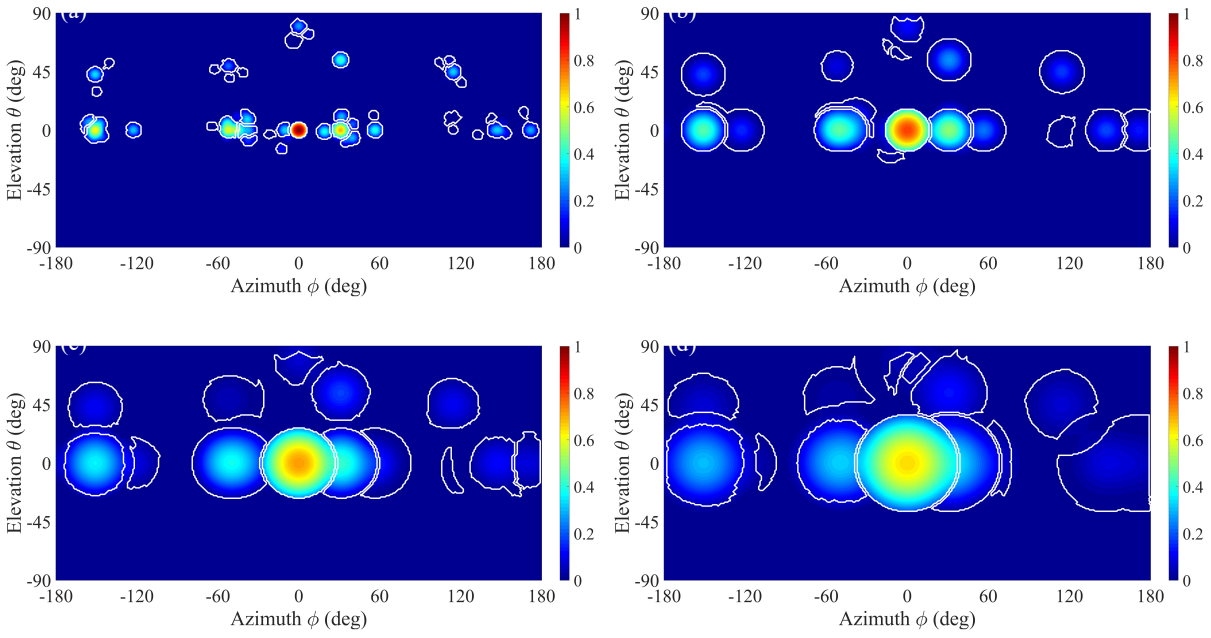


Figure 11 Résultat de la segmentation avec transformation du bassin versant avec une largeur de faisceau de (a) 5°; (b) 13°; (c) 21°; (d) 29°

Pour valider la faisabilité de la segmentation pour le PAS à 60 GHz avec la méthode des bassins versants, des simulations sont effectuées sur la base des données de puissance angulaire obtenues à partir du modèle de canal de l'IEEE 802.11ad dans le scénario de la conférence. La Figure 11 montre le résultat de la segmentation des bassins versants pour le PAS avec des largeurs de faisceau de 5°, 13°, 21° et 29°. Les

courbes fermées blanches sont les étiquettes des groupes d'avant-plan éclairés. Le domaine bleu foncé est le domaine de l'arrière-plan. Les étiquettes des clusters distinguent clairement les domaines d'avant-plan adjacents. La majeure partie de la puissance au premier plan est rassemblée en grappes, et l'arrière-plan avec une intensité de puissance hebdomadaire est clairement exclu des grappes.

## 3.3. Regroupement pour le Canal 60 GHz par Bassin Versant

Parce que la segmentation des bassins versants vise à résoudre le problème de la K-Power-Means, celle-ci est l'une des méthodes avec lesquelles nous devrions comparer notre approche. La comparaison montre que la transformation des bassins versants, qui reconstruit localement le champ de gradient, est plus appropriée que les techniques classiques telles que l'algorithme bien connu de K-mean pour extraire les grappes éclairées de l'arrière-plan sombre et séparer les grappes adjacentes dans le PAS. En outre, les simulations avec le modèle de canal IEEE 802.11ad ont montré que la segmentation des bassins versants préserve les formes des grappes.

# 4. Identification Spatiale de la NLOS

## 4.1. Mécanisme Physique d'Identification

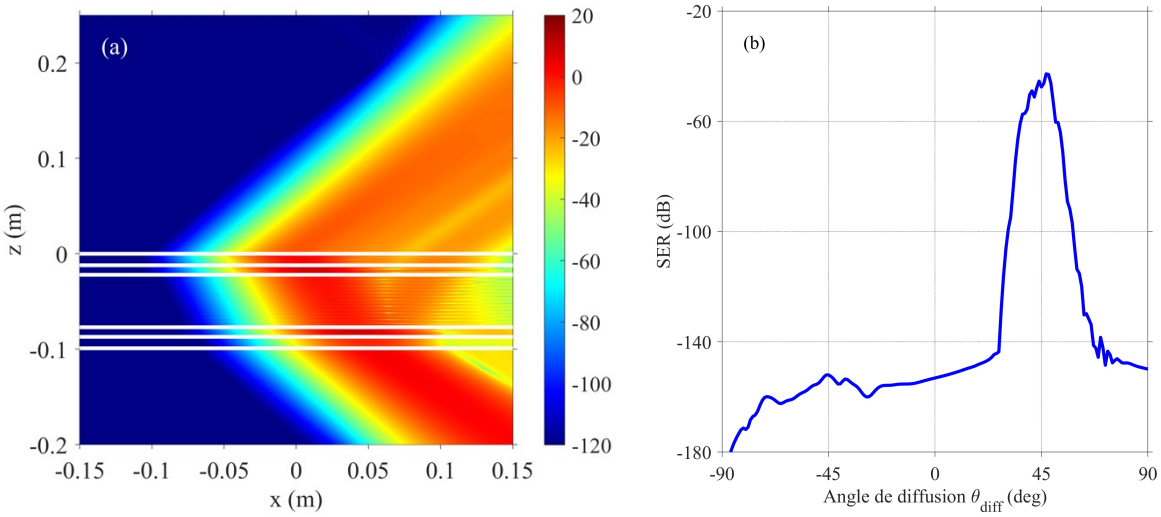


Figure 12 (a) Diffusion en champ proche et (b) Surface Equivalente Radar (SER) en champ lointain d'une onde TM incidente sur un mur en couches.

Dans le modèle IEEE 802.11ad, les grappes les plus simples sont générées par deux structures typiques pour les scénarios d'intérieur, à savoir un mur en couches et une surface rugueuse. Pour clarifier davantage le mécanisme physique à l'intérieur des grappes, la diffusion est simulée avec une méthode de simulation électromagnétique pleine onde, la méthode du moment (MOM), pour résoudre la diffusion des deux structures géométriques particulières. Sur la base du résultat de la simulation avec la MOM, une

caractéristique physique pour l'identification de la NLOS avec des faisceaux étroits est évidente. La forme des amas angulaires dans la carte PAS 2D est un moyen efficace d'étudier les caractéristiques des comportements de diffusion dans la transmission LOS ou NLOS, comme le montre la Figure 12. La configuration de la puissance transmise est préservée en raison de l'absence d'objets diffusants dans la transmission LOS. Cela illustre la motivation de notre travail.

## 4.2. Méthodes d'Identification

Le groupe de transmission LOS peut être identifié conjointement dans les domaines du temps et de l'espace. Dans le domaine temporel, le premier pic du CIR LOS est beaucoup plus fort que les autres pics. Cependant, le deuxième pic dans le cluster NLOS CIR est beaucoup plus fort. En général, le CIR LOS fluctue plus faiblement que les CIR NLOS, ce qui implique que la forme des fonctions de densité de probabilité (PDF) de l'amas LOS serait typiquement plus étroite que la PDF des amas NLOS par exemple. Dans le domaine des fréquences, le comportement sélectif du canal peut être observé dans la CFR. La CFR de la LOS est plate, tandis que la CFR de la NLOS présente des fluctuations, comme le montre la Figure 13.

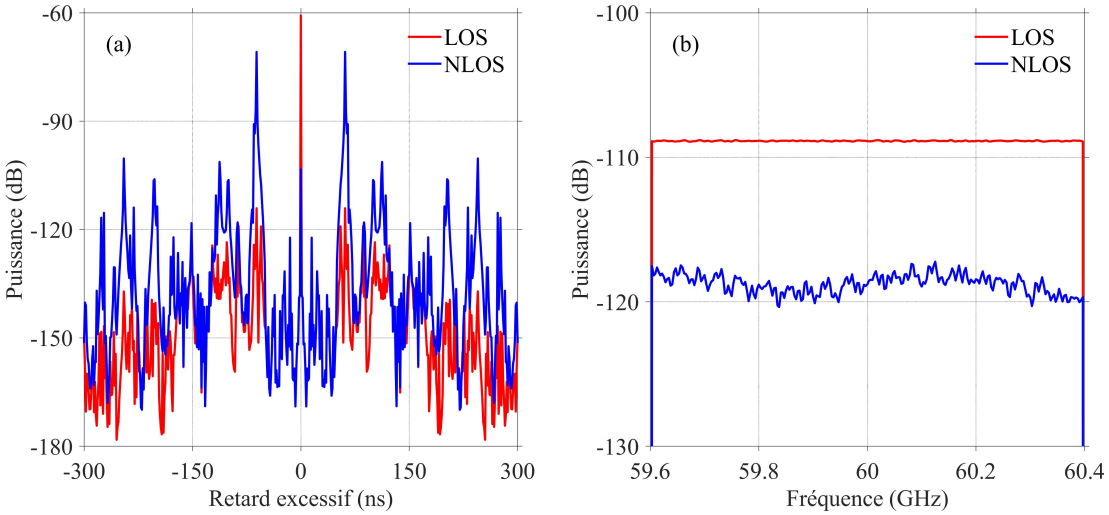


Figure 13 (a) CIR et (b) CFR des groupes LOS et NLOS de PAS générés par le modèle de canal IEEE 802.11ad.

Les pics de la CIR peuvent être caractérisés par une kurtosis, tandis que la fluctuation de fréquence dans la CFR peut être identifiée avec la largeur de bande de cohérence. Contrairement aux mesures liées à la distance, telles que l'énergie totale reçue et le retard excessif, le moment standard est une caractéristique intrinsèque indépendante de l'emplacement Rx-Tx. Le kurtosis est le moment standard du quatrième ordre pour évaluer la PDF. Le kurtosis de CIR $h(\tau)$ est

$$\kappa = \frac{E\left[\left(\left|h(\tau)\right| - \mu_{|h(\tau)|}\right)^4\right]}{E\left[\left(\left|h(\tau)\right| - \mu_{|h(\tau)|}\right)^2\right]^2} \tag{1}$$

Il s'agit du moment standard non biaisé d'ordre inférieur. Dans le domaine fréquentiel, si l'amas est en LOS, la fonction de transfert de fréquence est approximativement plate ; sinon, elle fluctuera sélectivement en fréquence en raison de la diffusion cohérente. La valeur moyenne éliminée par autocorrélation est pondérée par le niveau de puissance du signal reçu. La planéité du CFR $H(f)$ dans le band $B$ est évaluée par l'autocorrélation, après avoir supprimé la moyenne de $H(f)$ :

$$R(\Delta f) = \frac{1}{B}\int_0^B \left|\left(H(f) - \mu_H\right)\left(H(f-\Delta f) - \mu_H\right)\right| df \tag{2}$$

Dans le domaine spatial angulaire, limité par la capacité de la stratégie d'entraînement du faisceau, l'échantillonnage spatial grossier et la sélectivité limitée des faisceaux d'antenne rendent difficile l'évaluation précise de la PDF spatiale. Comme alternative, la forme des grappes est une métrique physique pour identifier le faisceau NLOS. La matrice de kurtosis utilisée pour évaluer la forme de la PDF est également efficace pour décrire la forme des grappes spatiales. La symétrie pondérée est une caractéristique intéressante pour représenter la forme des grappes. Le rapport entre les valeurs propres minimales et maximales (analyse en composantes principales) de la matrice de co-kurtosis peut être utilisé pour caractériser la symétrie de l'aplatissement des grappes.

$$\Sigma_k = \begin{bmatrix} k_{11}(\phi,\phi) & k_{12}(\phi,\theta) \\ k_{21}(\theta,\phi) & k_{22}(\theta,\theta) \end{bmatrix} \tag{3}$$

Où les éléments $k_{ij}$ sont la co-kurtosis pondérée par rapport aux angles d'azimut et d'élévation. L'analyse en composantes principales est effectuée en calculant le rapport entre les valeurs propres minimales et maximales par la décomposition de la matrice de co-kurtosis.

Dans notre travail, trois caractéristiques peuvent décrire un PAS, à savoir le rapport propre de la matrice de puissance $\hat{R}_P$, le rapport propre de la matrice de kurtosis temporelle $\hat{R}_t$ et le rapport propre de la matrice d'autocorrélation de fréquence $\hat{R}_f$. Par conséquent, les caractéristiques construisent un point de données avec les trois rapports ou chaque groupe dans l'espace des paramètres. Comme la transmission LOS est bénéfique pour la localisation, elle est donc définie comme l'hypothèse nulle de la vérification de l'hypothèse, tandis que l'hypothèse alternative est la transmission NLOS. Le test MLR et l'ANN sont utilisés pour classer les points de données LOS et NLOS.

# 4.3. Simulation Numérique

Avec le modèle de canal de l'IEEE 802.11ad, la faisabilité de l'identification NLOS est testée. Comme

première étape de validation, la méthodologie d'identification NLOS est d'abord mise en œuvre directement sur les données discrètes obtenues par le modèle de canal de l'IEEE 802.11ad. Ensuite, dans un deuxième temps, le Rx PAS est obtenu en effectuant une convolution de la réponse angulaire du canal discret avec le diagramme d'antenne. L'identification NLOS est ensuite appliquée sur ces PAS. Selon le résultat de la simulation de quatre scénarios dans le Tableau 1. La structure spatio-temporelle est séparée en grappes spatiales et la description temporelle à l'intérieur des grappes, ce qui signifie que les variables spatiales et temporelles sont distantes. Après avoir calculé les caractéristiques dans la coordonnée temporelle ou fréquentielle, la matrice spatiale de chaque grappe est extraite. La distribution bêta est induite pour s'adapter aux données échantillonnées. Le MLR et l'ANN sont utilisés pour identifier le type de transmission. Les erreurs des différents scénarios et la méthode de classification sont distinctes. En général, le MLR fournit une erreur de type I beaucoup plus élevée que le type II. La performance de l'ANN est bien meilleure que celle de la MLR pour l'identification NLOS.

Tableau 1 Probabilités d'erreur testées par MLR et ANN pour l'identification NLOS

| Erreur par canal | | Ratio Maximum de Vraisemblance | | | | Réseau Neuronal Artificiel |
|---|---|---|---|---|---|---|
| | | $\hat{R}_P$ | $\hat{R}_t$ | $\hat{R}_f$ | $\hat{R}_P\hat{R}_t\hat{R}_f$ | $(\hat{R}_P,\ \hat{R}_t,\ \hat{R}_f)$ |
| CM-1 | Type I | 0.3052 | 0.1408 | 0.2441 | 0.2113 | 0.0512 |
| | Type II | 0.0634 | 0.0685 | 0.0682 | 0.0668 | 0.0616 |
| CM-2 | Type I | 0.2074 | 0.0691 | 0.2166 | 0.1567 | 0.0865 |
| | Type II | 0.1457 | 0.1172 | 0.1392 | 0.1305 | 0.0398 |
| CM-3 | Type I | 0.1600 | 0.0550 | 0.1600 | 0.1550 | 0.0096 |
| | Type II | 0.0905 | 0.1007 | 0.0861 | 0.0871 | 0.0576 |
| CM-4 | Type I | 0.1972 | 0.0394 | 0.1362 | 0.0640 | 0.0421 |
| | Type II | 0.0570 | 0.0693 | 0.0594 | 0.0583 | 0.0472 |

# 4.4. Validation Expérimentale

Tableau 2 Probabilités d'erreur testées par MLR et ANN avec des caractéristiques mesurées

| Erreur | MLR | | | | ANN |
|---|---|---|---|---|---|
| | $\hat{R}_P$ | $\hat{R}_t$ | $\hat{R}_f$ | $\hat{R}_P\hat{R}_t\hat{R}_f$ | $(\hat{R}_P,\ \hat{R}_t,\ \hat{R}_f)$ |
| Type I | 0.3713 | 0.3832 | 0.4371 | 0.3533 | 0.1548 |
| Type II | 0.2892 | 0.2827 | 0.2885 | 0.2878 | 0.1627 |

Pour vérifier l'efficacité de la méthode d'identification NLOS ci-dessus, une validation expérimentale est effectuée en laboratoire. La procédure de validation est similaire au flux de simulation. Le PAS mesuré est regroupé avec l'algorithme de bassin versant. Le rapport entre la valeur propre minimale et la valeur propre maximale de la matrice d'aplatissement de puissance, de la matrice d'aplatissement temporel et de la matrice d'aplatissement de fréquence est utilisé comme mesure d'identification. Les données mesurées sont équipées d'une distribution généralisée des valeurs extrêmes. Le test de Kolmogorov-Smirnov est utilisé pour tester la qualité de l'ajustement. Le type de transmission est identifié par MLR et ANN. Pour l'identification NLOS, la performance de l'ANN est également bien meilleure que celle du MLR, comme le

montre la Tableau 2.

# 5. Conclusion

La bande millimétrique est un excellent candidat pour la localisation en intérieur en raison de la large bande disponible. La transmission en mode NLOS reste l'une des sources d'erreurs les plus importantes dans ce type de localisation. Le phénomène de blocage ou l'écrantage provoquée, dans la bande millimétrique, par la très grande directivité des antennes est compensé par des solutions de type formation de faisceau. La connexion entre objets s'en trouve améliorée mais cela présente l'inconvénient d'aggraver, pour la localisation, les effets liés à ce type de transmission NLOS. La précision de localisation est par conséquent grandement dégradée.

Pour résoudre cette difficulté, il faut être en mesure de se prononcer sur la présence, dans les signaux utiles, de la composante LOS et de mettre en place les stratégies pour réduire les effets des trajets NLOS.

La structure spatio-temporelle d'un canal de transmission est exploitée à cette fin pour identifier sans ambiguïté la transmission LOS. En effet, on montre en considérant aussi bien les résultats simulation que les résultats de mesure, que la symétrie de la grappe est une caractéristique essentielle de la transmission LOS. Les différentes analyses de la matrice de puissance, temporelle et spatiale restent des approches efficaces pour évaluer la symétrie des grappes dans différentes dimensions. Dans le cadre de l'évaluation des erreurs de type I et II, la performance de l'identification de l'ANN est bien meilleure que celle du MLR.